Winter 2001

Finite Element Analysis and Active Control for Nonlinear Flutter of Composite Panels Under Yawed Supersonic Flow

Khaled Abdel-Motagaly
Old Dominion University

FINITE ELEMENT ANALYSIS AND ACTIVE CONTROL FOR NONLINEAR FLUTTER OF COMPOSITE PANELS UNDER YAWED SUPERSONIC FLOW

by

Khaled Abdel-Motagaly
B.S. July 1991, Cairo University, Egypt
M.S. July 1995, Cairo University, Egypt

A Dissertation Submitted to the Faculty of
Old Dominion University in Partial Fulfillment of the
Requirement for the Degree of

DOCTOR OF PHILOSOPHY

AEROSPACE ENGINEERING

OLD DOMINION UNIVERSITY
December 2001

Approved by:

Chuh Mei (Director)

Osama Kandil (Member)

Jen-Kuang Huang (Member)

Donald Kunz (Member)

ABSTRACT

FINITE ELEMENT ANALYSIS AND ACTIVE CONTROL
FOR NONLINEAR FLUTTER OF COMPOSITE PANELS
UNDER YAWED SUPERSONIC FLOW

Khaled Abdel-Motagaly
Old Dominion University, 2001
Director: Dr. Chuh Mei

A coupled structural-electrical modal finite element formulation for composite panels with integrated piezoelectric sensors and actuators is presented for nonlinear panel flutter suppression under yawed supersonic flow. The first-order shear deformation theory for laminated composite plates, the von Karman nonlinear strain-displacement relations for large deflection response, the linear piezoelectricity constitutive relations, and the first-order piston theory of aerodynamics are employed. Nonlinear equations of motion are derived using the three-node triangular MIN3 plate element. Additional electrical degrees of freedom are introduced to model piezoelectric sensors and actuators. The system equations of motion are transformed and reduced to a set of nonlinear equations in modal coordinates. Modal participation is defined and used to determine the number of modes required for accurate solution.

Analysis results for the effect of arbitrary flow yaw angle on nonlinear supersonic panel flutter for isotropic and composite panels are presented. The results show that the flow yaw angle has a major effect on the panel limit-cycle oscillation amplitude and deflection shape. The effect of combined aerodynamic and acoustic pressure loading on the nonlinear dynamic response of isotropic and composite panels is also presented. It is found that combined acoustic and aerodynamic loads have to be considered for high aerodynamic pressure values.

Simulation studies for nonlinear panel flutter suppression using piezoelectric self-sensing actuators under yawed supersonic flow are presented for isotropic and composite panels. Different control strategies are considered including linear quadratic Gaussian (LQG), linear quadratic regulator (LQR) combined with the extended Kalman filter (EKF), and optimal output feedback. Closed loop criteria based on the norm of feedback

control gain (NFCG) and on the norm of Kalman filter estimator gain (NKFEG) are used to determine the optimal location of piezoelectric actuators and sensors, respectively. Optimal sensor and actuator locations for a range of yaw angles are determined by grouping the optimal locations for different angles within the range. The results demonstrate the effectiveness of piezoelectric materials and of the nonlinear output controller comprised of LQR state feedback and EKF nonlinear state estimator in suppressing nonlinear flutter of isotropic and composite panels at different flow yaw angles.

ACKNOWLEDGMENTS

I would like to express my sincere thanks and deepest appreciation to Professor Chuh Mei for his everlasting assistance, encouragement, support, and patience. His guidance, inspiring ideas, and enlightening discussion played a key role in the production of this work. I would also like to extend my sincere thanks and deep gratitude to the other members of my dissertation committee: Professors Osama Kandil, Donald Kunz, and Jen-Kuang Huang. Their invaluable comments and advice are much appreciated and are an added value to this dissertation. I gratefully acknowledge the financial support of the Aerospace Engineering Department during the course of my research.

I extend my thanks and gratitude to Professor Sayed Dessoki, who taught me a lot during my entire career. Last, but not least, special acknowledgment and thanks go to my parents and my wife for their everlasting love and encouragement. Without their support, this work would have been impossible.

TABLE OF CONTENTS

Page

LIST OF TABLES viii

LIST OF FIGURES ix

LIST OF SYMBOLS xiv

Chapter

I. INTRODUCTION AND LITERATURE SURVEY 1

1.1 Introduction 1

1.2 Background and Literature Survey 2

1.2.1 Panel Flutter 2

1.2.2 Piezoelectric Sensors and Actuators 8

1.2.3 Panel Flutter Suppression Using Piezoelectric Materials 11

1.3 Outline of the Study 13

II. FINITE ELEMENT FORMULATION 19

2.1 Introduction 19

2.2 Element Displacement Functions 20

2.3 Nonlinear Strain-Displacement Relations 22

2.4 Electrical Field-Potential Relations 23

2.5 Linear Piezoelectricity Coupling Equations 24

2.6 Constitutive Equations 25

2.7 Laminate Resultant Forces and Moments 26

2.8 Aerodynamic Pressure Loading 27

2.9 Element Equations of Motion and Matrices 28

2.9.1 Generalized Hamilton's Principle 28

2.9.2 Element Stiffness and Electromechanical Coupling Matrices 29

2.9.3 Element Mass Matrices 34

2.9.4 Element Aerodynamic Matrices 35

2.9.5 Element Equations of Motion 36

2.10 System Equations of Motion 37

2.11 Piezoelectric Actuator and Sensor Equations 38

2.11.1 Piezoelectric Material as Actuators and Sensors 38
2.11.2 Piezoelectric Material as Self-Sensing Actuators 40
III. MODAL REDUCTION AND SOLUTION PROCEDURE 45
3.1 Introduction 45
3.2 Governing Equations 46
3.3 Modal Transformation and Reduction 48
3.4 Solution Procedure 51
3.4.1 Time Domain Method 51
3.4.2 Frequency Domain Method 51
3.4.2.1 Critical Flutter Boundary 51
3.4.2.2 Nonlinear Flutter Limit-Cycle Oscillation 53
IV. FINITE ELEMENT ANALYSIS RESULTS 57
4.1 Introduction 57
4.2 Finite Element Validation 57
4.2.1 Natural Frequencies 57
4.2.2 Piezoelectric Static Actuation 58
4.2.3 Linear and Nonlinear Flutter 58
4.2.4 Nonlinear Random Response 59
4.3 Effect of Flow Yaw angle on Nonlinear Panel Flutter 60
4.3.1 Isotropic Panels 60
4.3.2 Composite Panels 61
4.3.3 Triangular Panel 62
4.4 Effect of Combined Supersonic Flow and Acoustic Pressure Loading 62
4.4.1 Random Surface Pressure 62
4.4.2 Isotropic Panel 63
4.4.3 Composite Panel 64
4.5 Summary 65
V. CONTROL METHODS AND OPTIMAL PLACEMENT
OF PIEZOELECTRIC SENSORS AND ACTAUTORS 99
5.1 Introduction 99
5.2 State Space Representation 99

5.3 Control Methods 101
5.3.1 Linear Quadratic Regulator (LQR) 101
5.3.2 Optimal Linear State Estimation 102
5.3.3 Linear Quadratic Gaussian Controller (LQG) 103
5.3.4 Extended Kalman Filter (EKF) 104
5.3.5 Nonlinear Controller using EKF and LQR 104
5.3.6 Optimal Output Feedback 105
5.4 Optimal Placement of Piezoelectric Sensors and Actuators 105
VI. NONLINEAR PANEL FLUTTER SUPPRESSION RESULTS 109
6.1 Introduction 109
6.2 Square Isotropic Panel 109
6.2.1 Optimal Placement of Self-Sensing Piezoelectric Actuators 110
6.2.2 Controller Study 111
6.2.2.1 LQR Controller 112
6.2.2.2 LQG Controller 113
6.2.2.3 Nonlinear Output Controller (EKF+LQR) 113
6.2.2.4 Optimal Output Feedback Controller 114
6.2.2.5 Controller Robustness 115
6.2.3 Panel Flutter Control with Yawed Flow 116
6.3 Composite Panel 118
6.4 Triangular Panel 119
6.5 Summary 120
VII. SUMMARY AND CONCLUSIONS 158
REFERENCES 161
APPENDCIES 172
A. MIN3 ELEMENT STRAIN INTERPOLATION MATRICES 172
B. COORDINATE TRANSFORMATION 174
B.1 Transformation of Lamina Stiffness Matrices 174
B.2 Transformation of Piezoelectric Constants 175
C. SOLUTION PROCEDURE FOR OPTIMAL OUTPUT FEEDBACK 176
VITA 177

LIST OF TABLES

Table — Page

1.1 Panel Flutter Theories 16

1.2 Analogy between electrical and mechanical variables for piezoelectric materials 16

4.1 Material properties for the different materials used for finite element validation and analysis results 66

4.2 Comparison between natural frequencies using MIN3 element and using analytical solution for square isotropic panel 67

4.3 Comparison of static deflection for the piezoelectric bimorph beam (10^{-7} m) using different methods 67

4.4 Comparison of nondimensional linear flutter boundary using different methods at different flow angles 68

4.5 Comparison of the RMS (W_{max}/h) for a simply supported rectangular (15×12×0.04 in.) isotropic plate under acoustic pressure loading only using different methods and mode numbers 68

4.6 Modal participation values at various limit-cycle amplitudes and different flow angles for simply supported square panel 69

4.7 Modal participation values at various limit-cycle amplitudes and different flow angles for simply supported rectangular graphite/epoxy $[0/45/-45/90]_S$ panel ... 70

4.8 Modal participation values at various limit-cycle amplitudes and different flow angles for simply supported rectangular graphite/epoxy [-40/40/-40] panel 71

4.9 Modal convergence for clamped rectangular $[0/45/-45/90]_S$ graphite/epoxy panel at SPL = 120 dB and λ = 800 72

4.10 Modal participation for a clamped rectangular $[0/45/-45/90]_S$ graphite/epoxy panel at SPL = 120 dB and λ = 800 72

6.1 Mechanical and electrical properties for PZT5A piezoelectric ceramics 122

6.2 Comparison of different controllers performance for nonlinear panel flutter suppression 122

LIST OF FIGURES

Figure — Page

1.1 Explanation of nonlinear panel flutter phenomenon 17

1.2 Schematic of traditional isotropic piezoelectric element 18

2.1 Composite panel under yawed supersonic flow and acoustic pressure loading 42

2.2 Composite laminate composed of n layers with n_p piezoelectric layers 43

2.3 MIN3 element geometry and area coordinates 44

3.1 Configuration of self-sensing piezoelectric actuators for bending moment actuation and transverse displacement sensing 55

3.2 Iterative solution procedure for nonlinear panel flutter limit-cycle response 56

4.1 Typical MIN3 elements mesh used to model rectangular and triangular panels 73

4.2 Clamped piezoelectric bimorph beam modeled using MIN3 elements 74

4.3 Validation of flutter limit-cycle amplitude for simply supported square isotropic panel 75

4.4 Validation of flutter limit-cycle amplitude for simply supported square $[0/45/-45/90]_S$ laminate 76

4.5 Finite element mesh convergence for simply supported isotropic square panel at 45° flow angle and using 16 modes 77

4.6 Modal convergence for simply supported isotropic square panel at 0° flow angle 78

4.7 Modal convergence for simply supported isotropic square panel at 45° flow angle 79

4.8 Effect of flow yaw angle on limit-cycle amplitude for simply supported isotropic square panel 80

4.9 Effect of panel aspect ratio at different yaw angles on limit-cycle amplitude for simply supported isotropic panels 81

4.10 Flutter mode shape at different flow angles for simply supported isotropic square panel 82

4.11 Modal convergence for simply supported rectangular graphite/epoxy $[0/45/-45/90]_S$ panel at 45° flow angle 83
4.12 Effect of flow yaw angle on limit-cycle amplitude for simply supported rectangular graphite/epoxy $[0/45/-45/90]_S$ panel 84
4.13 Flutter mode shape at different flow angles for simply supported rectangular graphite/epoxy $[0/45/-45/90]_S$ panel 85
4.14 Modal convergence for simply supported rectangular graphite/epoxy [-40/40/-40] panel at 45° flow angle 86
4.15 Effect of flow yaw angle on limit-cycle amplitude for simply supported rectangular graphite/epoxy [-40/40/-40] panel 87
4.16 Flutter mode shape at different flow angles for simply supported rectangular graphite/epoxy [40/-40/40] panel 88
4.17 Modal convergence for simply supported triangular isotropic panel at 45° flow angle 89
4.18 Effect of flow yaw angle on limit-cycle amplitude for simply supported triangular isotropic panel 90
4.19 Power spectral density of random input pressure at SPL = 90dB 91
4.20 RMS of maximum deflection for simply supported square isotropic panel under combined acoustic and aerodynamic pressures 92
4.21 Time and frequency response for simply supported square isotropic panel at SPL = 100 dB and $\lambda = 0$ 93
4.22 Time and frequency response for simply supported square isotropic panel at SPL = 120 dB and $\lambda = 0$ 94
4.23 Time and frequency response for simply supported square isotropic panel at SPL = 0 dB and $\lambda = 800$ 95
4.24 Time and frequency response for simply supported square isotropic panel at SPL = 100 dB and $\lambda = 800$ 96
4.25 Time and frequency response for simply supported square isotropic panel at SPL = 120 dB and $\lambda = 800$ 97
4.26 RMS of maximum deflection for clamped rectangular graphite/epoxy $[0/45/-45/90]_S$ panel 98

5.1 Block diagram representation of the LQG controller 107
5.2 Nonlinear dynamic compensator for nonlinear panel flutter suppression using EKF and LQR 108
6.1 Contours of (a) NFCG and (b) NKFEG for simply supported square isotropic panel at 0° flow angle 123
6.2 Contours of (a) NFCG and (b) NKFEG for simply supported square isotropic panel at 45° flow angle 124
6.3 Selected self-sensing piezoelectric actuators placement and size for optimal actuation and optimal sensing on square isotropic panel at 0° flow angle 125
6.4 Self-sensing piezoelectric actuators placement and size for optimal actuation and optimal sensing on square isotropic panel at 45° flow angle 126
6.5 Variation of first 4 linear modes versus λ for isotropic panel with and without added piezoelectric material 127
6.6 Open loop poles for isotropic square panels with embedded piezoelectric material at different values of nondimensional dynamic pressure 128
6.7 Limit-cycle amplitude and control inputs time history for square isotropic panel using LQR control at $\lambda = 1500$ 129
6.8 Comparison between actual LCO amplitude and estimated LCO amplitude using Kalman filter at $\lambda = 1000$ 130
6.9 Comparison between actual LCO amplitude and estimated LCO amplitude using Kalman filter at $\lambda = 2000$ 131
6.10 Performance of LQG controller at $\lambda = 1500$ 132
6.11 Performance of LQG controller at the maximum suppressible dynamic pressure, $\lambda max = 920$ 133
6.12 Comparison between actual and estimated LCO amplitude using extended Kalman filter at $\lambda = 2000$ 134
6.13 Performance of LQR+EKF nonlinear output compensator at $\lambda = 1500$ 135
6.14 Performance of LQR+EKF nonlinear output controller at $\lambda = 1500$ with (a) -25% and (b) +25% uncertainty in the model nonlinear stiffness matrix 136
6.15 Performance of optimal output feedback controller using two self-sensing actuators at $\lambda max = 1000$ 137

6.16 Performance of optimal output feedback controller using single leading edge actuator and two displacement sensors at λmax = 1100 138

6.17 Effect of +25% mismatch in λ between design model and simulation model on LQR and LQR+EKF control performance at λ = 1200 139

6.18 Effect of design model linear stiffness variation on The LQR+EKF controller performance at λ = 1500 140

6.19 Effect of design model linear stiffness variation on optimal output feedback controller performance at λ = 1100 141

6.20 Performance of EKF+LQR controller designed for zero flow angle at λ = 800 and 45 deg flow angle 142

6.21 Optimal actuator and sensor placement at different flow angles from 0 to 90° for square isotropic panel 143

6.22 Placement of four self-sensing piezoelectric actuators for optimal actuation and optimal sensing over the range of [0, 90°] flow angle for square isotropic panel 144

6.23 Comparison of panel flutter suppression performance using LQR+EKF control at different flow yaw angles and using different piezoelectric placement configurations for a square isotropic panel 145

6.24 Performance of LQR+EKF controller for square isotropic panel with 4 self-sensing piezoelectric actuators at 0° flow yaw angle and λ = 1500 146

6.25 Performance of LQR+EKF controller for square isotropic panel with 4 self-sensing piezoelectric actuators at 45° flow yaw angle and λ = 1500 147

6.26 Performance of LQR+EKF controller for square isotropic panel with 4 self-sensing piezoelectric actuators at 90° flow yaw angle and λ = 1500 148

6.27 Optimal actuator placement at different flow angles for $[0/45/-45/90]_S$ composite rectangular panel 149

6.28 Optimal placement of 2 embedded piezoelectric actuators that cover flow angles from 0° to 90° for $[0/45/-45/90]_S$ composite rectangular panel 150

6.29 Comparison of panel flutter suppression performance using LQR+EKF control at different flow yaw angles and using different piezoelectric actuator configurations for $[0/45/-45/90]_S$ rectangular composite panel 151

6.30 Performance of LQR+EKF controller for rectangular composite panel at 0^{o} flow yaw angle and $\lambda = 900$ 152

6.31 Performance of LQR+EKF controller for rectangular composite panel at 45^{o} flow yaw angle and $\lambda = 900$ 153

6.32 Performance of LQR+EKF controller for rectangular composite panel at 90^{o} flow yaw angle and $\lambda = 900$ 154

6.33 Optimal actuator placement at different flow angles for clamped triangular isotropic panel 155

6.34 Optimal placement of a single self-sensing piezoelectric actuator that approximately cover all angles from 90^{o} to 180^{o} for triangular clamped isotropic panel 156

6.35 Performance of the LQR+EKF controller in suppressing nonlinear panel flutter using different piezoelectric actuator configurations for the clamped triangular isotropic panel 157

CHAPTER I

INTRODUCTION AND LITERATURE SURVEY

1.1 Introduction

Recently, there has been a renewed interest in flight vehicles that operate at high supersonic and hypersonic Mach numbers, such as the X-38 Crew Return Vehicle spacecraft for the International Space Station, the X-33 Advanced Technology Demonstrator, the X-34 Reusable Technology Demonstrator for a launch vehicle, and the recent NASA Space Launch Initiative (SLI) project. The exterior panels of such vehicles will be affected by supersonic panel flutter phenomena. These flight vehicles will usually operate for a range of flow yaw angles and will also be subjected to additional loading due to random pressure fluctuations (sonic fatigue). This brings an urgent need for panel flutter analysis at supersonic speeds considering the effect of flow yaw angle and the effect of additional acoustic loading.

The requirements of energy-efficient, high-strength, and minimum-weight vehicles have generated an interest in advanced lightweight composite materials. In addition, higher performance can be obtained by using the recently developed smart or adaptive materials such as piezoelectric ceramics that are embedded into the laminated composite panels to control and suppress undesired panel vibrations.

The primary objectives of this study are: (1) to develop a finite element tool for analyzing nonlinear supersonic flutter of composite panels considering the effects of flow yaw angle and the effect of additional acoustic loading and (2) to design practical control methodologies that suppress nonlinear supersonic panel flutter of composite and isotropic panels using piezoelectric sensors and actuators considering the effect of flow yaw angle. The next sections present an overview and literature survey for the main topics of this research including classical and finite element analysis methods for nonlinear panel flutter, piezoelectric sensors and actuators, and panel flutter suppression using piezoelectric materials. An outline of the dissertation is then given at the end of the chapter.

The journal model used for this dissertation is the *AIAA Journal*.

1.2 Background and Literature Survey

1.2.1 Panel Flutter

Supersonic panel flutter is a self-excited oscillation of panels exposed to aerodynamic flow with high Mach numbers. Figure 1.1 shows four different schematics explaining the panel flutter phenomenon. For dynamic pressures, q, less than the flutter boundary, random pressure fluctuations due to turbulent boundary layer control the panel response. At this regime, the panel response can be determined using standard linear sonic fatigue (noise) analysis techniques and is usually in the small displacement region, i.e., maximum panel displacement divided by panel thickness (W_{max}/h) is much less than one. As the dynamic pressure increases, the panel stiffness is modified by the aerodynamic loading such that the first mode natural frequency, ω, increases while the second mode natural frequency decreases. At the flutter boundary, the two modes coalesce and the panel motion becomes unstable, based on linear structure theory. However, due to the structural nonlinearities (inplane stretching forces) and unlike the catastrophic failure for wing flutter, the panel motion is limited to a constant amplitude oscillation. The inplane stretching forces tend to restrain the panel motion so that bounded limit-cycle oscillations (LCO) are observed as shown in Figure 1.1. The amplitude of the LCO grows as the dynamic pressure increases. The existence of LCO implies that large deflection nonlinear structural theory should be used beyond the flutter critical dynamic pressure to estimate panel response and fatigue life. The flutter LCO deflection shape depends on many factors such as flow yaw angle, panel boundary conditions, and composite laminate stacking. An example of flutter deflection shape for an isotropic simply supported square panel is shown in Figure 1.1.

Since the late fifties and early sixties, there have been many articles in the literature addressing linear and nonlinear panel flutter. An excellent review article for linear and nonlinear panel flutter theories and analysis through 1970 is given by Dowell [1]. Recently, Mei et al. [2], have produced an extensive review of various analytical and experimental results for nonlinear supersonic and hypersonic panel flutter up to 1999. Dowell [1] has grouped the vast amount of theoretical literature on panel flutter into four categories based on the structural and aerodynamic theories used. Gray and Mei [3]

added a fifth category for hypersonic flow. The five different categories of linear and nonlinear panel flutter are shown in Table 1.1. The weakness and remedies for the first four types of analysis were discussed in detail by Dowell. A review of the finite element method of type-1 panel flutter analysis was given by Bismark-Nasr [4]. A survey on various analytical methods, including finite element method for nonlinear supersonic panel flutter type-3 analysis, was given by Zhou et al. [5]. The fundamental theories and physical understanding of panel flutter are given in detail in published books, [6] and [7]. This study is concerned with the type-3 panel flutter analysis that uses nonlinear structure theory and linear piston theory of aerodynamics with yawed supersonic flow.

As disclosed by these survey papers, a vast quantity of literature exists on panel flutter using different aerodynamic theories. The aerodynamic theory employed for the most part of panel flutter at high supersonic Mach numbers ($M_\infty > 1.6$) is the quasi-steady first order piston theory developed by Ashley and Zartarian [8]. If aerodynamic damping is neglected, the quasi-steady piston theory simplifies to the quasi-static Ackeret theory. The piston theory, although several decades old, has generally been employed to approximate the aerodynamic loads on the panel from local pressures generated by the body's motion as related to the local normal component of the fluid velocity and the local pressure. For supersonic Mach numbers, the quasi-steady aerodynamic theory reasonably estimates the aerodynamic pressures and shows fair agreement between theory and experiment for plates exposed to static pressure loads and buckled by uniform thermal expansion, as was shown by Ventres and Dowell [9]. For airflow with Mach numbers close to one, the full-linearized inviscid potential theory of aerodynamics is usually employed [10]. For hypersonic panel flutter, the nonlinear unsteady third-order piston theory is used to develop the aerodynamic pressure, [11] and [3].

The partial nonlinear behavior of a fluttering panel was first considered by several investigators such as [12-14]. They were primarily concerned with determining stability boundaries of two-dimensional plates. For nonlinear limit-cycle behavior, a variety of methods have been employed to assess the panel flutter problem. Galerkin's method was used to reduce the governing partial differential equations to a set of coupled ordinary differential equations in time, which were numerically integrated using arbitrary initial conditions. The integration was continued until a limit-cycle oscillation of constant

amplitude, independent of the initial conditions, was reached. The nonlinear oscillations of simply supported [15], and clamped [16, 17] fluttering plates were studied using this method. Dowell [15] determined that the direct numerical integration approach required a minimum of 6 linear modes, as the Galerkin approximate functions, to achieve a converged solution for displacements. Recently, the limit-cycle oscillation of a cantilever plate was studied by Weiliang and Dowell [18]. They employed a Rayleigh-Ritz approach in conjunction with the direct numerical integration and showed that the length-to-width ratio of the cantilever plate was a significant factor on the flutter vibration.

Various techniques in the temporal domain such as harmonic balance and perturbation techniques have been successfully employed to study the problem of nonlinear panel flutter. The harmonic balance method requires less computational time than the method of direct integration and is mathematically comprehensible and systematic, but it is extremely tedious to implement. The method was used by Bolotin [14] and Kobayashi [17] with two-mode Galerkin solution to obtain the limit-cycle motions. Rectangular plates were treated by Kuo et al. [19], Eastep and McIntosh [20], Eslami and Ibrahim [21], and Yuen and Lau [22]. The Rayleigh-Ritz approximation to Hamilton's variational principle was employed by Eastep and McIntosh to obtain the equations of motion in the spatial domain. Special orthotropic panels were studied by Eslami and Ibrahim. A hinged two-dimensional fluttering plate with moderately high postbuckling loads using a four-mode expansion and an incremental harmonic balance method was reported by Yuen and Lau. The perturbation method was employed to the problem of nonlinear panel flutter by Morino [23] and Kuo et al. [19]. Detailed extensions and stability analysis of this technique to nonlinear panel flutter were studied by Morino and Kuo [24] and Smith and Morino [25]. Correlation between perturbation techniques and the harmonic balance method has been shown to be in good agreement by Kuo et al. [19] and Morino and Kuo [24].

All of the early studies in nonlinear panel flutter using classical methods have been limited to isotropic or orthotropic, two or three-dimensional, rectangular plates with all four edges simply supported or clamped. Extension of the finite element method to study the linear panel flutter problem was due to Olson [26, 27] using a frequency domain eigenvalue solution. Because of its versatile applicability, effects of aerodynamic

damping, complex panel configurations and support conditions, laminated composite anisotropic panel properties, flow angularities, inplane stresses, and thermal loads can be easily and conveniently included in the finite element formulation. A survey on the finite element methods for linear panel flutter was given by Yang and Sung [28] and Bismark-Nasr [4], and for nonlinear panel flutter by Zhou et al. [5]. Application of the finite element method to study the supersonic limit-cycle oscillations of two-dimensional panels was given by Mei [29] using an iterative frequency domain solution. Mei and Rogers [30] implemented the two-dimensional panel flutter analysis into NASTRAN. Rao and Rao [31] investigated the supersonic flutter of two-dimensional panels with ends restrained elastically against rotation. Sarma and Varadan [32] studied the nonlinear behavior of two-dimensional panels using two solution procedures, both in the frequency domain. Further extension of the finite element method to treat supersonic limit-cycle oscillations of three-dimensional rectangular plates was given by Mei and Weidman [33]. The effects of damping, aspect ratio, inplane forces, and boundary conditions were considered. Mei and Wang [34] employed an 18-degree of freedom (DOF) triangular plate bending element to study supersonic limit-cycle behavior of three-dimensional triangular plates. Han and Yang [35] used the 54-DOF high order triangular plate element to study nonlinear panel flutter of three-dimensional rectangular plates with inplane forces.

Few papers in the literature have investigated supersonic limit-cycle oscillations of composite panels. Dixon and Mei [36] studied the nonlinear flutter of rectangular composite panels. The limit-cycle response was obtained using a 24-DOF rectangular plate element and a linearized updated mode with nonlinear time function (LUM/NTF) approximate solution procedure. The LUM/NTF solution procedure in the frequency domain was developed by Gray [11]. Because of the renewed interest in panel flutter at high-supersonic/hypersonic speeds [37], Gray et al. [3] and [11] extended the finite element method to investigate the hypersonic limit-cycle oscillations of composite panels using the full third-order piston aerodynamic theory. In practice, aerodynamic heating will cause thermal loading on the panel in addition to the aerodynamic loading. Xue et al. [38, 39] investigated flutter boundaries of thermally buckled two-dimensional and three-dimensional isotropic panels of arbitrary shape using the discrete Kirchhoff theory (DKT)

triangular plate element. The finite element equations in structure node DOF were separated into two sets of equations and then solved sequentially. The first set of equations yields the thermal-aerodynamic equilibrium position using Newton-Raphson iterative method, and the second set of equations leads to the flutter limit-cycle motions using the LUM/NTF approximate method. The use of LUM/NTF approximate method has been successful in studying nonlinear panel flutter. However, the application of the LUM/NTF method to the system equations has three disadvantages: (1) the number of structure node DOF of $\{W\}$ is usually very large, (2) at each iteration, the element nonlinear stiffness matrices have to be evaluated and the system nonlinear matrices have to be assembled, and (3) the periodic and chaotic panel motions can not be determined. Zhou et al. [40] introduced a solution to these problems by transforming the structure DOF system equations of motion into a set of modal coordinates of rather small DOF. The structural system equations of motion are thus transformed to the general Duffing-type reduced modal equations with constant nonlinear modal stiffness matrices.

The effect of flow yawing on the critical flutter dynamic pressure for isotropic and orthotropic rectangular panels at supersonic speeds was investigated in the late sixties and early seventies. Kordes and Noll [41], and Bohon [42] have theoretically studied the influence of arbitrary flow angles on isotropic and orthotropic rectangular panels with classical simply supported boundary conditions. Durvasula [43, 44] used the Rayleigh-Ritz method and 16-term beam functions to study the flow yawing and plate obliquity effects of simply supported and clamped rectangular isotropic panels. Kariappa et al. [45] and Sander et al. [46] used the finite element method to study the effects of flow yawing of isotropic parallelogram panels. The dependence of critical dynamic pressure on the flow angle and flexible supports has been shown experimentally and theoretically by Shyprykevich and Sawyer [47] and by Sawyer [48]. It was found that orthotropic panels mounted on flexible supports experience large reductions in critical flutter dynamic pressure for only small changes in flow angle.

An exhaustive search of the literature reveals that there are very few investigations on nonlinear panel flutter considering the effects of flow yawing. Friedmann and Hanin [49] were the first to study supersonic nonlinear flutter of rectangular isotropic and orthotropic panels with arbitrary flow direction. They used the

first order piston theory for aerodynamic pressure and Galerkin's method in the spatial domain to analyze nonlinear panel flutter with yawed supersonic flow. The reduced coupled nonlinear ordinary differential modal equations were solved with numerical integration. Using a 4×2 modes model, four natural modes in the x-direction and two modes in the y-direction, LCO were obtained for simply supported isotropic and orthotropic rectangular panels. Chandiramani et al. [50] used the third-order piston theory and Galerkin's method in the spatial domain. The reduced coupled nonlinear ordinary differential modal equations were solved using a predictor and a Newton-Raphson type corrector technique for limit-cycle periodic solutions. Direct numerical integration was employed for nonperiodic and chaotic solutions. A 2×2 modes model, two natural modes in the x- and y-directions, was used for simply supported rectangular laminated panels. Abdel-Motagaly et al. [51] have recently extended the finite element method to study nonlinear flutter of composite panels with yawed supersonic flows using the MIN3 triangular element developed by Tessler and Hughes [52] and extended for nonlinear analysis by Chen [53]. It was found that, for laminated composite panels [54], the flow direction could greatly affect the limit-cycle behavior.

In addition to the aerodynamic loading, aircraft and spacecraft panels are subjected to high levels of acoustic loading (sonic fatigue), due to high frequency random pressure fluctuation. A comprehensive review of sonic fatigue technology up to 1989 is given by Clarkson [55] where various types of pressure loading, developments of theoretical methods, and comparisons of experimental and analytical results were given. Recently, Wolfe et al. [56] gave a review of sonic fatigue design guides, classical and finite element approaches, and identification technology including experimental investigation of nonlinear beams and plates response. Sonic fatigue design guides based on test data and simplified single mode solutions were given by Rudder and Plumblee [57] for isotropic panels and by Holehouse [58] for composite panels. A Solution method based on Galerkin procedure and on time domain Monte Carlo approach was developed by Vaicaitis [59] for nonlinear response of isotropic panels under acoustic and thermal loads. Composite panels were considered by Arnold and Vaicaitis [60], and by Vaicaitis and Kavallieratos [61]. Bolotin [62] used the Fokker-Planck-Kolmogorov (FPK) exact method to solve single DOF forced Duffing equation. The finite element/equivalent

linearization method was used by Chiang [63] to analyze the large deflection random response of complex panels.

Sonic fatigue and panel flutter have been independently considered for aircraft, spacecraft, and missiles. However, up to very recently there was no study for nonlinear panel response under combined acoustic and aerodynamic loading. Abdel-Motagaly et al. [64] presented a study for nonlinear composite panels response under combined acoustic and aerodynamic loading, which is based on the research presented in this thesis.

1.2.2 Piezoelectric Sensors and Actuators

Since the discovery of piezoelectricity by the Curie brothers in 1880 [65], there have been many applications in various fields using piezoelectric materials, such as ultrasonic transducers, telephone transducers, and accelerometers. Piezoelectric materials basically convert mechanical energy to electrical energy and vice-versa. When mechanical force or strain is applied to a piezoelectric material, electrical charge or voltage is generated within the material, this is known as the direct piezoelectricity effect. Conversely, when electrical charge or voltage is applied to the piezoelectric material, the material generates mechanical force or strain, this is known as the converse piezoelectricity effect. The piezoelectric direct and converse effects are the basis for using them as sensors and actuators, respectively. The linear piezoelectricity constitutive relations that relate the mechanical and electrical variables for linear material behavior are given by [65]:

$$\begin{aligned} \{\sigma\} &= [Q]^E \{\varepsilon\} - [e]^T \{E\} \\ \{D\} &= [e]\{\varepsilon\} + [\in]^\varepsilon \{E\} \end{aligned} \tag{1.1}$$

where $\{\sigma\}$, $\{\varepsilon\}$, $\{D\}$, and $\{E\}$ are stress, strain, electrical displacement, and electrical field, respectively, $[Q]^E$ is the piezoelectric stiffness matrix at constant electrical field, $[\in]^\varepsilon$ is the dielectric permittivity matrix measured at constant strain, and [e] is the piezoelectric electro-mechanical coupling constants matrix. Based on the principle of virtual work, a useful analogy between piezoelectric electrical and mechanical variables can be determined as given in Table 1.2. For example, the electrical field applied or sensed in the piezoelectric material is analogous to mechanical strain.

Although piezoelectricity was discovered a long time ago, the application of distributed sensing and actuation using piezoelectric materials for flexible structures is relatively new. Bonding or embedding piezoelectric sensors and actuators to flexible structures allows for measuring and applying mechanical strains and consequently suppressing undesired structure vibrations, hence improving the life duration and performance of the structure. Figure 1.2 shows a typical piezoelectric element that could be used as sensors or actuators. Traditional isotropic piezoelectric material is usually manufactured from lead zirconate titanate (PZT) or polyvinylidene fluoride (PVDF) piezoelectric ceramics. Piezoelectric properties are induced in the ceramics using the polling process during which a high dc electrical field is applied to the ceramic in a specific direction.

Recently, many articles dealing with piezoelectric sensors and actuator modeling for active structure vibration have appeared in the literature. A review article of the applications and modeling of distributed piezoelectric sensors and actuators in flexible structures up to 1994 is given by Rao and Sunar [65]. A general review for intelligent structures including piezoelectric sensors and actuators is given by Crawley [66]. The governing equations for piezoelectric sensors and actuators using the classical approach were considered by many authors [67-69]. This research is concerned with the modeling of piezoelectric sensors and actuators embedded in composite panels using the finite element method. The first article for modeling piezoelectric continua using finite element was given by Allik and Hughes [70], where they formulated finite element equations for piezoelectric continua based on linear piezoelectric constitutive relations and using an isoparametric tetrahedral element. Tzou and Tseng [71] developed a new thin piezoelectric solid finite element with internal degrees of freedom that is more suitable for modeling distributed piezoelectric sensors and actuators in plate and shell structures. Ha et al. [72] used an eight-node three-dimensional composite brick element to model dynamic and static response of laminated composites containing piezoelectric sensors and actuators. Hwang and Park [73] used Hamilton's principle to derive the equations of motion of a laminated plate with piezoelectric sensors and actuators. They used a new, two-dimensional, four-node, 12 degrees of freedom quadrilateral plate bending element with one additional electrical degree of freedom to eliminate the problems associated

with using solid elements and to reduce the size of the finite element equations. A conforming rectangular plate element based on classical plate theory was also developed by Zhou [74] to model composite panels with piezoelectric actuators. This formulation was used for panel flutter suppression analysis. The same element was used by Liu et al. [75] for vibration control of composite plates. Suleman and Venkayya [76] used a 4-node bilinear Mindlin plate element with additional electrical degree of freedom. Detwiler et al. [77] modified the QUAD4 isoparametric quadrilateral element to handle laminated composite plates containing piezoelectric sensors and actuators. Sze and Yao [78] used and compared the performance of various solid shell and membrane elements to model surface bonded piezoelectric patches. Recently, Bevan [79] modified the shear deformable MIN6 shell element to model composite shell structures integrated with piezoelectric sensors and actuators.

One new concept for piezoelectric sensors and actuators that is utilized in this research is the self-sensing piezoelectric actuators introduced by Dosch et al. [80] and by Anderson and Hagood [81]. This concept combines the sensing and actuation functions into a single piezoelectric piece through the use of an electrical circuit that measures the sensing charge output of piezoelectric actuators. The use of such concept allows for collocated sensing and actuation, which is a preferable property for active vibration control. Another new concept is the use of anisotropic piezoelectric actuators with interdigital electrodes, such as the active fiber composites (AFC) piezoelectric actuator [82], and the Macro-Fiber Composite (MFC) piezoelectric actuator [83]. For both AFC and MFC, the polling and excitation fields run parallel to the plane of actuation compared to vertical to the plane of actuation for traditional piezoelectric materials. This permits the use of the more efficient "33" piezoelectric coupling constant which is usually twice the value of the traditional piezoelectric "31" and "32" coupling constants (see [84] for detailed electrical and mechanical properties of piezoelectric ceramics).

One important problem when using distributed piezoelectric sensors and actuators for active structural control is the optimal placement of sensors and actuators. Some examples for the methods used in the literature for optimal actuator and sensor placement are given in [85-92]. Some of the methods used are based on open loop criteria such as maximum controllability and observability [85, 86]. Another class of methods is based on

minimization of a linear quadratic regulator (LQR) cost function using gradient optimization methods [87-90]. A third class of methods is based on using more rigorous optimization methods such as the genetic algorithm [91] and gradient based [92] optimization techniques. More details for piezoelectric sensor and actuator placement for the problem of panel flutter suppression will be discussed in the next subsection.

1.2.3 Panel Flutter Suppression Using Piezoelectric Materials

Many researchers have investigated the effectiveness of using piezoelectric materials for passive or active control of flexible structures. However, only few studies have been reported for linear and nonlinear supersonic panel flutter suppression using piezoelectric materials. Scott and Weisshaar [93] were the first to study the suppression of linear panel flutter using piezoelectric materials. The piezoelectric materials covered the full surface of the panel and were used to generate bending moments to control panel flutter. Four modes were retained using the Ritz method, and the panel was modeled as a simply supported isotropic plate. Linear optimal control theory using full state feedback LQR was employed in the simulation. Hajela and Glowasky [94] applied piezoelectric elements in linear panel flutter suppression. Finite element models for panels with surface bonded and embedded piezoelectric materials were generated to determine the response. The actuation forces generated by the piezoelectric material were incorporated as static prestress in the finite element models. Using a multi-criterion optimization scheme, the optimal panel configuration with minimum weight and optimal sizing and layout of the piezoelectric elements for maximum flutter dynamic pressure were determined. Using a finite element approach, Suleman and Goncalves [95], and Suleman [96] recently investigated a passive control methodology for linear panel flutter suppression. The methodology induces tensile inplane loads from bonded or embedded piezoelectric patches to increase panel critical dynamic pressure. They proposed the use of the physical programming optimization method to determine optimal actuator configuration. Surace et al. [97] used piezoelectric sensors and actuators to suppress linear supersonic panel flutter using robust control techniques based on structured singular values for a simply supported composite panel over a range of Mach numbers. The panel was modeled using Galerkin's method with classical plate theory and linear piston theory for aerodynamic loading. Frampton et al. [98] employed a collocated direct rate feedback control scheme

for the active control of linear panel flutter. The linearized potential flow aerodynamics was used for the full transonic and supersonic Mach number range. They demonstrated that a significant increase in the flutter boundary was achieved for a simply supported square steel panel.

The first study of nonlinear panel flutter suppression using PZT piezoelectric actuators was given by Abou-Amer [99]. He used piezoelectric layers to generate inplane tension forces and consequently increase the panel flutter boundary. He showed that the PZT material is more capable of preventing nonlinear panel flutter compared to using active constrained layer damping. Lai et al. [100-102] studied the control of nonlinear flutter of a simply supported isotropic plate using piezoelectric actuators. The Galerkin's method was adopted in obtaining the nonlinear modal equations. The optimal control theory and numerical integration were used in the simulation. They concluded that the bending moment induced by piezoelectric actuators is much more effective than inplane forces for flutter suppression. Zhou et al. [103, 104] and [74] used the finite element method to control isotropic and composite panels with surface bonded or embedded piezoelectric patches. The finite element formulation considered coupling between structural and electrical fields. An optimal full state feedback LQR controller was developed based on the linearized modal equations. The norms of the feedback control gain (NFCG) were used to provide the optimal shape and location of the piezoelectric actuators. Numerical simulations showed that the critical flutter dynamic pressure is increased about four times and two times for simply supported and clamped isotropic panels, respectively. Dongi et al. [105] have presented a finite element method for investigations on adaptive panels with self-sensing piezoelectric actuators. The LUM/NTF algorithm was extended to include the linear and nonlinear active stiffness matrices due to output feedback. A control approach based on output feedback for active compensation of aerodynamic stiffness (ACAS) terms is developed. They showed that the ACAS control is able to increase the linear flutter boundary Mach number from M_∞ = 3.22 to M_∞ = 6.67 for a simply supported isotropic panel. Wind tunnel testing performed by Ho et al. [106] has shown that panel limit-cycle motions observed in the wind tunnel can be successfully reduced for composite panels with one-sided surface mounted piezoelectric actuators and strain sensors using an iterative root locus based gain tuning

algorithm. Their wind tunnel testing showed the leading edge piezoelectric actuator patches to be more effective than the trailing edge patches in suppressing panel flutter. Very recently, Kim and Moon [107] presented a comparison between active control and passive damping using piezoelectric actuators for nonlinear panel flutter. The finite element method was used to model the panel and LQR control method was used for active control. The shape and location of the piezoelectric actuators was determined using genetic algorithms.

With this exhaustive search for panel flutter suppression studies, two main findings are determined. First, the effect of flow yaw angle has never been considered in the literature for both linear and nonlinear panel flutter suppression, despite its great effect on the panel flutter mode shape and, consequently, on the optimal location of piezoelectric actuators and sensors. Second, most of the studies used LQR full state feedback control assuming that all the states are available without any consideration for the problem of state estimation for the nonlinear system dynamics or used non-optimal output feedback based on iterative design methods.

1.3 Outline of the Study

This study presents multi-disciplinary research that includes nonlinear finite element modeling of composite panels, aeroelasticity, modeling and optimal placement of piezoelectric sensors and actuators, and control theory. It could be divided into two parts. The first part covers finite element modeling and analysis for nonlinear flutter of composite panels considering the effect of flow yaw angle and the effect of additional high acoustic pressure loading. The second part covers nonlinear flutter suppression for composite panels under yawed supersonic flow using piezoelectric sensors and actuators including optimal sensor and actuator placement and controller design.

The thesis is organized as follows. In Chapter 1, background material and literature survey are given for the main topics of this research including nonlinear panel flutter analysis, piezoelectric sensors and actuators, and panel flutter suppression methodologies followed by an outline of the thesis contents. The derivation of finite element coupled nonlinear equations of motion for composite panels with integrated piezoelectric sensors and actuators under yawed supersonic aerodynamic flow and acoustic loading is presented in Chapter 2 using the three-node triangular MIN3 plate

element with improved transverse shear [48]. The MIN3 element is modified to handle piezoelectric sensors and actuators by using an additional DOF for electrical potential per each piezoelectric layer. In Chapter 3, modal transformation and reduction, and solution procedure for nonlinear panel response are presented. The system governing equations are transformed into the modal coordinates using the panel linear vibration modes to obtain a set of nonlinear dynamic modal equations of lesser order that can be easily used to solve the problems of linear and nonlinear flutter boundaries and to analyze panel response under combined acoustic and aerodynamic pressures. The reduced modal equations of motion are also used to design control laws and to simulate panel flutter suppression. Solution procedures based on time domain numerical integration methods and based on frequency domain methods for nonlinear panel flutter are also described in this chapter. Validation of the MIN3 finite element modal formulation and analysis results are presented in Chapter 4. The MIN3 finite element modal formulation is validated by comparison with other finite element and analytical solutions. Analysis results for the effect of arbitrary flow yaw angle on nonlinear supersonic panel flutter for isotropic and composite panels are presented using the frequency domain solution method. In addition, the effect of combined supersonic aerodynamic and acoustic pressure loading on the nonlinear dynamic response of isotropic and composite panels is presented. Description of the different control methodologies used for nonlinear panel flutter is presented in Chapter 5. Optimal control strategies [104] are the main focus for the suppression of nonlinear panel flutter in this study. The linear quadratic Gaussian (LQG) control, which combines both linear quadratic optimal feedback (LQR) and Kalman filter state estimator, is considered as systematic linear dynamic compensator. In addition, extended Kalman filter (EKF) for nonlinear systems [105-108] is also considered and combined with optimal feedback to form a nonlinear dynamic output compensator [109]. Finally, a more practical approach based on optimal output feedback is used. Closed loop criteria based on the norm of feedback control gains (NFCG) for actuators and on the norm of Kalman filter estimator gains (NKFEG) for sensors are described to determine the optimal location of self-sensing piezoelectric actuators. Simulation studies for the suppression of nonlinear panel flutter using piezoelectric material under yawed supersonic flow are presented in Chapter 6. Comparison of the

different controllers considered is performed to determine the effect of different control strategies on the panel flutter suppression performance. In addition, results for nonlinear panel flutter suppression under yawed supersonic for a specific range of yaw angles, including optimal actuator and sensor location, are presented for both isotropic and composite panels. In Chapter 7, summary, conclusions, main contributions, and recommendation for future work are given.

Table 1.1 Panel Flutter Theories

Type	Structure Theory	Aerodynamic Theory	Range of Mach No.
1	Linear	Linear Piston	$\sqrt{2} < M_\infty < 5$
2	Linear	Linearized Potential Flow	$1 < M_\infty < 5$
3	Nonlinear	Linear Piston	$\sqrt{2} < M_\infty < 5$
4	Nonlinear	Linearized Potential Flow	$1 < M_\infty < 5$
5	Nonlinear	Nonlinear Piston	$M_\infty > 5$

Table 1.2 Analogy between electrical and mechanical variables for piezoelectric materials

Mechanical	Electrical
Displacement u (vector)	Electric Potential ϕ (scalar)
Stress σ (2^{nd} order tensor)	Charge flux density (Electrical Displacement) D (vector)
Strain ε (2^{nd} order tensor)	Electric field E (vector)

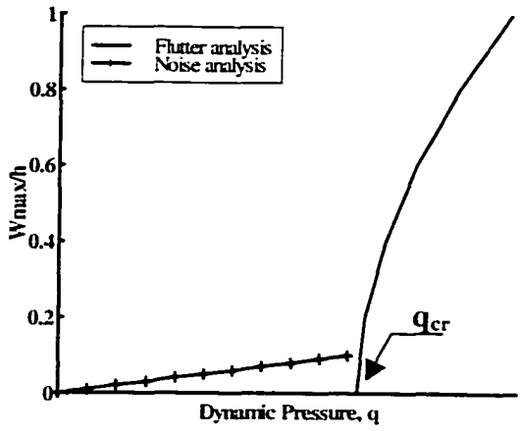

Panel response

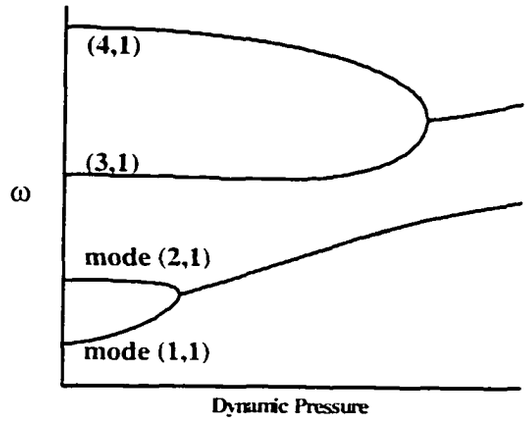

Mode coalescence

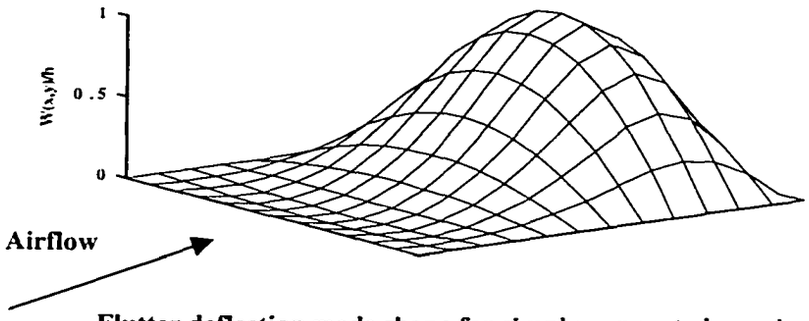

Flutter deflection mode shape for simply supported panel

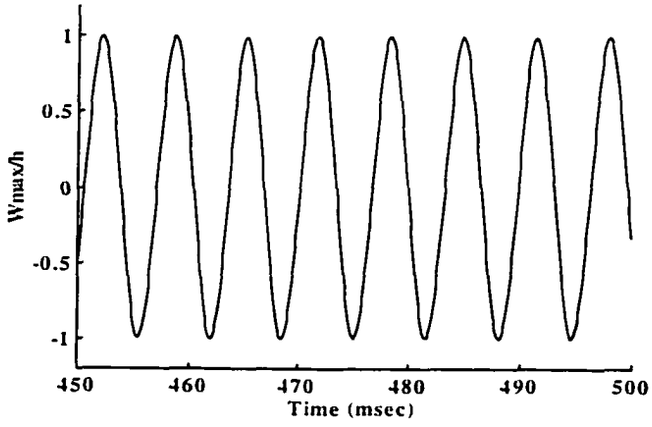

Flutter limit-cycle oscillation

Figure 1.1 Explanation of nonlinear panel flutter phenomenon

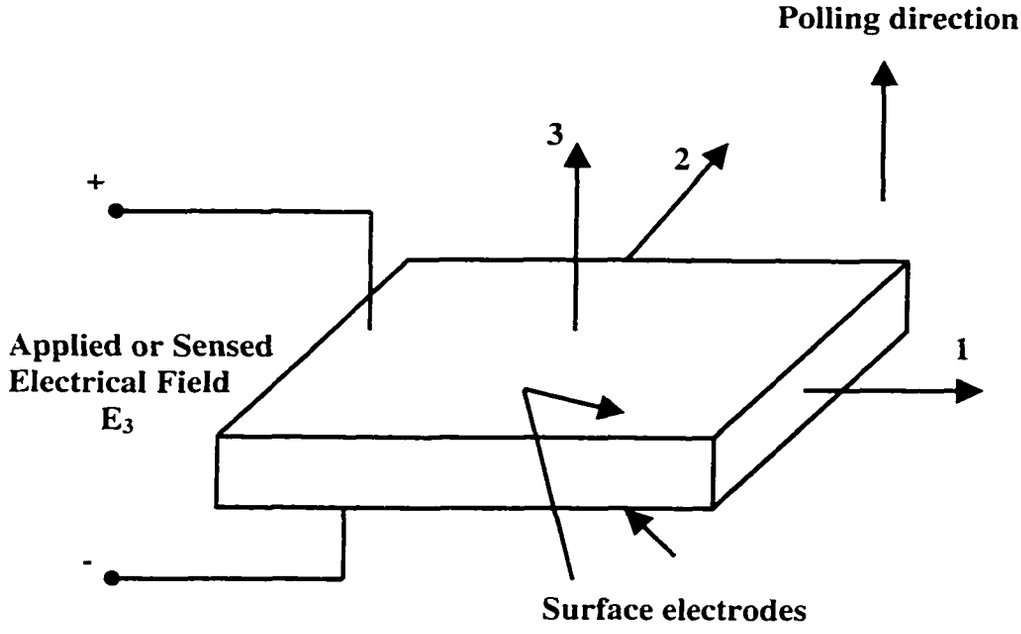

Figure 1.2 Schematic of traditional isotropic piezoelectric element

CHAPTER II

FINITE ELEMENT FORMULATION

2.1 Introduction

The three-node triangular Mindlin (MIN3) plate element with improved transverse shear, developed by Tessler and Hughes [52], is used in this study. This element has five degrees of freedom per node and it uses a special interpolation scheme, anisoparametric interpolation, to avoid the problem of shear locking commonly arising when using the standard isoparametric interpolation approach. Additionally, an element-appropriate shear correction factor is used to enhance element transverse shear energy. Due to these improvements, the MIN3 element produces a well-conditioned element stiffness matrix over the entire range of thickness to length ratios. Based on extensive numerical testing of the MIN3 element, Tessler and Hughes concluded that this element is an excellent element for linear problems and is a very viable candidate for laminated composites and nonlinear problems. Furthermore, Chen [53] demonstrated the efficiency of this element for nonlinear problems by using it for the analysis of nonlinear panel response under thermal and acoustic loading.

The MIN3 element is modified to handle piezoelectric sensors and actuators by using an additional DOF for electrical potential per each piezoelectric layer. By doing this, the modified MIN3 element becomes a fully coupled electrical-structure composite plate element. The following are the main assumptions used in the formulation:

- Thin skin panels with embedded or bonded piezoelectric layers.
- Bending theory of Mindlin (first order shear deformation theory).
- Composite laminate theory.
- First order piston theory is used to model aerodynamic pressure for yawed supersonic flow ($1.6 < M_\infty < 5$).
- Large deflection effect is considered using nonlinear von-Karman strain displacement relations.
- Linear constitutive relations for mechanical-electrical coupling are used (linear piezoelectricity).

In the following sections, the detailed derivation of the nonlinear dynamic equations of motion for a laminated composite plate with embedded or bonded piezoelectric sensors and actuators is given. The loads considered are aerodynamic pressure due to supersonic yawed flow, random acoustic loading, and piezoelectric electrical loading (see Figure 2.1). This general system of coupled nonlinear equations will later be used to analyze nonlinear panel flutter under yawed supersonic flow and nonlinear panel response under combined aerodynamic and acoustic loading. In addition, these governing equations form the basis for the design and simulation of control system design for nonlinear panel flutter suppression.

2.2 Element Displacement Functions

Based on the Mindlin plate bending theory, the element displacement functions are given by:

$$\begin{aligned} u_x &= u(x, y, t) + z\psi_y(x, y, t) \\ u_y &= v(x, y, t) + z\psi_x(x, y, t) \\ u_z &= w(x, y, t) \end{aligned} \tag{2.1}$$

where u_x, u_y, u_z are the displacement components at any point within the element; u, v, w are the displacements of the plate mid-plane; and ψ_x, ψ_y are the rotations of the mid-plane normals due to bending only.

The electrical potential DOF is assumed constant for each piezoelectric layer; i.e. w_ϕ is assumed constant over the element area.

$$w_\phi(x, y, z, t) = w_\phi(z_k, t) \tag{2.2}$$

where z_k is the z coordinate of the k^{th} piezoelectric layer.

Then the element degrees of freedom are defined as:

$$\{w\}^T = \lfloor \lfloor w_b \rfloor \ \lfloor \psi \rfloor \ \lfloor w_m \rfloor \ \lfloor w_\phi \rfloor \tag{2.3}$$

$$\begin{aligned} \{w_b\}^T &= \lfloor w_1 \quad w_2 \quad w_3 \rfloor \\ \{\psi\}^T &= \lfloor \psi_{x1} \quad \psi_{x2} \quad \psi_{x3} \quad \psi_{y1} \quad \psi_{y2} \quad \psi_{y3} \rfloor \\ \{w_m\}^T &= \lfloor u_1 \quad u_2 \quad u_3 \quad v_1 \quad v_2 \quad v_3 \rfloor \\ \{w_\phi\}^T &= \lfloor V_1 \quad \ldots \quad V_{np} \rfloor \end{aligned} \tag{2.4}$$

where V is the electrical potential (voltage) for each piezoelectric layer and np is the total number of piezoelectric layers per element (see Figure 2.2).

Displacement fields over the element are expressed in terms of element nodal DOF and element interpolation functions as follows:

$$\begin{aligned} w(x,y,t) &= \lfloor H_w \rfloor \{w_b\} + \lfloor H_{w\psi} \rfloor \{\psi\} \\ \psi_x(x,y,t) &= \lfloor H_{\psi x} \rfloor \{\psi\} \\ \psi_y(x,y,t) &= \lfloor H_{\psi y} \rfloor \{\psi\} \\ u(x,y,t) &= \lfloor H_u \rfloor \{w_m\} \\ v(x,y,t) &= \lfloor H_v \rfloor \{w_m\} \end{aligned} \tag{2.5}$$

The element interpolation functions are expressed in terms of element area coordinates (see Figure 2.3), and the element quadratic interpolation polynomials as given by equation (2.6).

$$\begin{aligned} \lfloor H_w \rfloor &= \lfloor \xi_1 \quad \xi_2 \quad \xi_3 \rfloor \\ \lfloor H_{w\psi} \rfloor &= \lfloor L_1 \quad L_2 \quad L_3 \quad M_1 \quad M_2 \quad M_3 \rfloor \\ \lfloor H_{\psi x} \rfloor &= \lfloor H_u \rfloor = \lfloor \xi_1 \quad \xi_2 \quad \xi_3 \quad 0 \quad 0 \quad 0 \rfloor \\ \lfloor H_{\psi y} \rfloor &= \lfloor H_v \rfloor = \lfloor 0 \quad 0 \quad 0 \quad \xi_1 \quad \xi_2 \quad \xi_3 \rfloor \end{aligned} \tag{2.6}$$

Element area coordinates, ξ_i, are related to the element geometric coordinates using the following transformation:

$$\begin{aligned} \begin{Bmatrix} 1 \\ x \\ y \end{Bmatrix} &= \begin{bmatrix} 1 & 1 & 1 \\ x_1 & x_2 & x_3 \\ y_1 & y_2 & y_3 \end{bmatrix} \begin{Bmatrix} \xi_1 \\ \xi_2 \\ \xi_3 \end{Bmatrix} \\ \begin{Bmatrix} \xi_1 \\ \xi_2 \\ \xi_3 \end{Bmatrix} &= \frac{1}{2A} \begin{bmatrix} x_2 y_3 - x_3 y_2 & y_2 - y_3 & x_3 - x_2 \\ x_3 y_1 - x_1 y_3 & y_3 - y_1 & x_1 - x_3 \\ x_1 y_2 - x_2 y_1 & y_1 - y_2 & x_2 - x_1 \end{bmatrix} \begin{Bmatrix} 1 \\ x \\ y \end{Bmatrix} \end{aligned} \tag{2.7}$$

where (x_i, y_i) are the coordinates of node i, and A is the triangular element area given by:

$$A = \frac{1}{2}(x_2 - x_1)(y_3 - y_1) - (x_3 - x_1)(y_2 - y_1).$$

The element interpolation polynomials are defined as:

$$
\begin{aligned}
&L_1 = \frac{1}{8}(b_3 N_4 - b_2 N_6), \quad L_2 = \frac{1}{8}(b_1 N_5 - b_3 N_4) \\
&L_3 = \frac{1}{8}(b_2 N_6 - b_1 N_5), \quad M_1 = \frac{1}{8}(a_2 N_6 - a_3 N_4) \\
&M_2 = \frac{1}{8}(a_3 N_4 - a_1 N_5), \quad M_3 = \frac{1}{8}(a_1 N_5 - a_2 N_6) \\
&N_4 = 4\xi_1\xi_2, \quad N_5 = 4\xi_2\xi_3, \quad N_6 = 4\xi_3\xi_1 \\
&a_1 = x_3 - x_2, \quad a_2 = x_1 - x_3, \quad a_3 = x_2 - x_1 \\
&b_1 = y_2 - y_3, \quad b_2 = y_3 - y_1, \quad b_3 = y_1 - y_2
\end{aligned}
\tag{2.8}
$$

2.3 Nonlinear Strain-Displacement Relations

The von-Karman large deflection strain-displacement relations for a plate undergoing extension and bending at any point z through the plate thickness are given by:

$$
\{\varepsilon\} = \left\{\varepsilon^o\right\} + z\{\kappa\} = \left\{\varepsilon_m^o\right\} + \left\{\varepsilon_\theta^o\right\} + z\{\kappa\} = \left\{\varepsilon_m^o\right\} + \frac{1}{2}[\theta]\{\theta\} + z\{\kappa\} \tag{2.9}
$$

$$
\{\varepsilon\} = \begin{Bmatrix} \varepsilon_x \\ \varepsilon_y \\ \gamma_{xy} \end{Bmatrix}, \quad \left\{\varepsilon_m^o\right\} = \begin{Bmatrix} u_{,x} \\ v_{,y} \\ u_{,y} + v_{,x} \end{Bmatrix}, \quad \{\kappa\} = \begin{Bmatrix} \psi_{y,x} \\ \psi_{x,y} \\ \psi_{x,x} + \psi_{y,y} \end{Bmatrix}
$$

$$
[\theta] = \begin{bmatrix} w_{,x} & 0 \\ 0 & w_{,y} \\ w_{,y} & w_{,x} \end{bmatrix}, \quad \{\theta\} = \begin{Bmatrix} w_{,x} \\ w_{,y} \end{Bmatrix} \tag{2.10}
$$

where "," denotes derivative with respect to the subscript. The shear strain-displacement relations are:

$$
\{\gamma\} = \begin{Bmatrix} \gamma_{yz} \\ \gamma_{xz} \end{Bmatrix} = \begin{Bmatrix} w_{,y} \\ w_{,x} \end{Bmatrix} + \begin{Bmatrix} \psi_x \\ \psi_y \end{Bmatrix} \tag{2.11}
$$

Substituting the MIN3 element interpolation functions, equation (2.5), the strain components in equations (2.9) and (2.11) can be expressed in terms of element nodal coordinates as follows:

$$
\begin{aligned}
&\left\{\varepsilon_m^o\right\} = [C_m]\{w_m\} \\
&\{\theta\} = [C_{\psi b}]\{w_b\} + [C_{\psi\psi}]\{\psi\} \\
&\{\kappa\} = [C_b]\{\psi\} \\
&\{\gamma\} = [C_{\gamma b}]\{w_b\} + [C_{\gamma\psi}]\{\psi\}
\end{aligned}
\tag{2.12}
$$

where the strain interpolation matrices are given by equations (2.13) through (2.16).

$$[C_m]=\begin{bmatrix} \lfloor H_u \rfloor_{,x} \\ \lfloor H_v \rfloor_{,y} \\ \lfloor H_v \rfloor_{,x}+\lfloor H_u \rfloor_{,y} \end{bmatrix} \tag{2.13}$$

$$[C_{wb}]=\begin{bmatrix} \lfloor H_w \rfloor_{,x} \\ \lfloor H_w \rfloor_{,y} \end{bmatrix},\quad [C_{w\psi}]=\begin{bmatrix} \lfloor H_{w\psi} \rfloor_{,x} \\ \lfloor H_{w\psi} \rfloor_{,y} \end{bmatrix} \tag{2.14}$$

$$[C_b]=\begin{bmatrix} \lfloor H_{\psi_y} \rfloor_{,x} \\ \lfloor H_{\psi_x} \rfloor_{,y} \\ \lfloor H_{\psi_x} \rfloor_{,x}+\lfloor H_{\psi_y} \rfloor_{,y} \end{bmatrix} \tag{2.15}$$

$$[C_{\gamma b}]=\begin{bmatrix} \lfloor H_w \rfloor_{,y} \\ \lfloor H_w \rfloor_{,x} \end{bmatrix},\quad [C_{\gamma\psi}]=\begin{bmatrix} \lfloor H_{w\psi} \rfloor_{,y}+\lfloor H_{\psi_x} \rfloor \\ \lfloor H_{w\psi} \rfloor_{,x}+\lfloor H_{\psi_y} \rfloor \end{bmatrix} \tag{2.16}$$

Expressions for these strain interpolation matrices as functions of element geometry and area coordinates are given in Appendix A.

2.4 Electrical Field-Potential Relations

Based on the analogy given in chapter 1 between electrical and mechanical quantities for piezoelectric materials, the electrical field-potential relations are analogous to mechanical strain-displacement relations. Assuming that the electrical degrees of freedom are constant over each piezoelectric layer in the element, the electrical field is related to the electrical DOF by:

$$\begin{Bmatrix} E_1 \\ \vdots \\ E_{np} \end{Bmatrix} = -[B_\phi]\{w_\phi\} = -\begin{bmatrix} \frac{1}{h_1} & \cdots & 0 \\ \vdots & \ddots & \vdots \\ 0 & \cdots & \frac{1}{h_{np}} \end{bmatrix} \begin{Bmatrix} V_1 \\ \vdots \\ V_{np} \end{Bmatrix} \tag{2.17}$$

Both traditional isotropic piezoelectric materials and anisotropic piezoelectric actuators, such as active fiber composite (AFC) [82] and macro-fiber composite (MFC) [83], are covered by the presented formulation. For isotropic piezoelectric materials, the polarization direction is the "3" direction; consequently, $\{E_i\}$ is the electrical field in the 3 direction and h_i is the thickness of the piezoelectric layer. For anisotropic piezoelectric

actuators such as MFC or AFC, the polling direction is the "1" direction. For this case, $\{E_i\}$ is the electrical field in the 1 direction and h_i is the electrode spacing.

2.5 Linear Piezoelectricity Coupling Equations

The stress, strain, electrical field, and electrical displacement within a piezoelectric layer can be fully described by the following linear electromechanical relationships [65]:

$$\begin{aligned}\{\sigma\} &= [Q]^E\{\varepsilon\} - [e]^T\{E\} \\ \{D\} &= [e]\{\varepsilon\} + [\in]^\varepsilon\{E\}\end{aligned} \tag{2.18}$$

where $[Q]^E$ is the piezoelectric layer stiffness matrix at constant electrical field, $[\in]^\varepsilon$ is the permittivity matrix measured at constant strain (clamped), $[e]$ is the piezoelectric constant matrix. In practice, the constants $[e]$ and $[\in]^\varepsilon$ may be unavailable. They are expressed in equation (2.19) in terms of permittivity at constant stress $[\in]^\sigma$, and the piezoelectric constant matrix $[d]$, which are more commonly available

$$\begin{aligned}[e] &= [d][Q]^E \\ [\in]^\varepsilon &= [\in]^\sigma - [d][Q]^E[d]^T\end{aligned} \tag{2.19}$$

By substituting (2.19) into (2.18), the linear electromechanical coupling constitutive relations for mechanical stress and electrical displacement can be written as:

$$\begin{aligned}\{\sigma\} &= [Q]^E\left(\{\varepsilon\} - [d]^T\{E\}\right) \\ \{D\} &= [d]\{\sigma\} + [\in]^\sigma\{E\}\end{aligned} \tag{2.20}$$

The electrical displacement, $\{D\}$, in these equations represents electrical charge flux density and is analogous to mechanical stress. For an isotropic piezoelectric element with its poling axis in the "3" direction, the matrix of piezoelectric constants $[d]$ has the form:

$$[d] = \begin{bmatrix} 0 & 0 & 0 & 0 & d_{15} & 0 \\ 0 & 0 & 0 & d_{12} & 0 & 0 \\ d_{31} & d_{32} & d_{33} & 0 & 0 & 0 \end{bmatrix} \tag{2.21}$$

The first term in the subscript refers to the axis of applied electrical field and the second subscript refers to the axis of resulting mechanical strain. For thin piezoelectric ceramics, $d_{33} = d_{15} = 0$ and $d_{31} = d_{32}$. For the case of anisotropic piezoelectric, MFC or AFC, with

the poling axis in the "1" direction, the constants d_{31} and d_{32} are replaced by d_{11} and d_{12} which are determined experimentally [83].

2.6 Constitutive Equations

Lamina stress-strain relations are derived based on the Mindlin plate theory and on the linear electromechanical piezoelectric coupling equations. It is assumed that all laminas are perfectly bonded with zero glue thickness. For a laminated fiber reinforced composite panel with embedded or bonded piezoelectric layers, the k[th] layer stress-strain relationships in the material principal axes (1,2,3) are given by:

$$\begin{Bmatrix}\sigma_1\\ \sigma_2\\ \tau_{12}\end{Bmatrix}_k = \begin{bmatrix}Q_{11} & Q_{12} & 0\\ Q_{12} & Q_{22} & 0\\ 0 & 0 & Q_{66}\end{bmatrix}_k \left(\begin{Bmatrix}\varepsilon_1\\ \varepsilon_2\\ \gamma_{12}\end{Bmatrix} - E_{ik} \begin{Bmatrix}d_{i1}\\ d_{i2}\\ 0\end{Bmatrix}_k \right) \tag{2.22}$$

The k[th] layer could be either structure lamina ($E_{ik} = \{d\}_k = 0$) or piezoelectric layer. The transverse shear stress-strain relations are also given by:

$$\begin{Bmatrix}\tau_{23}\\ \tau_{13}\end{Bmatrix}_k = \begin{bmatrix}Q_{44} & 0\\ 0 & Q_{55}\end{bmatrix}_k \begin{Bmatrix}\gamma_{23}\\ \gamma_{13}\end{Bmatrix} \tag{2.23}$$

For regular isotropic piezoelectric layers $i = 3$, corresponding to applied or sensed electrical field in the "3" directions while for MFC or AFC piezoelectric actuators $i = 1$, corresponding to applied or sensed electrical field in the "1" direction.

In laminate reference axes (x, y, z), the constitutive equations are:

$$\begin{Bmatrix}\sigma_x\\ \sigma_y\\ \tau_{xy}\end{Bmatrix}_k = \begin{bmatrix}\overline{Q}_{11} & \overline{Q}_{12} & \overline{Q}_{16}\\ \overline{Q}_{12} & \overline{Q}_{22} & \overline{Q}_{26}\\ \overline{Q}_{16} & \overline{Q}_{26} & \overline{Q}_{66}\end{bmatrix}_k \left(\begin{Bmatrix}\varepsilon_x\\ \varepsilon_y\\ \gamma_{xy}\end{Bmatrix} - E_{ik} \begin{Bmatrix}d_x\\ d_y\\ d_{xy}\end{Bmatrix}_k \right) \tag{2.24}$$

$$\begin{Bmatrix}\tau_{yz}\\ \tau_{xz}\end{Bmatrix}_k = \begin{bmatrix}\overline{Q}_{44} & \overline{Q}_{45}\\ \overline{Q}_{45} & \overline{Q}_{55}\end{bmatrix}_k \begin{Bmatrix}\gamma_{yz}\\ \gamma_{xz}\end{Bmatrix} \tag{2.25}$$

In matrix compact format these equations can be written as:

$$\begin{aligned}\{\sigma\}_k &= [\overline{Q}]_k (\{\varepsilon\} - E_{ik}\{d\}_k)\\ \{\tau\}_k &= [\overline{Q}_S]_k \{\gamma\}\end{aligned} \tag{2.26}$$

where, $[\overline{Q}]$ and $[\overline{Q}_S]$ are the lamina transformed reduced stiffness matrices for plane stress and transverse shear respectively, and $\{d\}$ is the transformed piezoelectric

constants vector. Details of the derivation of transformed stiffness and piezoelectric constants using laminated composite theory are given in Appendix B.

In addition to mechanical stress, the electrical displacement of piezoelectric layers, given in equation (2.20), can be written as:

$$D_{ik} = \{d\}_k^T [\overline{Q}]_k (\{\varepsilon\} - E_{ik} \{d\}_k) + \in_{iik}^{\sigma} E_{ik} \tag{2.27}$$

Thus, equations (2.26) and (2.27) represent the constitutive relations for a general composite lamina or a piezoelectric layer.

2.7 Laminate Resultant Forces and Moments

In a general composite laminate, stress is different from one layer to another. The resultant stresses for the laminate, or forces and moments per unit length, are obtained by integrating stress over the laminate thickness, h, as:

$$\begin{aligned} (\{N\},\{M\}) &= \int_{-h/2}^{h/2} \{\sigma\}_k (1, z)\, dz \\ \{R\} &= \int_{-h/2}^{h/2} \{\tau\}_k \, dz \end{aligned} \tag{2.28}$$

Using the lamina constitutive relations, the force and moment resultants are written as:

$$\begin{aligned} \begin{Bmatrix} N \\ M \end{Bmatrix} &= \begin{bmatrix} A & B \\ B & D \end{bmatrix} \begin{Bmatrix} \varepsilon^o \\ \kappa \end{Bmatrix} - \begin{Bmatrix} N_\phi \\ M_\phi \end{Bmatrix} \\ \{R\} &= [A_s]\{\gamma\} \end{aligned} \tag{2.29}$$

where the laminate extension, extension-bending, bending, and shear stiffness matrices, $[A]$, $[B]$, $[D]$, $[A_S]$, are defined as:

$$\begin{aligned} ([A],[B],[D]) &= \int_{-h/2}^{h/2} [\overline{Q}]_k (1, z, z^2) dz \\ [A_s] &= \int_{-h/2}^{h/2} [\overline{Q}_s]_k \, dz \end{aligned} \tag{2.30}$$

and the piezoelectric resultant force and moment are:

$$(\{N_\phi\},\{M_\phi\}) = \int_{-h/2}^{h/2} [\overline{Q}]_k \{d\}_k E_{ik} (1, z) dz \tag{2.31}$$

These force and moment resultants can be expressed in terms of element nodal DOF using equation (2.12) for $\{\varepsilon^o\}$ and $\{\kappa\}$, and equation (2.17) for E_{ik} as follows:

$$\begin{aligned}
\{N\} &= [A][C_m]\{w_m\} + \frac{1}{2}[A][\theta]\left([C_{\psi b}]\{w_b\} + [C_{\psi\psi}]\{\psi\}\right) + [B][C_b]\{\psi\} - \{N_\phi\} \\
\{M\} &= [B][C_m]\{w_m\} + \frac{1}{2}[B][\theta]\left([C_{\psi b}]\{w_b\} + [C_{\psi\psi}]\{\psi\}\right) + [D][C_b]\{\psi\} - \{M_\phi\} \\
\{R\} &= [A_s][C_{\gamma b}]\{w_b\} + [A_s][C_{\gamma\psi}]\{\psi\}
\end{aligned} \tag{2.32}$$

and the resultant piezoelectric force and moment as:

$$\begin{aligned}
\{N_\phi\} &= -[P_N]\ [B_\phi]\{w_\phi\} \\
\{M_\phi\} &= -[P_M]\ [B_\phi]\{w_\phi\}
\end{aligned} \tag{2.33}$$

where the piezoelectric matrices $[P_N]$ and $[P_M]$ are defined as:

$$\begin{aligned}
[P_N] &= \left[\ [\overline{Q}]_1\{d\}_1 h_1 \ \ \ldots \ \ [\overline{Q}]_k\{d\}_k h_k \ \ \ldots \ \ [\overline{Q}]_{np}\{d\}_{np} h_{np}\ \right] \\
[P_M] &= \frac{1}{2}\left[\ [\overline{Q}]_1\{d\}_1 (z_2 - z_1)^2 \ \ \ldots \ \ [\overline{Q}]_k\{d\}_k (z_{k+1} - z_k)^2 \right. \\
&\qquad \left. \ldots \ \ [\overline{Q}]_{np}\{d\}_{np} (z_{np+1} - z_{np})^2\ \right]
\end{aligned} \tag{2.34}$$

2.8 Aerodynamic Pressure Loading

Assuming an airflow that is parallel to the panel surface, the aerodynamic pressure loading is expressed using the first-order piston theory. This theory relates the aerodynamic pressure and panel transverse deflection as follows:

$$\Delta p_a = -\frac{2q_a}{\beta}\left(w_{,x}\cos\alpha + w_{,y}\sin\alpha + \frac{M_\infty^2 - 2}{M_\infty^2 - 1}\frac{1}{V_\infty} w_{,t} \right) \tag{2.35}$$

where $q_a = \rho_a V_\infty^2 / 2$ is the dynamic pressure, ρ_a is the air density, V_∞ is the airflow velocity, w is the panel transverse displacement, M_∞ is the Mach number, α is the flow yaw angle, and $\beta = \sqrt{M_\infty^2 - 1}$. Using non-dimensional parameters, equation (2.35) can be written as:

$$\Delta p_a = -\left(\lambda \frac{D_{110}}{a^3}\left[w_{,x}\cos\alpha + w_{,y}\sin\alpha \right] + \frac{g_a}{\omega_o}\frac{D_{110}}{a^4} w_{,t} \right) \tag{2.36}$$

where

$$\lambda = \frac{2q_a a^3}{\beta D_{110}}, \quad g_a = \frac{\rho_a V_\infty (M_\infty^2 - 2)}{\rho h \omega_o \beta^3}, \quad c_a = \frac{g_a^2}{\lambda}, \quad \omega_o = \sqrt{\frac{D_{110}}{\rho h a^4}} \tag{2.37}$$

are the non-dimensional dynamic pressure, non-dimensional aerodynamic damping, aerodynamic damping coefficient, and panel reference frequency, respectively. D_{110} is the first entry of the laminate bending stiffness matrix [*D*] determined with all fibers of the composite layers are in the x-direction as a reference. ρ, a, and h are the panel density, length and thickness, respectively.

Equation (2.36) shows that the aerodynamic loading on the panel is function of both local panel slopes in the x and y directions and of the panel vibration velocity; therefore panel flutter is a self-excited vibration. Using the MIN3 element interpolation functions, the aerodynamic pressure can be expressed in terms of element nodal DOF as follows:

$$\begin{aligned} \Delta p_a = & -\lambda \frac{D_{110}}{a_3} \lfloor \cos\alpha \quad \sin\alpha \rfloor \left([C_{wb}]\{w_b\} + [C_{w\psi}]\{\psi\} \right) \\ & - \frac{g_a}{\omega_o} \frac{D_{110}}{a_4} \left(\lfloor H_w \rfloor \{\dot{w}_b\} + \lfloor H_{w\psi} \rfloor \{\dot{\psi}\} \right) \end{aligned} \tag{2.38}$$

2.9 Element Equations of Motion and Matrices

2.9.1 Generalized Hamilton's Principle

Element matrices and nonlinear coupled electrical and structural equations of motion for a composite laminated plate element with piezoelectric layers are derived using the generalized Hamilton's principle. In addition to aerodynamic loading, a random surface pressure is also considered to allow the study of panel response under combined aerodynamic and acoustic loading. The generalized Hamilton's principle is:

$$\int_{t_2}^{t_1} \delta (T - U + W_{elec} + W_{ext}) dt = 0 \tag{2.39}$$

where T is the kinetic energy, U is the strain energy, W_{elec} is the electrical energy, and W_{ext} is the work done by externally applied forces and electrical voltage. These energy terms are defined by the following volume integrals:

$$T = \int_{Vol} \frac{1}{2} \rho \left(\{\dot{w}\}^T \{\dot{w}\} + \{\dot{u}\}^T \{\dot{u}\} + \{\dot{v}\}^T \{\dot{v}\} \right) dV \tag{2.40}$$

$$U = \int_{Vol} \frac{1}{2}\{\varepsilon\}^T \{\sigma\} dV \tag{2.41}$$

$$W_{elec} = \int_{Vol} \frac{1}{2}\{E\}^T \{D\} dV \tag{2.42}$$

The work done by external forces and voltage is given by the surface integrals:

$$W_{ext} = \int_{S_1} \{w\}^T \{F_s\} dS - \int_{S_2} V \rho_{cs} dS \tag{2.43}$$

where $\{F_s\}$ represents the surface loading on the element due to aerodynamic pressure and acoustic pressure, S_1 is the area of the surface loading, V is the applied voltage, ρ_{cs} is the surface charge density of the piezoelectric layer, and S_2 is the area of piezoelectric layer. All variations at times t_1 and t_2 must vanish in the Hamilton's principle, and thus it can be written as:

$$\begin{aligned} &\int_{Vol} [\ \frac{1}{2}\rho\left(\{\delta\dot{w}\}^T \{\dot{w}\} + \{\delta\dot{u}\}^T \{\dot{u}\} + \{\delta\dot{v}\}^T \{\dot{v}\}\right) - \{\delta\varepsilon\}^T \{\sigma\} \\ &+ \{\delta E\}^T \{D\}\ ] dV + \int_{S_1} \{\delta w\}^T \{F_s\} dS - \int_{S_2} \delta V \rho_{cs} dS = 0 \end{aligned} \tag{2.44}$$

The element matrices are determined by evaluating equation (2.44) term by term to arrive at the element nonlinear dynamic equations of motion.

2.9.2 Element Stiffness and Electromechanical Coupling Matrices

Element stiffness matrices including piezoelectric electromechanical coupling terms are derived using the variation of strain energy and electrical energy terms.

Strain Energy:

Using the definition of stress force and moment resultant, the strain energy variation term can be written as:

$$\delta U = \int_A \left(\{\delta\varepsilon^o\}^T \{N\} + \{\delta\kappa\}^T \{M\} + \alpha_s \{\delta\gamma\}^T \{R\} \right) dA \tag{2.45}$$

where α_s is the MIN3 element shear correction factor, which is defined as function of the ratio of the diagonal shear and bending stiffness coefficients associated with the rotational degrees of freedom:

$$\alpha_s = \frac{1}{1 + 0.5 \sum_{i=1}^{6} k_{s\psi ii} \Big/ \sum_{i=1}^{6} k_{\psi ii}}$$

The exact definition of element shear and bending stiffness matrices will be given later. More details about the selection of the shear correction factor are given in [52].

Substituting for strain and stress resultants in terms of element interpolation matrices and element nodal DOF into equation (2.45), the strain energy variation can be expressed as:

$$\delta U = \int_A \Big\{ \left(\{\delta w_m\}^T [C_m]^T + \{\delta w_b\}^T [C_{\psi b}]^T [\theta]^T + \{\delta\psi\}^T [C_{\psi\psi}]^T [\theta]^T\right)$$

$$\Big([A][C_m]\{w_m\} + \frac{1}{2}[A][\theta][C_{\psi b}]\{w_b\} \qquad (2.46)$$

$$+ \frac{1}{2}[A][\theta][C_{\psi\psi}]\{\psi\} + [B][C_b]\{\psi\} + [P_N][B_\phi]\{w_\phi\}\Big)$$

$$+ \{\delta\psi\}^T [C_b]^T \Big([B][C_m]\{w_m\} + \frac{1}{2}[B][\theta][C_{\psi b}]\{w_b\}$$

$$+ \frac{1}{2}[B][\theta][C_{\psi\psi}]\{\psi\} + [D][C_b]\{\psi\} + [P_M][B_\phi]\{w_\phi\}\Big) \qquad (2.47)$$

$$+ \alpha_s \left(\{\delta w_b\}^T [C_{\gamma b}]^T + \{\delta\psi\}^T [C_{\gamma\psi}]^T\right)$$

$$\left([A_s][C_{\gamma b}]\{w_b\} + [A_s][C_{\gamma\psi}]\{\psi\}\right) \Big\} dA \qquad (2.48)$$

Electrical Energy:

By substituting equation (2.27) for electrical displacement, the variation of electrical energy can be written as:

$$\delta W_{elec} = \int_A \left[\int_{-h/2}^{h/2} \delta E_{ik} \left(\{d\}_k^T [\overline{Q}]_k (\{\varepsilon\} - E_{ik}\{d\}_k) + \in_{iik}^{\sigma} E_{ik}\right) dz \right] dA \qquad (2.49)$$

Using the definition of piezoelectric matrices $[P_N]$ and $[P_M]$, the electrical energy variation becomes:

$$\delta W_{elec} = \int_A \{\delta E_i\}^T \left([P_N]^T \{\varepsilon^o\} + [P_M]^T \{\kappa\} + [P_\phi][B_\phi]^{-1}\{E_i\}\right) dA \qquad (2.50)$$

where the new piezoelectric matrix $[P_o]$ is defined as:

$$[P_\phi]=\begin{bmatrix} \in_{iil}^{\sigma} -\{d\}_1^T[\overline{Q}]_1\{d\}_1 & \cdots & 0 \\ \vdots & \in_{iik}^{\sigma} -\{d\}_k^T[\overline{Q}]_k\{d\}_k & \vdots \\ 0 & \cdots & \in_{iinp}^{\sigma} -\{d\}_{np}^T[\overline{Q}]_{np}\{d\}_{np} \end{bmatrix} \tag{2.51}$$

Using the strain-displacement relations, the electrical energy variation can be expressed in terms of nodal DOF as follows:

$$\delta W_{elec} = \int_A \{\delta w_\phi\}^T [B_\phi]^T \left\{ [P_N]^T \left([C_m]\{w_m\} + \frac{1}{2}[\theta][C_{\psi b}]\{w_b\} + \frac{1}{2}[\theta][C_{\psi\psi}]\{\psi\} \right) + [P_M]^T [C_b]\{\psi\} + [P_\phi]\{w_\phi\} \right\} dA \tag{2.52}$$

The linear and nonlinear element stiffness and electromechanical coupling matrices can be found now from the variation of both strain and electrical energies by writing the sum of δU and δW_{elec} in matrix form as follows:

$$\begin{Bmatrix} \delta w_b \\ \delta\psi \\ \delta w_m \\ \delta w_\phi \end{Bmatrix}^T \left(\begin{bmatrix} 0 & 0 & 0 & 0 \\ 0 & [k]_\psi & [k]_{\psi m} & [k]_{\psi\phi} \\ 0 & [k]_{m\psi} & [k]_m & [k]_{m\phi} \\ 0 & [k]_{\phi\psi} & [k]_{\phi m} & [k]_\phi \end{bmatrix} + \alpha_s \begin{bmatrix} [k_s]_b & [k_s]_{b\psi} & 0 & 0 \\ [k_s]_{\psi b} & [k_s]_\psi & 0 & 0 \\ 0 & 0 & 0 & 0 \\ 0 & 0 & 0 & 0 \end{bmatrix} + \right.$$

$$\begin{bmatrix} 0 & [k_1]_{b\psi} & [k_1]_{bm} & [k_1]_{b\phi} \\ [k_1]_{\psi b} & [k_1]_\psi & [k_1]_{\psi m} & [k_1]_{\psi\phi} \\ [k_1]_{mb} & [k_1]_{m\psi} & 0 & 0 \\ [k_1]_{\phi b} & [k_1]_{\phi\psi} & 0 & 0 \end{bmatrix} + \begin{bmatrix} [k_{1N\phi}]_b & [k_{1N\phi}]_{b\psi} & 0 & 0 \\ [k_{1N\phi}]_{\psi b} & [k_{1N\phi}]_\psi & 0 & 0 \\ 0 & 0 & 0 & 0 \\ 0 & 0 & 0 & 0 \end{bmatrix} +$$

$$\begin{bmatrix} [k_{1Nm}]_b & [k_{1Nm}]_{b\psi} & 0 & 0 \\ [k_{1Nm}]_{\psi b} & [k_{1Nm}]_\psi & 0 & 0 \\ 0 & 0 & 0 & 0 \\ 0 & 0 & 0 & 0 \end{bmatrix} + \begin{bmatrix} [k_{1Nb}]_b & [k_{1Nb}]_{b\psi} & 0 & 0 \\ [k_{1Nb}]_{\psi b} & [k_{1Nb}]_\psi & 0 & 0 \\ 0 & 0 & 0 & 0 \\ 0 & 0 & 0 & 0 \end{bmatrix} +$$

$$\left. \begin{bmatrix} [k_2]_b & [k_2]_{b\psi} & 0 & 0 \\ [k_2]_{\psi b} & [k_2]_\psi & 0 & 0 \\ 0 & 0 & 0 & 0 \\ 0 & 0 & 0 & 0 \end{bmatrix} \right) \begin{Bmatrix} w_b \\ \psi \\ w_m \\ w_\phi \end{Bmatrix} = \delta U + \delta W_{elec} \tag{2.53}$$

where the element sub-matrices in equation (2.53) are defined by the following equations.

Linear stiffness sub-matrices:

$$[k]_{\psi} = \int_A [C_b]^T [D][C_b]dA \tag{2.54}$$

$$[k]_{\psi m} = \int_A [C_b]^T [B][C_m]dA = [k]_{m\psi}^T \tag{2.55}$$

$$[k]_m = \int_A [C_m]^T [A][C_m]dA \tag{2.56}$$

Piezoelectric coupling sub-matrices

$$[k]_{m\phi} = \int_A [C_m]^T [P_N][B_\phi]dA = [k]_{\phi m}^T \tag{2.57}$$

$$[k]_{\psi\phi} = \int_A [C_b]^T [P_M][B_\phi]dA = [k]_{\phi\psi}^T \tag{2.58}$$

Piezoelectric capacitance sub-matrix

$$[k]_\phi = \int_A [B_\phi]^T [P_\phi]dA \tag{2.59}$$

Shear stiffness sub-matrices

$$[k_s]_b = \int_A [C_{\gamma b}]^T [A_s][C_{\gamma b}]dA \tag{2.60}$$

$$[k_s]_{b\psi} = \int_A [C_{\gamma b}]^T [A_s][C_{\gamma\psi}]dA = [k_s]_{\psi b}^T \tag{2.61}$$

$$[k_s]_{\psi} = \int_A [C_{\gamma\psi}]^T [A_s][C_{\gamma\psi}]dA \tag{2.62}$$

First-order nonlinear stiffness matrix

The following nonlinear element sub-matrices are first order functions of the element transverse displacement through $[\theta]$

$$[k_1]_{b\psi} = \frac{1}{2}\int_A [C_{\psi b}]^T [\theta]^T [B][C_b]dA = [k_1]_{\psi b}^T \tag{2.63}$$

$$[k_1]_{bm} = \frac{1}{2}\int_A [C_{\psi b}]^T [\theta]^T [A][C_m]dA = [k_1]_{mb}^T \tag{2.64}$$

$$[k_1]_{\psi} = \frac{1}{2}\int_A [C_b]^T [B][\theta][C_{\psi\psi}]dA + \int_A [C_{\psi\psi}]^T [\theta]^T [B][C_b]dA \tag{2.65}$$

$$[k_1]_{m\psi} = \frac{1}{2}\int_A [C_m]^T [A][\theta][C_{\psi\psi}]dA = [k_1]_{m\psi}^T \tag{2.66}$$

First-order piezoelectric coupling matrices

The following nonlinear element sub-matrices are first order functions of the element transverse displacement through geometric matrix $[\theta]$

$$[k_1]_{b\phi} = \frac{1}{2}\int_A [C_{\psi b}]^T [\theta]^T [P_N][B_\phi] dA = [k_1]_{\phi b}^T \tag{2.67}$$

$$[k_1]_{\psi\phi} = \frac{1}{2}\int_A [C_{\psi\psi}]^T [\theta]^T [P_N][B_\phi] dA = [k_1]_{\phi\psi}^T \tag{2.68}$$

The following nonlinear element sub-matrices are first order functions of the element electrical displacement through piezoelectric resultant force $\{N_\phi\}$.

$$[k_{1N\phi}]_b = -\frac{1}{2}\int_A [C_{\psi b}]^T [N_\phi][C_{\psi b}] dA \tag{2.69}$$

$$[k_{1N\phi}]_{b\psi} = -\frac{1}{2}\int_A [C_{\psi b}]^T [N_\phi][C_{\psi\psi}] dA = [k_{1N\phi}]_{\psi b}^T \tag{2.70}$$

$$[k_{1N\phi}]_\psi = -\frac{1}{2}\int_A [C_{\psi\psi}]^T [N_\phi][C_{\psi\psi}] dA \tag{2.71}$$

where the force resultant matrix $[N]$ is found from the force resultant vector $\{N\}$ as follows:

$$\{N\} = \begin{Bmatrix} N_x \\ N_y \\ N_{xy} \end{Bmatrix}, \quad [N] = \begin{bmatrix} N_x & N_{xy} \\ N_{xy} & N_y \end{bmatrix} \tag{2.72}$$

First-order nonlinear stiffness matrix due to $\{N_m\}$

The following sub-matrices are first-order nonlinear functions of plate membrane displacement $\{w_m\}$ through the membrane resultant force $\{N_m\}=[A]\{\varepsilon^0_m\}$

$$[k_{1Nm}]_b = \frac{1}{2}\int_A [C_{\psi b}]^T [N_m][C_{\psi b}] dA \tag{2.73}$$

$$[k_{1Nm}]_{b\psi} = \frac{1}{2}\int_A [C_{\psi b}]^T [N_m][C_{\psi\psi}] dA = [k_{1Nm}]_{\psi b}^T \tag{2.74}$$

$$[k_{1Nm}]_\psi = \frac{1}{2}\int_A [C_{\psi\psi}]^T [N_m][C_{\psi\psi}] dA \tag{2.75}$$

First-order nonlinear stiffness matrix due to $\{N_b\}$

The following sub-matrices are first-order nonlinear functions of plate rotational displacement $\{\psi\}$ through the membrane resultant force $\{N_b\}=[B]\{\kappa\}$

$$[k_{1Nb}]_b = \frac{1}{2}\int_A [C_{\psi b}]^T [N_b][C_{\psi b}]dA \tag{2.76}$$

$$[k_{1Nb}]_{b\psi} = \frac{1}{2}\int_A [C_{\psi b}]^T [N_b][C_{\psi\psi}]dA = [k_{1Nb}]^T_{\psi b} \tag{2.77}$$

$$[k_{1Nb}]_{\psi} = \frac{1}{2}\int_A [C_{\psi\psi}]^T [N_b][C_{\psi\psi}]dA \tag{2.78}$$

Second-order nonlinear stiffness matrix

The following nonlinear element sub-matrices are second-order functions of the element transverse displacement through geometric matrix $[\theta]$

$$[k_2]_b = \frac{1}{2}\int_A [C_{\psi b}]^T [\theta]^T [A][\theta][C_{\psi b}]dA \tag{2.79}$$

$$[k_2]_{b\psi} = \frac{1}{2}\int_A [C_{\psi b}]^T [\theta]^T [A][\theta][C_{\psi\psi}]dA = [k_2]^T_{\psi b} \tag{2.80}$$

$$[k_2]_{\psi} = \frac{1}{2}\int_A [C_{\psi\psi}]^T [\theta]^T [A][\theta][C_{\psi\psi}]dA \tag{2.81}$$

2.9.3 Element Mass Matrices

Element mass matrices are determined using the variation of kinetic energy term in the generalized Hamilton's principle. Using MIN3 element interpolation function, the kinetic energy variation can be written as

$$\begin{aligned}\delta T = \int_A \rho h\Big\{&\{\delta w_m\}^T (\{H_u\}\lfloor H_u \rfloor\{\ddot{w}_m\}+\{H_v\}\lfloor H_v \rfloor\{\ddot{w}_m\}) \\ &+\left(\{\delta w_b\}^T\{H_w\}+\{\delta\psi\}^T\{H_{w\psi}\}\right)\left(\lfloor H_w \rfloor\{\delta\ddot{w}_b\}+\lfloor H_{w\psi}\rfloor\{\delta\ddot{\psi}\}\right)\Big\}dA\end{aligned} \tag{2.82}$$

Equation (2.82) can be written in matrix form as:

$$\delta T = \begin{Bmatrix}\delta w_b\\ \delta\psi\\ \delta w_m\\ \delta w_\phi\end{Bmatrix}^T \frac{1}{\omega_o^2}\begin{bmatrix}[m]_b & [m]_{b\psi} & 0 & 0\\ [m]_{\psi b} & [m]_{\psi} & 0 & 0\\ 0 & 0 & [m]_m & 0\\ 0 & 0 & 0 & 0\end{bmatrix}\begin{Bmatrix}\ddot{w}_b\\ \ddot{\psi}\\ \ddot{w}_m\\ \ddot{w}_\phi\end{Bmatrix} \tag{2.83}$$

where the element mass sub-matrices are defined as:

$$[m]_b = \int_A \lfloor H_w \rfloor^T \frac{D_{110}}{a^4}\lfloor H_w \rfloor dA \tag{2.84}$$

$$[m]_{b\psi} = \int_A \lfloor H_w \rfloor^T \frac{D_{110}}{a^4}\lfloor H_{w\psi} \rfloor dA = [m]^T_{\psi b} \tag{2.85}$$

$$[m]_{\psi} = \int_A \lfloor H_{w\psi} \rfloor^T \frac{D_{110}}{a^4} \lfloor H_{w\psi} \rfloor dA \tag{2.86}$$

$$[m]_m = \int_A (\lfloor H_u \rfloor + \lfloor H_v \rfloor)^T \frac{D_{110}}{a^4} (\lfloor H_u \rfloor + \lfloor H_v \rfloor)\, dA \tag{2.87}$$

2.9.4 Element Aerodynamic and Force Matrices

The element aerodynamic stiffness and aerodynamic damping matrices, and load vectors are determined by examining the variation of work done by externally applied loads and electrical charge. The external work variation can be written as:

$$\delta W_{ext} = \int_A \left(\{\delta w_b\}^T \{H_w\} + \{\delta\psi\}^T \{H_{w\psi}\} \right) (\Delta p_a + p(x, y, t))\, dA - \int_A \{\delta w_\phi\}^T \{\rho_{cs}\} dA \tag{2.88}$$

where $p(x,y,t)$ is the acoustic pressure loading that could affect the panel in addition to the supersonic aerodynamic pressure loading. Substituting for the aerodynamic pressure loading using the first-order piston theory, equation (2.38), the external work variation can be written in a matrix form as follows:

$$\delta W_{ext} = \begin{Bmatrix} \delta w_b \\ \delta\psi \\ \delta w_m \\ \delta w_\phi \end{Bmatrix}^T \left(\lambda \begin{bmatrix} [a_a]_b & [a_a]_{b\psi} & 0 & 0 \\ [a_a]_{\psi b} & [a_a]_{\psi} & 0 & 0 \\ 0 & 0 & 0 & 0 \\ 0 & 0 & 0 & 0 \end{bmatrix} \begin{Bmatrix} w_b \\ \psi \\ w_m \\ w_\phi \end{Bmatrix} + \frac{g_a}{\omega_o} \begin{bmatrix} [g]_b & [g]_{b\psi} & 0 & 0 \\ [g]_{\psi b} & [g]_{\psi} & 0 & 0 \\ 0 & 0 & 0 & 0 \\ 0 & 0 & 0 & 0 \end{bmatrix} \begin{Bmatrix} \dot{w}_b \\ \dot{\psi} \\ \dot{w}_m \\ \dot{w}_\phi \end{Bmatrix} + \begin{Bmatrix} p_b \\ p_\psi \\ 0 \\ p_\phi \end{Bmatrix} \right) \tag{2.89}$$

where the element aerodynamic stiffness sub-matrices are defined as:

$$[a_a]_b = \int_A \bar{a} \lfloor H_w \rfloor^T (\cos\alpha \lfloor H_w \rfloor_{,x} + \sin\alpha [H_w]_{,y})\, dA \tag{2.90}$$

$$[a_a]_{b\psi} = \int_A \bar{a} \lfloor H_w \rfloor^T (\cos\alpha \lfloor H_{w\psi} \rfloor_{,x} + \sin\alpha \lfloor H_{w\psi} \rfloor_{,y})\, dA \tag{2.91}$$

$$[a_a]_{\psi b} = \int_A \bar{a} \lfloor H_{w\psi} \rfloor^T (\cos\alpha \lfloor H_w \rfloor_{,x} + \sin\alpha [H_w]_{,y})\, dA \tag{2.92}$$

$$[a_a]_{\psi} = \int_A \bar{a} \lfloor H_{w\psi} \rfloor^T (\cos\alpha \lfloor H_{w\psi} \rfloor_{,x} + \sin\alpha \lfloor H_{w\psi} \rfloor_{,y})\, dA \tag{2.93}$$

The element aerodynamic damping matrices are the same as element bending mass matrices given by equation (2.84) through (2.86)

$$[g]_b = [m]_b, \quad [g]_{b\psi} = [g]_{\psi b}^T = [m]_{b\psi}, \quad [g]_\psi = [m]_\psi \tag{2.94}$$

Finally, the element load vectors due to acoustic random pressure and applied electrical charge are defined as:

$$\{p_b\} = \int_A [H_w]^T p(x,y,t)dA \tag{2.95}$$

$$\{p_\psi\} = \int_A [H_{w\psi}]^T p(x,y,t)dA \tag{2.96}$$

$$\{p_\phi\} = -\int_A \{\rho_{cs}\}dA \tag{2.97}$$

For the case of panel flutter analysis and suppression, the acoustic pressure, $p(x,y,t)$, will be set to zero. However, some of the analysis cases given in Chapter 4 will consider the combined effect of acoustic loading and supersonic aerodynamic pressure.

2.9.5 Element Equations of Motion

Using the element stiffness, mass, aerodynamic matrices and load vectors, the fully coupled nonlinear electromechanical equations of motion for a composite laminate with piezoelectric layers subject to supersonic aerodynamic and acoustic loading using the MIN3 element can be written as:

$$\frac{1}{\omega_o^2}\begin{bmatrix} [m]_b & [m]_{b\psi} & 0 & 0 \\ [m]_{\psi b} & [m]_\psi & 0 & 0 \\ 0 & 0 & [m]_m & 0 \\ 0 & 0 & 0 & 0 \end{bmatrix}\begin{Bmatrix} \ddot{w}_b \\ \ddot{\psi} \\ \ddot{w}_m \\ \ddot{w}_\phi \end{Bmatrix} + \frac{g_a}{\omega_o}\begin{bmatrix} [g]_b & [g]_{b\psi} & 0 & 0 \\ [g]_{\psi b} & [g]_\psi & 0 & 0 \\ 0 & 0 & 0 & 0 \\ 0 & 0 & 0 & 0 \end{bmatrix}\begin{Bmatrix} \dot{w}_b \\ \dot{\psi} \\ \dot{w}_m \\ \dot{w}_\phi \end{Bmatrix} +$$

$$\left(\lambda\begin{bmatrix} [a_a]_b & [a_a]_{b\psi} & 0 & 0 \\ [a_a]_{\psi b} & [a_a]_\psi & 0 & 0 \\ 0 & 0 & 0 & 0 \\ 0 & 0 & 0 & 0 \end{bmatrix} + \begin{bmatrix} 0 & 0 & 0 & 0 \\ 0 & [k]_\psi & [k]_{\psi m} & [k]_{\psi\phi} \\ 0 & [k]_{m\psi} & [k]_m & [k]_{m\phi} \\ 0 & [k]_{\phi\psi} & [k]_{\phi m} & [k]_\phi \end{bmatrix} + \right.$$

$$\left. \alpha_s\begin{bmatrix} [k_s]_b & [k_s]_{b\psi} & 0 & 0 \\ [k_s]_{\psi b} & [k_s]_\psi & 0 & 0 \\ 0 & 0 & 0 & 0 \\ 0 & 0 & 0 & 0 \end{bmatrix} + \begin{bmatrix} 0 & [k_1]_{b\psi} & [k_1]_{bm} & [k_1]_{b\phi} \\ [k_1]_{\psi b} & [k_1]_\psi & [k_1]_{\psi m} & [k_1]_{\psi\phi} \\ [k_1]_{mb} & [k_1]_{m\psi} & 0 & 0 \\ [k_1]_{\phi b} & [k_1]_{\phi\psi} & 0 & 0 \end{bmatrix} + \right.$$

$$\begin{bmatrix} [k_{1N\phi}]_b & [k_{1N\phi}]_{b\psi} & 0 & 0 \\ [k_{1N\phi}]_{\psi b} & [k_{1N\phi}]_{\psi} & 0 & 0 \\ 0 & 0 & 0 & 0 \\ 0 & 0 & 0 & 0 \end{bmatrix} + \begin{bmatrix} [k_{1Nm}]_b & [k_{1Nm}]_{b\psi} & 0 & 0 \\ [k_{1Nm}]_{\psi b} & [k_{1Nm}]_{\psi} & 0 & 0 \\ 0 & 0 & 0 & 0 \\ 0 & 0 & 0 & 0 \end{bmatrix} +$$

$$\begin{bmatrix} [k_{1Nb}]_b & [k_{1Nb}]_{b\psi} & 0 & 0 \\ [k_{1Nb}]_{\psi b} & [k_{1Nb}]_{\psi} & 0 & 0 \\ 0 & 0 & 0 & 0 \\ 0 & 0 & 0 & 0 \end{bmatrix} + \begin{bmatrix} [k_2]_b & [k_2]_{b\psi} & 0 & 0 \\ [k_2]_{\psi b} & [k_2]_{\psi} & 0 & 0 \\ 0 & 0 & 0 & 0 \\ 0 & 0 & 0 & 0 \end{bmatrix} \Bigg) \begin{Bmatrix} w_b \\ \psi \\ w_m \\ w_\phi \end{Bmatrix} = \begin{Bmatrix} p_b \\ p_\psi \\ 0 \\ p_\phi \end{Bmatrix} \quad (2.98)$$

One important thing to note for this equation is that, all element matrices are symmetric except the aerodynamic stiffness matrices, which are skew symmetric. For abbreviation from now on, the element bending DOF $\{w_b\}$ and $\{\psi\}$ are combined together in a single vector. Thus, the 4 matrices with subscripts b, $b\psi$, ψb, and ψ are all combined in a single matrix denoted with the subscript b.

2.10 System Equations of Motion

The system equation of motion for the complete plate can be found by following the standard finite element assembly, and using the specified structural and electrical boundary conditions. The electrical DOF also follows the traditional finite element assembly procedure where the electrical boundary condition stipulates equal potential across element boundaries for each continuous piezoelectric patch. Using the new notation for bending DOF:

$$\{W_b\} = \sum_{all\ elemnts} \begin{Bmatrix} w_b \\ \psi \end{Bmatrix} \quad (2.99)$$

where the summation sign represents the finite element assembly procedure. Combining the shear and linear bending stiffness matrices in a single stiffness matrix $[K]$, then the system equations of motion for a composite panel embedded with piezoelectric layers and subject to supersonic aerodynamic pressure and acoustic pressure can be written as:

$$\frac{1}{\omega_o^2}\begin{bmatrix} M_b & 0 & 0 \\ 0 & M_m & 0 \\ 0 & 0 & 0 \end{bmatrix}\begin{Bmatrix} \ddot{W}_b \\ \ddot{W}_m \\ \ddot{W}_\phi \end{Bmatrix} + \frac{g_a}{\omega_o}\begin{bmatrix} G_a & 0 & 0 \\ 0 & 0 & 0 \\ 0 & 0 & 0 \end{bmatrix}\begin{Bmatrix} \dot{W}_b \\ \dot{W}_m \\ \dot{W}_\phi \end{Bmatrix} +$$

$$\left(\lambda \begin{bmatrix} A_a & 0 & 0 \\ 0 & 0 & 0 \\ 0 & 0 & 0 \end{bmatrix} + \begin{bmatrix} K_b & K_{bm} & K_{b\phi} \\ K_{mb} & K_m & K_{m\phi} \\ K_{\phi b} & K_{\phi m} & K_\phi \end{bmatrix} + \begin{bmatrix} K1_{N\phi} & 0 & 0 \\ 0 & 0 & 0 \\ 0 & 0 & 0 \end{bmatrix} + \right.$$

$$\left(\begin{bmatrix} Kl_b + Kl_{Nm} + Kl_{Nb} & Kl_{bm} & Kl_{b\phi} \\ Kl_{mb} & 0 & 0 \\ Kl_{\phi b} & 0 & 0 \end{bmatrix} + \begin{bmatrix} K2 & 0 & 0 \\ 0 & 0 & 0 \\ 0 & 0 & 0 \end{bmatrix}\right)\begin{Bmatrix} W_b \\ W_m \\ W_\phi \end{Bmatrix} = \begin{Bmatrix} P_b \\ 0 \\ P_\phi \end{Bmatrix} \tag{2.100}$$

where $[M]$, $[G_a]$, $[A_a]$, and $[K]$ are the system mass, aerodynamic damping, aerodynamic stiffness and linear stiffness matrices, respectively; $[Kl]$ and $[K2]$ are the first-order and second-order nonlinear stiffness matrices, which are linear and quadratic functions of the unknown displacements $\{W_b\}$ and $\{W_m\}$ respectively; and $[Kl_{No}]$ is the piezoelectric first order stiffness matrix which depends linearly on the electrical DOF $\{W_o\}$. In the absence of acoustic pressure loading, $\{P_b\} = 0$, equation (2.100) reduces to the problem of nonlinear panel flutter under yawed supersonic flow. However, by setting λ and g_a to zero, equation (2.100) describes nonlinear random response of composite panels subjected to high acoustic excitations. The formulation is kept in a general form with both effects to allow the study of nonlinear panel response under combined acoustic and aerodynamic loading. However, $\{P_b\}$ will be dropped when nonlinear panel flutter analysis and control are considered.

2.11 Piezoelectric Actuator and Sensor Equations

The system equation (2.100) represents a system of coupled electrical-structural nonlinear equations. Collecting the structure degrees of freedom $\{W_b\}$ and $\{W_m\}$ in one vector denoted as $\{W\}$, equation (2.100) can then be simplified as follows:

$$\begin{aligned} &\frac{1}{\omega_o^2}\begin{bmatrix} M & 0 \\ 0 & 0 \end{bmatrix}\begin{Bmatrix} \ddot{W} \\ \ddot{W}_\phi \end{Bmatrix} + \frac{g_a}{\omega_o}\begin{bmatrix} G & 0 \\ 0 & 0 \end{bmatrix}\begin{Bmatrix} \dot{W} \\ \dot{W}_\phi \end{Bmatrix} + \left(\lambda\begin{bmatrix} A & 0 \\ 0 & 0 \end{bmatrix} + \begin{bmatrix} K_w & K_{w\phi} \\ K_{\phi w} & K_\phi \end{bmatrix} + \right. \\ &\left.\begin{bmatrix} Kl & Kl_{w\phi} \\ Kl_{\phi w} & 0 \end{bmatrix} + \begin{bmatrix} K2 & 0 \\ 0 & 0 \end{bmatrix}\right)\begin{Bmatrix} W \\ W_\phi \end{Bmatrix} = \begin{Bmatrix} P \\ P_\phi \end{Bmatrix} \end{aligned} \tag{2.101}$$

Any piezoelectric layer in the composite laminate could be used as a sensor, actuator, or a self-sensing actuator. First, the case of a plate equipped with piezoelectric sensors and actuators is examined, then the case of self-sensing piezoelectric actuators.

2.11.1 Piezoelectric Material as Actuators and Sensors

For this case it is assumed that each piezoelectric patch is either used as a sensor or as actuator. The electrical DOF are partitioned into sensor DOF and actuator DOF, or a sensor voltage vector and an actuator voltage vector as follows:

$$\{W_\phi\}=\begin{bmatrix} W_\phi^s & W_\phi^a \end{bmatrix}^T \tag{2.102}$$

Similarly, the piezoelectric coupling and capacitance matrices can be partitioned into sensor and actuator contributions as given by equation (2.103)

$$[K_{\phi v}]=\begin{bmatrix} K_{\phi v}^s \\ K_{\phi v}^a \end{bmatrix},\ [K1_{\phi v}]=\begin{bmatrix} K1_{\phi v}^s \\ K1_{\phi v}^a \end{bmatrix},\ [K_\phi]=\begin{bmatrix} K_\phi^s & 0 \\ 0 & K_\phi^a \end{bmatrix} \tag{2.103}$$

For the piezoelectric sensors, there is no externally applied charge to the sensor electrodes and hence the electrical loading vector can be written as:

$$\{P_\phi\}=\begin{Bmatrix} 0 \\ P_\phi^a \end{Bmatrix} \tag{2.104}$$

Based on the above partition, we can now write the commonly known piezoelectric sensor and actuator equations.

Sensor Equation:

From the second row of system coupled equation (2.101) and using equations (2.102) through (2.104), the piezoelectric sensing equation is:

$$\{W_\phi^s\}=-[K_\phi^s]^{-1}\left([K_{\phi v}^s]+[K1_{\phi v}^s]\right)\{W\} \tag{2.105}$$

This provides the equation for piezoelectric sensor voltage output. If instead, the sensor is used as a charge sensor, the sensor output can be determined based on the electrical relation: $q = C\ V$ where V is voltage, C the electrical capacitance, and q the electrical charge. Noting that $[K_\phi]$ is the piezoelectric capacitance, then the output of a charge sensor is given by:

$$\{q^s\}=-\left([K_{\phi v}^s]+[K1_{\phi v}^s]\right)\{W\} \tag{2.106}$$

where $\{q^s\}$ is the collected sensor charge.

Actuator Equation

For the actuator DOF, the second row of equation (2.101) gives:

$$\left([K_{\phi v}^a]+[K1_{\phi v}^a]\right)\{W\}+[K_\phi^a]\{W_\phi^a\}=\{P_\phi^a\} \tag{2.107}$$

A piezoelectric actuator could be driven either by voltage or charge. For a charge driven actuator, $\{P_\phi^a\}$ is known and equation (2.107) can be used to find the actuator electrical

DOF $\{W_\phi^a\}$ as a function of the structural DOF $\{W\}$ and the known applied charge as follows:

$$\{W_\phi^a\} = [K_\phi^a]^{-1}\{\{P_\phi^a\} - ([K_{\phi w}^a] + [K1_{\phi w}^a])\{W\}\} \tag{2.108}$$

The actuator electrical DOF is then substituted in the first row of equation (2.101) to obtain the actuator equation for a charge driven actuator. However, in the usual actuator application, a driving voltage is used instead of a charge. In this case, the actuator voltage $\{W_\phi^a\}$ is known and the charge drawn onto the piezoelectric electrodes in response to this voltage is not of interest. Therefore, equation (2.107) is ignored. For the voltage driven piezoelectric actuator, the actuator equation can be written as follows:

$$\frac{1}{\omega_o^2}[M]\{\ddot{W}\} + \frac{g_a}{\omega_o}[G]\{\dot{W}\} + (\lambda[A] + [K_w] + [K1] + [K2])\{W\} = \{P\} + \{P_{act}\} \tag{2.109}$$

where $\{P_{act}\}$ represents the piezoelectric force due to the voltage at both sensor and actuator and is given by:

$$\{P_{act}\} = -([K_{w\phi}^s] + [K1_{w\phi}^s])\{W_\phi^s\} - ([K_{w\phi}^a] + [K1_{w\phi}^a])\{W_\phi^a\} \tag{2.110}$$

Since the actuation voltage is much bigger than the sensor voltage, the sensor term in equation (2.110) is neglected and the actuator equation for a voltage driven actuator is finally given as:

$$\begin{aligned}&\frac{1}{\omega_o^2}[M]\{\ddot{W}\} + \frac{g_a}{\omega_o}[G]\{\dot{W}\} + (\lambda[A] + [K_w] + [K1] + \\ &[K2])\{W\} = \{P\} - ([K_{w\phi}^a] + [K1_{w\phi}^a])\{W_\phi^a\}\end{aligned} \tag{2.111}$$

2.11.2 Piezoelectric Material as Self-Sensing Actuators

For these devices, each layer of piezoelectric material is used as sensor and actuator simultaneously. Therefore, there is no need to partition $\{W_o\}$ for this case. Equation (2.101) can be then written as two separate equations to represent actuation and sensing as follows:

$$\begin{aligned}&\frac{1}{\omega_o^2}[M]\{\ddot{W}\} + \frac{g_a}{\omega_o}[G]\{\dot{W}\} + (\lambda[A] + [K_w] + [K1] \\ &+ [K2])\{W\} = \{P\} - ([K_{w\phi}] + [K1_{w\phi}])\{W_\phi\}\end{aligned} \tag{2.112}$$

$$\left(\left[K_{\phi v}\right]+\left[K1_{\phi v}\right]\right)\{W\}=\{P_{\phi}\}-\left[K_{\phi}\right]\{W_{\phi}\} \tag{2.113}$$

The key to self-sensing piezoelectric actuators is measuring the electrical charge drawn to the electrodes, $\{P_o\}$. This electrical charge can then be combined with the piezoelectric capacitance and applied electrical voltage, the term $[K_o]\{W_o\}$ in equation (2.113), to get a signal proportional to the structure DOF. Analog circuits such as the ones given in [80] and [81] can be used to implement the right hand side of equation (2.113). In practice, the compensation for the piezoelectric capacitance is not perfect and could affect the sensor performance. In this study, the difference between the piezoelectric capacitance and the electric circuit compensation will be neglected, i.e., perfect implementation of the right hand side of equation (2.113) is assumed. Therefore, the sensor output charge for self-sensing piezoelectric actuators is given by:

$$\{q^s\}=-\left(\left[K_{\phi v}\right]+\left[K1_{\phi v}\right]\right)\{W\} \tag{2.114}$$

Thus, equations (2.112) and (2.114) are the actuator and sensor equations, respectively, for self-sensing piezoelectric actuators.

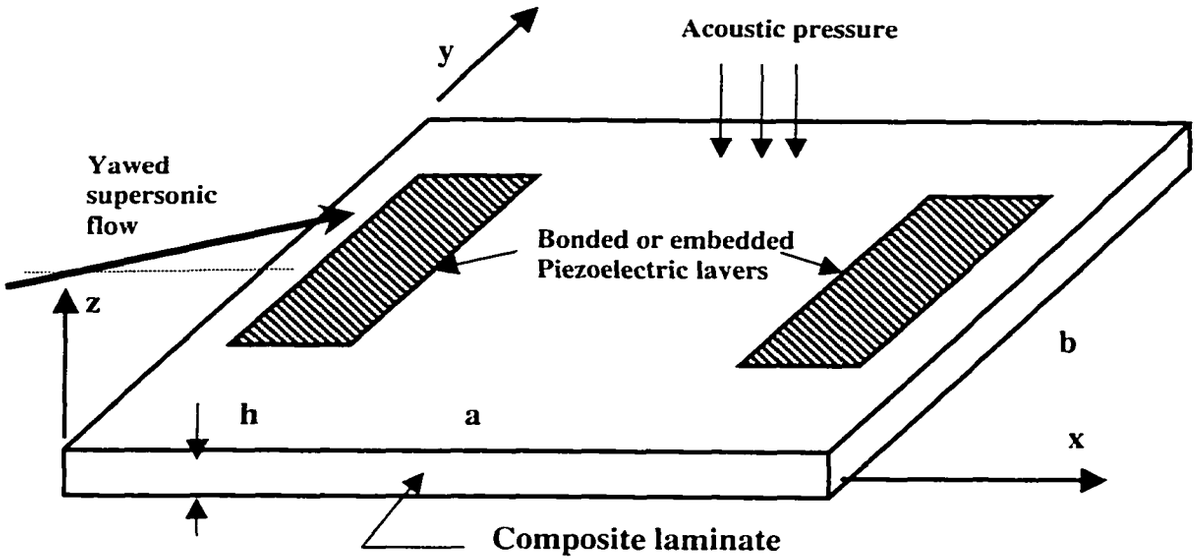

Figure 2.1 Composite panel under yawed supersonic flow and acoustic pressure loading

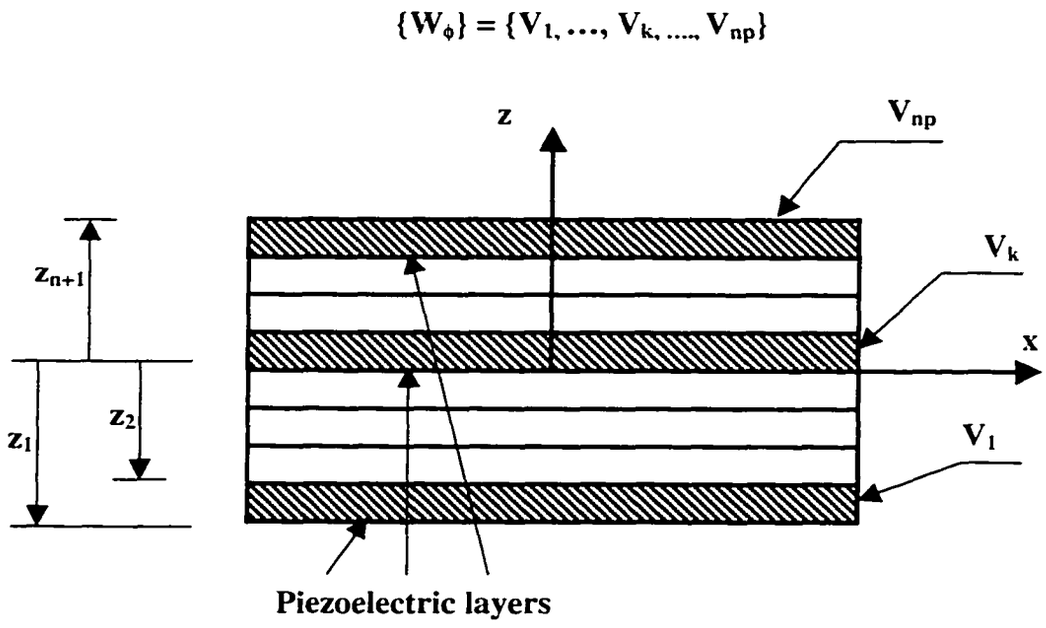

Figure 2.2 Composite laminate composed of *n* layers with *np* piezoelectric layers

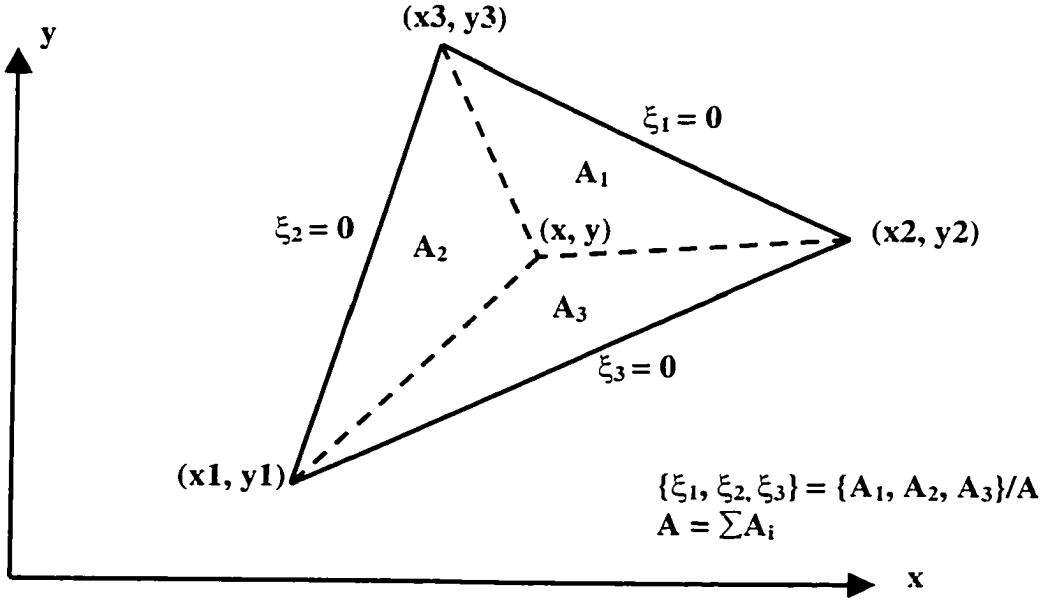

Figure 2.3 MIN3 element geometry and area coordinates

CHAPTER III

MODAL REDUCTION AND SOLUTION PROCEDURE

3.1 Introduction

The nonlinear dynamic equations derived in the pervious chapter represent the equation of motion in the structural node DOF. These equations could be used to solve nonlinear panel response for flutter and combined aerodynamic and acoustic loading. However, it is not efficient to do so due to the large number of structure node DOF and due to the nonlinear stiffness matrices, which have to be updated. Additionally, a reduced order system that only retains the important modes of the system should be used for control system design.

In this chapter, the system governing equations are transformed into the modal coordinates using the panel linear vibration modes to obtain a set of nonlinear dynamic modal equations of lesser number. The reduced modal equations can be easily used to solve the problems of linear and nonlinear flutter boundaries and to analyze panel response under combined acoustic and aerodynamic pressures. Linear and nonlinear panel flutter problems can be solved using either time domain methods such as numerical integration, or frequency domain methods (eigenvalue problem solution). However, the problem of nonlinear panel response under combined aerodynamic and acoustic loading must be solved using time domain methods. The reduced modal equations of motion will also be used to design control laws and to simulate panel flutter suppression. The following are the main assumptions used in the modal reduction and solution procedure:

- General composite laminate, symmetric or unsymmetric.
- Inplane inertia is neglected. This is justified as the frequencies of inplane vibration modes are much higher frequency than the out of plane bending modes.
- Self-sensing piezoelectric actuators are assumed. Therefore, equations (2.112) and (2.114) represent the coupled actuation and sensing equations, respectively.
- The piezoelectric actuators bonded to the surface or embedded within the laminate produce only bending moment and not inplane force. In other words, the piezoelectric resultant force, $\{N_o\}$, is zero. This is achieved by having a pair of

self-sensing piezoelectric actuators at the top and bottom surfaces of the laminate and by applying equal and opposite voltage to these two actuators (see Figure 3.1). This can be justified because the main purpose for the piezoelectric actuators is to suppress nonlinear panel flutter and because it was concluded in pervious work by [101] and [103] that piezoelectric actuators with bending moment are much more efficient than inplane tension for nonlinear panel flutter suppression.

3.2 Governing Equations

Recall the system equation of motion (sensor and actuator equations) derived in chapter 2, equations (2.112) and (2.114):

$$\frac{1}{\omega_o^2}\begin{bmatrix} M_b & 0 \\ 0 & M_m \end{bmatrix}\begin{Bmatrix} \ddot{W}_b \\ \ddot{W}_m \end{Bmatrix} + \frac{g_a}{\omega_o}\begin{bmatrix} G_a & 0 \\ 0 & 0 \end{bmatrix}\begin{Bmatrix} \dot{W}_b \\ \dot{W}_m \end{Bmatrix} + \left(\lambda \begin{bmatrix} A_a & 0 \\ 0 & 0 \end{bmatrix} + \right.$$

$$\begin{bmatrix} K_b & K_{bm} \\ K_{mb} & K_m \end{bmatrix} + \begin{bmatrix} K1_{N\phi} & 0 \\ 0 & 0 \end{bmatrix} + \begin{bmatrix} K1_b + K1_{Nm} + K1_{Nb} & K1_{bm} \\ K1_{mb} & 0 \end{bmatrix} + \tag{3.1}$$

$$\left. \begin{bmatrix} K2 & 0 \\ 0 & 0 \end{bmatrix} \right) \begin{Bmatrix} W_b \\ W_m \end{Bmatrix} = \begin{Bmatrix} P_b \\ 0 \end{Bmatrix} - \left(\begin{bmatrix} K_{b\phi} \\ K_{m\phi} \end{bmatrix} + \begin{bmatrix} K1_{b\phi} \\ 0 \end{bmatrix} \right) \{W_\phi\}$$

$$\{q^s\} = -\left(\begin{bmatrix} K_{\phi b} & K_{\phi m} \end{bmatrix} + \begin{bmatrix} K1_{\phi b} & 0 \end{bmatrix} \right) \begin{Bmatrix} W_b \\ W_m \end{Bmatrix} \tag{3.2}$$

By setting the piezoelectric resultant inplane force, $\{N_o\}$, to zero, as was assumed in the pervious section, then all linear and nonlinear element and system stiffness matrices that are function of piezoelectric inplane force resultant $\{N_o\}$ vanish. In addition, the element vector of electrical DOF, $\{w_o\}$, becomes a scalar for each element since the electrical DOF at the pair of top and bottom piezoelectric layers are equal and opposite. Therefore, the following matrices $[K_{m\phi}]$, $[K1_{N\phi}]$, and $[K1_{b\phi}]$ become zero matrices, see equations (2.57), (2.67), and (2.70). Using this in equations (3.1) and (3.2) and by neglecting the inplane inertia as mentioned in the pervious section, the equations of motion then become:

Actuator Equation:

$$\frac{1}{\omega_o^2}\begin{bmatrix} M_b & 0 \\ 0 & 0 \end{bmatrix}\begin{Bmatrix} \ddot{W}_b \\ \ddot{W}_m \end{Bmatrix}+\frac{g_a}{\omega_o}\begin{bmatrix} G_a & 0 \\ 0 & 0 \end{bmatrix}\begin{Bmatrix} \dot{W}_b \\ \dot{W}_m \end{Bmatrix}+\left(\lambda\begin{bmatrix} A_a & 0 \\ 0 & 0 \end{bmatrix}+\begin{bmatrix} K_b & K_{bm} \\ K_{mb} & K_m \end{bmatrix}+\right.$$

$$\left.\begin{bmatrix} K1_b + K1_{Nm} + K1_{Nb} & K1_{bm} \\ K1_{mb} & 0 \end{bmatrix}+\begin{bmatrix} K2 & 0 \\ 0 & 0 \end{bmatrix}\right)\begin{Bmatrix} W_b \\ W_m \end{Bmatrix}=\begin{Bmatrix} P_b \\ 0 \end{Bmatrix}-\begin{bmatrix} K_{b\phi} \\ 0 \end{bmatrix}\{W_\phi\} \quad (3.3)$$

Sensor Equation:

$$\{q^s\}=-[K_{\phi b} \quad 0]\begin{Bmatrix} W_b \\ W_m \end{Bmatrix} \quad (3.4)$$

It is worth mentioning that the pure transverse displacement sensor signal in equation (3.4) is obtained by summing the charge outputs from the pair of top and bottom piezoelectric layers (see Figure 3.1). Equation (3.3) can be partitioned to two separate equations for bending and inplane DOF. The inplane DOF, $\{W_m\}$, can be expressed in terms of the bending DOF, $\{W_b\}$, as:

$$\{W_m\}=-[K_m]^{-1}([K_{mb}]+[K1_{mb}])\{W_b\} \quad (3.5)$$

and the system equations in terms of the bending displacement $\{W_b\}$ as:

$$\frac{1}{\omega_o^2}[M_b]\{\ddot{W}_b\}+\frac{g_a}{\omega_o}[G_a]\{\dot{W}_b\}+([K_L]+[K_{NL}])\{W_b\}=\{P_b\}-[K_{b\phi}]\{W_\phi\} \quad (3.6)$$

where the linear and nonlinear stiffness matrices are given by:

$$[K_L]=\left(\lambda[A_a]+[K_b]-[K_{bm}][K_m]^{-1}[K_{mb}]\right) \quad (3.7)$$

$$\begin{aligned}[K_{NL}]=&-[K_{bm}][K_m]^{-1}[K1_{mb}]+[K1_b]+[K1_{Nm}]+[K1_{Nb}]+\\&+[K2]-[K1_{bm}][K_m]^{-1}([K_{mb}]+[K1_{mb}])\end{aligned} \quad (3.8)$$

The system equation of motion in structural DOF, equation (3.6), has two major drawbacks. First, the element nonlinear stiffness matrices have to be evaluated and the system nonlinear stiffness $[K_{NL}]$ is assembled and updated at each iteration or numerical integration step. Second, the number of structure node DOF $\{W_b\}$ is usually very large which is not suitable for control laws design and computationally costly for both frequency domain and time domain solution methods. To overcome these drawbacks, the system equations are reduced using modal transformation and modal reduction based on the values of modal participation. This results in a system of coupled nonlinear modal

equations with much lesser number of DOF that could be used for control design, numerical integration, and frequency domain solution.

3.3 Modal Transformation and Reduction

Assuming that the panel deflection can be expressed as a linear combination of some known function as

$$\{W_b\} = \sum_{r=1}^{n} q_r(t)\{\phi_r\} = [\Phi]\{q\} \tag{3.9}$$

where the number of retained linear modes n is much smaller than the number of structure node DOF in bending, $\{W_b\}$. The normal mode $\{\phi_r\}$, which is normalized with the maximum component to unity, and the linear natural frequency ω_r are obtained from the linear vibration of the system.

$$\omega_r^2[M_b]\{\phi_r\} = [K_b]\{\phi_r\} \tag{3.10}$$

Since the nonlinear matrices $[K1_{mb}]$, $[K1_{bm}]$, $[K1_{Nb}]$, and $[K2]$ are all function of the unknown bending DOF $\{W_b\}$, they can be expressed as the sum of products of modal coordinates and nonlinear modal stiffness matrices as

$$\begin{aligned} ([K1_{mb}], [K1_{bm}], [K1_{Nb}]) &= \sum_{r=1}^{n} q_r \left([K1_{mb}]^{(r)}, [K1_{bm}]^{(r)}, [K1_{Nb}]^{(r)}\right) \\ [K2] &= \sum_{r=1}^{n}\sum_{s=1}^{n} q_r q_s [K2]^{(rs)} \end{aligned} \tag{3.11}$$

where the super-indices of those nonlinear modal stiffness matrices denote that they are assembled from the corresponding element nonlinear stiffness matrices. Those element nonlinear stiffness matrices are evaluated with the corresponding element components $\{w_b\}^{(r)}$ obtained from the known system linear mode $\{\phi_r\}$. Therefore, those nonlinear modal stiffness matrices are constant matrices. This is a great advantage, as these matrices do not need to be evaluated at the element level and assembled at each iteration or time integration step.

The first-order nonlinear stiffness matrix $[K1_{Nm}]$ is a linear function of the inplane displacement $\{W_m\}$. From equation (3.5), $\{W_m\}$ consists of two terms as:

$$\{W\}_m = -[K]_m^{-1}[K_{mb}][\Phi]\{q\} - [K]_m^{-1}\left(\sum_{r=1}^{n} q_r [K1_{mb}]^{(r)}\right)[\Phi]\{q\}$$
$$= -\sum_{r=1}^{n} q_r \{\phi_r\}_m - \sum_{r=1}^{n}\sum_{s=1}^{n} q_r q_s \{\phi_{rs}\}_m \tag{3.12}$$

where the two inplane modes corresponding to the r-th bending mode $\{\phi_r\}$ are defined as:

$$\{\phi_r\}_m = [K_m]^{-1}[K_{mb}]\{\phi_r\}$$
$$\{\phi_{rs}\}_m = [K_m]^{-1}[K1_{mb}]^{(r)}\{\phi_s\} \tag{3.13}$$

Thus, the nonlinear stiffness matrix $[K1_{Nm}]$ can be expressed as the sum of two nonlinear modal stiffness matrices as:

$$[K1_{Nm}] = -\sum_{r=1}^{n} q_r [K1_{Nm}]^{(r)} - \sum_{r=1}^{n}\sum_{s=1}^{n} q_r q_s [K2_{Nm}]^{(rs)} \tag{3.14}$$

The nonlinear modal stiffness matrices $[K1_{Nm}]^{(r)}$ and $[K2_{Nm}]^{(rs)}$ are assembled from the corresponding element nonlinear stiffness matrices. Those element nonlinear stiffness matrices are evaluated with the corresponding element components $\{w_m\}^{(r)}$ obtained from the known inplane modes $\{\phi_r\}_m$ and $\{\phi_{rs}\}_m$, respectively. Thus, the nonlinear modal stiffness matrices are constant matrices. Using equations (3.11) and (3.14), the system equation, (3.6), is transformed to the following reduced nonlinear system in the modal coordinates

$$\frac{1}{\omega_o^2}[\overline{M}_b]\{\ddot{q}\} + \frac{g_a}{\omega_o}[\overline{G}]\{\dot{q}\} + 2\zeta_r\omega_r\frac{M_r}{\omega_o^2}[I]\{\dot{q}\} +$$
$$\left([\overline{K}_L] + [K_q] + [K_{qq}]\right)\{q\} = \{\overline{P}_b\} - [\overline{K}_{b\phi}]\{W_\phi\} \tag{3.15}$$

And the sensing equation in the modal coordinates is:

$$\{q^s\} = -[\overline{K}_{\phi b}]\{q\} \tag{3.16}$$

As for the electrical DOF, there is no need to do reduction since the number of electrical DOF, $\{W_o\}$, is usually small.

The modal matrices are given by:

$$([\overline{M}_b], [\overline{G}], [\overline{K}_L]) = [\Phi]^T([M_b], [G], [K_L])[\Phi] \tag{3.17}$$

and the quadratic and cubic terms in modal coordinates are:

$$[K_q]=[\Phi]^T\sum_{r=1}^{n}q_r\left(-[K_{bm}][K_m]^{-1}[K1_{mb}]^{(r)}+[K1_b]^{(r)}-[K1_{Nm}]^{(r)}\right.$$
$$\left.+[K1_{Nb}]^{(r)}-[K1_{bm}]^{(r)}[K_m]^{-1}[K_{mb}]\right)[\Phi] \tag{3.18}$$

$$[K_{qq}]=[\Phi]^T\sum_{r=1}^{n}\sum_{s=1}^{n}q_r\,q_s\left([K2]^{(rs)}-[K2_{Nm}]^{(rs)}-\right.$$
$$\left.[K1_{bm}]^{(r)}\,[K_m]^{-1}[K1_{mb}]^{(s)}\right)[\Phi] \tag{3.19}$$

and the modal load vector and piezoelectric control force are:

$$\{\overline{P}_b\}=[\Phi]^T\{P_b\} \tag{3.20}$$

$$[\overline{K}_{b\phi}]=[\Phi]^T[K_{b\phi}]=[\overline{K}_{\phi b}]^T \tag{3.21}$$

The nonlinear first order modal matrix $[K_q]$ usually represents a softening effect while the second order nonlinear matrix $[K_{qq}]$ represents a hard spring or stiffening effect. For the special case of symmetric panels, $[K_q]$ is zero (due to $[B] = 0$) and the modal equations of motion reduces to a multi DOF coupled Duffing system. Structural damping modal matrix, $[\overline{C}]=2\zeta_r\omega_r(M_r/\omega_o^2)[I]$, has been added to the system modal equation (3.15) where ζ_r, ω_r, and M_r are the modal damping, frequency, and mass, respectively, and $[I]$ is the identity matrix. The modal damping ratio can be determined based on testing or on performance of similar structures.

The advantages of the modal equations of motion given by equation (3.15) are: (i) there is no need to assemble and update the nonlinear stiffness matrices at each iteration since all the nonlinear modal matrices are constant, and (ii) the number of modal equations is much smaller than the structure equations. This approach has been successfully used for nonlinear panel flutter of composite panels at elevated temperature by Zhou et al. [104]. This approach has also been demonstrated for nonlinear panel flutter of composite panels under yawed supersonic flow by Abdel-Motagaly et al. [51] and for nonlinear response of composite panels under combined acoustic and aerodynamic loading by Abdel-Motagaly et al. [64].

The determination of the number of modes required for a specific problem is not a trivial task and requires some special attention to make sure the important modes are

retained. The few influential modes to be kept can be determined by the modal participation value, which is defined as:

$$\textit{Participation of the r-th mode} = |q_r| \Big/ \sum_{i=1}^{n} |q_i| \tag{3.22}$$

For the problem of nonlinear panel flutter, the number of modes used can be determined based on accurate and converged magnitude and frequency of limit-cycle oscillation (LCO). By doing this, it is guaranteed to get accurate flutter mode shape, which is crucial for panel flutter suppression problem. For the problem of acoustic loading in the form of uniform random pressure input, the lowest few symmetric modes are usually used. In summary, modal reduction is problem dependent and should be performed based on a systematic modal convergence and participation procedure.

3.4 Solution Procedure

3.4.1 Time Domain Method

Nonlinear panel response could be simply solved by using numerical integration of the modal dynamic equations of motion. For the case of combined loading, the random surface pressure is generated and the panel response is determined at each time step. For the case of nonlinear panel flutter, numerical integration is carried out using any arbitrary initial conditions at a given value of nondimensional dynamic pressure, λ. After some time, the solution converges to a limit cycle and the limit cycle oscillation (LCO) amplitude and frequency can then be determined at the given λ. This approach is accurate and general as it could easily handle both structural and aerodynamic damping. However, the frequency domain solution introduced in the next subsection is more effective computationally for the case of nonlinear panel flutter when the interest is only to determine the panel LCO response and the flutter mode shape. For control design and simulation, numerical integration must be used.

3.4.2 Frequency Domain Method

3.4.2.1 Critical Flutter Boundary

Linear panel flutter equations of motion can be determined by neglecting the nonlinear stiffness matrices, and by setting the piezoelectric actuation and random surface pressure to zero in equation (3.15).

$$\frac{1}{\omega_o^2}[\overline{M}_b]\{\ddot{q}\}+\frac{g_a}{\omega_o}[\overline{G}]\{\dot{q}\}+2\zeta_r\omega_r\frac{M_r}{\omega_o^2}[I]\{\dot{q}\}+[\overline{K}_L]\{q\}=\{0\} \tag{3.23}$$

This equation represents a dynamic eigenvalue problem and a solution for the unknown modal coordinates $\{q\}$ can be assumed in the form of:

$$\{q\}=\{q_o\}e^{\Omega t} \tag{3.24}$$

where $\{q_o\}$ is the eigenvector and $\Omega = \beta + i\omega$ is the panel motion parameter (β is damping rate and ω is frequency). Flutter will occur if the panel motion becomes unstable, i.e., when the damping rate becomes positive. Using the fact that $[G] = [M_b]$ and neglecting the structural damping, the linear panel flutter eigenvalue problem can be written as follows:

$$\left(-\kappa_j[\overline{M}_b]+[\overline{K}_L]\right)\{q_o\}e^{\Omega t}=\{0\} \tag{3.25}$$

where the eigenvalue, κ_j, is defined in terms of aerodynamic damping and reference frequency as:

$$\kappa=-\left(\frac{\Omega}{\omega_o}\right)^2-g_a\frac{\Omega}{\omega_o} \tag{3.26}$$

As the nondimensional dynamic pressure, λ, increases, the panel symmetric stiffness matrix will be perturbed by the skew symmetric aerodynamic matrix (see equation (3.7) for the definition of $[K_L]$). This will result in one eigenvalues κ_1 to increase and another eigenvalue κ_2 to decrease until they coalesce. If λ is increased further, the two eigenvalues become complex conjugate:

$$\kappa_{1,2} = \kappa_R \pm i\kappa_I. \tag{3.27}$$

For the case of zero aerodynamic damping, $g_a = 0$, the damping rate is zero at the coalescence of the two eigenvalues and hence this defines the flutter critical boundary, λ_{cr}, (i.e. at $\kappa_I = 0$). In the presence of aerodynamic damping, the damping rate will vanish after the coalescence. Substituting (3.26) into (3.27) and using the definition of Ω, it is found that $\beta = 0$ when $\kappa_I/\kappa_R = g_a$. The value of λ_{cr} in the presence of aerodynamic damping is thus slightly higher than that with no aerodynamic damping. Based on linear theory, the panel motion will grow exponentially beyond λ_{cr}. In reality, this is not the case due to inplane stretching forces. Thus, the nonlinear matrices must be considered to

determine the panel limit-cycle oscillation (LCO) response beyond the critical flutter boundary.

3.4.2.2 Nonlinear Flutter Limit-Cycle Oscillation

The reduced nonlinear modal equations for the nonlinear eigenvalue problem of panel flutter could be solved using the linearized updated mode with nonlinear time function (LUM/NTF) approximate method introduced and applied by Gray [11] for nonlinear hypersonic panel flutter and by Xue [39] for nonlinear supersonic panel flutter. The LUM/NTF method is an iterative method. It was originally applied in the structure node DOF and thus requires evaluation and assembly of element matrices at each iteration. An efficient solution procedure, presented here for the first time, is to apply the LUM/NTF method to the reduced modal equations. The presented solution procedure is efficient and has a great advantage in computation time and thus could be used for the study of nonlinear LCO amplitude and for flutter mode shape determination of composite panels.

The LUM/NTF solution procedure is based on using harmonic response assumption and on linearization of nonlinear time functions. Since the intent is to determine LCO amplitude and frequency, the solution of the modal DOF is assumed in a harmonic form similar to equation (3.25):

$$\{q\} = \{q_o\} e^{\Omega t} = e^{\beta t} \{q_o\} (\cos \omega t + i \sin \omega t) \tag{3.28}$$

Using equation (3.15), the nonlinear panel flutter eigenvalue problem can be written as follows:

$$\left(-\kappa_j [\overline{M}_b] + [\overline{K}_L] + [K_q] + [K_{qq}]\right) \{q_o\} e^{\Omega t} = \{0\} \tag{3.29}$$

For a stable limit cycle, the modal solution in equation (3.28) can be written by setting β to zero and by choosing either $\cos(\omega t)$ or $\sin(\omega t)$ for the harmonic solution. Using this modal solution, equation (3.29) becomes:

$$\left(-\kappa_j [\overline{M}_b] \cos \omega t + [\overline{K}_L] \cos \omega t + [\overline{K}_q] \cos^2 \omega t + [\overline{K}_{qq}] \cos^3 \omega t\right) \{q_o\} = \{0\} \tag{3.30}$$

Using linear approximation for the nonlinear time functions ($\cos^2 \omega t$ and $\cos^3 \omega t$), the linearized eigenvalue problem for LCO of nonlinear panel flutter can be written as:

$$\kappa_j [\overline{M}_b]\{q_o\} = \left([\overline{K}_L] + \frac{\sqrt{2}}{2}[\overline{K}_q] + \frac{3}{4}[\overline{K}_{qq}] \right)\{q_o\} \tag{3.31}$$

Equation (3.31) represents a nonlinear eigenvalue problem where the matrices $[\overline{K}_q]$ and $[\overline{K}_{qq}]$ are function of the unknown eigenvector $\{q_o\}$. It can be solved using an iterative linearized eigenvalue solution procedure. The nonlinear stiffness matrices are evaluated at iteration $j+1$ using the eigenvector solution from iteration j. The eigenvalue and eigenvector can then be determined based on certain convergence criterion (see Figure 3.2). For a given maximum panel deflection (W_{max}), the LCO occurs at a specific nondimensional dynamic pressure value denoted as λ_{LCO}. At this value of dynamic pressure the damping rate vanishes ($\beta = 0$). If the aerodynamic damping is neglected, this will occur when two eigenvalues of equation (3.31) coalesce. In the presence of aerodynamic damping, the value of λ_{LCO} is reached after of κ_j become complex conjugate ($\kappa = \kappa_R \pm i\kappa_I$) at the point where $g_a = \kappa_I / \sqrt{\kappa_R}$ (similar to the linear flutter case). Figure 3.2 describes the search algorithm and the iterative linearized eigenvalue solution procedure used to determine λ_{LCO} for a given LCO amplitude.

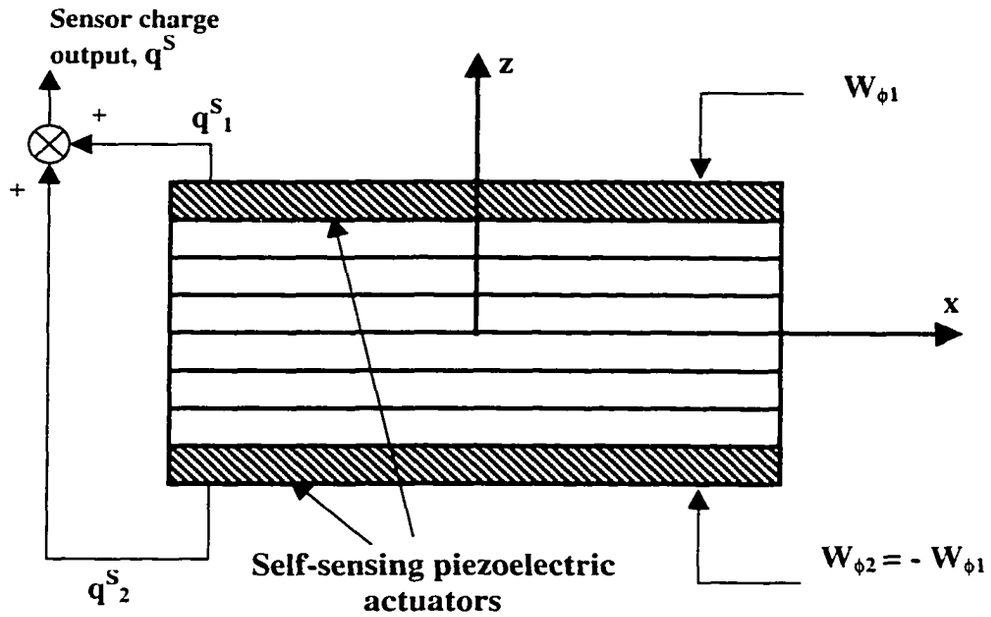

Figure 3.1 Configuration of self-sensing piezoelectric actuators for bending moment actuation and transverse displacement sensing

Step 1: For a Given LCO amplitude W_{max}, Assume $\{q_o\}$

Step 2: Assume a value for λ

Step 3: Solve the linearized eigen equation for the j-th iteration:

$$\kappa_j [\overline{M}_b]\{q_o\}_j = ([\overline{K}_L]+[\overline{K}_{NL}])\{q_o\}_j$$

$$[\overline{K}_{NL}]=\frac{\sqrt{2}}{2}\left[K_q\left(\{q_o\}_{j-1}\right)\right]+\frac{3}{4}\left[K_{qq}\left(\{q_o\}_{j-1}\right)\right]$$

where $\{q_o\}_j$ is the updated modal solution

Step 4: Get $\{W_b\}$ from $\{q_o\}_j$ using $\{W_b\} = [\Phi]\{q_o\}_j$ and find $(W_{max})_j$

then adjust $\{q_o\}_j$ to result in the required W_{max} using:

$$\{q_o\}_j = \{q_o\}_j \frac{(W_{\max})_{given}}{(W_{\max})_j}$$

Step 5: Test for convergence of $\{q_o\}$, if not go to step 3

Step 6: Check for coalescence of the eigenvalues:

- if not, $\lambda = \lambda + \Delta\lambda$ then go to step 2
- if yes $\lambda_{LCO} = \lambda$ then exit

Figure 3.2 Iterative solution procedure for nonlinear panel flutter limit-cycle response

CHAPTER IV

FINITE ELEMENT ANALYSIS RESULTS

4.1 Introduction

Validation of the MIN3 finite element modal formulation and analysis results are presented in this chapter. The MIN3 finite element modal formulation is validated by comparison with other finite element and analytical solutions. The validation tests performed include: linear free vibration, piezoelectric static actuation, linear and nonlinear panel flutter, time and frequency domain solutions, and nonlinear panel response under random acoustic pressure loading.

Using the verified MIN3 Modal formulation, analysis results for the effect of arbitrary flow yaw angle on nonlinear supersonic panel flutter for isotropic and composite panels are presented using the frequency domain solution method. The effect of combined supersonic aerodynamic and acoustic pressure loading on the nonlinear dynamic response of isotropic and composite panels is also considered.

Results are presented for isotropic material (Aluminum) and for graphite/epoxy fiber reinforced composite with different laminate stacking sequence. The properties of the different materials used in this chapter are given in Table 4.1. As for the panel geometry, the MIN3 triangular element is used to model square, rectangular, and triangular panels using different mesh sizes. Figure 4.1 shows a typical MIN3 finite element mesh used to model both rectangular and triangular panels.

4.2 Finite Element Validation

4.2.1 Natural Frequencies

The first validation test is comparing the first few natural frequencies versus analytical values for a simply supported square isotropic panel performed to verify the linear stiffness and mass matrices. The panel dimensions are 12×12×0.05 in., corresponding to panel length, a, panel width, b, and panel thickness, h, respectively. The analytical natural frequencies (rad/s) are determined using the classical plate theory solution and are given by:

$$\omega_{nm} = \sqrt{\frac{D}{\rho h}\left[\left(\frac{n\pi}{a}\right)^2 + \left(\frac{m\pi}{b}\right)^2\right]} \tag{4.1}$$

where $D = \frac{Eh^3}{12(1-\nu^2)}$. Table 4.2 show the first six natural frequencies calculated using equation (4.1) and a 12×12 MIN3 finite element mesh (total of 288 elements). It can be seen that the difference between the MIN3 solution and analytical solution is less than 0.5%.

4.2.2 Piezoelectric Static Actuation

The piezoelectric finite element formulation is validated using the cantilevered bimorph beam shown in Figure 4.2 (symmetric half of the beam). The bimorph beam consists of two identical PVDF piezoelectric layers with polling axis in the 3 direction but with opposite polarities. Hence, this beam will bend when electrical field is applied in the vertical direction. The mechanical and electrical constants for PVDF are given in Table 4.1. A unit electrical voltage is applied across the thickness and the beam lateral deflection at different points is determined. The results obtained using a 5×2 MIN3 elements mesh are compared against the analytical solution of [69], the solid finite element of [78], and the QUAD4 finite element of [77]. Table 4.3 shows that the deflections obtained using the MIN3 element formulation are in good agreement with other analytical and finite element solutions.

4.2.3 Linear and Nonlinear Flutter

The MIN3 modal finite element solution using the lowest 25 modes and a 12×12 mesh is used to compare the critical nondimensional dynamic pressure, λ_{cr}, values versus the CQ conforming quadrilateral element solution [46] and analytical solutions [15] for simply supported isotropic rectangular panels with different aspect ratios and at different flow yaw angles. All solutions assume zero aerodynamic damping and λ_{cr} is nondimensional with respect to the panel length, a. Table 4.4 shows that, the solution of the MIN3 modal formulation is in very good agreement with the CQ element and with the analytical solution for different aspect ratios and different flow angles with maximum difference of less than 2%.

The limit-cycle oscillations (LCO) response for a simply supported (with immovable inplane edges) square (12×12×0.05 in.) isotropic panel with zero yaw angle using a 12×12 MIN3 mesh and 6 modes in the x direction are shown in Figure 4.3. Results using both frequency domain and time domain solution methods are shown in this figure. The LCO obtained by [15] with a 6-mode model using Galerkin's method and numerical integration is also shown in this figure for comparison. The aerodynamic damping coefficient, c_a, is set to 0.1 (see equation 2.37). Both time and frequency domain solutions using the modal MIN3 element formulation are shown to be in good agreement with the analytical solution.

For composite panels, the limit-cycle results of a simply supported 8-layer $[0/45/-45/90]_S$ graphite/epoxy square (12×12×0.048 in.) panel obtained by [40] using the C^1 conforming rectangular plate element and time domain-modal formulation are compared with those obtained using the present formulation with time domain solution. The complete plate is modeled with 12×12 mesh and using 6 modes in x direction. The LCO response at zero yaw angle, shown in Figure 4.4, demonstrates the accuracy of the MIN3 element and the present finite element formulation.

4.2.4 Nonlinear Random Response

The last validation test is intended to verify the panel nonlinear random vibration under acoustic pressure loading. Table 4.5 shows the root mean square (RMS) of the panel maximum deflection divided by panel thickness (W_{max}/h) obtained using present formulation and other available solution methods for different sound pressure levels, SPL, (see section 4.4.1 for the details of the acoustic pressure loading). The MIN3 finite element modal formulation is used for a rectangular isotropic panel (15×12×0.04 in.) using a 12×12 mesh. The lowest four symmetric modes are included for uniform input random pressure distribution analysis. The Fokker-Planck-Kolmogorov (FPK) equation method [62] is an exact solution for the single DOF forced Duffing equation. The finite element/equivalent linearization (FE/EL) method [63] assumes that the equivalent linearized system is stationary Gaussian, whereas the present time domain numerical integration method does not assume that the displacement response is Gaussian. Therefore, the present method should be more accurate.

4.3 Effect of Flow Yaw angle on Nonlinear Panel Flutter

The effect of flow yaw angle, α, on nonlinear panel flutter LCO is presented in this section. The panels considered include: isotropic and composite material, square, rectangular, and triangular panels. The frequency domain solution method is used in this section since it is more efficient computationally than the time domain numerical integration method. The aerodynamic damping coefficient, c_a, is set to 0.01 for all cases and structural aerodynamic damping is neglected.

4.3.1 Isotropic Panels

A simply supported square isotropic panel (12×12×0.05 in.) with immovable inplane edges ($u = v = 0$) at different flow angles is studied in detail. First, convergence of the LCO response using various finite element mesh sizes is studied. Three mesh sizes of 8×8 (128 elements), 10×10 (200 elements) and 12×12 (288 elements) are used to model the simply supported square isotropic panel. Limit-cycle amplitude values versus nondimensional dynamic pressure using 16 modes, mode (1,1) to (4,4), for the three mesh sizes at $\alpha = 45^\circ$ are shown in Figure 4.5. The maximum difference of the nondimensional dynamic pressure between the 10×10 and 12×12 models in Figure 4.5 is less than 1 %.

Modal convergence is also studied in detail for the square panel at different flow angles. The panel is modeled using a 12×12 mesh or 288 MIN3 elements. The number of structure DOF $\{W_b\}$ is of 407 and it is reduced to the modal coordinates to include the selected n modes. The modal participation values using 4 modes in x direction and 4 modes in y direction (4×4 modes, total of 16 modes) for two limit-cycle amplitudes $W_{max}/h = 0.01$ and 0.8 at $\alpha = 0^\circ$, 45° and 90° are given in Tables 4.6. The modal participation values indicate that a 4-mode model in the flow direction would yield accurate and convergent limit-cycle results for $\alpha = 0$ and 90°, while a combination of x direction and y direction modes is required for $\alpha = 45^\circ$. The modal convergence is further confirmed by the convergence of the nondimensional dynamic pressure versus the number of modes used in model reduction as shown in Figure 4.6 for 0° yaw angle and in Figure 4.7 for 45° yaw angle. These figures confirm that, a 16 modes model is required for all yaw angles to yield convergent LCO amplitude. For the 0° yaw angle case, Figure

4.6 shows that using the well-known 6 modes in x direction and using 16 modes, (1,1) to (4,4), yield almost the same LCO amplitude. From symmetry, the same will apply for the 90° yaw angle case. The 16 modes model is used in order to have one model for all yaw angle that can be used for the control system design in the next chapters.

The variation of limit-cycle amplitude versus nondimensional dynamic pressure for α = 0°, 15°, 30°, and 45° are given in Figure 4.8. It is seen that increasing the flow angle has the effect of slightly increasing the critical nondimensional dynamic pressure, λ_{cr}, at zero limit-cycle amplitude (linear flutter boundary) for this square isotropic panel. However, as the LCO amplitude, W_{max}/h, increases the difference in λ between different flow angles decreases at fixed W_{max}/h. This effect is due to the different nonlinear effect resulting from having different flutter mode shapes as the flow angle changes. Figure 4.9 shows the effect of aspect ratio (a/b) on the nondimensional dynamic pressure at α = 0 and 45°. It is seen that increasing the flow angle for isotropic panels with $(a/b) > 1$ causes the nondimensional dynamic pressure to increase at fixed limit-cycle amplitude.

The flutter deflection shapes at W_{max}/h = 1.0 for flow angles of α = 0°, 45°, and 90° are given in Figure 4.10. It is clear how the flow angle greatly changes the flutter deflection shape. This necessitates having different controllers and different actuator and sensor locations for different flow angles as will be studied in detail in Chapter 6.

4.3.2 Composite Panels

Two simply supported rectangular (15×12×0.048 in.) graphite/epoxy composite panels with two different laminate stacking sequences are considered. Both panels are modeled using a 12×12 MIN3 finite element mesh. The first laminate considered is an 8-layer $[0/45/-45/90]_S$ panel. Table 4.7 shows the modal participation values for this panel using the lowest 16 modes in increasing frequency order. Figure 4.11 shows the LCO amplitude convergence using different number of modes and confirms that convergent LCO amplitude can be obtained using the 16 modes model for this panel. Figure 4.12 shows the effect of flow yaw angle on the nonlinear panel flutter response and Figure 4.13 shows the same effect on flutter deflection shape. Figure 4.12 shows that as α increases from 0 to 90°, λ increases at the same LCO amplitude, W_{max}/h. However, as W_{max}/h increases the difference in λ decreases due to the different nonlinear effect for the

different flutter deflection shapes resulting for different flow angles, as shown in Figure 4.13.

The second composite panel considered is a 3-layer [-40/40/-40] laminate. Modal convergence is given by Table 4.8 and Figure 4.14 which confirm the validity of a 16 modes model for this panel. Figures 4.15 and 4.16 show the effect of flow yaw angle on nonlinear panel flutter response and on flutter deflection shape, respectively. It is seen how the nondimensional dynamic pressure, λ, at 45° yaw angle is less than that of 0° and 90° at the same limit-cycle amplitude. The laminate considered is a good example to demonstrate the importance of the effect of the flow yaw angle on the nonlinear panel flutter. It is also seen that, unlike the isotropic case, the flutter deflection shape for $\alpha = 0°$ and 90° is clearly not symmetric about x or y. This is because the [-40/40/-40] composite laminate is anisotropic.

4.3.3 Triangular Panel

To take advantage of the triangular MIN3 element, a clamped isotropic triangular panel is also considered. The panel dimensions are 12×12×0.05 in. and the panel is modeled using a 10×10 finite element mesh (see Figure 4.1). Figure 4.17 shows modal convergence for this panel using the lowest 16, 25 and 36 modes. Based on this figure a 25 modes model is used for this panel. Figure 4.18 shows the effect of flow yaw angle on nonlinear panel response. It is noted that the linear flutter boundary for $\alpha = 0°$ and 180° is the same, but λ becomes different as the LCO amplitude increases because of the different nonlinear effect for the different flutter deflection shape of 0° and 180° yaw angles. The same applies for $\alpha = 45°$ and 225°. It is also seen that the worst case for this panel is when the flow is yawed with 315° (–45°), i.e., along the tilted edge.

4.4 Effect of Combined Supersonic Flow and Acoustic Pressure Loading

4.4.1 Random Surface Pressure

The input acoustic surface pressure is assumed as a band limited Gaussian random white noise that is uniformly distributed over the panel surface. The pressure time sequence is generated by using a randomly generated Gaussian pressure filtered by a Chebyshev low pass filter with the specified cut-off frequency, f_c. The pressure power spectral density (PDS) is given by:

$$S(f) = p_o^2 10^{SPL/10} \qquad 0 \le f \le f_c$$
$$= 0 \qquad f > f_c \tag{4.2}$$

where p_o is the reference pressure (p_o = 2.9×10^{-9} psi) and SPL is the sound pressure spectrum level measured in decibels. The power spectral density (PSD) of the input pressure at SPL = 90 dB is shown in Figure 4.19. In practice, the acoustic pressure loading could be determined from recorded flight data. The formulation derived in Chapters 2 and 3 combined with time domain numerical integration solution is general in the sense that it could handle both stationary Gaussian as well as non-stationary non-Gaussian random loads.

4.4.2 Isotropic Panel

The response of a simply supported square isotropic panel (12×12×0.05 in.) under combined aerodynamic and acoustic pressure loading is studied in detail. The panel is modeled using a 12×12 MIN3 element mesh. The modes considered are (1,1) to (6,1) for panel flutter and (1,1), (1,3), (3,1), and (3,3) for random uniform pressure loading. No modal participation values are needed for this well studied problem. The aerodynamic damping coefficients, c_a, is assumed to be 0.01 and a structural modal damping of 1% is added to all modes. No flow yaw angle is introduced for this analysis.

Figure 4.20 shows the root mean square (RMS) of panel maximum deflection divided by panel thickness for SPL = 0, 100, 110, and 120 dB. The case of 0 dB SPL corresponds to the case of nonlinear panel flutter and the points at λ = 0 correspond to conventional nonlinear panel response under acoustic excitation only. The maximum deflection is located at three quarter length from the leading edge (3a/4, a/2) for panel flutter and at plate center (a/2, a/2) for pure acoustic excitation. The maximum location for the combined load cases is somewhere between 3a/4 and a/2 depending on the values of SPL and λ. It is seen from Figure 4.20 that a stiffening effect causes the RMS of maximum deflection to decrease as λ increases until flutter λ_{cr} is approached. This is due to the anti-symmetric aerodynamic stiffness matrix perturbation, which increases the frequency of mode (1,1) and decreases the frequency of mode (2,1). Mode (1,1) is a major contributor mode to the panel random response while the anti-symmetric mode (2,1) has no effect on the panel random response. The RMS of maximum deflection starts

increasing again as soon as λ_{cr} is reached. This figure clearly demonstrates the importance of the effect of combined aerodynamic and acoustic loading on the panel nonlinear response.

Time and frequency response of the panel maximum deflection is studied in detail for five different combinations of SPL and λ. The results are given in Figures 4.21 through 4.25. Figures 4.21 and 4.22 represent the panel response at low (100 dB) and high (120 dB) SPL, respectively. At low SPL, the panel experiences small deflection within the linear random vibration with mode (1,1) being the dominant mode. At high SPL, the panel experiences large deflection nonlinear random vibration. The nonlinear behavior at SPL = 120 dB is demonstrated in Figure 4.22 via the broadening and shifting to higher values of the frequency peaks in the deflection PSD. At λ = 800 and 0 dB SPL, the panel response is the expected pure panel flutter limit-cycle oscillation with a single dominant frequency, as shown in Figure 4.23. For the combined load case of λ = 800 and SPL = 100, shown in Figures 4.24, the panel response is dominated by the panel flutter behavior as the random pressure effect is small compared to the aerodynamic loading. This is clear from the single dominant frequency in the deflection PSD plot. For the case of λ = 800 and SPL = 120, shown in Figure 4.25, the panel response is dominated more by random vibration since the SPL is high. This is demonstrated in the PSD plot by the broadening of the frequency peaks.

4.4.3 Composite Panel

The effect of combined loading for a clamped rectangular (15×12×0.048 in.) 8-layer $[0/45/-45/90]_S$ graphite/epoxy panel is also considered. The panel is modeled using a 12×12 MIN3 finite element mesh. The system equation of motion is reduced using the lowest n linear vibration modes. Table 4.9 shows the effect of the number of modes used on the RMS of panel maximum deflection at λ = 800 and SPL = 120 dB. It is shown that a 16, 20, or 25 modes model would yield convergent results. The modal convergence is further verified by the modal participation of the lowest 25 modes given in Table 4.10. By retaining the 13 modes with participation values > 1% in the analysis, a very accurate RMS of W_{max}/h can also be obtained, as shown in Table 4.9. Figure 4.26 shows the panel nonlinear response under combined loading for different values of λ and SPL. These

results are obtained by using the most dominant 13 modes defined by modal participation >1%. Similar to the isotropic case, this figure shows clearly the importance of considering both aerodynamic and acoustic loading in the analysis of composite panels especially at high SPL.

4.5 Summary

Validation of the MIN3 modal finite element formulation and analysis results for nonlinear panel flutter and for nonlinear panel response under combined aerodynamic and acoustic pressures are presented in this chapter. The finite element formulation is validated by comparison with other finite element and analytical solutions including validation of linear free vibration frequencies, piezoelectric static actuation, linear and nonlinear panel flutter, and nonlinear panel response under random acoustic pressure loading. Analysis results for the effect of arbitrary flow yaw angle on nonlinear supersonic panel flutter for both isotropic and composite panels are presented using the modal LUM/NTF solution method. Results are presented for square, rectangular, and triangular panels. The results showed that the effect of flow yaw angle completely changes the shape of the panel limit-cycle deflection. It also showed the effect of the yaw angle to be a very important parameter especially for composite panels where the flow direction may increase or decrease the nondimensional dynamic pressure at fixed limit-cycle amplitude depending on the panel lamination. The effect of combined supersonic aerodynamic and acoustic pressures loading on the nonlinear dynamic response of isotropic and composite panels is also presented. It is found that for panels at supersonic flow, only acoustic pressure (sonic fatigue) is to be considered for low dynamic pressures ($\lambda << \lambda_{cr}$) while both acoustic and aerodynamic pressures have to be considered for significant and high aerodynamic pressures.

Table 4.1 Material properties for the different materials used for finite element validation and analysis results

Isotropic (aluminum)	
E	10.5 Msi
ν	0.3
ρ	0.2588×10^{-3} lb-sec^2/in.^{4}

Composite (graphite/epoxy)	
E_1	22.5 Msi
E_2	1.17 Msi
G_{12}	0.66 Msi
G_{23}	0.44 Msi
ν_{12}	0.22
ρ	0.1458×10^{-3} lb-sec^2/in.^{4}

PVDF (for bimorph pointer)	
E	2.0 Gpa
ν_{12}	0.29
$d_{31} = d_{32}$	2.2e-11 m/V

Table 4.2 Comparison between natural frequencies using MIN3 element and using analytical solution for square isotropic panel

Mode (n,m)	Frequency (Hz)	
	12×12 MIN3	Analytical
(1,1)	66.5482	66.4903
(2,1)	165.9355	166.2259
(2,2)	266.8552	265.9614
(3,1)	332.4625	332.4517
(3,2)	430.1436	432.1872
(3,3)	564.7975	565.1679

Table 4.3 Comparison of static deflection for the piezoelectric bimorph beam (10^{-7} m) using different methods (see Figure 4.2)

Position	1	2	3	4	5
Analytical [69]	0.138	0.552	1.242	2.208	3.450
Solid FE [78]	0.138	0.552	1.242	2.208	3.450
QUAD4 [77]	0.14	0.55	1.24	2.21	3.45
MIN3	0.149	0.587	1.289	2.256	3.487

Table 4.4 Comparison of nondimensional linear flutter boundary using different methods at different flow angles

a/b	Method	Nondimensional Critical Dynamic Pressure, λ_{cr}				
		$\alpha = 0^o$	$\alpha = 30^o$	$\alpha = 45^o$	$\alpha = 60^o$	$\alpha = 90^o$
0.5	CQ [46]	382	213	172	151	135
	Analytical [15]	385	-	-	-	138.7
	MIN3 Modal	378	215	177	155	138
1.0	CQ [46]	503	516	523	516	503
	Analytical [15]	512.6	-	-	-	512.6
	MIN3 Modal	513	522	527	522	513
2.0	CQ [46]	1081	1206	1388	1703	3056
	Analytical [15]	1110	-	-	-	3080
	MIN3 Modal	1117	1237	1414	1712	3020

*All values are obtained for neglected aerodynamic damping

Table 4.5 Comparison of the RMS (W_{max}/h) for a simply supported rectangular (15×12×0.04 in.) isotropic plate under acoustic pressure loading only using different methods and mode numbers

SPL (dB)	FPK [62]	FE/EL [63]		Present
	1 mode	1 mode	4 modes	4 modes
90	0.249	0.238	0.238	0.266
100	0.592	0.532	0.533	0.489
110	1.187	1.030	1.031	1.092
120	2.200	1.902	1.905	2.113

Table 4.6 Modal participation values at various limit-cycle amplitudes and different flow angles for simply supported square panel

Mode	Modal Participation, %					
	$\alpha = 0^o$ Wmax/h		$\alpha = 45^o$ Wmax/h		$\alpha = 90^o$ Wmax/h	
	0.01	0.8	0.01	0.8	0.01	0.8
q_{11}	42.18	45.28	31.17	34.41	42.18	45.28
q_{12}	0.32	0.23	22.62	22.11	42.61	39.17
q_{13}	0.00	0.79	4.68	4.66	11.95	10.68
q_{14}	0.02	0.03	0.93	1.16	2.44	2.44
q_{21}	42.61	39.17	22.62	22.11	0.32	0.23
q_{22}	0.25	0.18	9.04	7.38	0.25	0.18
q_{23}	0.00	0.64	1.26	0.77	0.05	0.06
q_{24}	0.01	0.01	0.31	0.30	0.09	0.10
q_{31}	11.95	10.68	4.68	4.66	0.00	0.79
q_{32}	0.05	0.06	1.26	0.77	0.00	0.64
q_{33}	0.00	0.22	0.09	0.03	0.00	0.22
q_{34}	0.01	0.02	0.01	0.04	0.00	0.08
q_{41}	2.44	2.44	0.93	1.16	0.02	0.03
q_{42}	0.09	0.10	0.31	0.30	0.01	0.01
q_{43}	0.00	0.08	0.01	0.04	0.01	0.02
q_{44}	0.01	0.02	0.00	0.02	0.01	0.02

Table 4.7 Modal participation values at various limit-cycle amplitudes and different flow angles for simply supported rectangular graphite/epoxy $[0/45/-45/90]_S$ panel

Mode	Modal Participation, %					
	$\alpha = 0^o$ Wmax/h		$\alpha = 45^o$ Wmax/h		$\alpha = 90^o$ Wmax/h	
	0.01	0.8	0.01	0.8	0.01	0.8
q_1	24.85	29.87	22.74	25.24	25.62	27.43
q_2	16.54	12.64	29.59	24.37	41.11	36.57
q_3	31.92	33.52	17.47	21.17	3.61	4.04
q_4	5.58	3.45	5.22	4.65	7.19	6.38
q_5	1.16	0.07	11.93	9.91	13.13	12.15
q_6	15.37	15.03	3.35	5.74	0.12	1.65
q_7	0.48	1.01	1.47	0.43	1.55	2.29
q_8	0.68	0.21	0.92	0.83	0.28	0.78
q_9	0.04	0.07	3.27	3.00	4.08	4.27
q_{10}	0.01	0.18	0.07	0.04	0.11	0.81
q_{11}	3.10	3.38	0.77	1.60	0.01	0.00
q_{12}	0.02	0.07	0.36	0.01	0.20	0.10
q_{13}	0.16	0.09	0.39	0.61	0.01	0.01
q_{14}	0.00	0.06	2.21	2.00	2.89	2.88
q_{15}	0.01	0.09	0.01	0.03	0.01	0.52
q_{16}	0.00	0.17	0.16	0.30	0.00	0.05

Table 4.8 Modal participation values at various limit-cycle amplitudes and different flow angles for simply supported rectangular graphite/epoxy [-40/40/-40] panel

Mode	Modal Participation, %					
	$\alpha = 0^o$ Wmax/h		$\alpha = 45^o$ Wmax/h		$\alpha = 90^o$ Wmax/h	
	0.01	0.8	0.01	0.8	0.01	0.8
q_1	25.33	26.38	28.85	28.95	25.65	25.90
q_2	41.18	35.26	44.90	40.35	39.10	32.55
q_3	4.17	7.01	2.55	2.80	7.94	10.76
q_4	11.38	9.79	12.06	11.55	9.87	8.67
q_5	2.83	2.73	0.73	1.00	3.45	3.54
q_6	6.15	6.75	6.15	7.25	4.52	5.25
q_7	1.46	2.54	1.67	2.22	3.08	4.51
q_8	2.32	2.13	0.18	0.27	2.10	2.13
q_9	0.84	1.22	0.74	1.31	0.32	0.70
q_{10}	1.05	1.55	0.89	1.61	1.06	1.58
q_{11}	1.22	1.21	0.01	0.07	0.95	1.05
q_{12}	0.13	0.51	0.17	0.67	0.04	0.44
q_{13}	0.24	0.39	0.20	0.33	0.64	0.97
q_{14}	0.74	1.17	0.65	1.22	0.64	1.01
q_{15}	0.83	1.02	0.09	0.00	0.42	0.74
q_{16}	0.07	0.26	0.07	0.32	0.15	0.13

Table 4.9 Modal convergence for clamped rectangular $[0/45/-45/90]_S$ graphite/epoxy panel at SPL = 120 dB and $\lambda = 800$

Number of Modes	RMS(Wmax/h)
1	0.5557
2	0.5845
6	0.7814
9	0.7798
16	0.8279
20	0.8110
25	0.8183
Selected 13 modes	0.8124

Table 4.10 Modal participation for a clamped rectangular $[0/45/-45/90]_S$ graphite/epoxy panel at SPL = 120 dB and $\lambda = 800$

Mode	Participation, %	Mode	Participation, %
q_1	36.72	q_{14}	4.19
q_2	5.24	q_{15}	0.38
q_3	19.3	q_{16}	0.99
q_4	4.25	q_{17}	1.38
q_5	4.01	q_{18}	2.55
q_6	7.67	q_{19}	0.21
q_7	1.71	q_{20}	0.27
q_8	0.76	q_{21}	0.53
q_9	0.33	q_{22}	0.33
q_{10}	1.54	q_{23}	0.54
q_{11}	4.77	q_{24}	0.14
q_{12}	0.35	q_{25}	1.54
q_{13}	0.28		

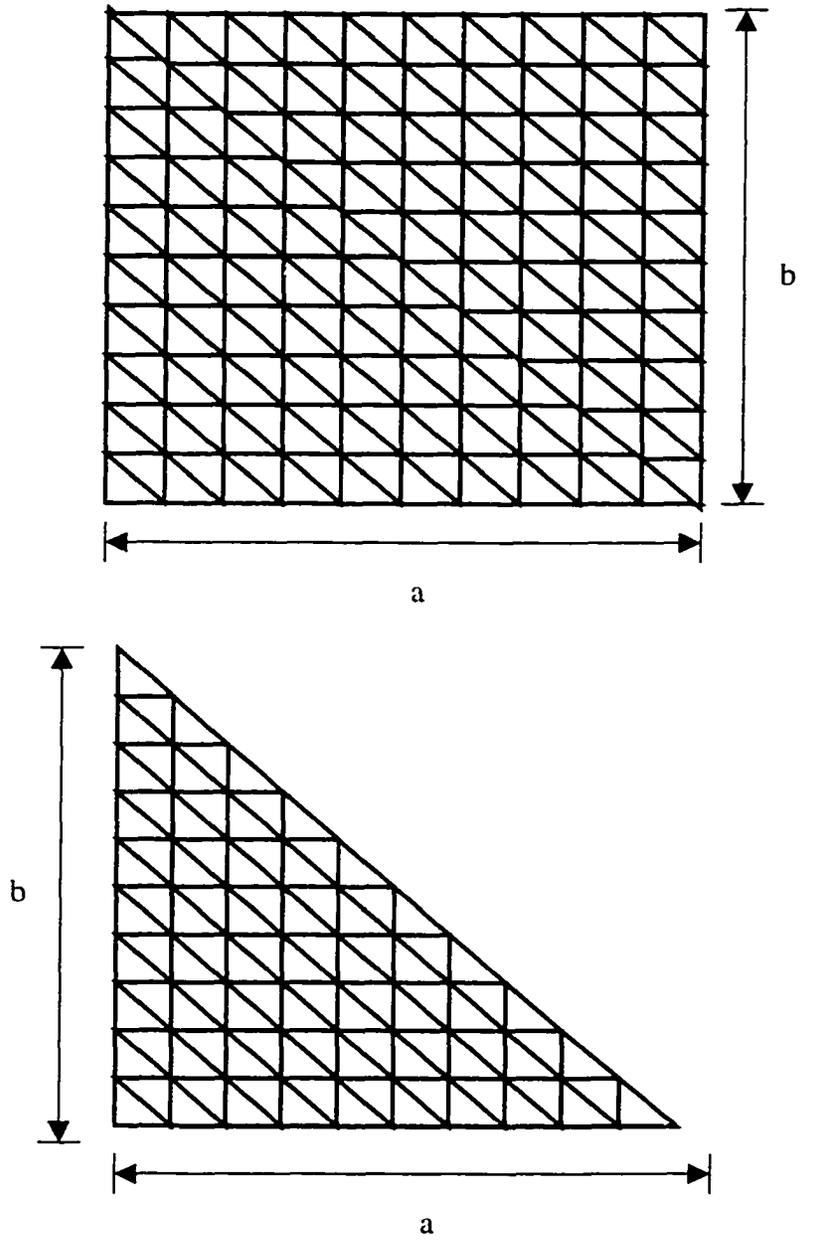

Figure 4.1 Typical MIN3 elements mesh used to model rectangular and triangular panels

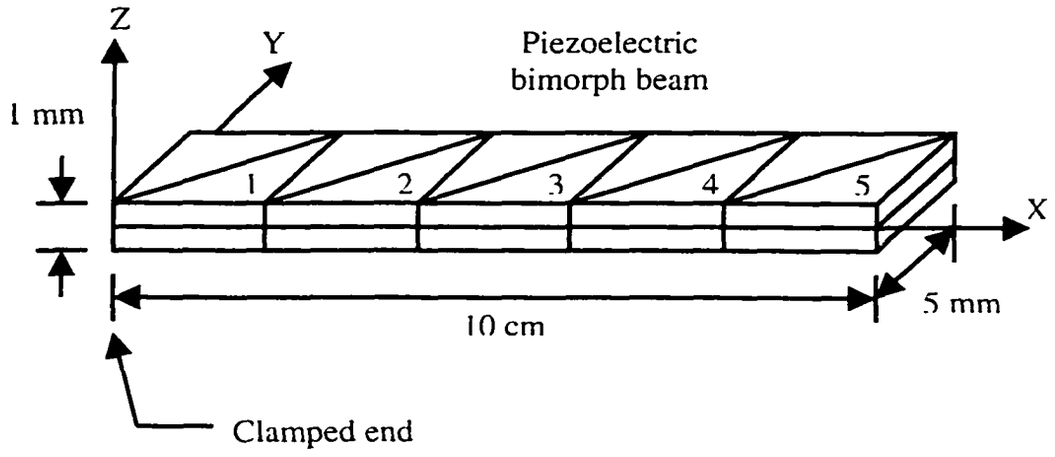

Figure 4.2 Clamped piezoelectric bimorph beam modeled using MIN3 elements

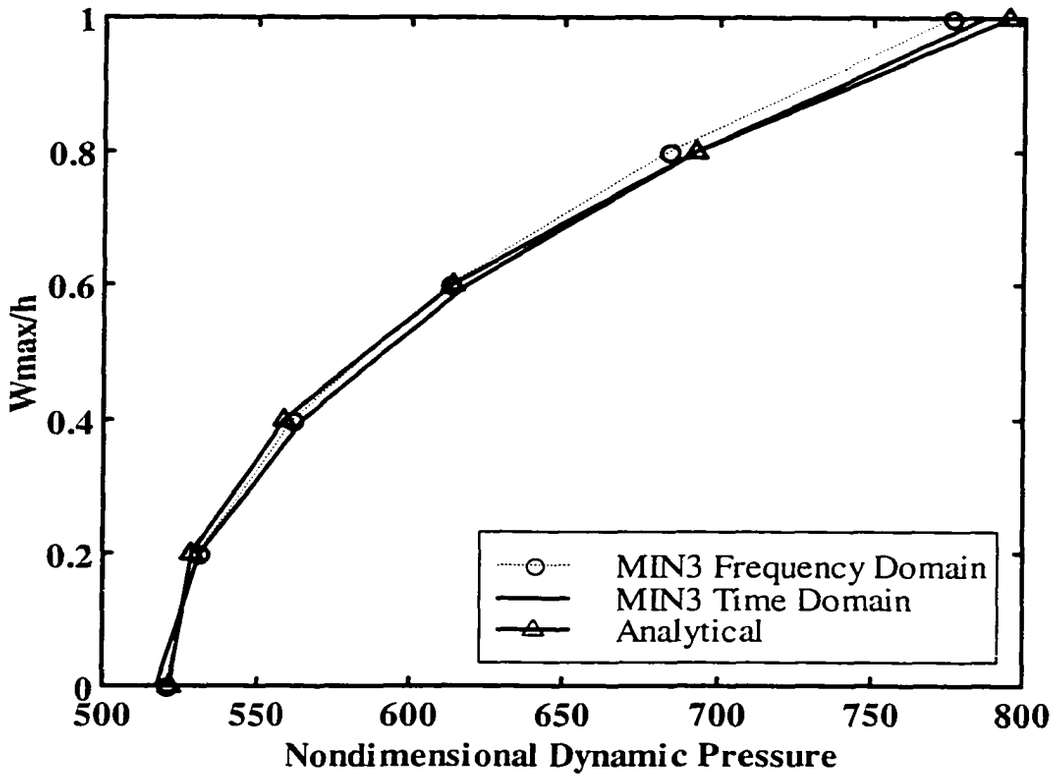

Figure 4.3 Validation of flutter limit-cycle amplitude for simply supported square isotropic panel

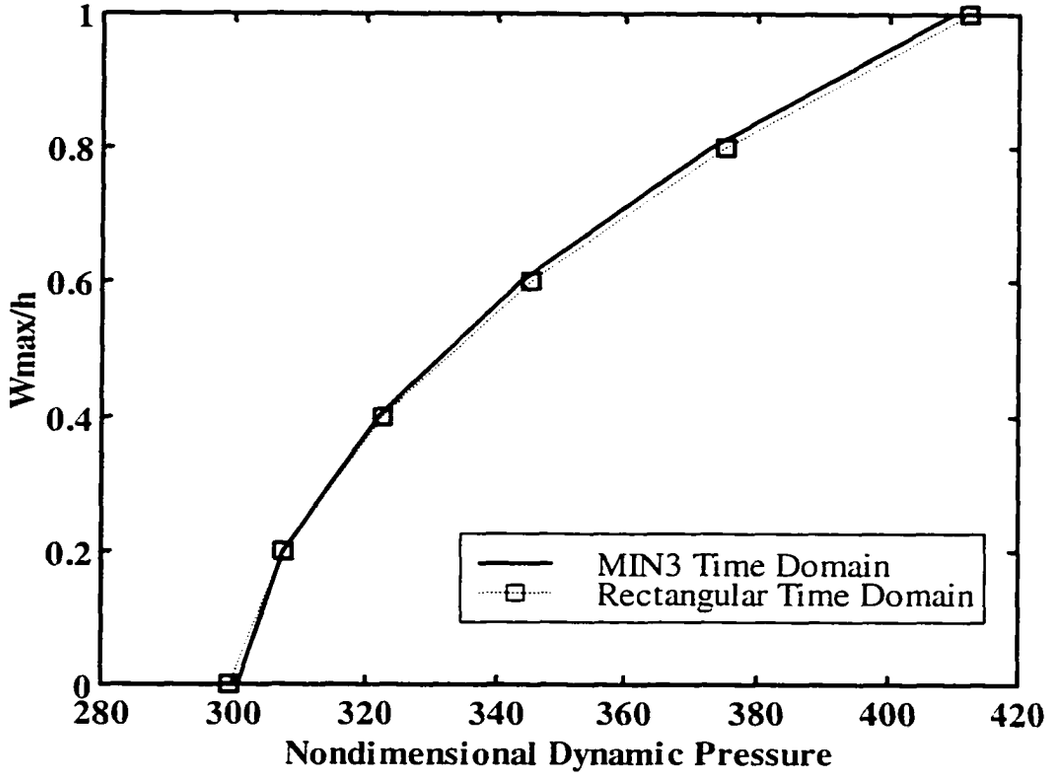

Figure 4.4 Validation of flutter limit-cycle amplitude for simply supported square $[0/45/-45/90]_S$ laminate

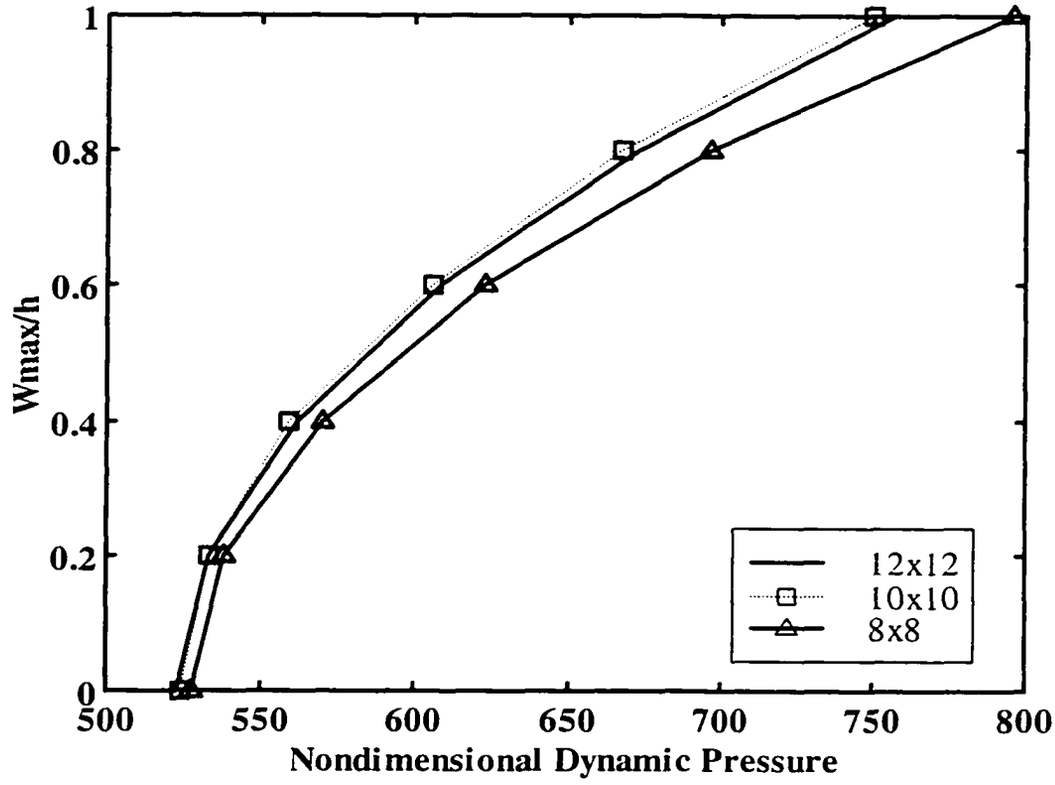

Figure 4.5 Finite element mesh convergence for simply supported isotropic square panel at 45° flow angle and using 16 modes

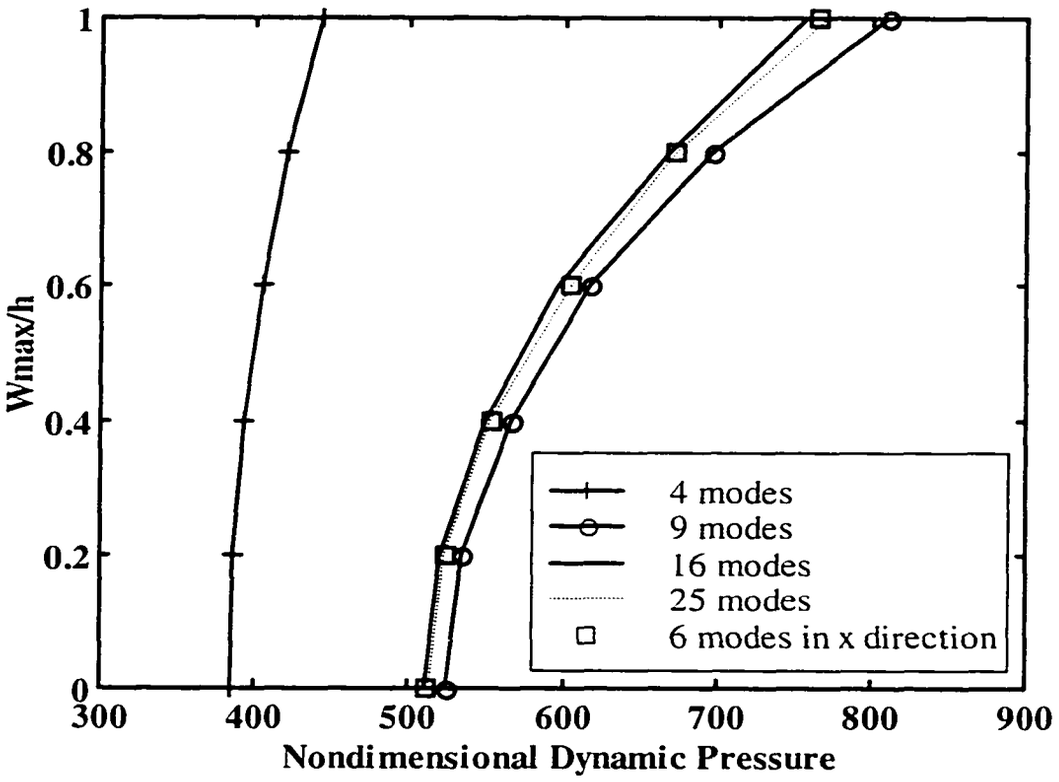

Figure 4.6 Modal convergence for simply supported isotropic square panel at 0° flow angle

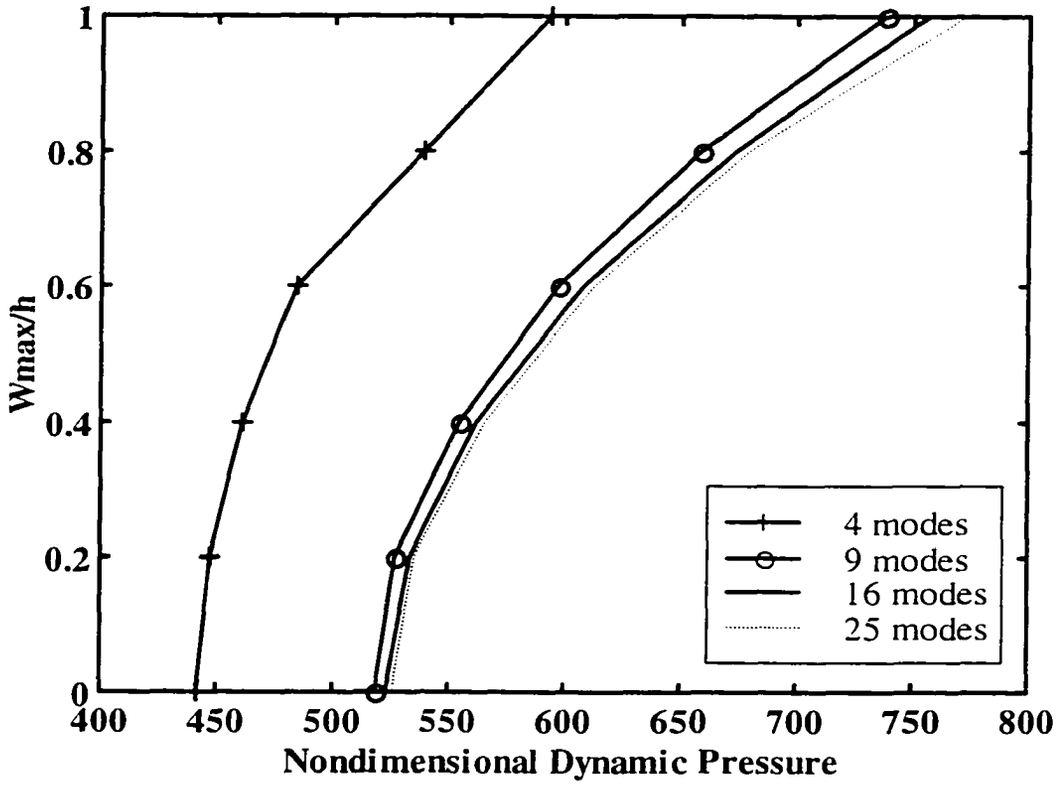

Figure 4.7 Modal convergence for simply supported isotropic square panel at 45° flow angle

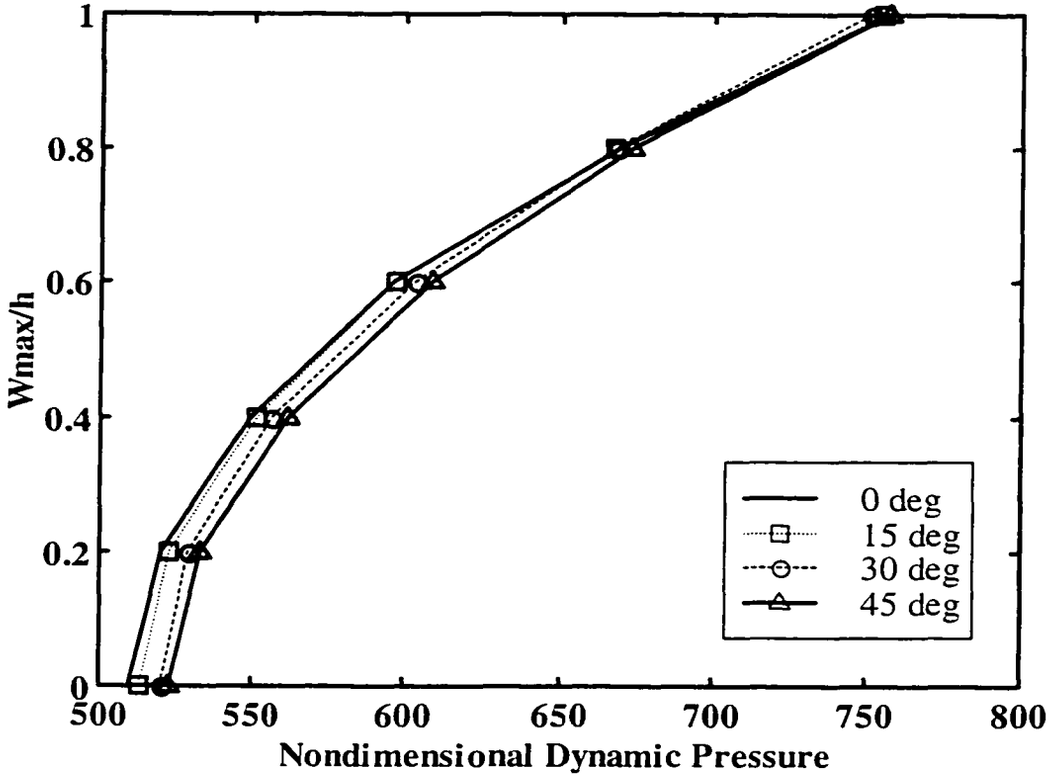

Figure 4.8 Effect of flow yaw angle on limit-cycle amplitude for simply supported isotropic square panel

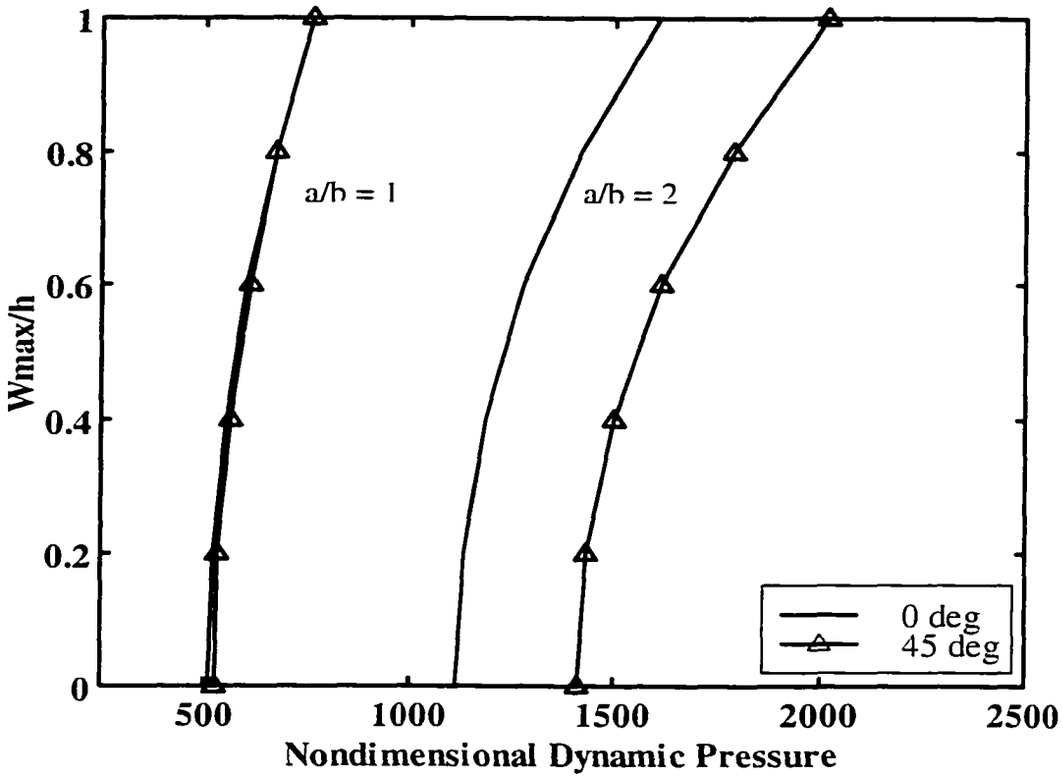

Figure 4.9 Effect of panel aspect ratio at different yaw angles on limit-cycle amplitude for simply supported isotropic panels

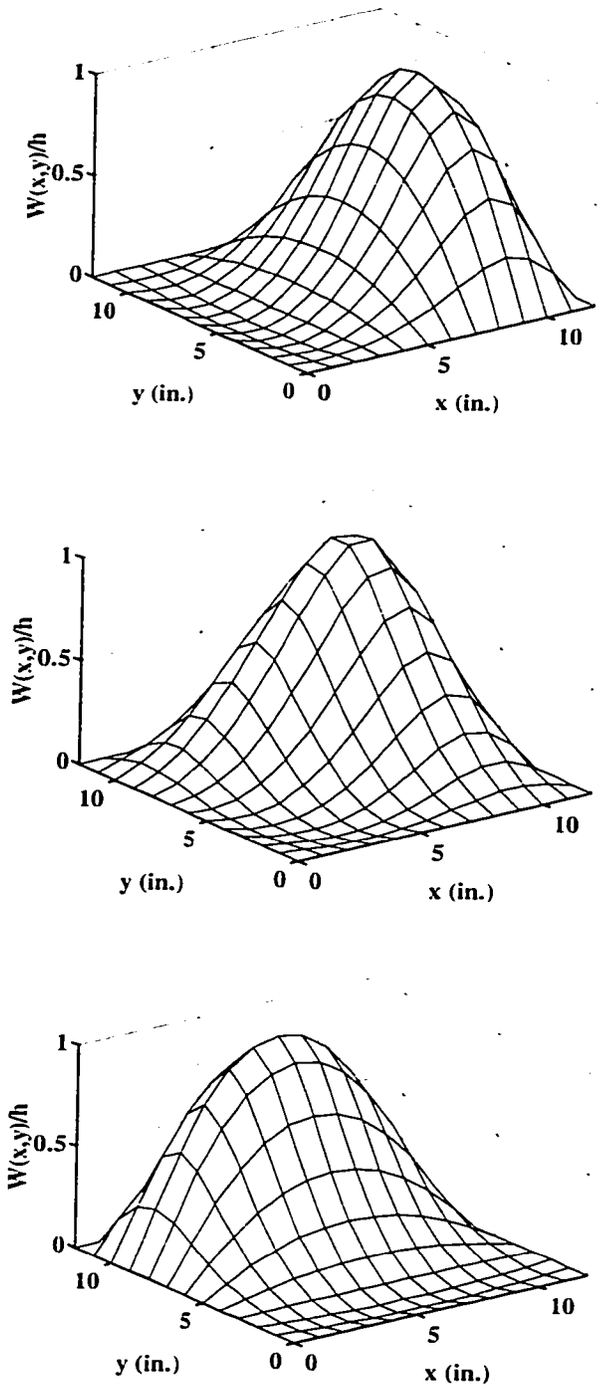

Figure 4.10 Flutter mode shape at different flow angles for simply supported isotropic square panel

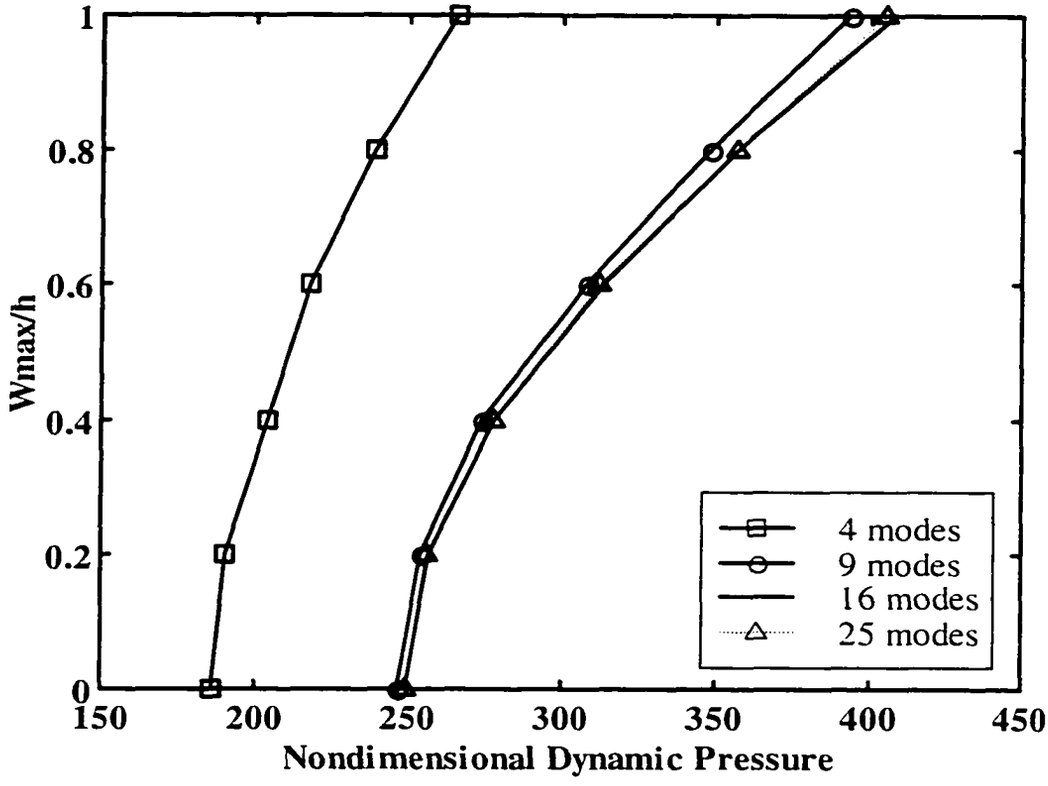

Figure 4.11 Modal convergence for simply supported rectangular graphite/epoxy $[0/45/-45/90]_S$ panel at 45° flow angle

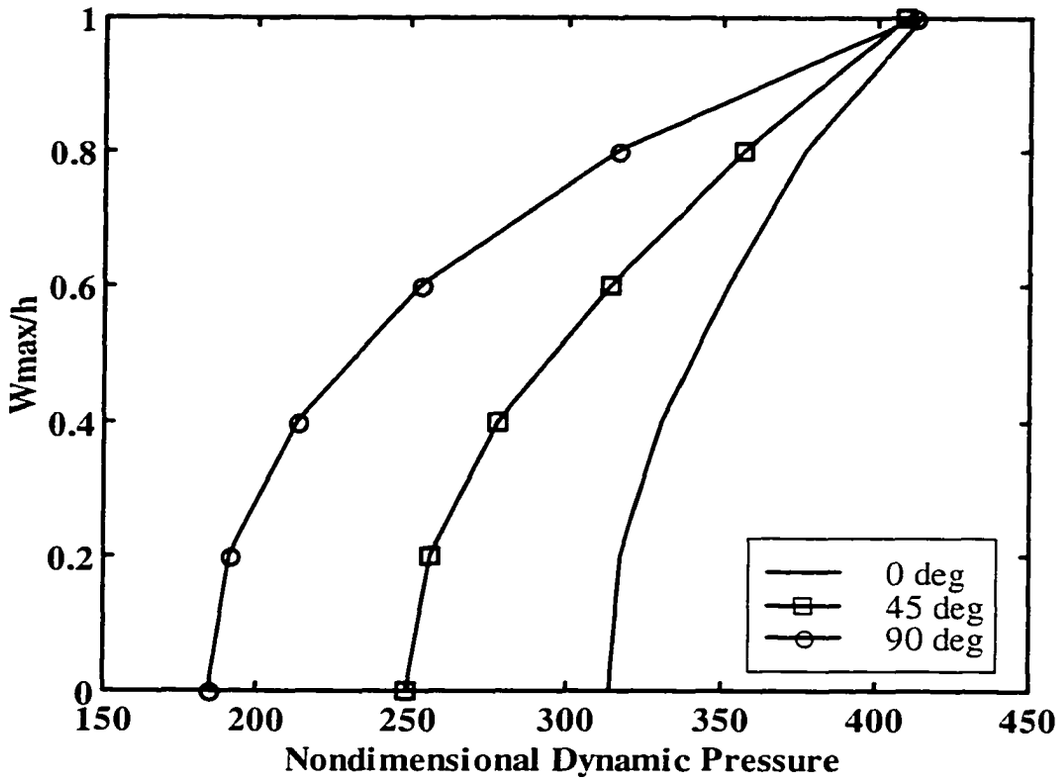

Figure 4.12 Effect of flow yaw angle on limit-cycle amplitude for simply supported rectangular graphite/epoxy $[0/45/-45/90]_S$ panel

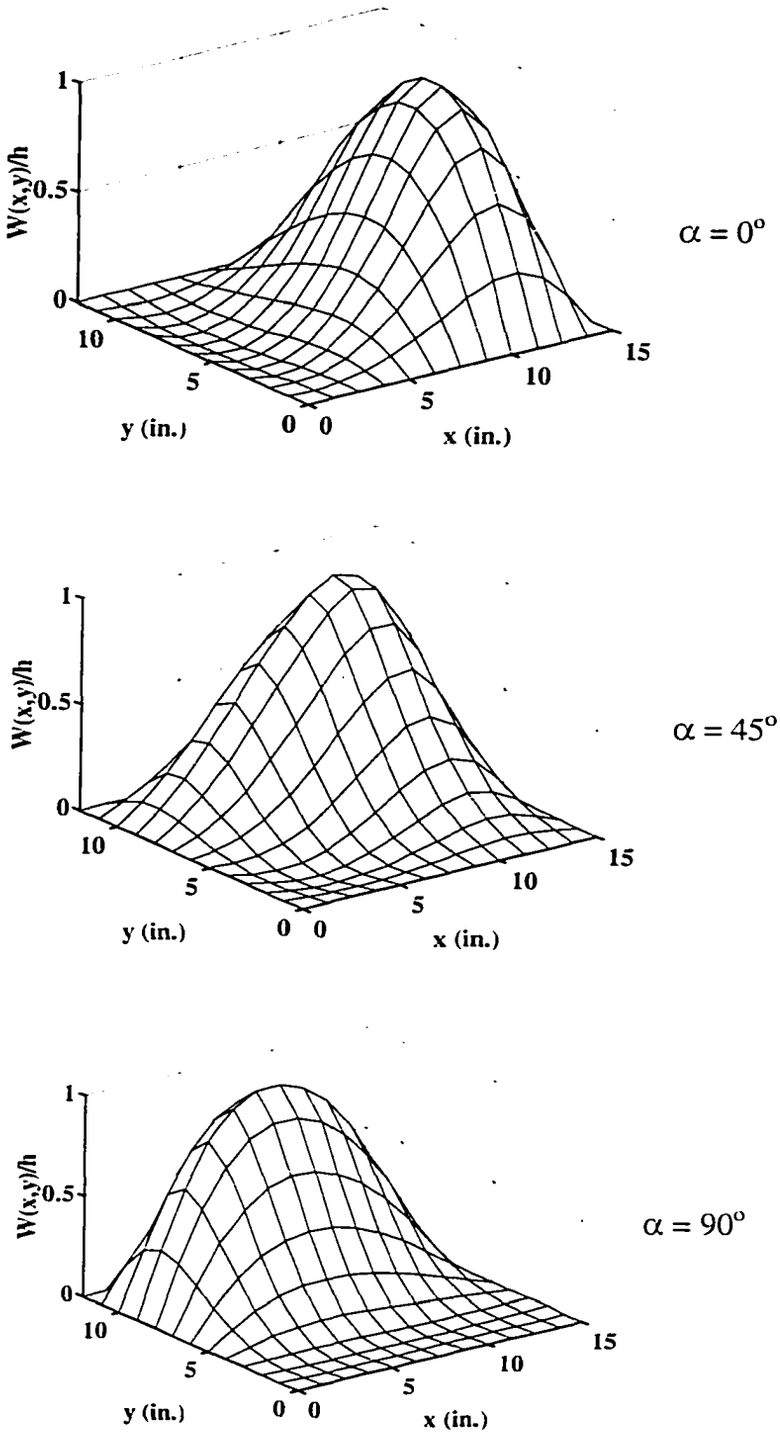

Figure 4.13 Flutter mode shape at different flow angles for simply supported rectangular graphite/epoxy $[0/45/-45/90]_S$ panel

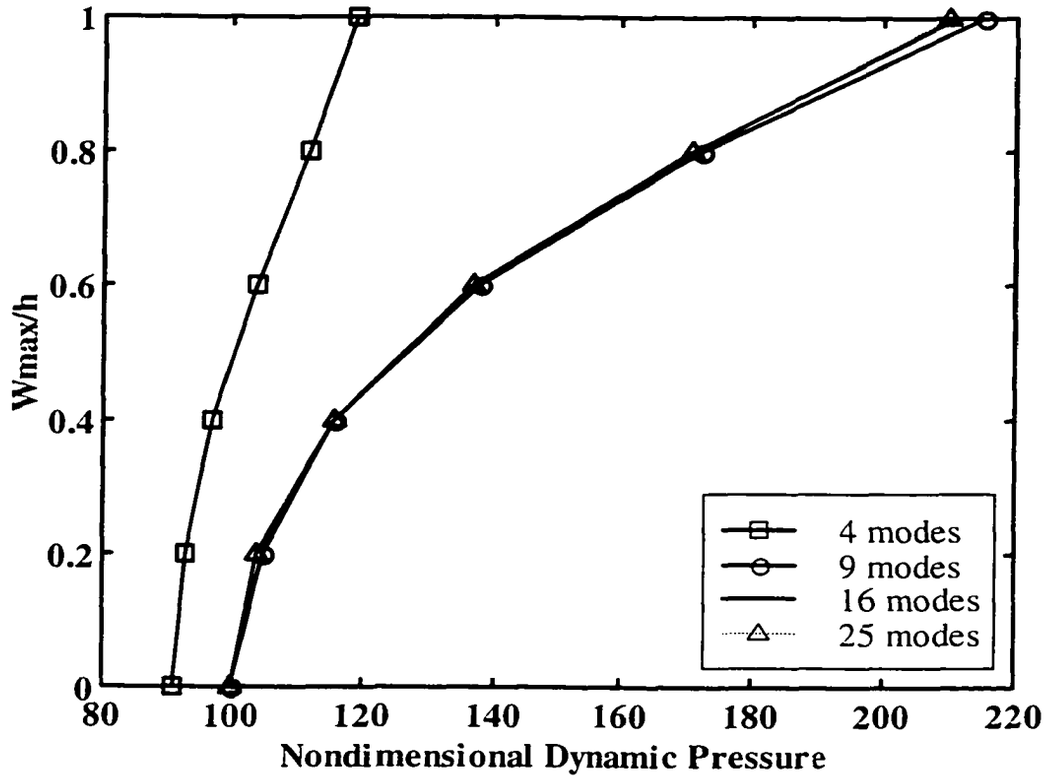

Figure 4.14 Modal convergence for simply supported rectangular graphite/epoxy [-40/40/-40] panel at 45° flow angle

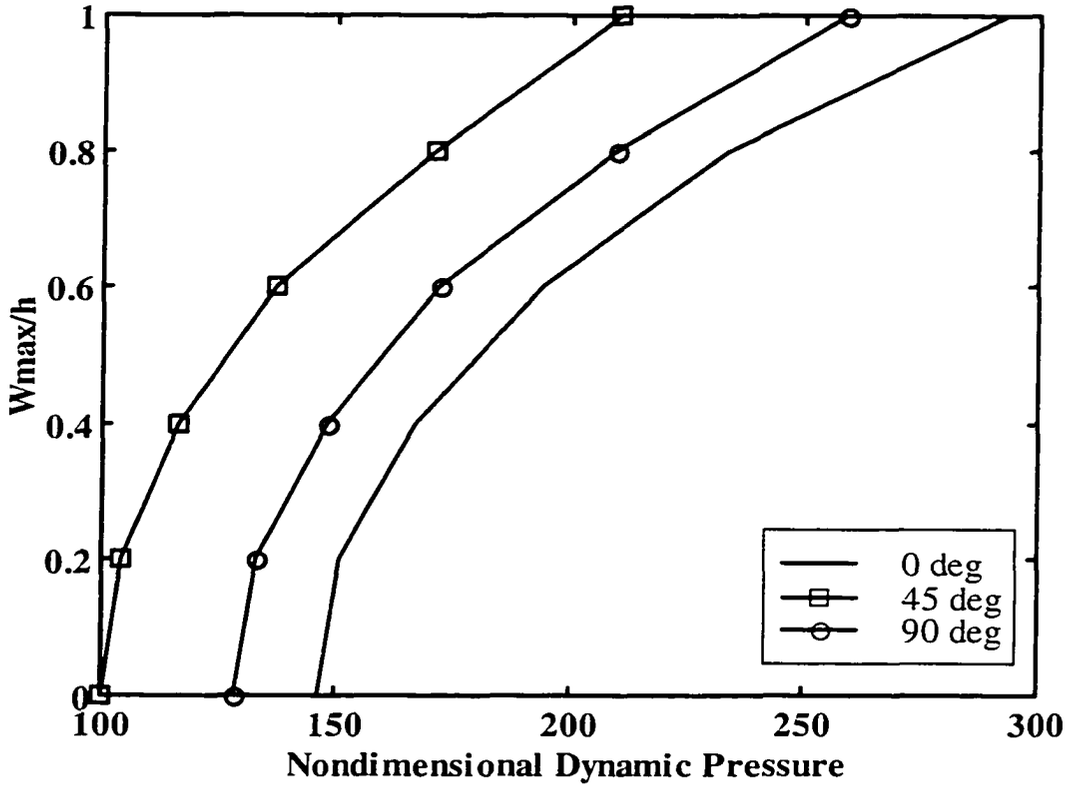

Figure 4.15 Effect of flow yaw angle on limit-cycle amplitude for simply supported rectangular graphite/epoxy [-40/40/-40] panel

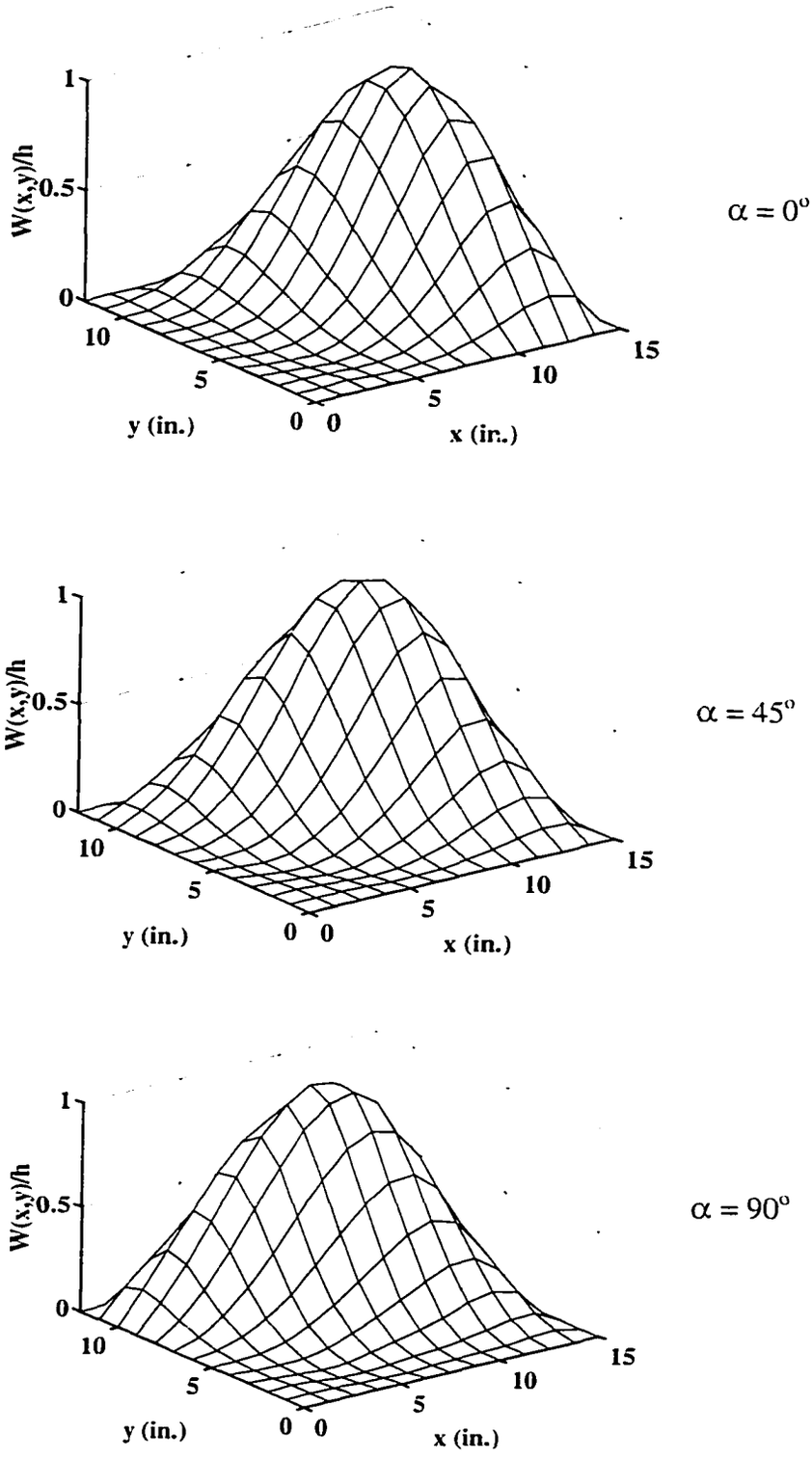

Figure 4.16 Flutter mode shape at different flow angles for simply supported rectangular graphite/epoxy [40/-40/40] panel

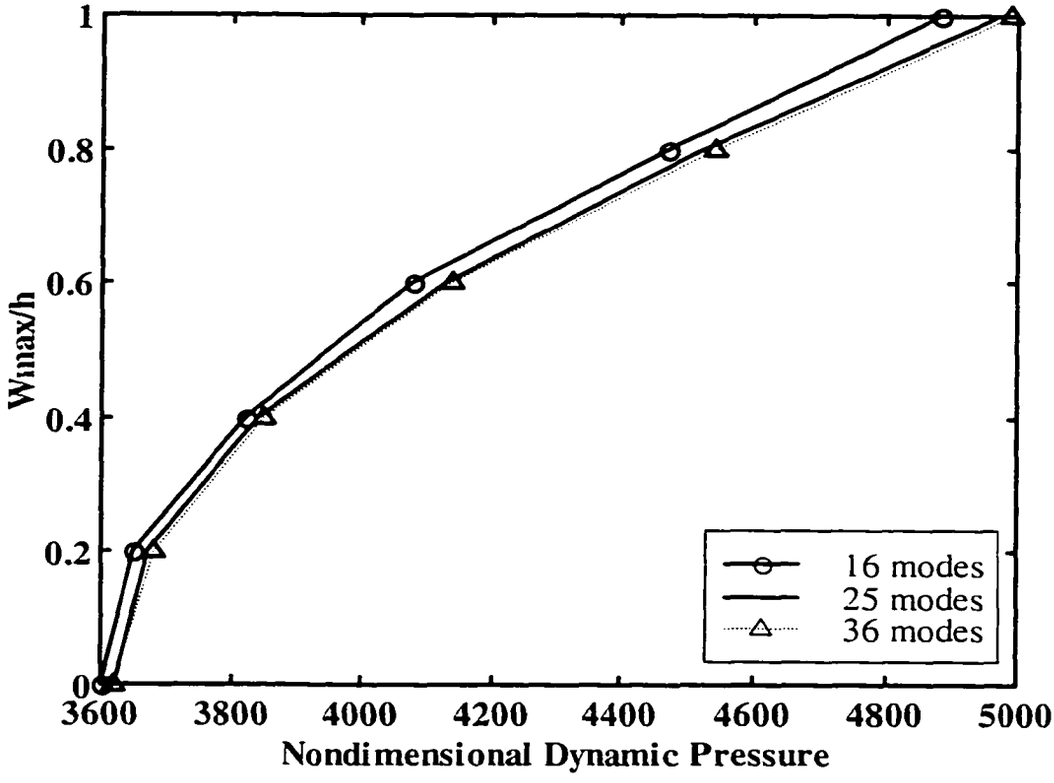

Figure 4.17 Modal convergence for simply supported triangular isotropic panel at 45° flow angle

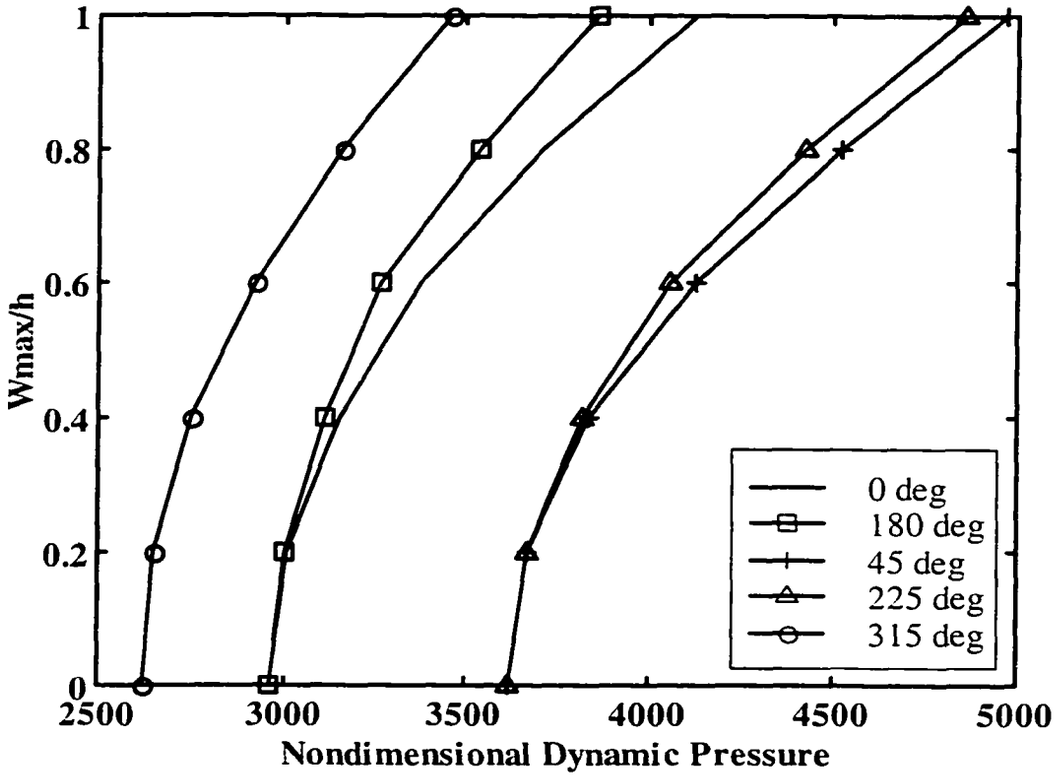

Figure 4.18 Effect of flow yaw angle on limit-cycle amplitude for simply supported triangular isotropic panel

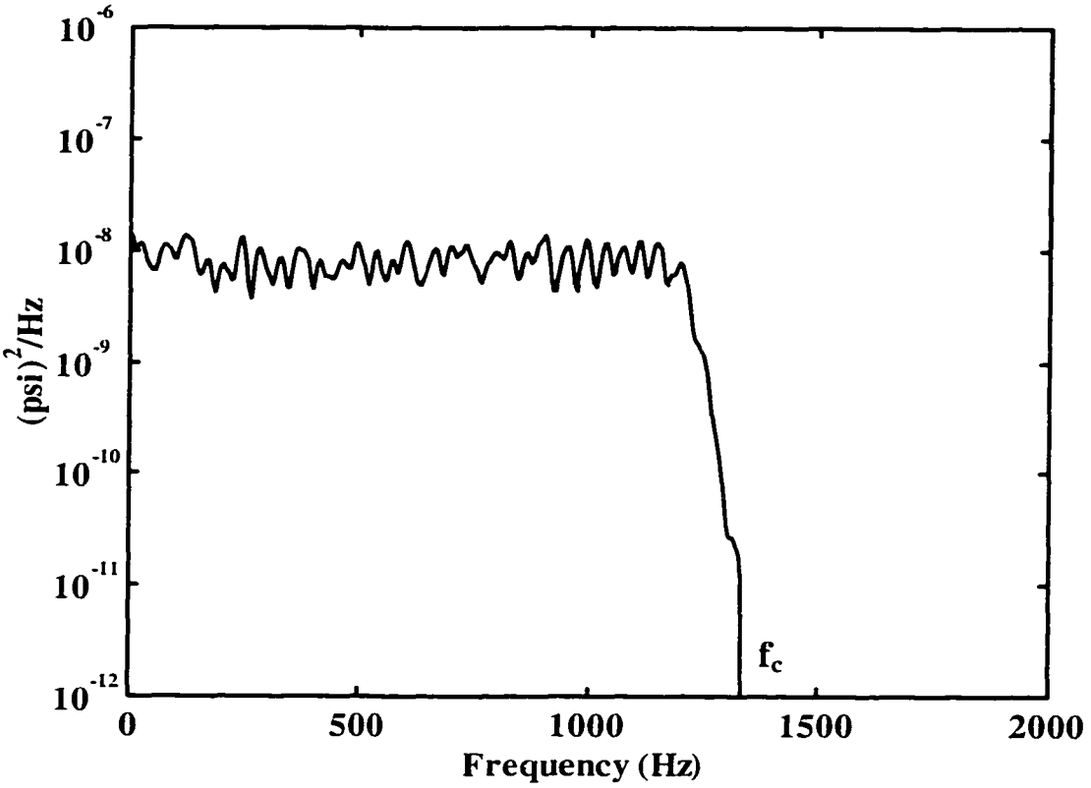

Figure 4.19 Power spectral density of random input pressure at SPL = 90dB

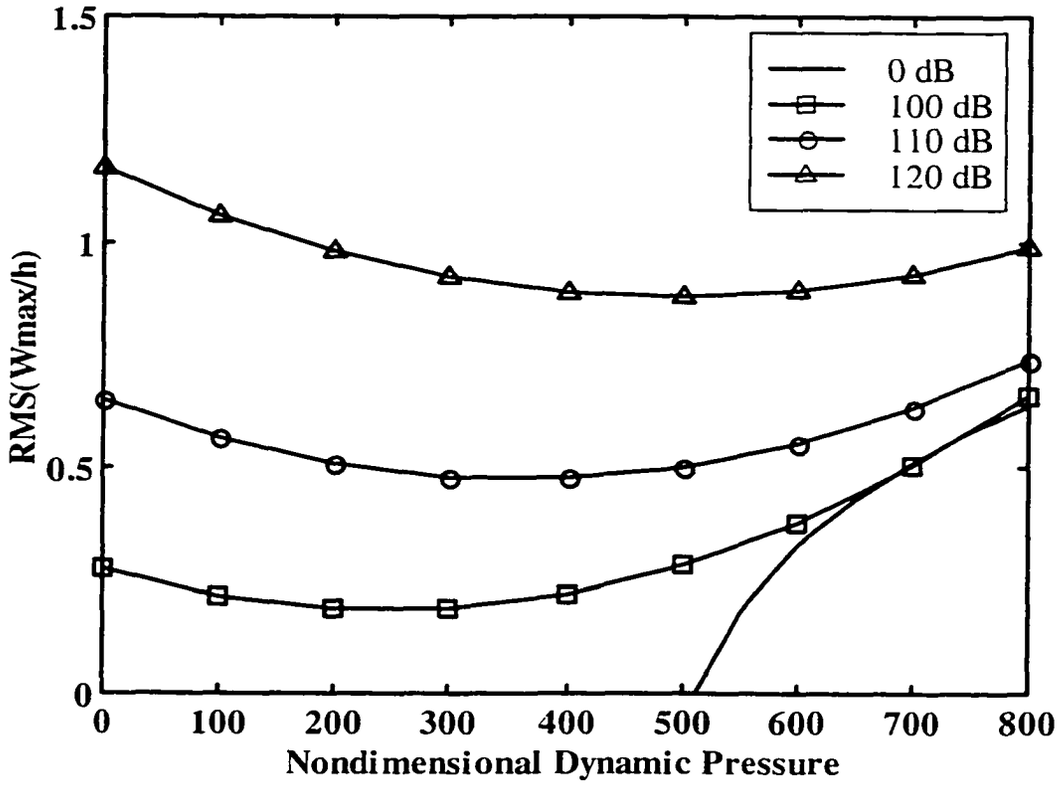

Figure 4.20 RMS of maximum deflection for simply supported square isotropic panel under combined acoustic and aerodynamic pressures

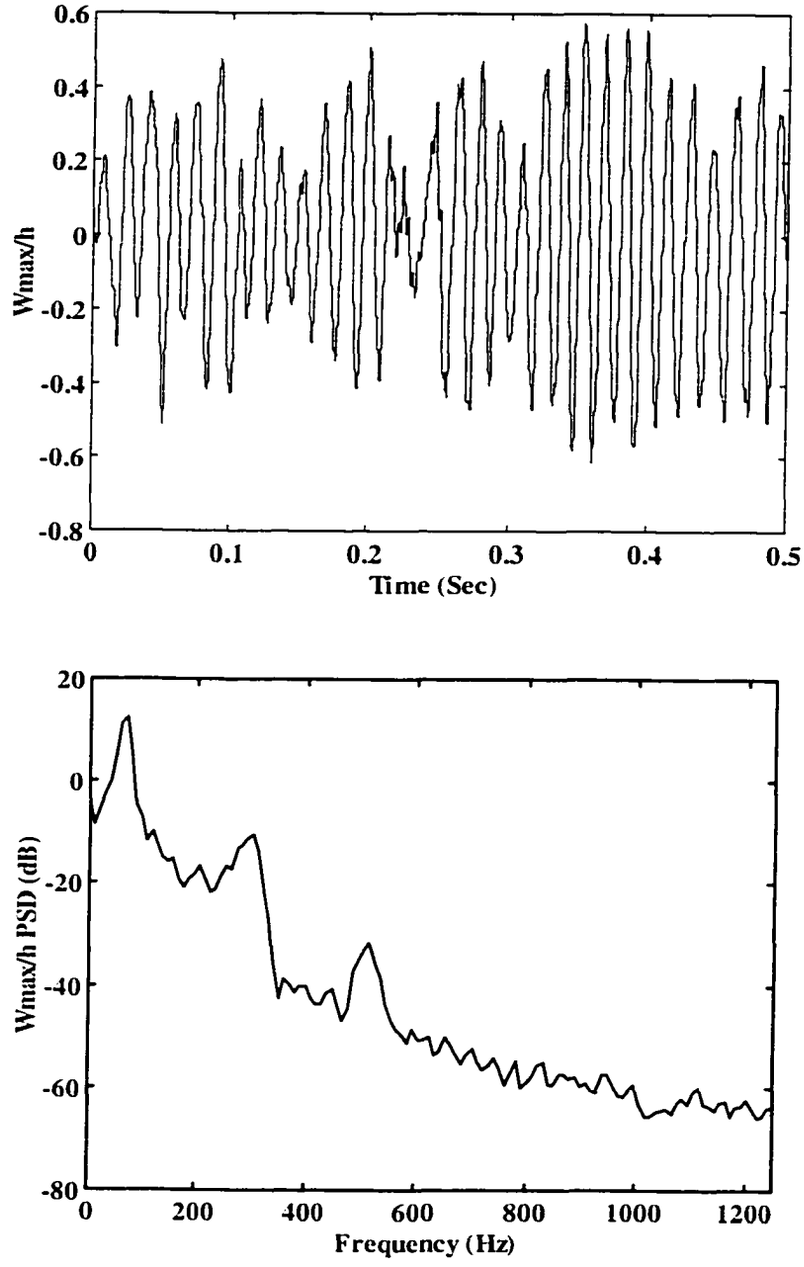

Figure 4.21 Time and frequency response for simply supported square isotropic panel at SPL = 100 dB and $\lambda = 0$

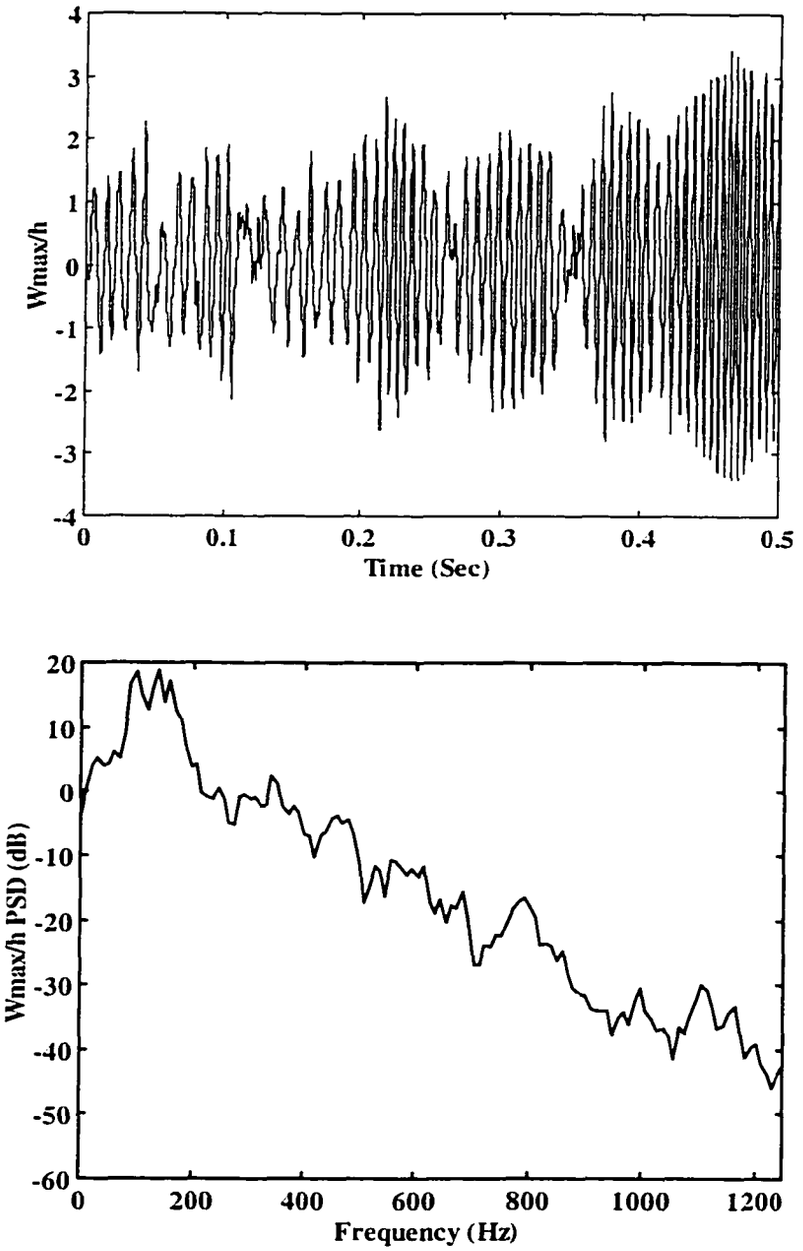

Figure 4.22 Time and frequency response for simply supported square isotropic panel at SPL = 120 dB and $\lambda = 0$

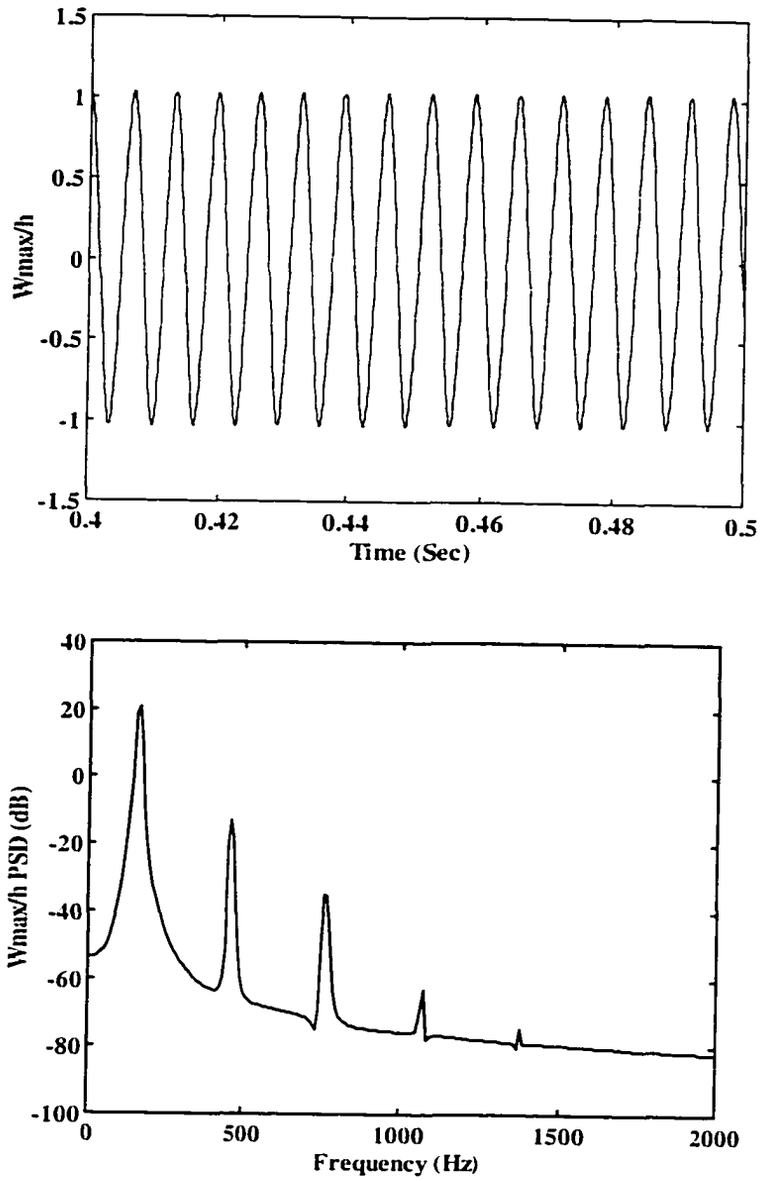

Figure 4.23 Time and frequency response for simply supported square isotropic panel at SPL = 0 dB and $\lambda = 800$

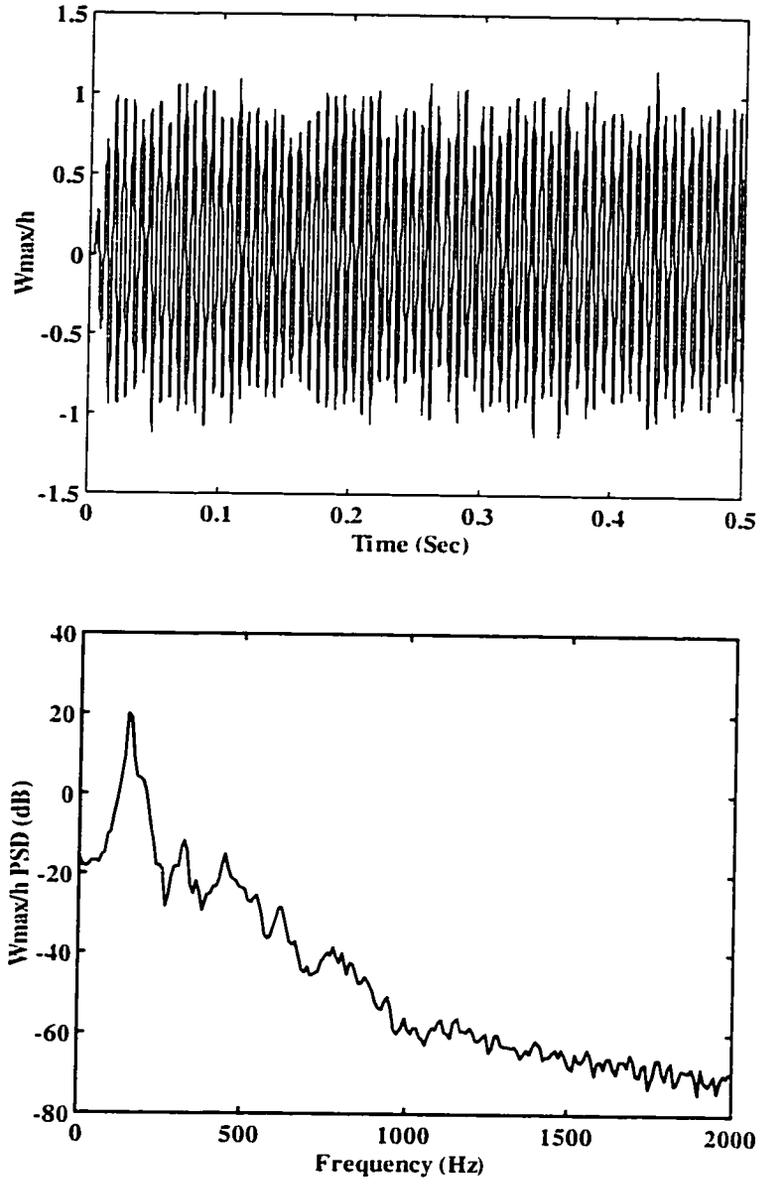

Figure 4.24 Time and frequency response for simply supported square isotropic panel at SPL = 100 dB and $\lambda = 800$

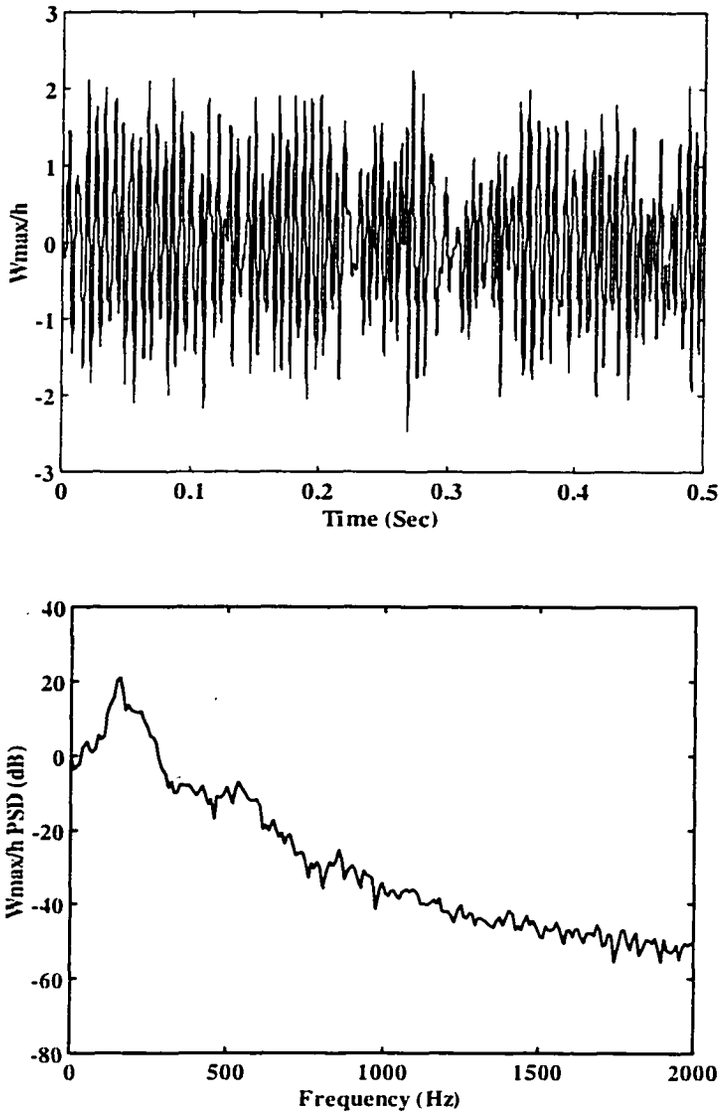

igure 4.25 Time and frequency response for simply supported square isotropic panel at SPL = 120 dB and λ = 800

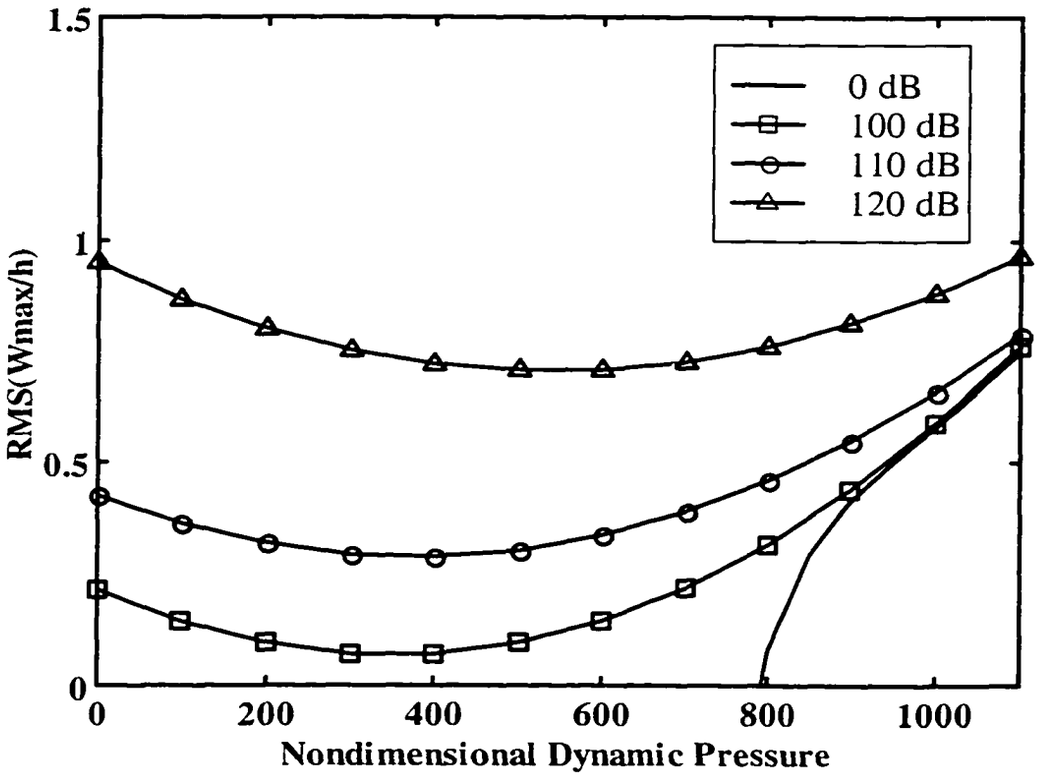

Figure 4.26 RMS of maximum deflection for clamped rectangular graphite/epoxy $[0/45/-45/90]_S$ panel

CHAPTER V

CONTROL METHODS AND OPTIMAL PLACEMENT OF PIEZOELECTRIC SENSORS AND ACTUATORS

5.1 Introduction

Many control strategies such as classical, optimal, H_∞, nonlinear, fuzzy logic, and adaptive control have been utilized for vibration control in the literature. Two major properties, the nonlinearity and the large dimension of the model, can characterize the nature of the problem of nonlinear panel flutter with yawed supersonic flow. Modern control techniques such as optimal control and H_∞ are very suitable for such systems, as they can easily handle large dimension and no prior knowledge of the controller structure is required.

In this study, optimal control strategies are the main focus for the suppression of nonlinear panel flutter. The linear quadratic Gaussian (LQG) control, which combines both linear quadratic regulator (LQR) optimal feedback and Kalman filter state estimator, is considered as systematic linear dynamic compensator. To address the issue of the flutter nonlinear dynamics involved, an extended Kalman filter for nonlinear systems is also considered and combined with optimal feedback to form a nonlinear dynamic compensator. Finally, a more practical approach based on optimal output feedback is used to alleviate the problem of state estimation. Closed loop criteria based on the norm of feedback control gains for actuators and on the norm of Kalman filter gains for sensors are used to determine the optimal location of self-sensing piezoelectric actuators.

5.2 State Space Representation

For control design and simulation, the nonlinear modal equations of motion given in Chapter 3, equations (3.15) and (3.16), need to be cast in the standard state space form. In state space representation, the system equations of motion are written in the form of coupled first order differential equations. State space models provide a standard and efficient representation of systems with large number of DOF and of multi-input multi-output (MIMO) systems in the time domain. Linearization about reference equilibrium points can be used to obtain a linear state space models that could be used for the design

of modern optimal and robust control laws. The system states, X, are defined as the panel modal deflections and modal velocities:

$$X = \begin{Bmatrix} q \\ \dot{q} \end{Bmatrix} \tag{5.1}$$

The control input, U, and sensor output, Y, are the self-sensing piezoelectric actuators input voltage and sensor charge output, respectively:

$$U = \{W_\phi\}, \quad Y = \{q^s\} \tag{5.2}$$

Thus, the system modal equations of motion in the continuous time domain state space form are:

$$\begin{aligned} \dot{X} &= (A + \Delta A_q)X + BU \\ Y &= CX + DU \end{aligned} \tag{5.3}$$

where the system matrices are given by:

$$\begin{aligned} [A] &= \begin{bmatrix} [0] & [I] \\ -\omega_0^2[\overline{M}_b]^{-1}[\overline{K}_L] & -\omega_0^2[\overline{M}_b]^{-1}[\overline{C}_d] \end{bmatrix} \\ [\Delta A_q] &= \begin{bmatrix} [0] & [0] \\ -\omega_0^2[\overline{M}_b]^{-1}([K_q] + [K_{qq}]) & [0] \end{bmatrix} \\ [B] &= \begin{bmatrix} [0] \\ -\omega_0^2[\overline{M}_b]^{-1}[\overline{K}_{b\phi}] \end{bmatrix}, \quad [C] = \begin{bmatrix} [\overline{K}_{\phi b}] & [0] \end{bmatrix}, \quad [D] = [0] \end{aligned} \tag{5.4}$$

The modal damping matrix $[\overline{C}_d]$ contains both modal aerodynamic and modal structural damping terms. The system matrix $[\Delta A_q]$ represents the effect of nonlinear stiffness matrices of the panel. By using linearization about the system reference point (point with no deflection, $\{q\} = 0$), the nonlinear system matrix vanishes and the state space model in (5.3) reduces to a linear state space model given by:

$$\begin{aligned} \dot{X} &= AX + BU \\ Y &= CX + DU \end{aligned} \tag{5.5}$$

If the sensor electrical circuit is set up to measure the time rate of electrical charge (current) instead of the electrical charge, then the output matrix C is:

$$[C] = [[0] \quad [\overline{K}_{\phi b}]] \tag{5.6}$$

It has to be noted that for non-ideal self-sensing piezoelectric actuators, i.e., with no perfect compensation for the piezoelectric capacitance term, the D matrix will be nonzero and will contain the residual feedforward effect resulting from imperfect compensation. As discussed in chapter 2, this effect is usually small and hence neglected in this study.

5.3 Control Methods

5.3.1 Linear Quadratic Regulator (LQR)

One of the most commonly used methods to design full state feedback control for linear systems is the LQR which seeks a solution for the linear full state feedback problem defined as:

$$U = -KX \tag{5.7}$$

that minimizes a quadratic performance index, J, that is function of both system states and control effort.

$$J = \int_0^\infty \left[X^T QX + U^T RU\right] dt \tag{5.8}$$

where Q is a symmetric positive semi-definite state weighting and R is a symmetric positive definite control effort weighting. The solution for the controller gains that minimize the performance index of equation (5.8) for the linear state space system give by equation (5.5) is:

$$K = R^{-1} B^T P \tag{5.9}$$

where P is a positive definite symmetric matrix determined from the solution of the Riccati equation defined as:

$$\dot{P} = A^T P + PA - PBR^{-1} B^T P + Q \tag{5.10}$$

In general, the optimal feedback gain sequence is time varying. For linear time invariant systems, the value of the optimal gain converges very quickly to a fixed value. The final fixed value gain could be used as a suboptimal solution since it is easier for implementation. For the case of fixed gain suboptimal feedback gain, the Riccati equation reduces to the well know algebraic Riccati equation (ARE):

$$A^T P + PA - PBR^{-1} B^T P + Q = 0 \tag{5.11}$$

The weighting matrices Q and R are used as control design tuning parameters. The selection of Q and R requires some trials to achieve certain system response characteristics.

5.3.2 Optimal Linear State Estimation

The application of LQR is not feasible in most cases because it is difficult to have sensors that measure all system states. In addition, sensor outputs are usually noisy and the system dynamics is not known exactly. One solution to this problem is the use of probabilistic approach for both process dynamics and sensor noise. This leads to the well known Kalman filter state estimator. Kalman filter is a set of recursive mathematical equations that provide a solution to the least squares optimal state estimation problem in the presence of process and sensor noise.

Consider a standard linear state space model as the one given in equation (5.5) with added process and sensor noise:

$$\begin{aligned} \dot{X} &= AX + BU + \eta \\ Y &= CX + DU + v \end{aligned} \tag{5.12}$$

where η and v are uncorrelated process and measurement Gaussian white noise with zero mean and known covariance matrices, $Q_e = E\{\eta\eta^T\}$ and $R_e = E\{vv^T\}$. Kalman filter achieves optimal state estimation by minimizing the covariance matrix of state estimation error defined as:

$$P_e = E\{ee^T\}, \quad e = X - \hat{X} \tag{5.13}$$

where $\hat{X}$ is the estimated state vector. The minimization of the error covariance matrix leads to the standard linear Kalman filter estimator described by the following dynamic equations:

$$\begin{aligned} \dot{\hat{X}} &= A\hat{X} + BU + K_e(Y - C\hat{X}) \\ \dot{P}_e &= AP_e + P_eA^T - P_eC^T R_e^{-1} CP_e + Q_e \\ K_e &= P_eC^T R_e^{-1} \end{aligned} \tag{5.14}$$

In these equations, the error covariance matrix, P_e, and the estimator gain, K_e, are time varying quantities. For the special case of linear time invariant systems with time invariant process and sensor noise, the error covariance time derivative converges very quickly to zero; hence, the Kalman filter gains become a constant matrix. For this case,

the error covariance matrix is determined using the solution of the estimator algebraic Riccati equation (ARE) given by:

$$AP_e + P_e A^T - P_e C^T R_e^{-1} C P_e + Q_e = 0 \tag{5.15}$$

As for the case of LQR, some tuning is required to select R_e and Q_e in order to achieve good filter performance.

5.3.3 Linear Quadratic Gaussian Controller (LQG)

LQR and Kalman filter can be combined together to form the more practical controller referred to LQG compensator shown in Figure (5.1). In LQG, the controller output is based on the estimated states instead of the actual states:

$$U = -K\hat{X} \tag{5.16}$$

The LQG controller is based on the linear systems separation principle that allows separate design of a feedback control gain and of an observer gain to form a dynamic compensator. Since the Kalman filter is a dynamic system, the LQG is then a linear dynamic regulator of the same kind used in classical control theory. However, unlike classical control, the design of LQG is systematic and does not require any knowledge of the controller structure. This makes LQG very suitable for designing stable control systems for high order MIMO systems such as the application at hand, nonlinear panel flutter suppression.

One popular method to design robust LQG compensator is to use the loop-transfer recovery technique (LQG/LTR). This technique is based on recovering the guaranteed robustness properties of the LQR (infinite gain margin and 60 degrees phase margin) to the corresponding LQG controller. This can be achieved by tuning the LQG Kalman filter weighting matrices Q_e and R_e to asymptotically recover LQR loop transfer function. One way to select the Kalman filter weighting is:

$$R_e = [I], \quad Q_e = \upsilon^2 BB^T \tag{5.17}$$

As ν goes to infinity, the loop transfer function of LQG controller approaches the loop transfer function of LQR. However, the value of ν should not be increased indefinitely as this leads to very high Kalman gains. The LQG/LTR is a frequency domain loop shaping approach that could be used to satisfy specific robustness bounds on the open loop transfer function.

5.3.4 Extended Kalman Filter (EKF)

One major drawback with the application of linear Kalman filter to the problem of nonlinear panel flutter suppression is that it assumes linearized system equations about the reference no deflection point. Hence, the nonlinear effects are not considered at all in the estimation process. As it will be shown in Chapter 6, this could deteriorate the state estimation performance for large limit cycle amplitudes. One solution to such a problem is to use Kalman filter that performs the linearization about a trajectory that is continuously updated with the estimated states. Such filter is referred to as extended Kalman filter (EKF) [109]. The equations of an EKF for the nonlinear state space model of panel flutter, equation (5.3), are given by:

$$\begin{aligned}
\dot{\hat{X}} &= \overline{A}\hat{X} + BU + K_e(Y - C\hat{X}) \\
\dot{P}_e &= \overline{A}P_e + P_e\overline{A}^T - P_eC^TR_e^{-1}CP_e + Q_e \\
K_e &= P_eC^TR_e^{-1} \\
\overline{A} &= A + \Delta A_q(\hat{X})
\end{aligned} \tag{5.18}$$

where the term $\Delta A_q(\hat{X})$ represents the nonlinear state space matrix evaluated using the current state estimate. Unlike the standard Kalman filter, the EKF gain sequence cannot be predetermined and has to be evaluated on-line. This adds more computational cost but should not be a problem especially with the advanced and fast real time processors available today. The EKF deviates from the standard linear Kalman filter because of the nonlinear feedback of the measurement into the system model and because the various random variables are no longer Gaussian after undergoing nonlinear transformation. Thus, the EKF is simply an ad hoc state estimator for nonlinear systems. However, it has proven to be successful in various applications [109-112].

5.3.5 Nonlinear Controller using EKF and LQR

The EKF can be combined with LQR to form a nonlinear dynamic output compensator for the control of nonlinear panel flutter, see Figure (5.2). Such controller is nonlinear because the estimated state and consequently the control effort, U, is a dynamic nonlinear function of the measured sensor output. The advantage of this controller over the LQG controller is the more accurate state estimation for the nonlinear panel flutter dynamics.

5.3.6 Optimal Output Feedback Control

A simpler control strategy for MIMO systems that avoid the need for state estimation is to design an output feedback compensator of the form:

$$U = -K_y Y \tag{5.19}$$

The output feedback gain matrix, K_y, can be determined using optimal control by minimizing the quadratic performance index given in equation (5.8). However, this leads to a feedback control gain that is dependent on the states initial conditions which is undesirable. This problem can be avoided by minimizing the expected value of the performance index, $E\{J\}$; hence, the minimization is performed over a distribution of possible values for the initial conditions. The design equations for optimal output feedback control are given by [108]:

$$\begin{aligned} &A_c^T P + PA_c + C^T K_y^T R K_y C + Q = 0 \\ &A_c S + SA_c^T + X_0 = 0 \\ &K_y = R^{-1} B^T PSC^T (CSC^T)^{-1} \end{aligned} \tag{5.20}$$

where

$$A_c = A - BKC, \qquad X_0 = E\left\{X(0)X^T(0)\right\} \tag{5.21}$$

The expected initial state is usually assumed uniformly distributed on the unit sphere in order to drive any initial state to zero. It can be seen from equation (5.20) that the solution for the optimal output feedback gain requires a solution of three coupled nonlinear algebraic matrix equations. These equations can be solved using the gradient-based iterative method described in Appendix C [108].

5.4 Optimal Placement of Piezoelectric Sensors and Actuators

The method adopted for actuator placement in this study is the method of norm of optimal feedback control gain matrix (NFCG) used for panel flutter suppression by [74] and [100]. This method determines the effectiveness of a piezoelectric actuator by using the norm of feedback gain designed using LQR and thus is a closed loop criterion.

$$NFCG = \left\| K_{LQR} \right\| \tag{5.22}$$

The higher the value of *NFCG*, the more effective is the actuator for panel flutter suppression.

The NFCG method is extended for optimal sensor location by using the norm of Kalman filter estimator gain (NKFEG).

$$NKFEG = \|K_{Kalman}\| \tag{5.23}$$

The higher the value of NKFEG, the more effective is the sensor for the problem of state estimation.

For the problem of panel flutter suppression, a number of piezoelectric patches equal to the number of finite element mesh size are used. The effectiveness of each element as an actuator and as a sensor is determined using the above two criteria. The shape and location of optimal actuator and sensor is then determined by combining the most effective elements. Although each piezoelectric patch might act as both actuator and sensor (self-sensing actuators), the optimal location for actuator and sensor might not be the same.

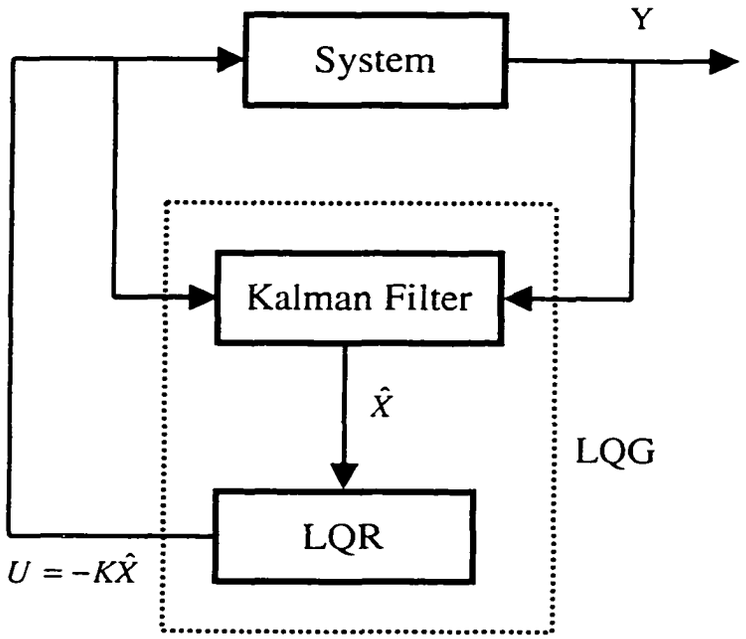

Figure 5.1 Block diagram representation of the LQG controller

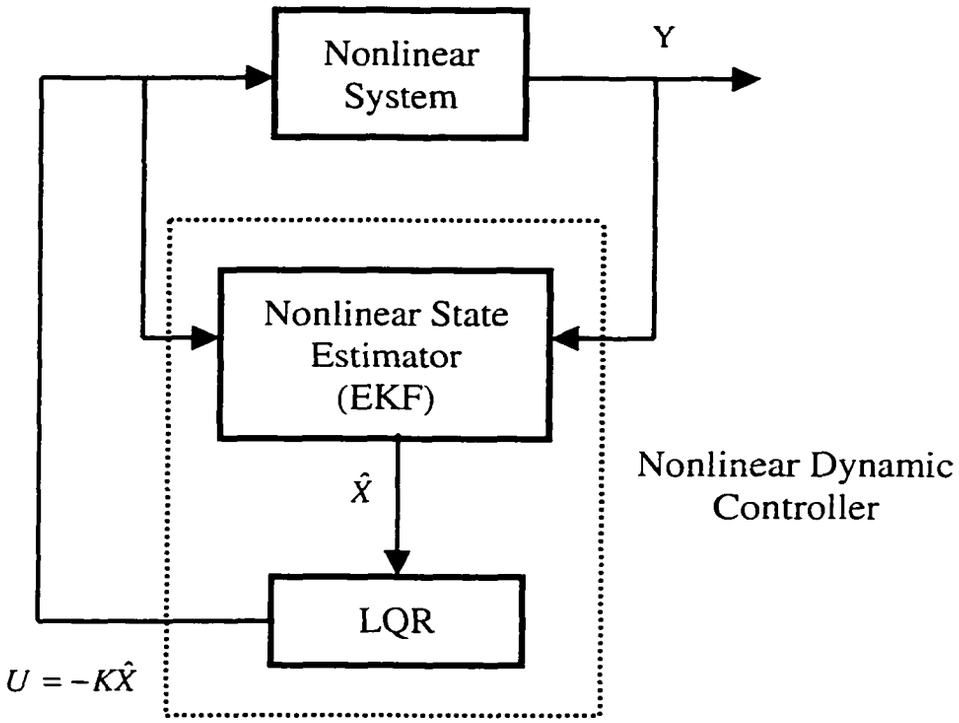

Figure 5.2 Nonlinear dynamic compensator for nonlinear panel flutter suppression using EKF and LQR

CHAPTER VI

NONLINEAR PANEL FLUTTER SUPPRESSION RESULTS

6.1 Introduction

Simulation studies for the suppression of nonlinear panel flutter using piezoelectric material under yawed supersonic flow are presented in this chapter. The time domain nonlinear finite element modal equations of motion are used to simulate the panel nonlinear flutter using the Runge-Kutta integration method. The studies presented have two main objectives. The first objective is the comparison of the controllers presented in Chapter 5 to determine the effect of different control strategies on the panel flutter suppression performance. The closed loop system performance is also studied under system parameter variations. This detailed controller performance study is performed for the case of zero flow yaw angle. The second objective is controlling nonlinear panel flutter under yawed supersonic for a specific range of yaw angles (the range selected in this study is from 0^{o} to 90^{o}).

Panel flutter suppression under yawed supersonic flow is considered for isotropic square, composite rectangular graphite/epoxy, and isotropic triangular panels. The properties for both isotropic and composite materials were given in Table 4.1. The main piezoelectric ceramic used in this study is the isotropic PZT5A. The mechanical and electrical material properties of PZT5A are given in Table 6.1. The piezoelectric layers are embedded on the top and bottom layers of the panel to avoid disturbing the flow filed over the panel. Each piezoelectric layer will be used as either self-sensing actuator or as actuator only.

6.2 Square Isotropic Panel

A square simply supported isotropic panel (12×12×0.05 in.) is first used to study different control methods and to study the control of panel flutter under a range of flow yaw angles. Piezoelectric layers are embedded on the top and bottom surfaces of the panel. The piezoelectric thickness is selected as 0.01 in. compared to the panel total thickness of 0.05 in. Using this thickness, the actuation voltage is then limited to 152

Volts (see Table 6.1). The aerodynamic damping coefficient, c_a, is assumed 0.01 and a structural modal damping ratio of 1% is added for all modes.

The panel is modeled using 10×10 finite element mesh and the nonlinear modal equations of motion are derived using a selected number of modes based on modal participation and modal convergence. For the case of zero flow yaw angle, four modes in the flow direction, mode (1,1) to (4,1), are used for modal reduction. This allows for a low order open loop system and, also, provides reasonably good accuracy for the flutter limit-cycle oscillation (LCO) amplitude (see modal participation values at $\alpha = 0^o$ in Table 4.6). This low order model is used for the detailed controller performance study. For the case of arbitrary yaw angle, the panel nonlinear modal equations of motion are derived using 16-mode model, mode (1,1) to (4,4). This makes the state space system of order 32.

6.2.1 Optimal Placement of Self-Sensing Piezoelectric Actuators

The first step is determining the optimal location of the embedded piezoelectric layers to achieve optimal actuation and optimal sensing. The panel is divided into 10×10 mesh size and is completely covered on top and bottom with piezoelectric layers (total of 100 piezoelectric actuators/sensors). The modal equations of motion are derived using the 16-mode model in order to be able to determine the optimal actuator and sensor locations for different yaw angles. The linearized system equations of motion about the zero displacement point, equation (5.5), are used to design both optimal feedback control (LQR) and optimal observer (Kalman filter). The resulting optimal feedback gain, $\boldsymbol{K}$, and observer gain, $\boldsymbol{K_e}$, are matrices with sizes 100×32 and 32×10, respectively. They represent the feedback and the estimator gain vectors for each patch of the 100 piezoelectric patches used. The methods of NFCG and NKFEG are then used to determine the effectiveness of each piezoelectric patch for optimal actuation and sensing.

Figures 6.1 and 6.2 show contours of the values of NFCG and NKFEG for the cases of 0^o and 45^o flow yaw angles, respectively (λ is set to 1000 for this case). These figures show clearly how the optimal actuator and sensor locations change completely for different flow angles. This indicates the importance of considering the flow yaw angle effect for the problem of panel flutter suppression. It is also seen that the optimal sensor location is at the trailing edge (TE), where the maximum panel deflection point is located, while the optimal actuator location is at the panel leading edge (LE) in the flow direction.

The optimal sensor location agrees with the standard structural vibration applications by placing the sensors at the maximum deflection point which gives minimum noise to signal ration. However, the optimal actuator location doesn't agree with the placement guidelines that are well known for structural vibration, which usually places piezoelectric actuators at the maximum curvature or maximum strain location. This is due to the aerodynamic loading involved in the panel flutter problem, which is proportional to the transverse deflection slopes (w_x and w_y). Thus for $\lambda > \lambda_{cr}$, considering the flutter deflection shape shown in Figure 4.10, the panel is subjected to a distributed pressure with maximum amplitude at the panel TE. It is found that the most effective piezoelectric actuators to counteract this forcing aerodynamic pressure are those located at the panel LE. This conclusion is in agreement with the experimental testing results performed by [106].

Figures 6.3 and 6.4 show the selected piezoelectric actuator and sensor location based on the NFCG and NKFEG methods for 0° and 45° yaw angles, respectively. Rectangular shaped piezoelectric patches are used to obtain practical sensor and actuator shapes. However, the optimal sensor and actuator shape can be refined by using more elements or triangular patches. The optimal sizing of piezoelectric actuators is outside the scope of this study and hence the size of both pieces is assumed by using the most effective 12 elements. This assumption is based on the studies performed by [74] which showed that the optimal size of actuator is between 10% and 20% of the panel area for nonlinear panel flutter suppression. Since self-sensing piezoelectric actuators are utilized in this study, the size of both patches located at the LE (optimal actuator) and at the TE (optimal sensor) is assumed to be the same, as both of them will be used as actuators. In practice, other types of sensors may be used such as accelerometers, displacement sensors, or strain gages. A case with single LE actuator and displacement sensors is considered when designing optimal output feedback control law.

6.2.2 Controller Study

A study of the performance of different controllers described in Chapter 5 is performed in this section. Two main categories of controllers are used. The first category is state feedback using LQR based on estimated states. Linear state estimation using standard Kalman filter is considered which leads to the LQG controller. In addition,

nonlinear state estimation using extended Kalman filter (EKF) is introduced. The second category considered is the optimal output feedback control.

The performance of different controllers is compared using their ability to suppress the panel nonlinear flutter. The measure used to asses performance is the maximum flutter-free dynamic pressure, λ_{max}, defined as the maximum dynamic pressure at which the control system can suppress the LCO of nonlinear panel flutter given the limitation of the actuator maximum voltage (saturation). This quantity is governed by controller performance, piezoelectric saturation voltage, and LCO amplitude. To obtain conservative values for λ_{max}, the controller will be activated after the convergence of LCO.

For the comparison performed in this section, the panel at 0^o yaw angle with the embedded PZT5A piezoelectric self-sensing actuators shown in Figure 6.3 is considered. The panel is modeled using the 4-mode model (state space model is of 8^{th} order). Figure 6.5 shows the change of panel frequencies as the nondimensional dynamic pressure, λ, increases for the panel with no piezoelectric material and with piezoelectric material added. It is seen how the addition of piezoelectric material decreases the panel stiffness compared to the original panel. This occurs because the piezoelectric material has heavier mass and slightly softer Young's modulus. Figure 6.6 shows the open loop poles at 3 different values of λ. It is seen how increasing λ beyond λ_{cr} results in 2 unstable poles (after mode (1,1) and (2,1) coalescence) and increasing it further results in 4 unstable modes as the other two modes, (3,1) and (4,1), coalesce.

6.2.2.1 LQR Controller

First a full state feedback using LQR is designed for the linearized model assuming all the states available. As discussed in Chapter 5, this is not a practical control method unless it is combined with state estimation. The state-weighting matrix, $\boldsymbol{Q}$, is selected using the energy method and the control-weighting matrix, $\boldsymbol{R}$, is selected as a constant multiplied by the identity matrix.

$$Q = \begin{bmatrix} K & 0 \\ 0 & M \end{bmatrix}, \qquad R = r[I] \tag{6.1}$$

Different values of r are tested until satisfactory performance is achieved using $r = 1000$. Figure 6.7 shows the performance of the LQR control for nonlinear panel flutter

suppression at $\lambda = 1500$. The controller is activated at $t = 100$ msec and it suppresses the LCO using the two self-sensing actuators at LE and TE within few cycles. λ_{max} using this controller was found to be 1760 compared to 512 for the original panel and to 449 for the panel with embedded piezoelectric material and with no control applied.

6.2.2.2 LQG Controller

A Kalman filter estimator is designed based on the system linearized equations of motion. Many values are used for the design parameters Q_e and R_e to arrive at satisfactory estimator performance. The performance of the Kalman filter estimation is shown in Figures 6.8 and 6.9 for $\lambda = 1000$ and 2000 respectively. It is seen how the estimated LCO amplitude degrade as λ increases. This is expected as the Kalman filter uses a linear model that does not consider the nonlinear effects at all, so it is trying to estimate a nonlinear process using a linear model. As λ increases, the effect of nonlinearity increases and hence the estimated LCO amplitude using Kalman filter is not accurate. The design parameters of the Kalman filters are selected as: $Q_e = [I]$, $R_e = [C][C]^T$.

Figure 6.10 shows that, unlike the LQR, the LQG controller cannot suppress the flutter LCO at $\lambda = 1500$. Comparing this figure to the LQR performance, shown in Figure 6.7, shows how the introduction of linear state estimation degrades the control system performance. The achieved λ_{max} using LQG is 920 compared to 1760 using LQR control, which is about 50% performance reduction due to linear state estimation. Figure 6.11 shows the performance of the LQG controller at the maximum flutter-free dynamic pressure.

6.2.2.3 Nonlinear Output Controller (EKF+LQR)

An extended Kalman filter estimator (EKF), which takes into account the system nonlinear dynamic by linearizing about the estimated state vector, is implemented using the same parameters as those of a Kalman filter (Q_e, R_e). The performance of state estimation using EKF is shown in Figure 6.12 at $\lambda = 2000$. Comparing this to Figure 6.9 shows how superior the performance of EKF is compared to the standard Kalman filter. It has to be noted that, in practice, the estimation performance will be further degraded due to sensor noise and system model uncertainty.

Combing the EKF with LQR control results in a dynamic nonlinear compensator. Figure 6.13 shows the performance of the EKF+LQR for nonlinear panel flutter suppression at $\lambda = 1500$. Using this controller, λ_{max} was found to be 1750. To show the performance of EKF+LQR control even with uncertainty in the model nonlinear matrix used by the EKF, the controller is used with +/-25% uncertainty in the system nonlinear matrix, ΔA_q, used in propagating the state estimate, see equation (5.16). Figure 6.14 shows that the flutter LCO can be successfully suppressed using the EKF+LQR controller with +/-25% uncertainty in ΔA_q. Therefore, using nonlinear state estimation instead of the standard linear state estimation for the problem of nonlinear panel flutter gives much better results even with some uncertainty in the nonlinear model matrix.

In all the controllers above, LQR, LQG, and EKF+LQR, the simulation results indicated that the self-sensing piezoelectric patch at the TE is not as effective as the LE patch from actuation point of view. However, the TE piezoelectric patch is acting as the optimal sensor to achieve better state estimation. Without this sensor, i.e., if the LE sensor is only used, the estimation performance will be degraded dramatically due to the high noise to signal ratio for the LE sensor resulting from smaller displacement at this location.

6.2.2.4 Optimal Output Feedback Controller

The iterative algorithm given in Appendix C is used to solve the coupled nonlinear equations given by equation (5.20) for optimal output feedback gain matrix. An initial stabilizing gain, $\boldsymbol{K_o}$, has to be first determined using some trail and error. The weighting matrices $\boldsymbol{Q}$ and $\boldsymbol{R}$ are the same as for the LQR case. For the panel configuration of 2 self-sensing piezoelectric actuators, the resulting output feedback gain matrix is of size 2×2. Using this configuration, an output feedback gain was successfully designed to suppress flutter LCO up to $\lambda_{max} = 1000$. Figure 6.15 shows the performance of the optimal output feedback controller at the maximum flutter-free dynamic pressure. It is noticed that this controller introduces less damping to the system compared to the full state feedback control. In practice, low pass filters have to be used to filter out the feedback signals from the sensors. This could degrade the optimal feedback performance even more.

Another panel configuration that uses only the LE actuator and uses two displacement sensors located at ($a/2$, $a/2$) and ($3a/4$, $a/2$) is considered. The output feedback gain for this configuration is of size 1×2. Figure 6.16 shows that the optimal output feedback can suppress LCO up to $\lambda_{max} = 1100$ for this case.

In conclusion, the optimal output feedback performance for panel flutter suppression is less than using EKF+LQR control. However, the optimal output feedback is much simpler for practical implementation as it does not require the on-line adaptation needed for EKF. The achieved values of λ_{max} for the different controllers used are summarized in Table 6.2.

6.2.2.5 Controller Robustness

A study for the effect of system parameter variation on the performance of both EKF+LQR and optimal output feedback controllers is given in this section. First with regard to the dynamic pressure λ, it was found that for LQR and optimal output feedback, the feedback gain determined at λ_{max} suppresses LCO for all values of $\lambda \leq \lambda_{max}$. However, for accurate state estimation λ needs to be known since the system model is a function of λ. Figure 6.17 shows the effect of +25% mismatch in λ between design model and reality (simulation model) for both LQR and EKF+LQR controllers when the simulation model has $\lambda = 1200$. It is seen how the performance of EKF+LQR is degraded in this case, mainly due to inaccurate state estimation.

The second type of system parameter variation considered is in the panel stiffness. In section 6.2.2.3, it was shown that, the EKF+LQR controller has a satisfactory performance with +/-25% uncertainty in the design model nonlinear stiffness matrix. In this section a +/-25% variation in the modal linear stiffness is considered, which corresponds to about +/-13% uncertainty in the panel natural frequencies. Figure 6.18 shows the effect of +/-25% variation in modal linear stiffness using EKF+LQR controller at $\lambda = 1500$. It is seen that the LCO cannot be suppressed with such system parameter variation. The performance of EKF+LQR is degraded with parameter variations because both the state estimation and the state feedback design are affected by the linear stiffness variation. Figure 6.19 shows the same effect for the optimal output feedback controller at $\lambda = 1100$ (using the configuration of single LE actuator and 2 displacement sensors). The

optimal output feedback controller is shown to be more robust to linear stiffness variation than the EKF+LQR controller.

6.2.3 Panel Flutter Control with Yawed Flow

In this section, nonlinear panel flutter suppression with flow yaw angle is considered. The nonlinear dynamic output compensator (EKF+LQR) is used in this study as it provides the best performance. First, the flow yaw angle, α, is considered as simply a perturbation that is not considered in the design at all, i.e., not considered in the piezoelectric placement or in the controller design. Figure 6.20 shows the performance of the controller designed for $\alpha = 0^{\circ}$ when the actual flow is at $\alpha = 45^{\circ}$ and $\lambda = 800$. The results clearly indicate that the flutter LCO cannot be suppressed for $\alpha = 45^{\circ}$ using the control system designed for $\alpha = 0^{\circ}$ even at such low dynamic pressure. This shows that flow yaw angle has to be considered in the design of active control systems for nonlinear panel flutter suppression. Figure 6.21 shows the effect of flow angle on the optimal location of self-sensing piezoelectric actuators for $\alpha = 0$, 15, 30, 45, and 90° flow yaw angles. The flow LE piezoelectric patch is the optimal actuator location d6etermined using NFCG while the TE patch is the optimal sensor location determined using NKFEG. It is seen how the change of flow angle has a major effect of the optimal actuator and sensor locations.

The objective is to design active control system including piezoelectric placement for the panel knowing that the panel will be subjected to a specific range of flow yaw angles. The range assumed in this study is from 0 to 90°. Performing optimization for piezoelectric placement over a range of α is not a simple task. The methodology proposed in this study is to optimize the piezoelectric sensor and actuator placement for different angles within the specified range, as was shown in Figure 6.21, then group the resulting optimal location together to find a single piezoelectric configuration that works over the entire range of angles.

Figure 6.22 shows optimal actuator and sensor location that covers all the yaw angles from 0 to 90°. The optimal actuator consists of 2 LE piezoelectric pieces in the directions normal to 0 and 90° while the optimal sensor consists of 2 TE piezoelectric pieces in the directions normal to 0 and 90°. As mentioned before, the piezoelectric patches required for optimal sensing can be replaced by other types of sensor such as

strain gages or can be smaller in size. However, since they will be used as actuators too, piezoelectric patches of the same size are used. Thus, the configuration of Figure 6.22 results in an outer square covering 48% of the panel surface with embedded PZT5A. The embedded piezoelectric is divided into 4 equal self-sensing actuators referred to as: 0LE and 90LE for the leading edge patches perpendicular to the 0 and 90° flow directions, and 0TE and 90TE for the trailing edge patches perpendicular to the 0 and 90° flow directions. Examining this configuration further, it is seen that it does not only cover yaw angles from 0 to 90° but due to the panel symmetry and the usage of self-sensing actuators, this configuration will cover all angles from 0 to 360°.

The performance of the EKF+LQR controller for nonlinear panel flutter suppression with yawed flow is now considered. Three different configurations for piezoelectric placement are considered for comparison. The first and second configurations are simply using the optimal placement determined at $\alpha = 0°$ and 45°, respectively, while the third configuration uses the optimized piezoelectric over the range of 0 to 90° with 4 self-sensing actuators, as was shown in Figure 6.22. Figure 6.23 shows a comparison of the achieved λ_{max} using these 3 configurations for flow yaw angles changing from 0 to 90°. It is seen that the piezoelectric optimized for 0° flow angle provides acceptable performance up to $\alpha = 45°$ with $\lambda_{max}/\lambda_{cr} = 3.03$ ($\lambda_{cr} = 512$), but $\lambda_{max}/\lambda_{cr}$ decreases to about 1.56 at $\alpha = 90°$ compared to 3.41 at $\alpha = 0°$. Therefore, this configuration is not a good candidate for yaw angles from 0 to 90°. However, it provides acceptable performance from 0 to 45° and consequently from –45° to 45° due to the panel symmetry. The second configuration, piezoelectric optimized for $\alpha = 45°$, is shown to provide good flutter suppression performance over the entire range yaw angles from 0 to 90°. The best performance is achieved at $\alpha = 45°$ with $\lambda_{max}/\lambda_{cr} = 3.71$ while $\lambda_{max}/\lambda_{cr} = 3.0$ at $\alpha = 0°$ and 90°. The third configuration with 4 self-sensing piezoelectric actuators is shown to provide the best performance of all configurations with a minimum of $\lambda_{max}/\lambda_{cr} = 3.52$ over the entire range of yaw angles. However, the second configuration uses only 24% covered panel compared to 48% for the third configuration. Figures 6.24 through 6.26 show the time history of maximum LCO and the control inputs to the four self-sensing piezoelectric actuators using the EKF+LQR controller at $\lambda = 1500$ for $\alpha =$

0°, 45°, and 90°, respectively. They clearly indicate the effectiveness of proposed controller and piezoelectric configuration in suppressing nonlinear panel flutter at different flow yaw angles.

6.3 Composite Panel

Nonlinear panel flutter suppression with yawed supersonic flow is also considered for a rectangular (15×12×0.048 in.) simply supported graphite/epoxy $[0/45/-45/90]_S$ panel. PZT5A actuators that have the thickness of 0.006 in. are embedded at the top and bottom layers, i.e., replacing the 0° layer. The maximum actuator applied voltage is limited to 91.2 Volts in this case. The panel is modeled using 10×10 MIN3 finite element mesh and the nonlinear modal equations of motion are derived using the lowest 16 modes. The aerodynamic damping coefficient, c_a, is assumed 0.01 and the modal structural damping ratio = 1%.

Adding too much piezoelectric material for this case will largely change the panel characteristics as it replaces the 0° layer and hence change the original panel directional properties. In addition, PZT5A mass density is very high compared to graphite/epoxy (about 5 times higher). To avoid adding too much piezoelectric material and changing the panel characteristics, piezoelectric material is only used as actuator for this panel and displacement sensors are used to provide output measurements for the estimation process. Similar to the isotropic panel case, the optimal actuator location is determined by dividing the panel into 10×10 piezoelectric actuator elements at the top and bottom then using LQR state feedback gain matrix from these actuators to select the elements with the highest NFCG. Figure 6.27 shows optimal piezoelectric actuator using this method for α = 0, 15, 30, 45, and 90° flow yaw angles at λ = 800. Considering a yaw angle range from 0 to 90°, the approximate shape of optimal piezoelectric actuator that cover all angles within this range is shown in Figure 6.28. It is basically the union of all elements at different angles shown in Figure 6.27. The piezoelectric actuator shown in Figure 6.27 is divided into two separate actuators one perpendicular to the 0° flow direction and the other to the 90° flow direction. Three displacement sensors are used at the locations of ($3a/4$, $b/2$), ($3a/4$, $3b/4$), and ($a/2$, $3b/4$) corresponding to the approximate location of maximum deflection for 0°, 45°, and 90° yaw angles, respectively.

Like to the isotropic panel, the performance of the EKF+LQR controller for nonlinear panel flutter suppression is studied using three different configurations for piezoelectric actuator placement: the optimal actuator for the case of $\alpha = 0^o$, the optimal actuator for $\alpha = 45^o$, and the optimized actuator over the range of 0 to 90° with 2 independent actuators, as shown in Figure 6.28. Figure 6.29 shows a comparison of the achieved λ_{max} using these 3 configurations for flow yaw angles changing from 0 to 90°. The critical dynamic pressure changes largely with flow angle for the original panel with no piezoelectric actuators added as was shown in Figure 4.12 (λ_{cr}=315, 250, and 185 for flow angles of 0°, 45°, and 90°, respectively). The conclusion drawn from this figure are very similar to those of the isotropic panel case and are summarized as follows:

- The actuator optimized for 0° flow angle does not provide good flutter suppression performance over the range of 0 to 90°. However, it is reasonably good for yaw angles from –45 to 45°.
- The best performance over the flow angles range of [0,90°] is achieved using the actuator optimized for this range with 2 LE actuators (0LE and 90LE).
- The actuator optimized for 45° angle provides reasonably good performance for all angles from 0 to 90° and has the advantage of being half the size of the actuator optimized for all angles from 0 to 90°.

Thus, the panel maximum flutter free dynamic pressure can be increased to a minimum of 750 over all yaw angles from 0 to 90° using the actuator optimized for 45° or to a minimum of 900 using the actuator optimized for all angles from 0 to 90°. This is compared to the minimum flutter-free dynamic pressure of 185 occurring at $\alpha = 90^o$ for the original panel. Figures 6.30 through 6.32 show the time history of maximum LCO and the control inputs to the two piezoelectric actuators using the EKF+LQR controller at $\lambda = 900$ and for $\alpha = 0^o$, 45°, and 90° respectively. It shows the effectiveness of proposed controller and piezoelectric configuration in suppressing nonlinear panel flutter at different flow yaw angles for composite panels.

6.4 Triangular Panel

The triangular (12×12×0.05 in.) clamped isotropic panel studied in Chapter 4 is considered for nonlinear panel flutter suppression. PZT5A layers with a thickness of 0.01

in. are used. The panel is modeled using 10×10 MIN3 finite element mesh and the nonlinear modal equations of motion are derived using the lowest 16 modes. The flow yaw angles range selected for this panel is between 90° and 180°. This range is selected since it encompasses the worst case yaw angle where the flow is parallel to the tilted edge (α= 135° or 315°), as was shown in Chapter 4.

The optimal actuator location is determined by dividing the panel into 100 triangular piezoelectric elements at the top and bottom then using the NFCG method. Figure 6.33 shows optimal piezoelectric actuator location using this method for different yaw angles between 90° and 180°. An approximate shape and location of a single piezoelectric actuator for the flow range from 90° to 180° is determined by combining the optimum actuators at different angles within this range of yaw angles as given in Figure 6.34. A single displacement sensor is used at (0.2a, 0.4b). This sensor location is determined based on the locations of maximum panel deflection at different flow angles which are (0.2a, 0.3b), (0.2a, 0.4b), and (0.2a, 0.5b) for α = 90, 135, and 180°, respectively.

The performance of the EKF+LQR controller for nonlinear panel flutter suppression is given in Figure 6.35. The panel maximum flutter free dynamic pressure is increased to a minimum of 6350 compared to a minimum of 2620 for the uncontrolled panel. The piezoelectric material and active control system for this panel is not as effective as the case of square isotropic panel (3.5 times increase in λ_{cr} for the square isotropic panel versus only 2.4 increase for the triangular panel). This is mainly due to the smaller size and clamped boundary conditions of the triangular panel, which make it stiffer.

6.5 Summary

Simulation studies for the suppression of nonlinear panel flutter using piezoelectric materials and different optimal control strategies are presented in this chapter. The control strategies considered include LQG controller, LQR combined with extended Kalman filter (EKF), and optimal output feedback. The nonlinear dynamic output compensator compromised of LQR and EKF results in a 3.5 times increase in the critical dynamic pressure compared to only 1.8 times for the LQG controller. Using optimal output feedback controller, the panel critical dynamic pressure was increased

about 2 times. However, the optimal output feedback is much simpler for practical implementation as it does not require the on-line adaptation needed for EKF. Suppression of nonlinear panel flutter under yawed supersonic flow is considered using the LQR and EKF nonlinear controller. The NFCG and NKFEG methods are used to determine the optimal location of piezoelectric actuators and sensors, respectively. Optimal actuator and sensor location for a range of flow yaw angles is determined by grouping the optimal locations for different angles within the specified range. Using this method with four self-sensing actuators, the critical flutter boundary was increased 3.5 times over the entire range of yaw angles from 0 to 360° for square isotropic panel. For a rectangular graphite/epoxy composite panel, the critical flutter dynamic pressure is increased to a minimum of 900 over all yaw angles from 0 to 90° compared to 185 for the original uncontrolled panel. Results for a clamped triangular isotropic panel showed that the critical flutter dynamic pressure can be increased about 2.5 times for a flow yaw angle range from 90 to 180°.

Table 6.1 Mechanical and electrical properties PZT5A piezoelectric ceramics

PZT5A	
E_1	9.9 Msi (69 Gpa)
E_2	9.9 Msi (69 Gpa)
G_{12}	3.82 Msi (26.3 Gpa)
G_{23}	3.82 Msi (26.3 Gpa)
d_{31}	-6.73×10^{-9} in/V (-171×10^{-12} m/V)
d_{32}	-6.73×10^{-9} in/V (-171×10^{-12} m/V)
ρ	0.72×10^{-3} lb-sec^2/in.^{4} (7700 Kg/m^3)
ν_{12}	0.31
h_e^*	Same as layer thickness
E_{max}	15240 V/in (600 V/mm)

* h_e: Electrode spacing

Table 6.2 Comparison of different controllers performance for nonlinear panel flutter suppression

Controller	λ_{max}
LQR	1760
LQG	920
EKF+LQR	1750
Optimal OFB	1000-1100

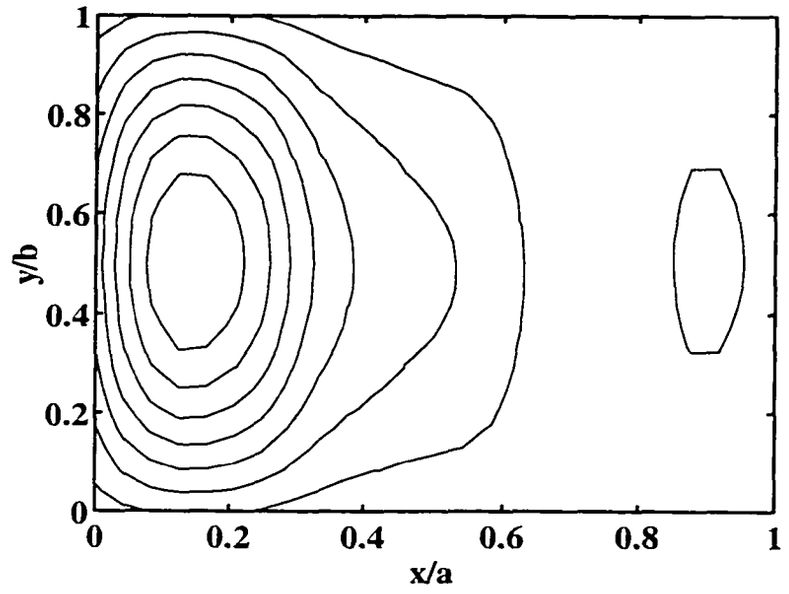

(a)

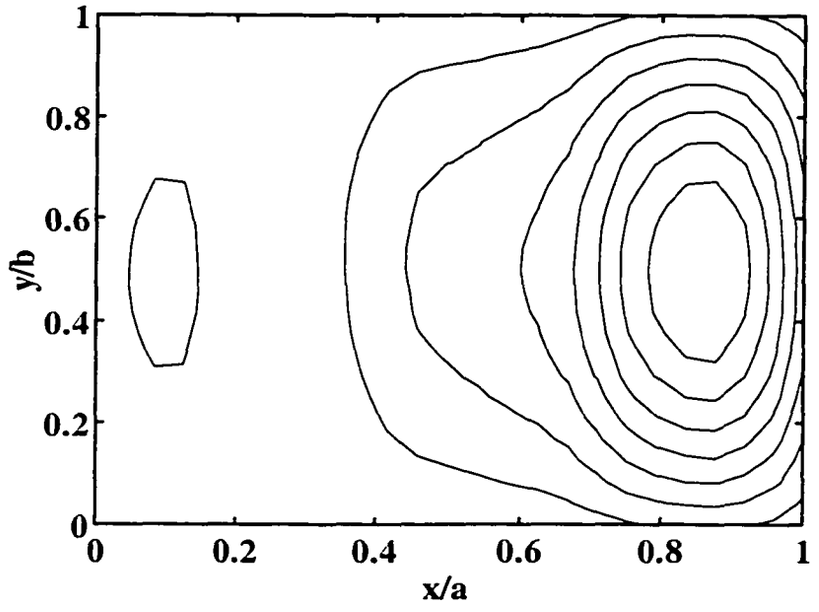

(b)

Figure 6.1 Contours of (a) NFCG and (b) NKFEG for simply supported square isotropic panel at 0^{o} flow angle

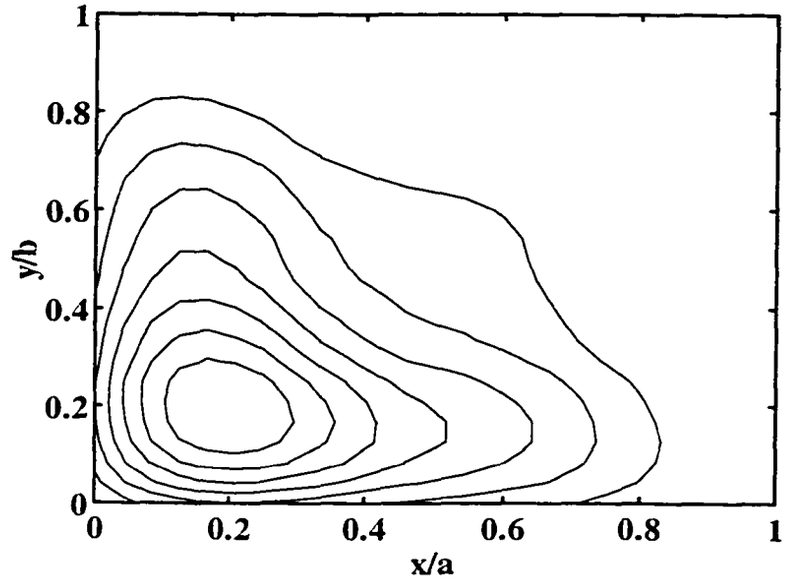

(a)

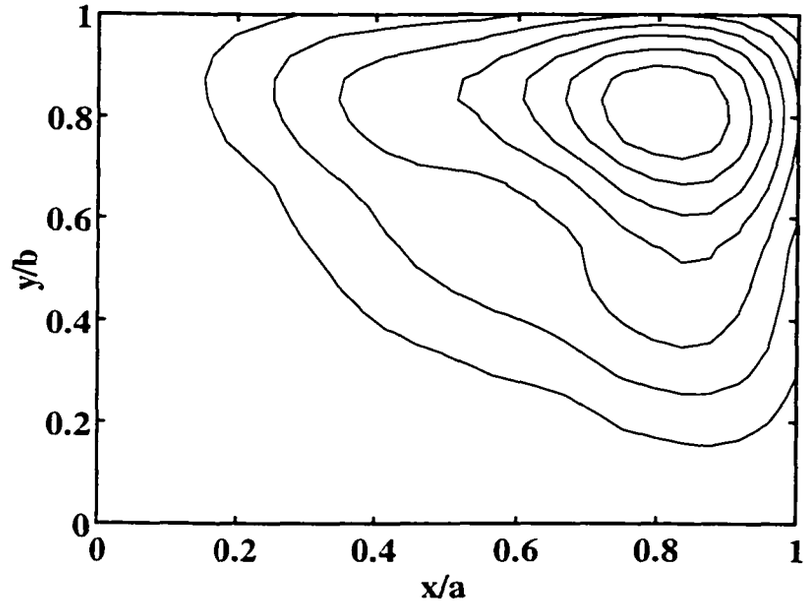

(b)

Figure 6.2 Contours of (a) NFCG and (b) NKFEG for simply supported square isotropic panel at 45° flow angle

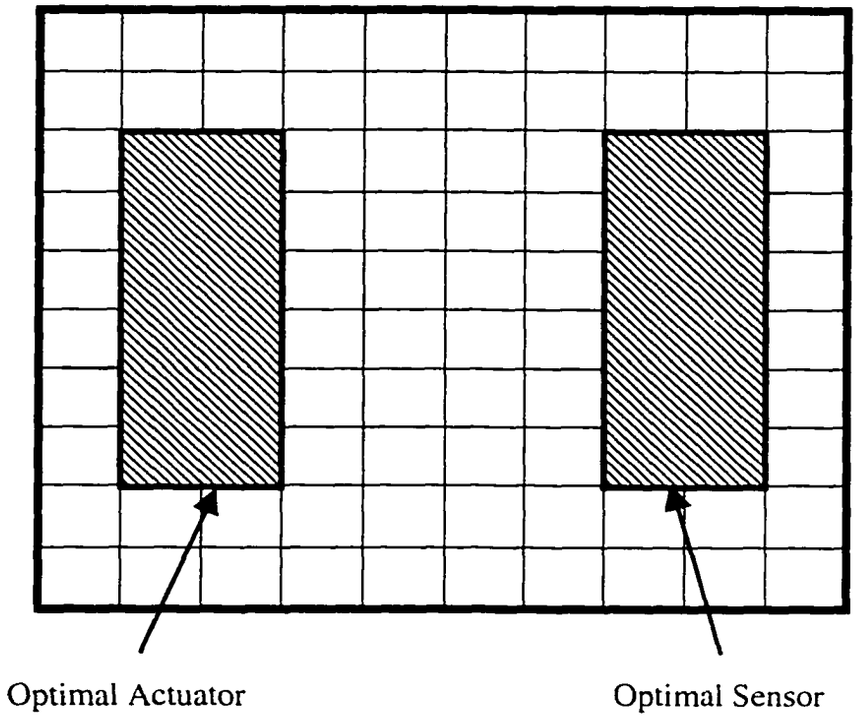

Figure 6.3 Selected self-sensing piezoelectric actuators placement and size for optimal actuation and optimal sensing on square isotropic panel at 0^{o} flow angle

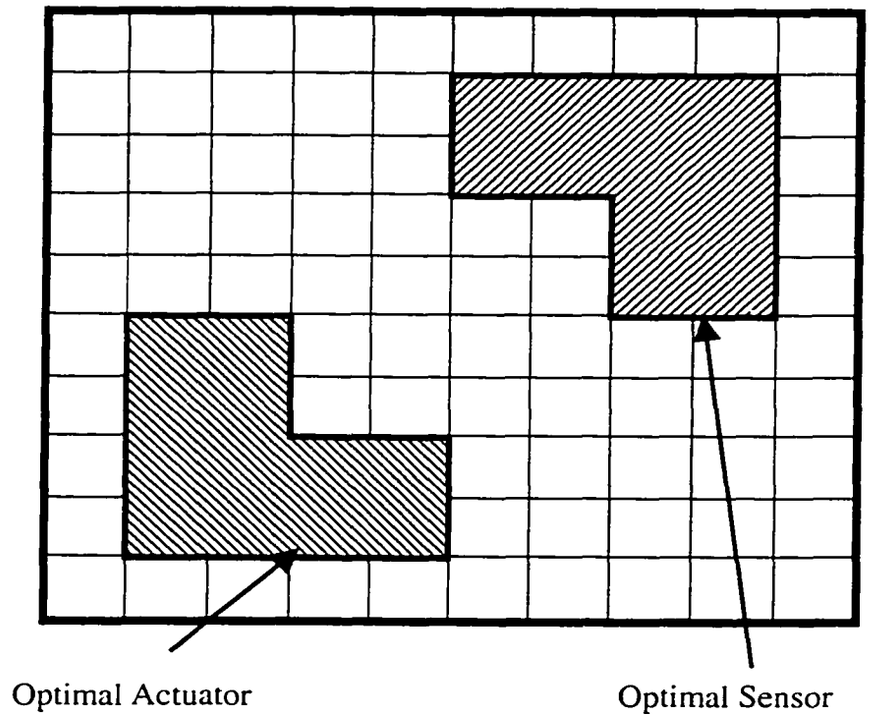

Figure 6.4 Self-sensing piezoelectric actuators placement and size for optimal actuation and optimal sensing on square isotropic panel at 45° flow angle

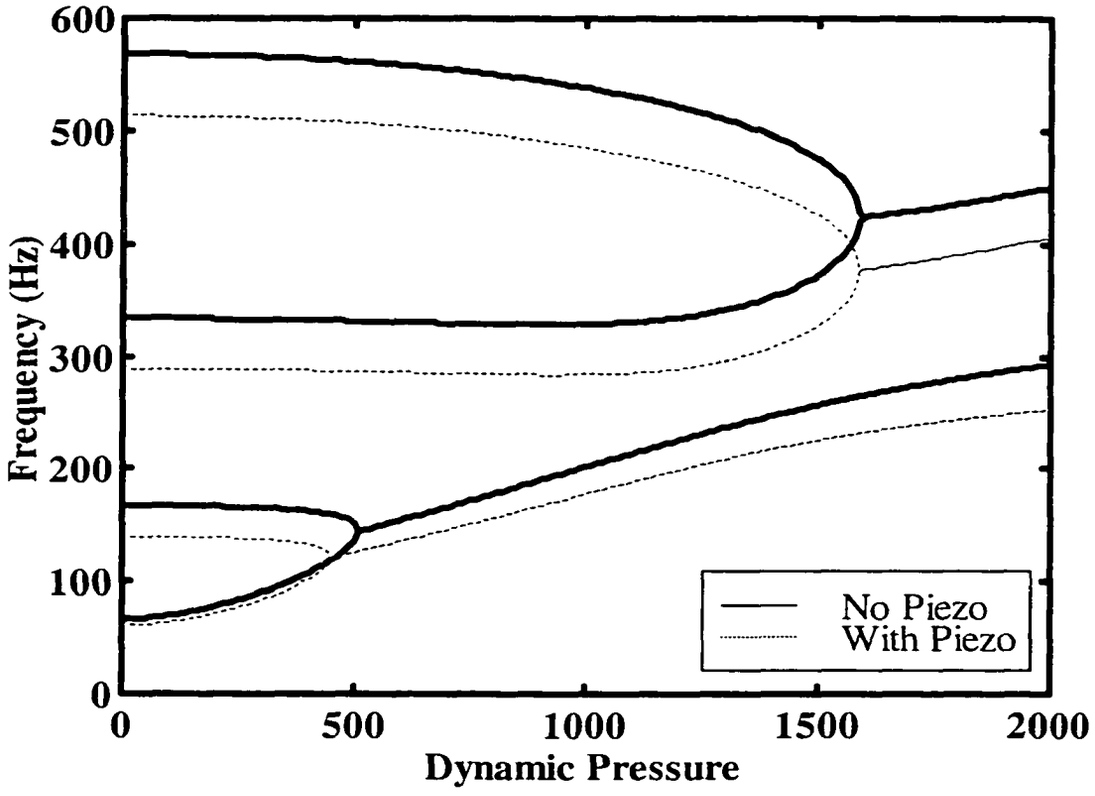

Figure 6.5 Variation of first 4 linear modes versus λ for isotropic panel with and without added piezoelectric material

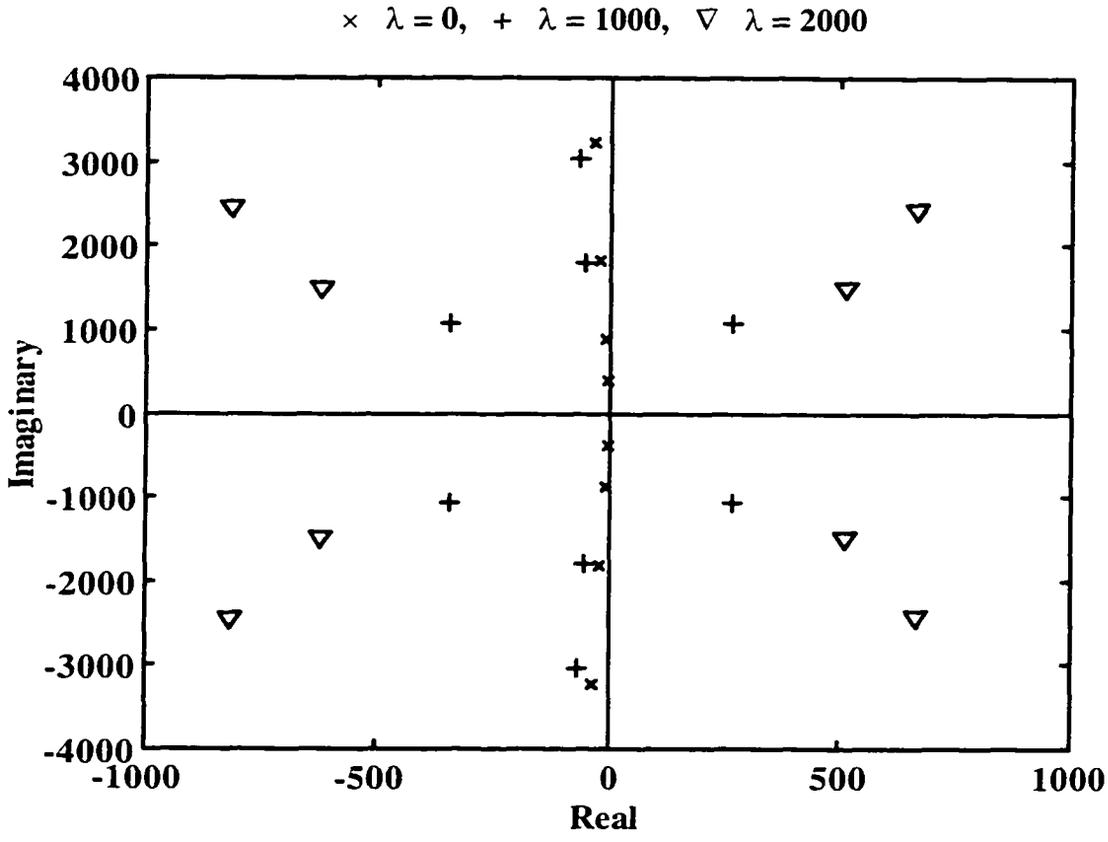

Figure 6.6 Open loop poles for isotropic square panels with embedded piezoelectric material at different values of nondimensional dynamic pressure

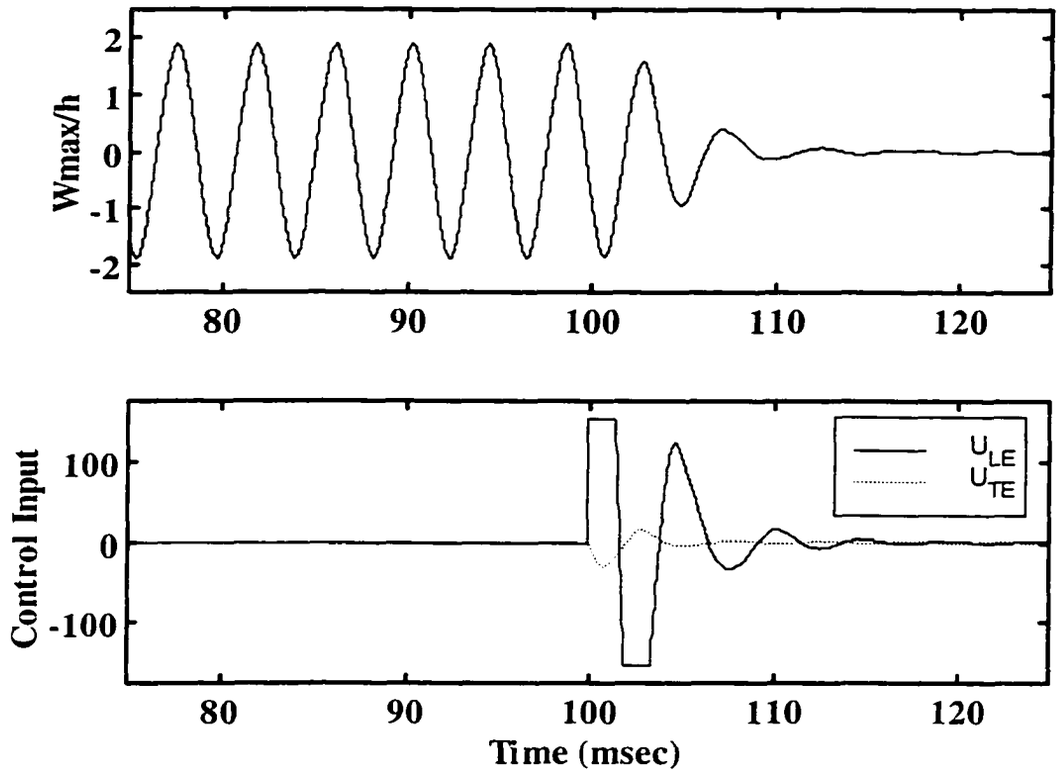

Figure 6.7 Limit-cycle amplitude and control inputs time history for square isotropic panel using LQR control at $\lambda = 1500$

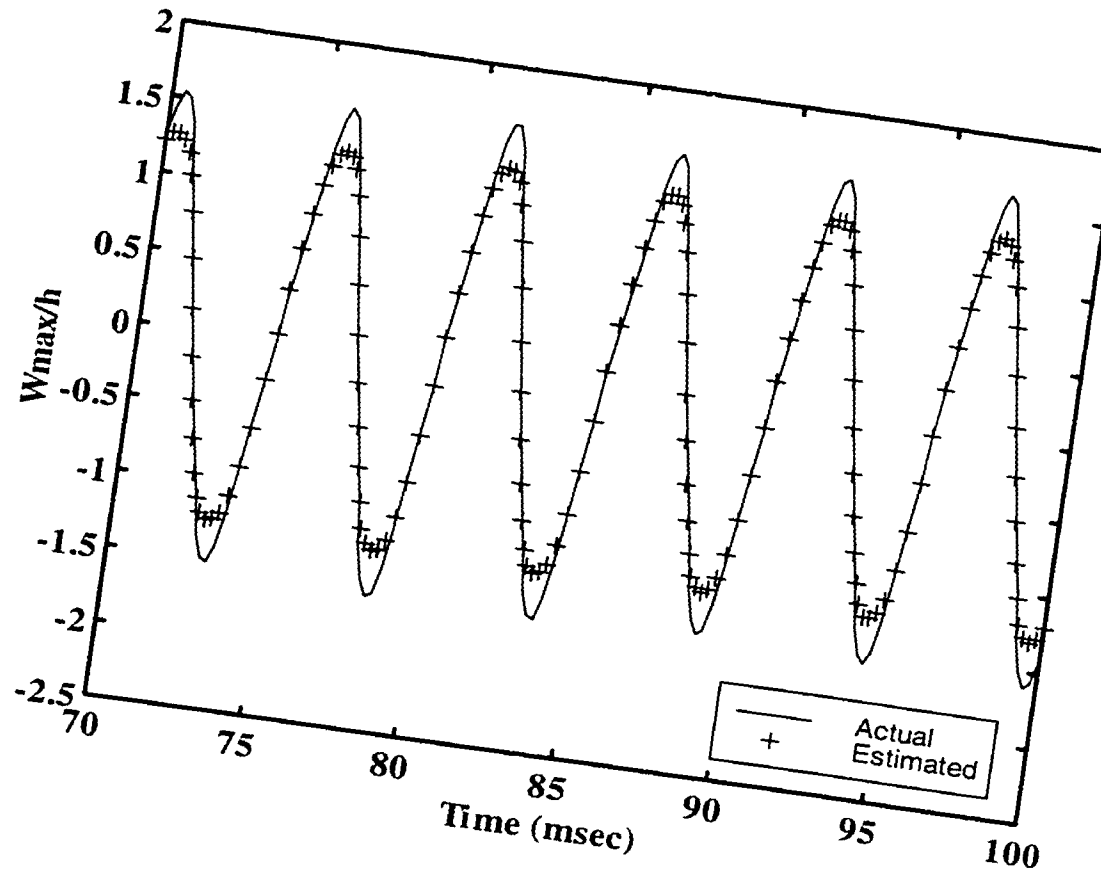

Figure 6.8 Comparison between actual LCO amplitude and estimated LCO amplitude using Kalman filter at $\lambda = 1000$

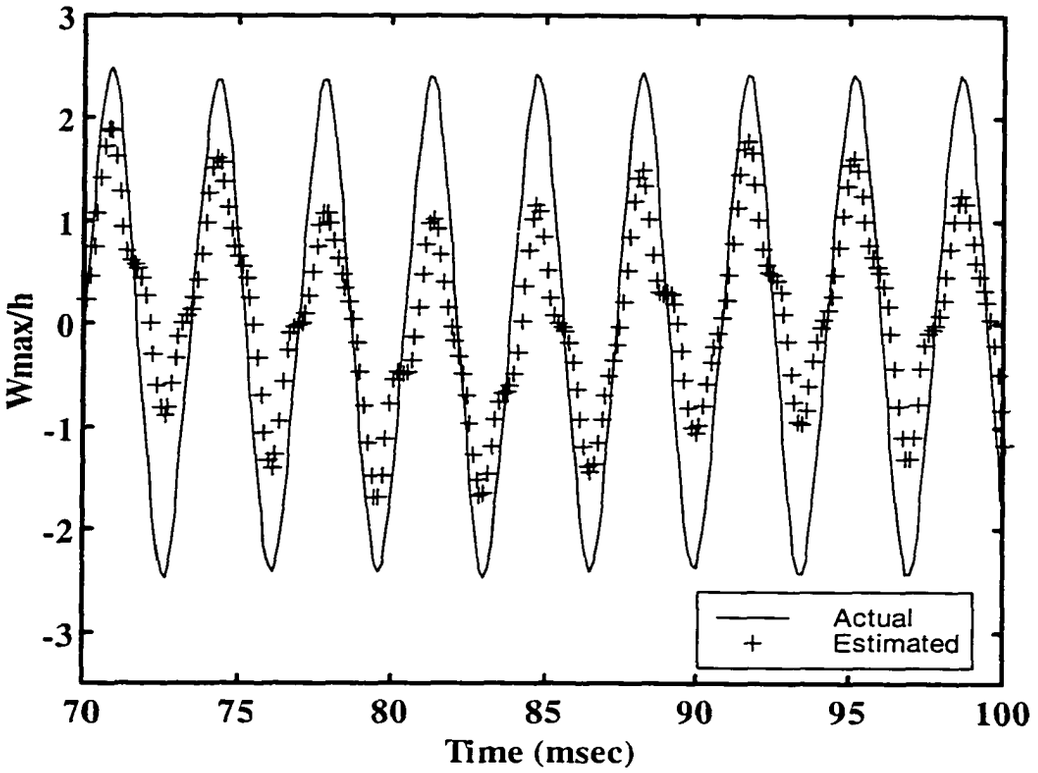

Figure 6.9 Comparison between actual LCO amplitude and estimated LCO amplitude using Kalman filter at $\lambda = 2000$

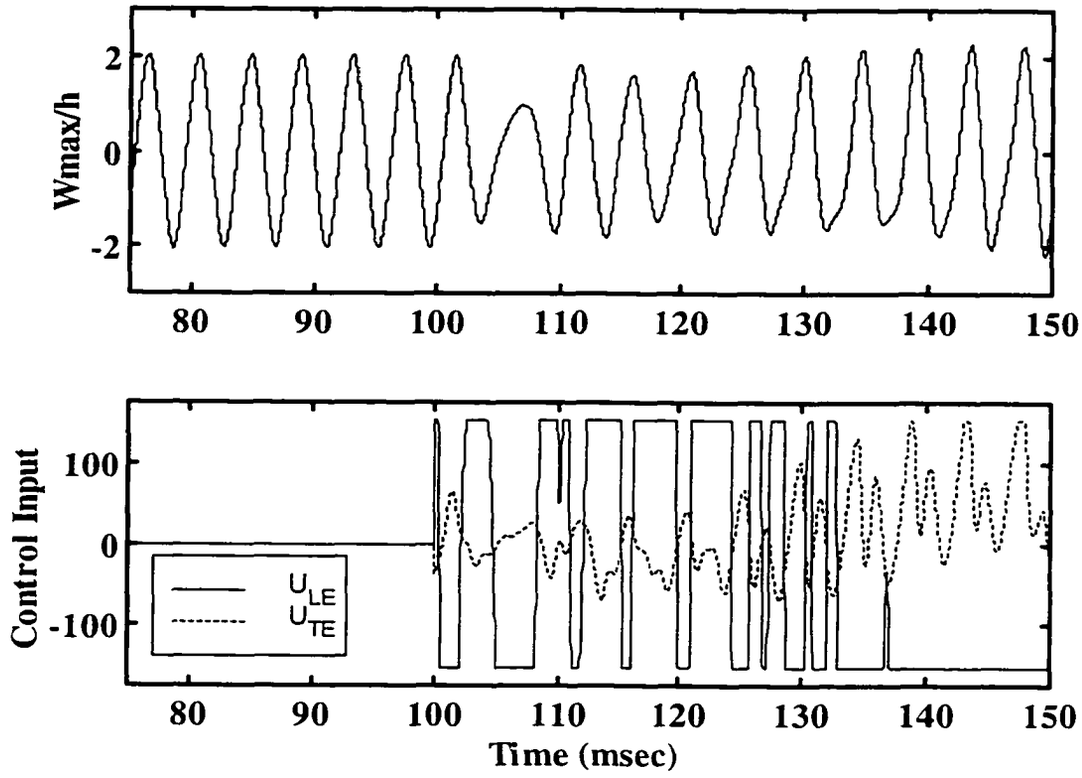

Figure 6.10 Performance of LQG controller at $\lambda = 1500$

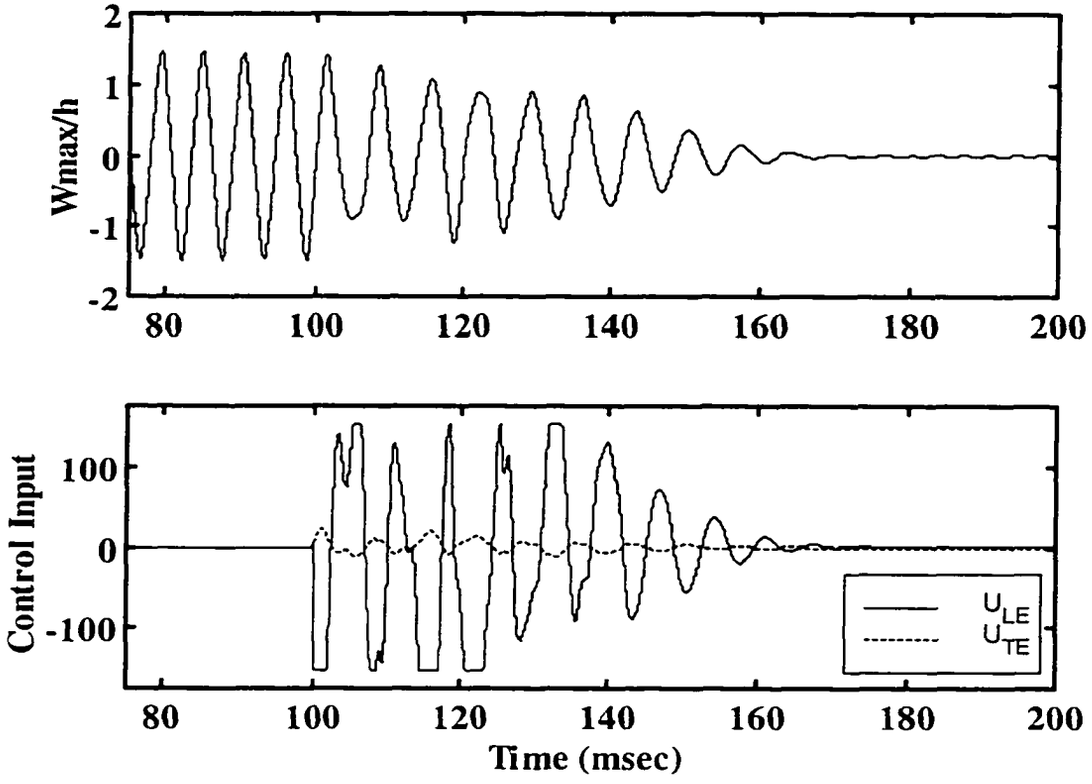

Figure 6.11 Performance of LQG controller at the maximum suppressible dynamic pressure, $\lambda max = 920$

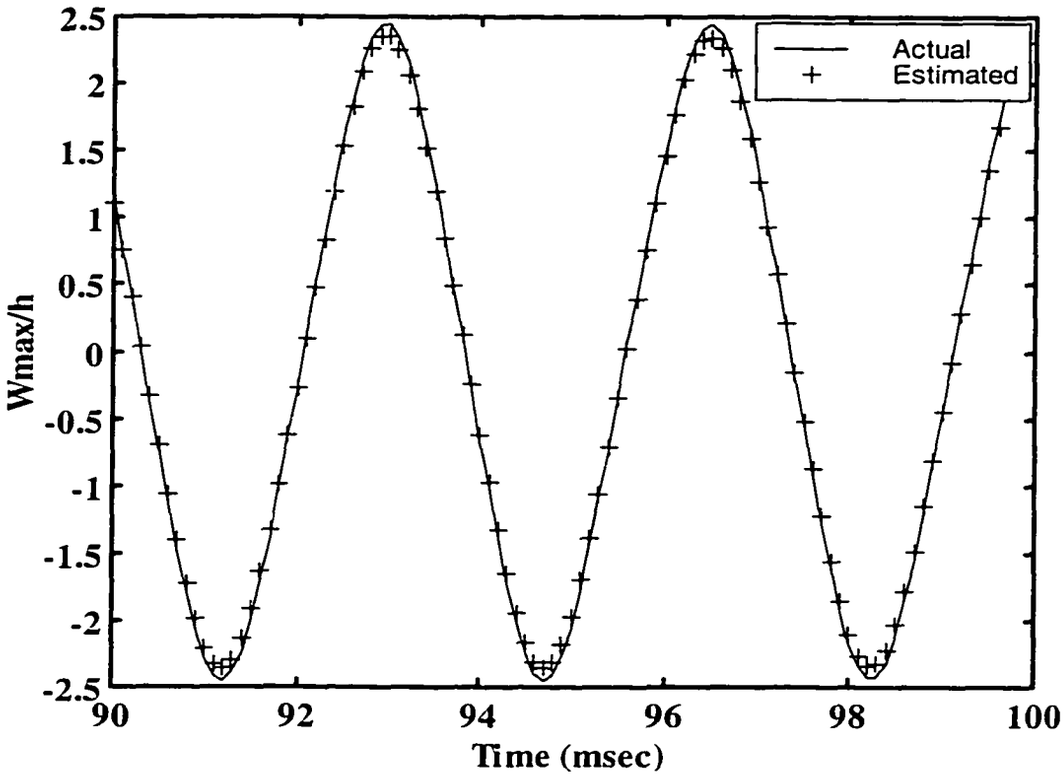

Figure 6.12 Comparison between actual and estimated LCO amplitude using extended Kalman filter at $\lambda = 2000$

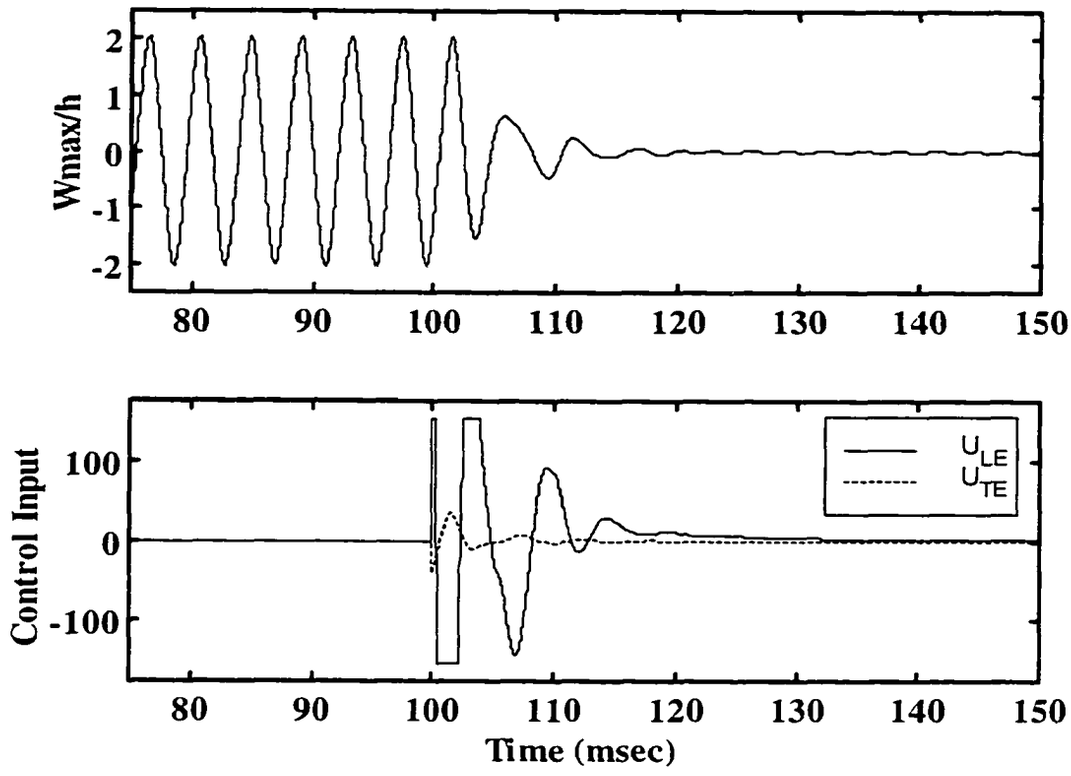

Figure 6.13 Performance of LQR+EKF nonlinear output compensator at $\lambda = 1500$

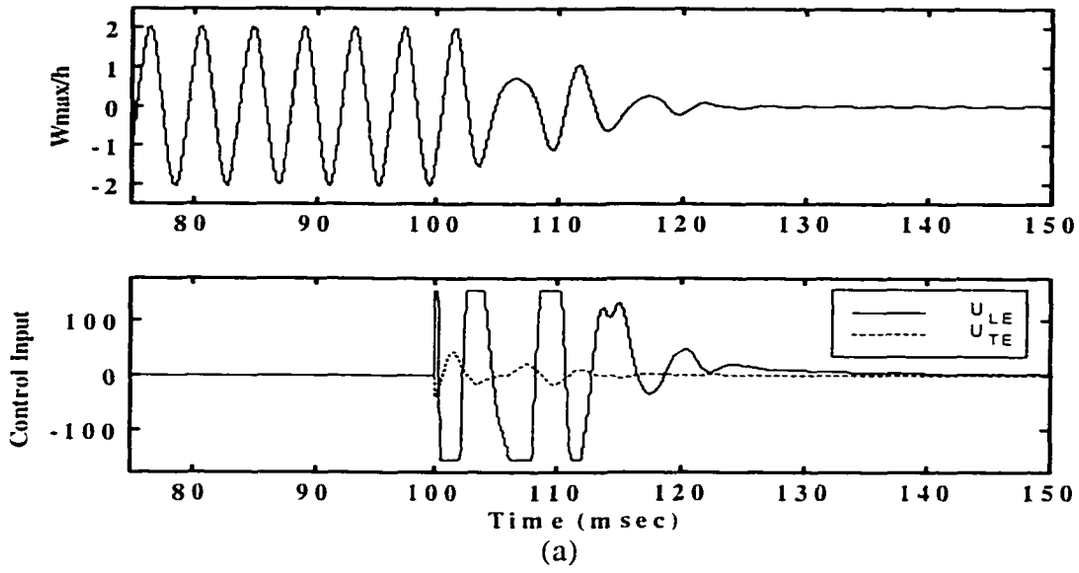

(a)

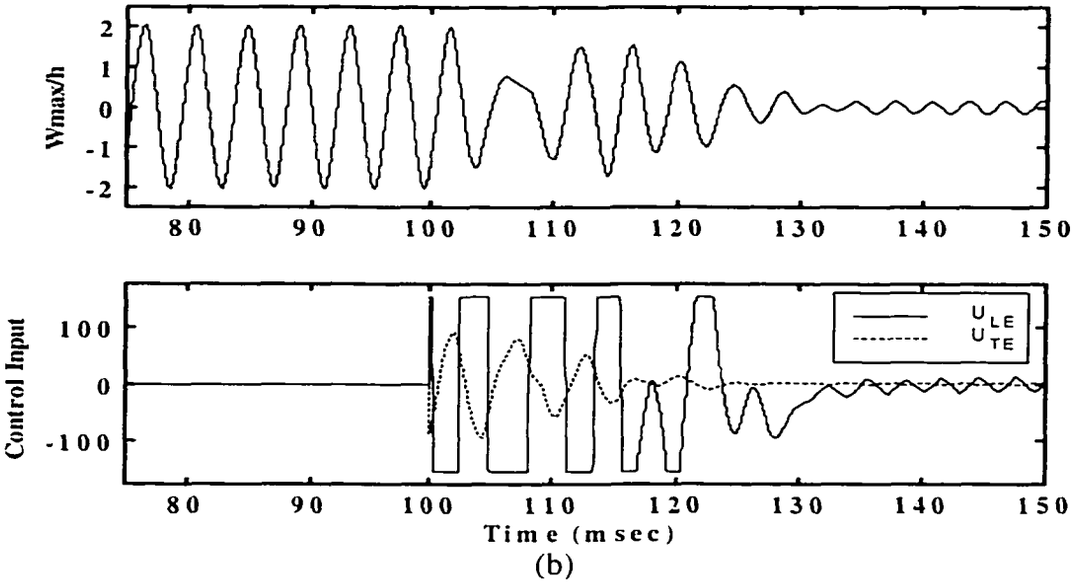

(b)

Figure 6.14 Performance of LQR+EKF nonlinear output controller at $\lambda = 1500$ with (a) -25% and (b) +25% uncertainty in the model nonlinear stiffness matrix

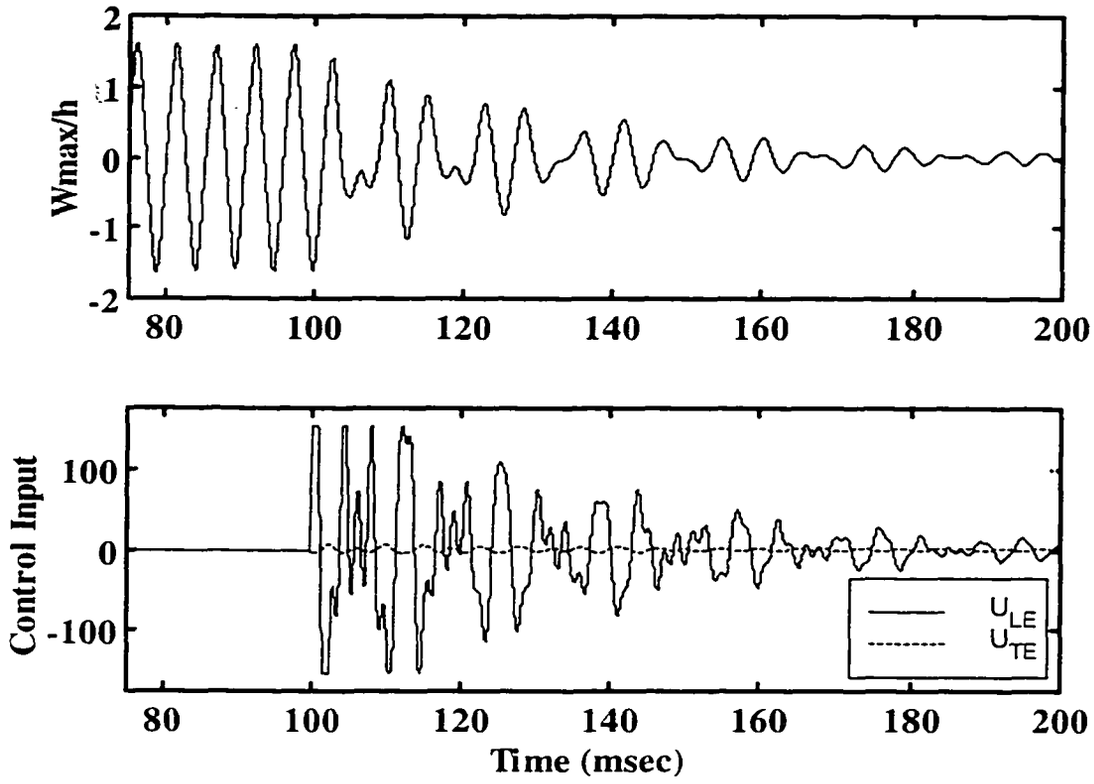

Figure 6.15 Performance of optimal output feedback controller using two self-sensing actuators at $\lambda max = 1000$

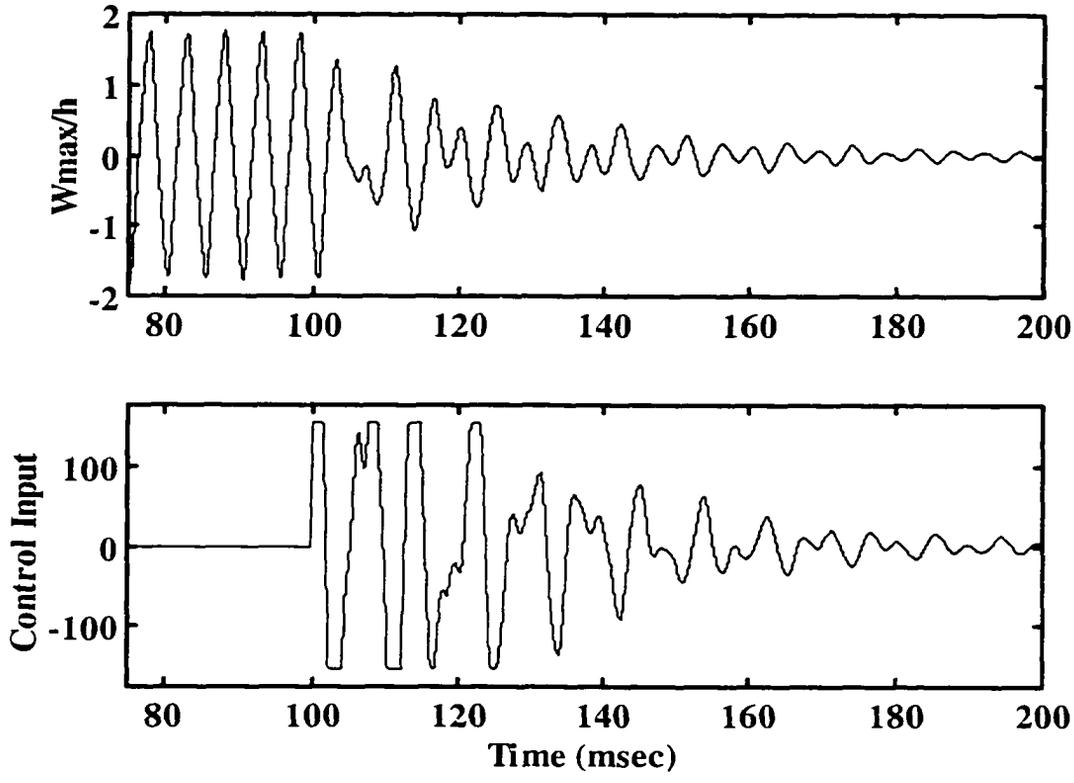

Figure 6.16 Performance of optimal output feedback controller using single leading edge actuator and two displacement sensors at $\lambda max = 1100$

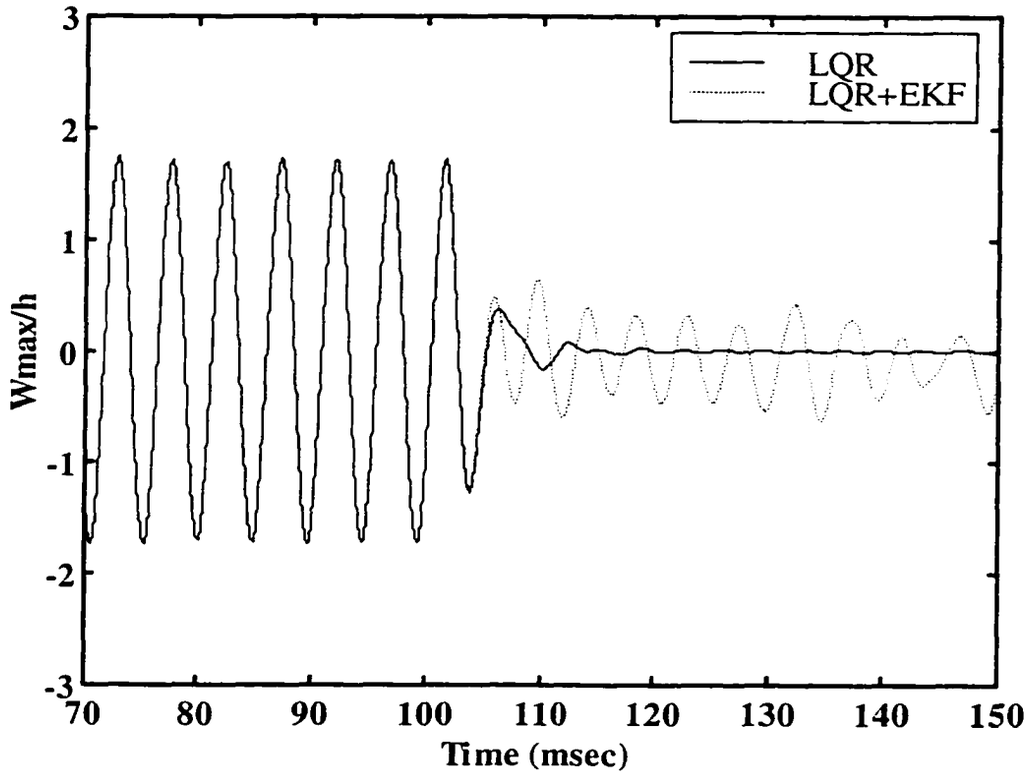

Figure 6.17 Effect of +25% mismatch in λ between design model and simulation model on LQR and LQR+EKF control performance at $\lambda = 1200$

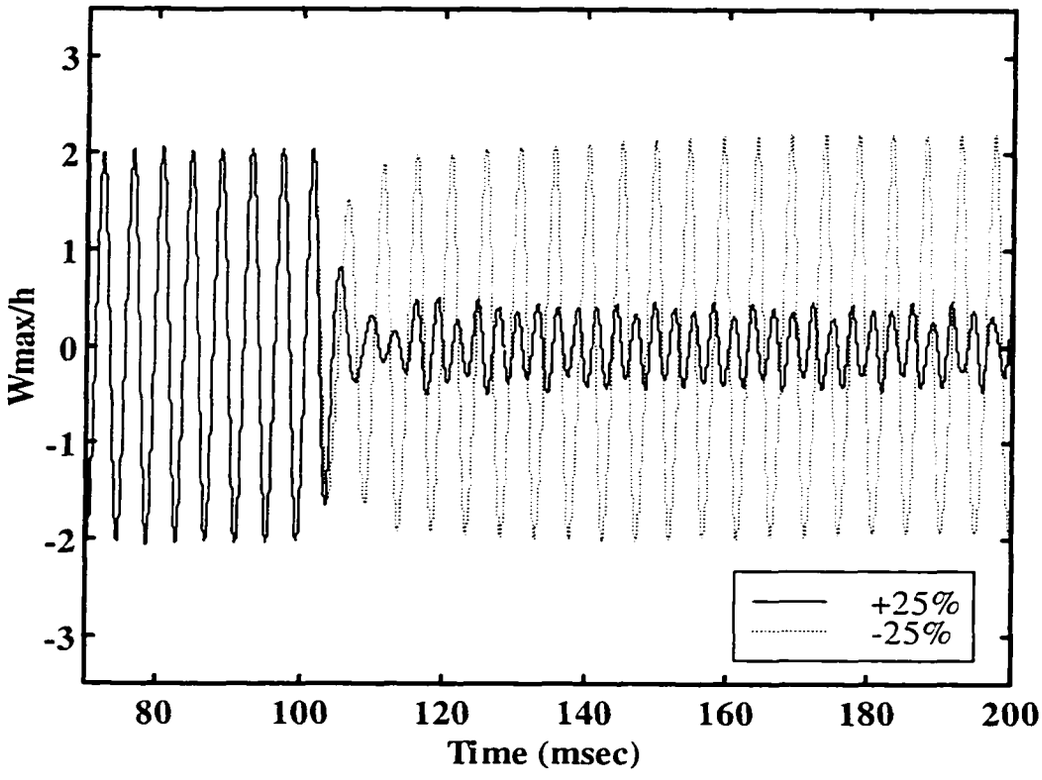

Figure 6.18 Effect of design model linear stiffness variation on
The LQR+EKF controller performance at $\lambda = 1500$

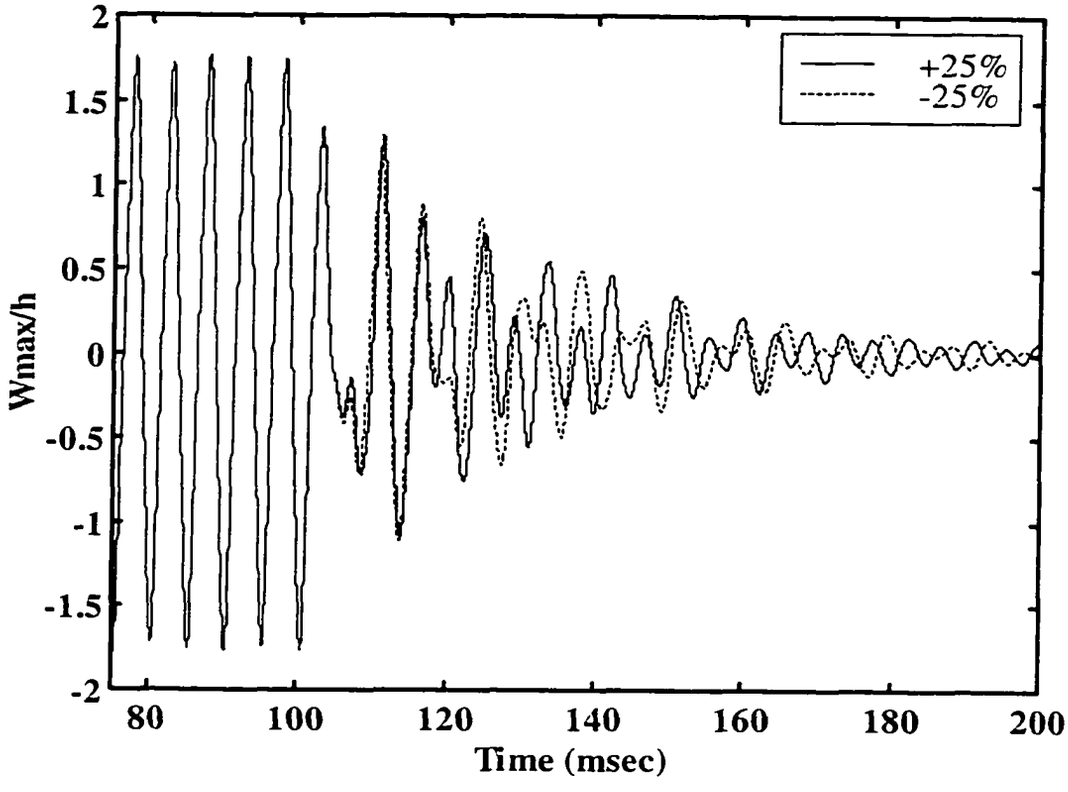

Figure 6.19 Effect of design model linear stiffness variation on optimal output feedback controller performance at $\lambda = 1100$

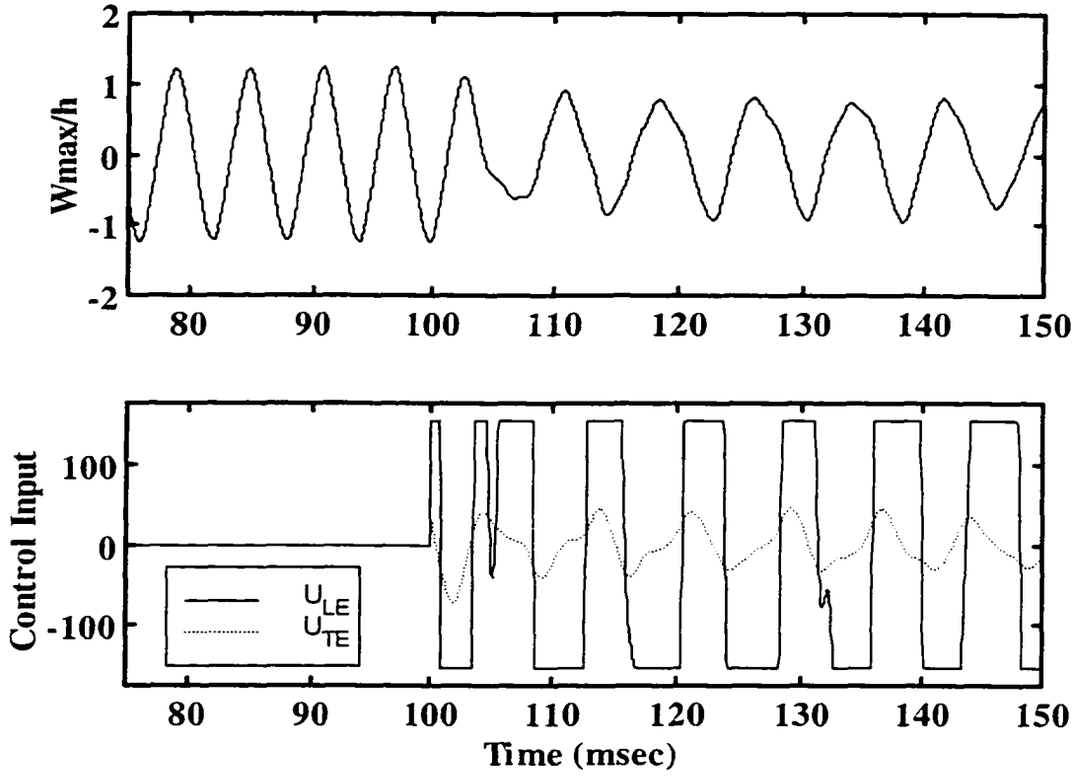

Figure 6.20 Performance of EKF+LQR controller designed for zero flow angle at λ = 800 and 45 deg flow angle

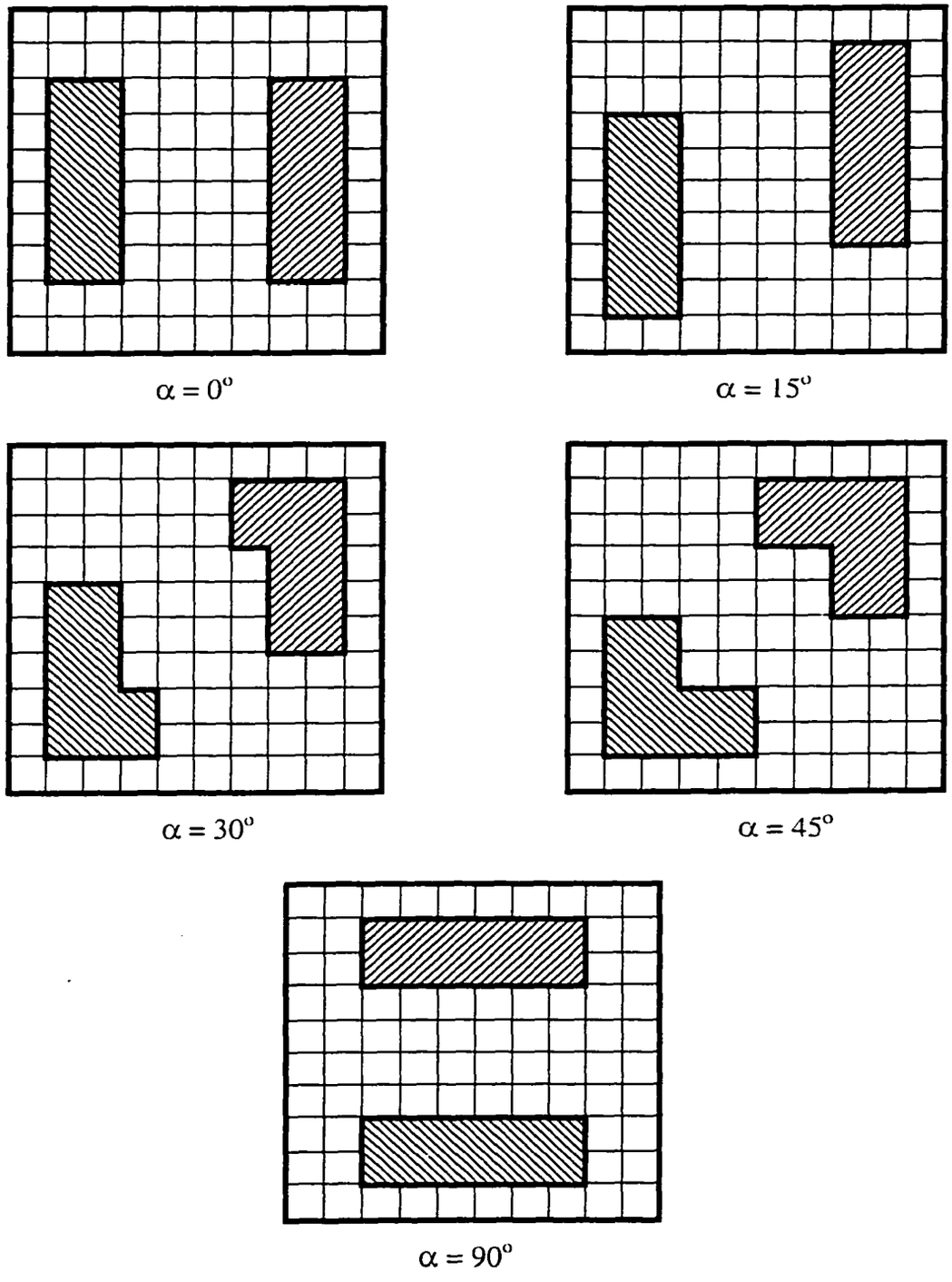

Figure 6.21 Optimal actuator and sensor placement at different flow angles from 0 to 90° for square isotropic panel

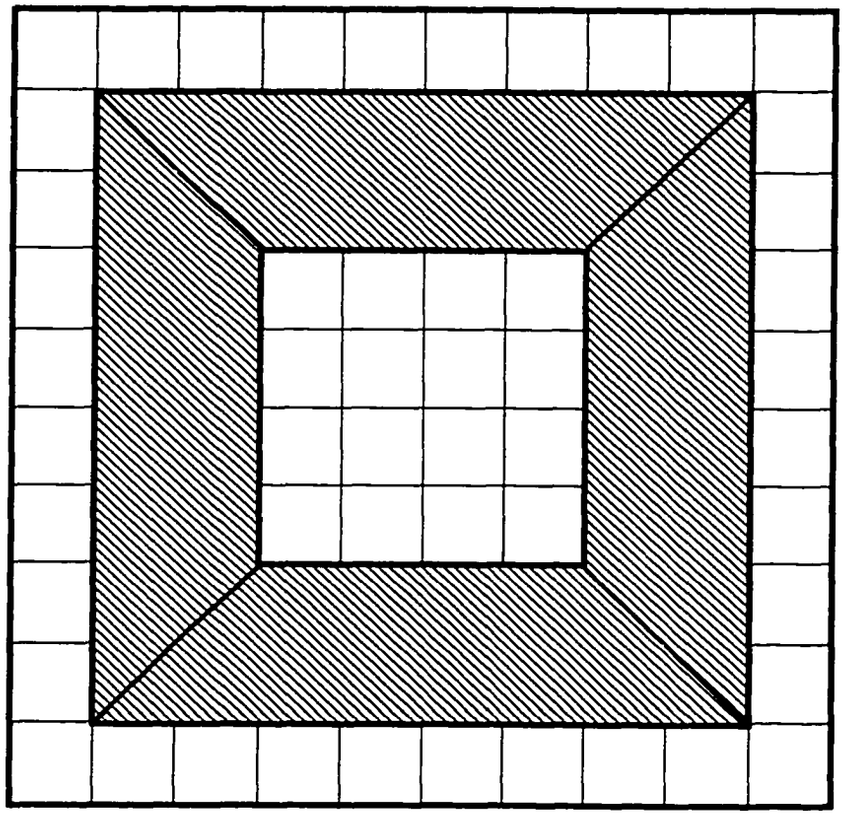

Figure 6.22 Placement of four self-sensing piezoelectric actuators for optimal actuation and optimal sensing over the range of [0, 90°] flow angle for square isotropic panel

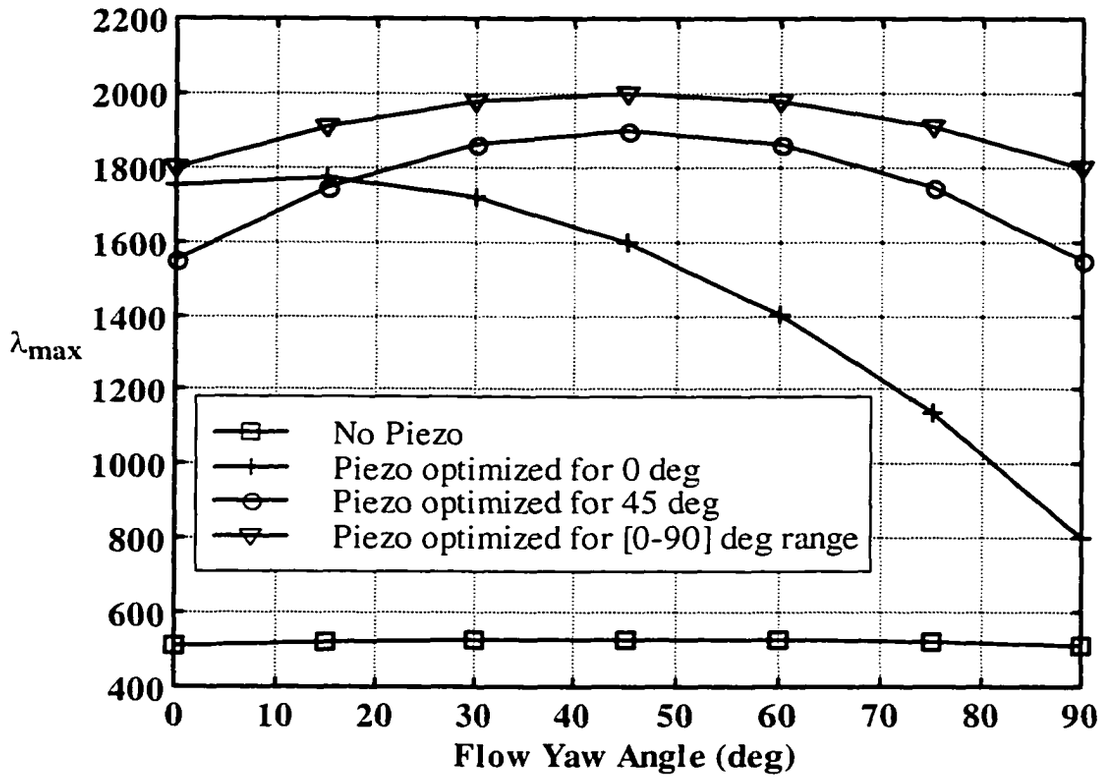

Figure 6.23 Comparison of panel flutter suppression performance using LQR+EKF control at different flow yaw angles and using different piezoelectric placement configurations for a square isotropic panel

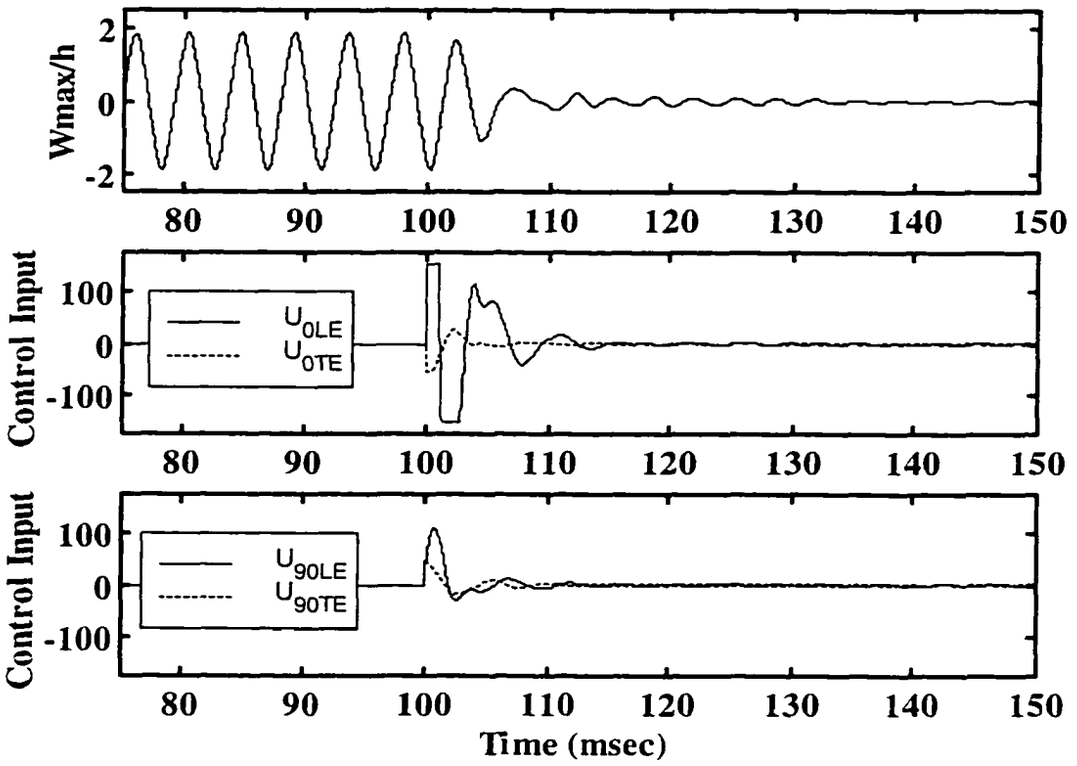

Figure 6.24 Performance of LQR+EKF controller for square isotropic panel with 4 self-sensing piezoelectric actuators at 0^{o} flow yaw angle and $\lambda = 1500$

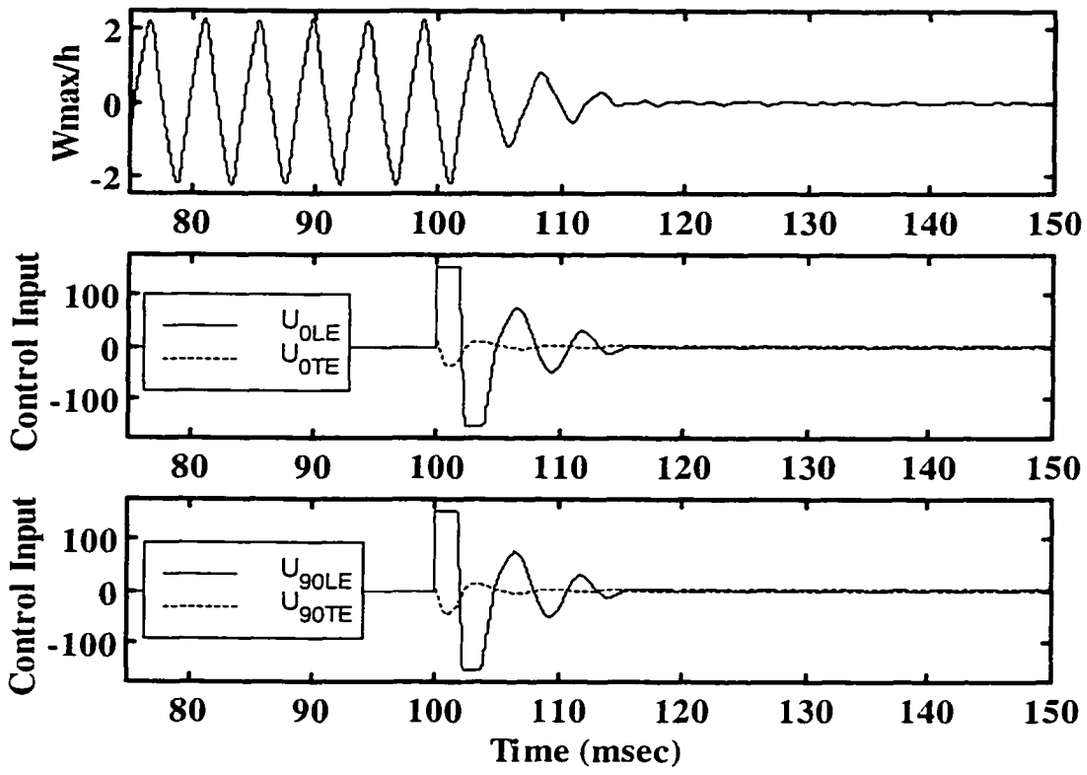

Figure 6.25 Performance of LQR+EKF controller for square isotropic panel with 4 self-sensing piezoelectric actuators at 45° flow yaw angle and $\lambda = 1500$

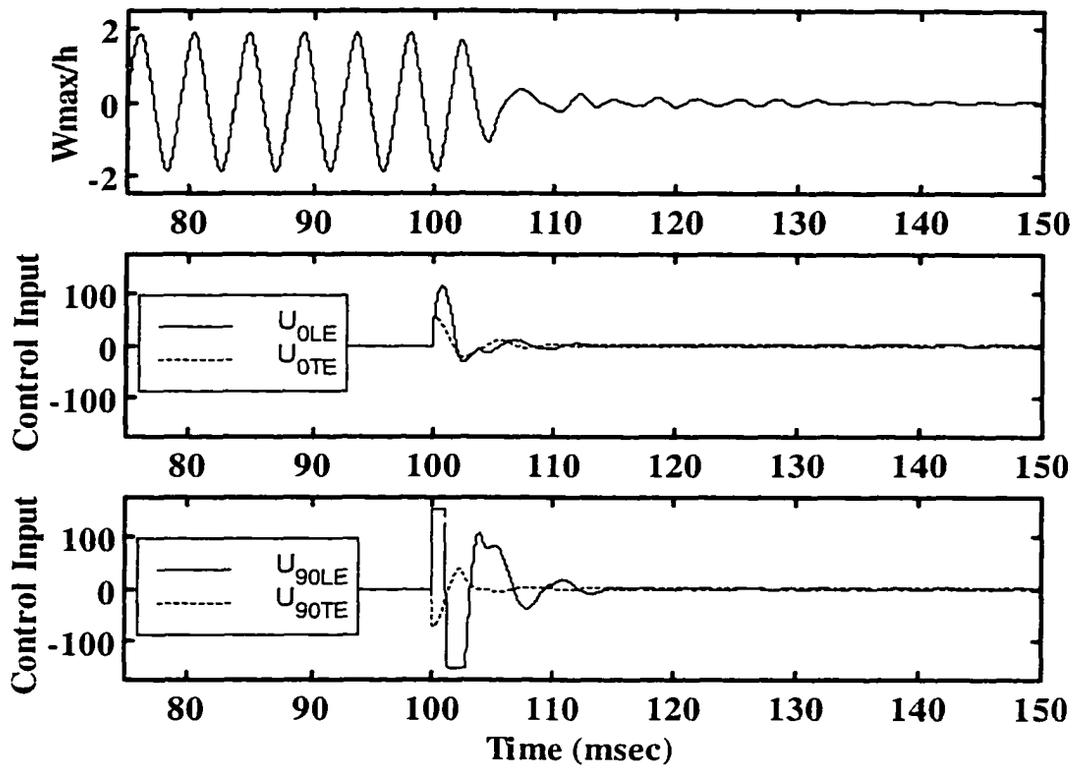

Figure 6.26 Performance of LQR+EKF controller for square isotropic panel with 4 self-sensing piezoelectric actuators at 90° flow yaw angle and λ = 1500

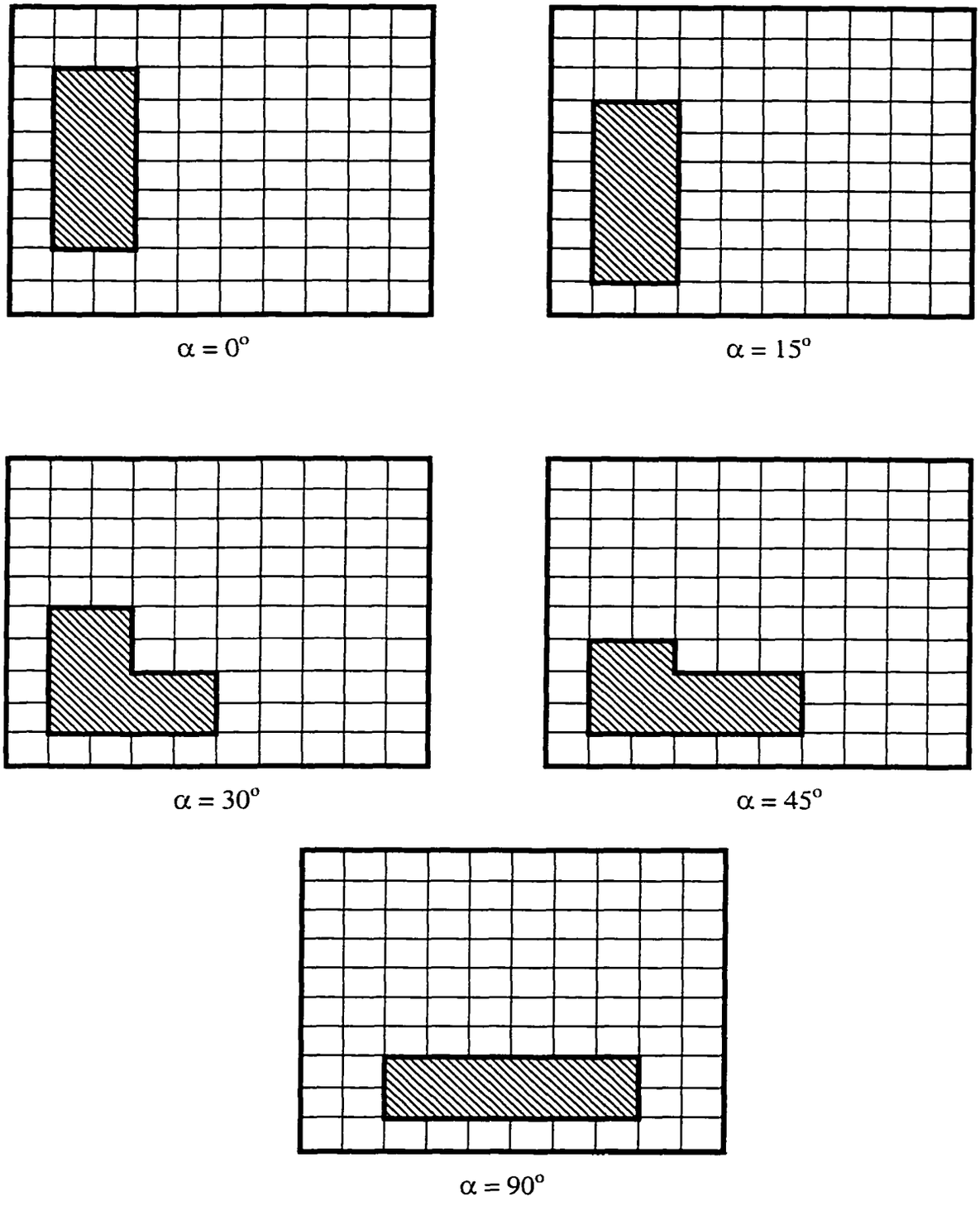

Figure 6.27 Optimal actuator placement at different flow angles for $[0/45/-45/90]_S$ composite rectangular panel

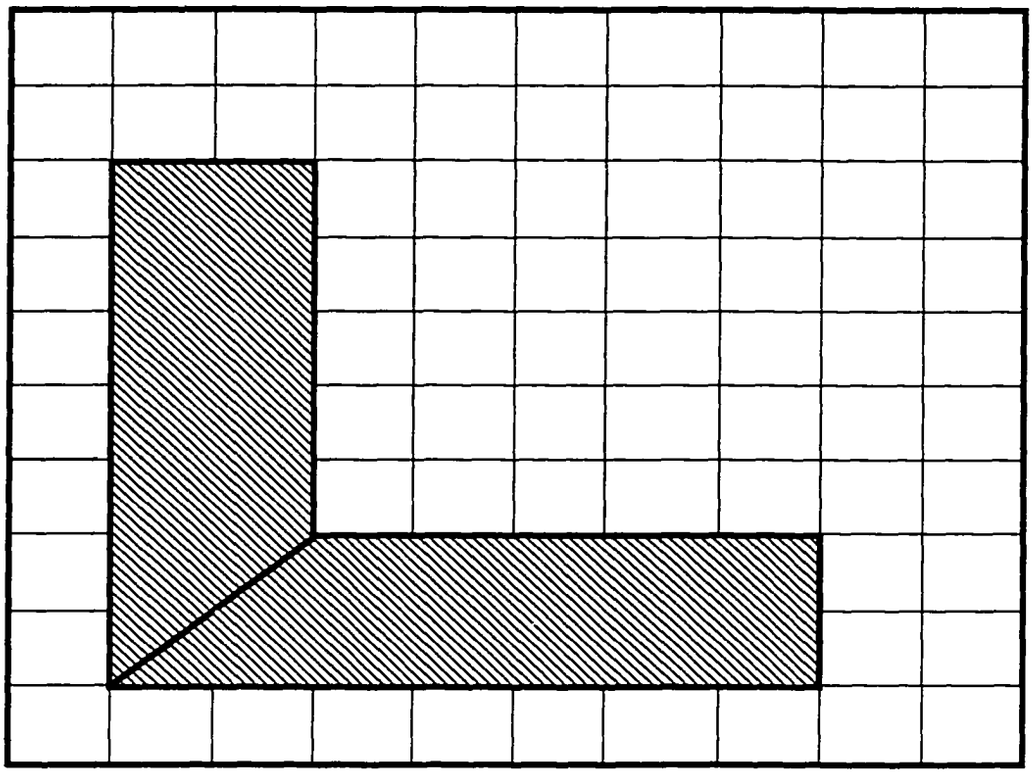

Figure 6.28 Optimal placement of 2 embedded piezoelectric actuators that cover flow angles from 0° to 90° for $[0/45/-45/90]_S$ composite rectangular panel

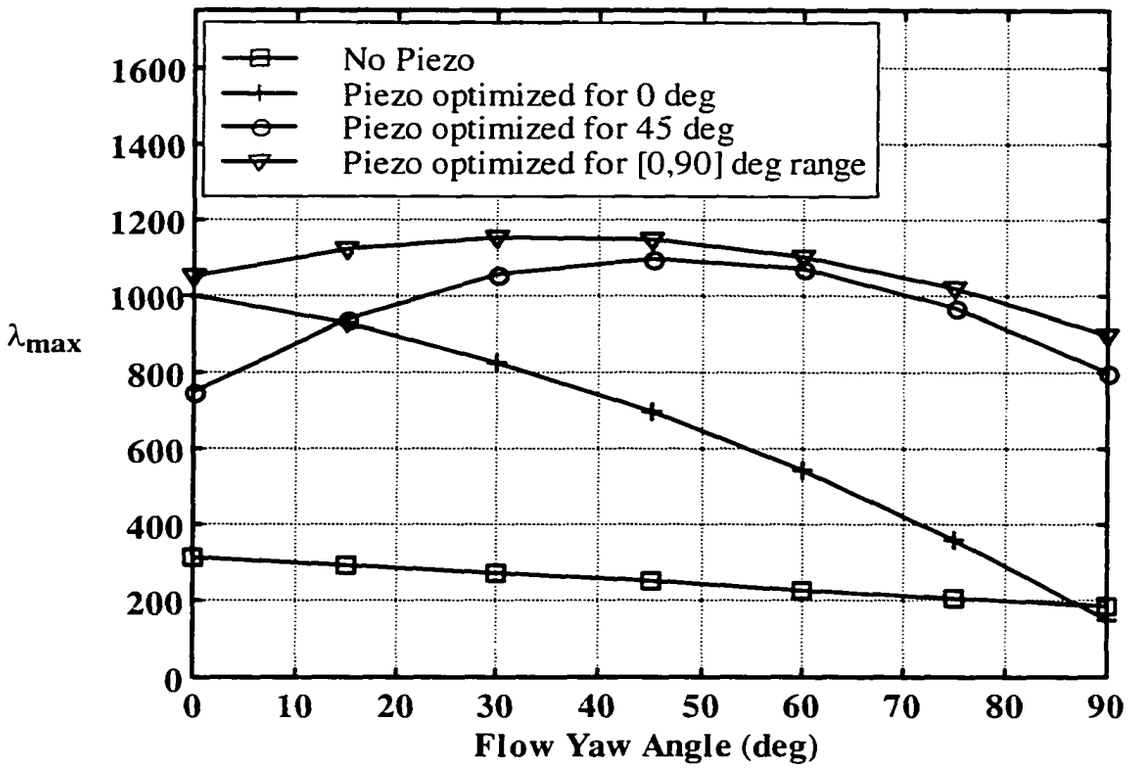

Figure 6.29 Comparison of panel flutter suppression performance using LQR+EKF control at different flow yaw angles and using different piezoelectric actuator configurations for $[0/45/-45/90]_S$ rectangular composite panel

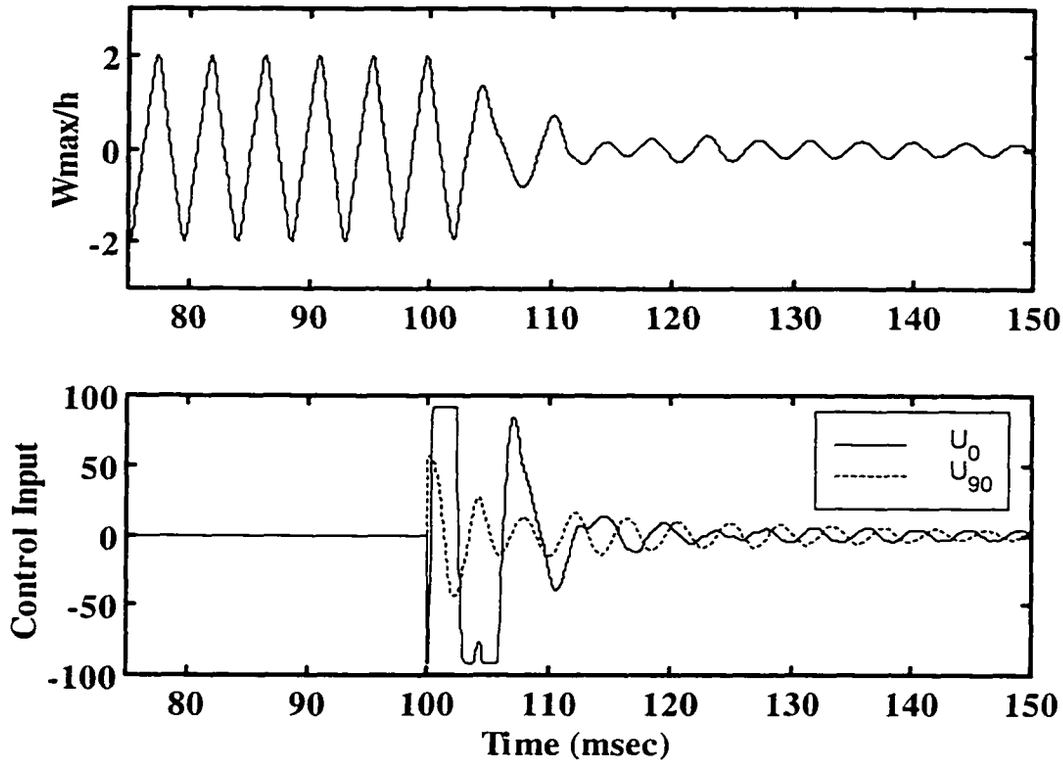

Figure 6.30 Performance of LQR+EKF controller for rectangular composite panel at 0^{o} flow yaw angle and $\lambda = 900$

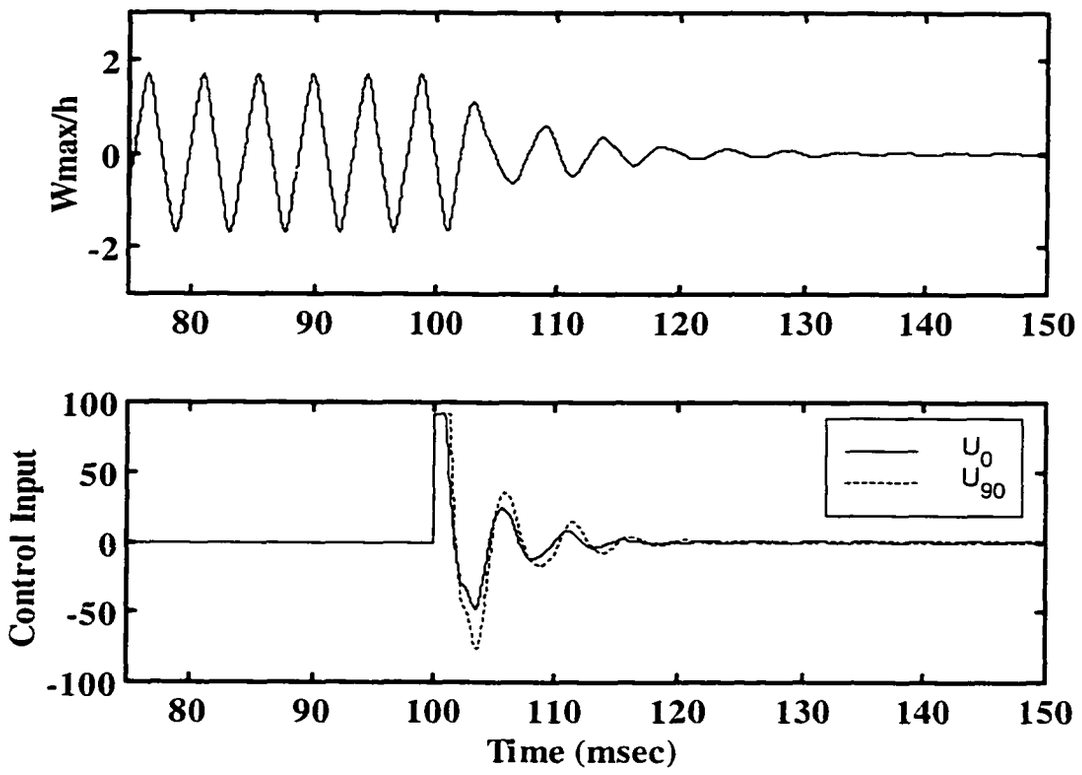

Figure 6.31 Performance of LQR+EKF controller for rectangular composite panel at 45° flow yaw angle and λ = 900

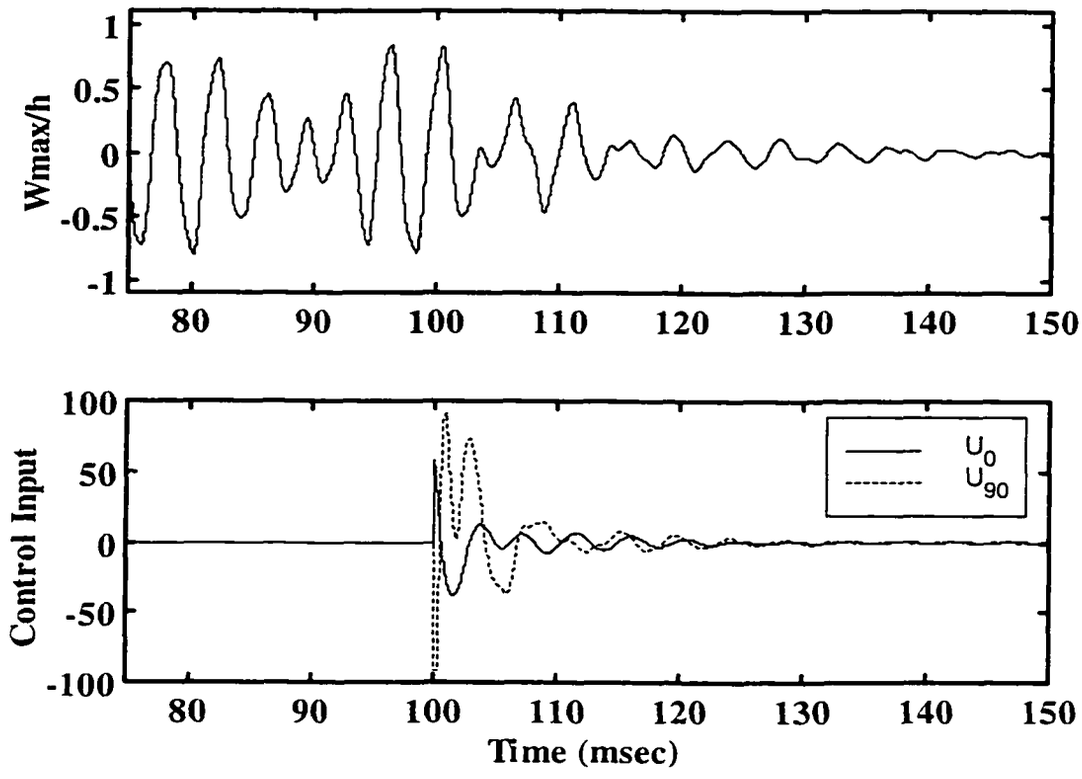

Figure 6.32 Performance of LQR+EKF controller for rectangular composite panel at 90° flow yaw angle and λ = 900

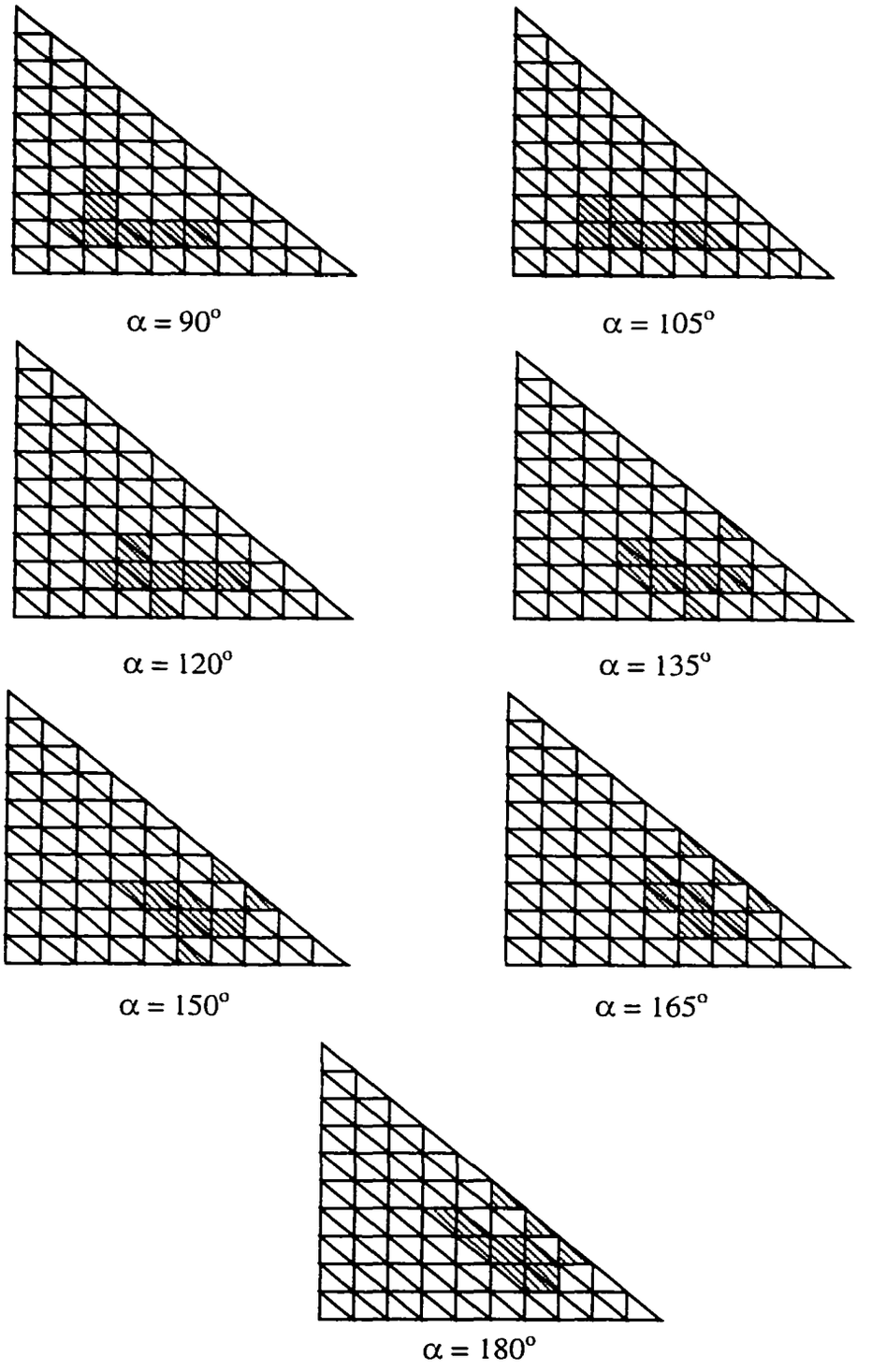

Figure 6.33 Optimal actuator placement at different flow angles for clamped triangular isotropic panel

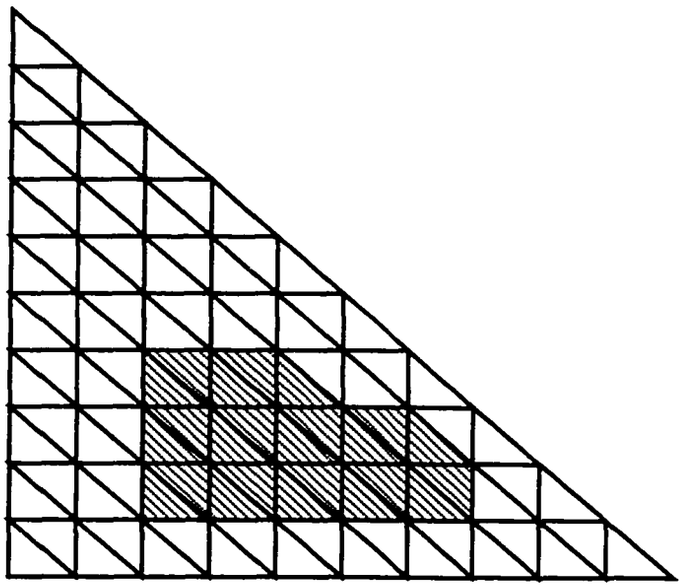

Figure 6.34 Optimal placement of a single self-sensing piezoelectric actuator that approximately cover all angles from 90° to 180° for triangular clamped isotropic panel

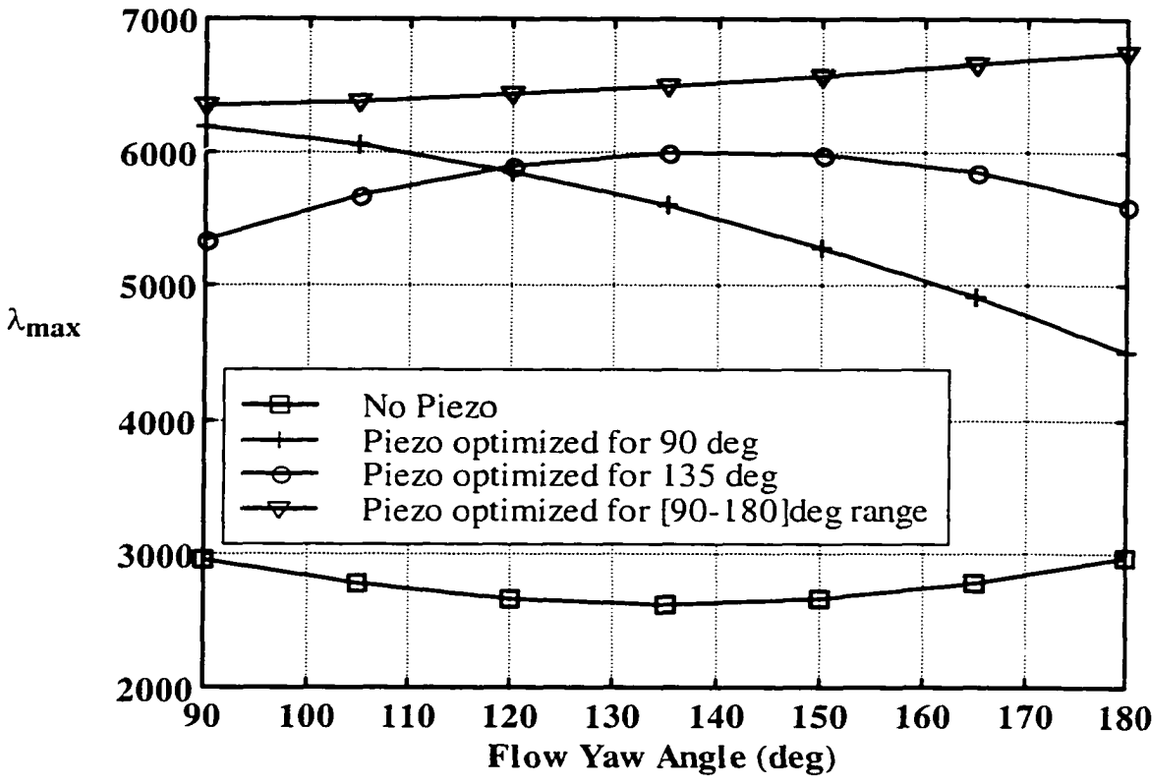

Figure 6.35 Performance of the LQR+EKF controller in suppressing nonlinear panel flutter using different piezoelectric actuator configurations for the clamped triangular isotropic panel

CHAPTER VII

SUMMARY AND CONCLUSIONS

A coupled structural-electrical modal finite element formulation for composite panels, with integrated piezoelectric sensors and actuators, is presented and used to analyze nonlinear supersonic panel flutter considering the effect of airflow yaw angle and the effect of additional high acoustic pressure loading. The finite element formulation is also used for nonlinear panel flutter suppression with yawed airflow using optimal control methods. The first-order shear deformation theory is used for laminated composite panels and the von-Karman nonlinear strain-displacement relations are employed for large deflection response. Structural-electrical coupling is considered using the linear piezoelectricity constitutive relations. The first-order piston theory and simulated Gaussian white noise are employed to model supersonic aerodynamic and acoustic pressures, respectively. The coupled nonlinear equations of motion are derived using the three-node triangular MIN3 plate element with improved transverse shear. Additional electrical DOF per each piezoelectric layer is used to handle piezoelectric sensors and actuators. Thus, the modified MIN3 element is a coupled structural-electrical shear-deformable element for the nonlinear analysis of smart composite structures. The system equations of motion in the structure node DOF are transformed into the modal coordinates using the panel linear vibration modes to obtain a set of nonlinear dynamic modal equations of lesser number. Modal participation is defined and used to determine the number of modes required for accurate solutions. A new and efficient solution procedure is presented using the LUM/LTF approximate method to solve the reduced nonlinear modal equations for nonlinear panel flutter limit-cycle response. The presented solution procedure has the advantage of using much less computational effort than solving the system equations of motion in the structure node DOF.

The presented finite element modal formulation is validated by comparison with other finite element and analytical solutions. Analysis results for the effect of arbitrary flow yaw angle on nonlinear supersonic panel flutter for isotropic and composite panels are presented using the modal LUM/NTF solution method. Results showed that the flow

yaw angle completely changes the shape of the limit-cycle deflection. It also showed that the effect of the yaw angle is a very important parameter especially for composite panels where the flow direction may increase or decrease the nondimensional dynamic pressure at fixed limit-cycle amplitude depending on the panel lamination. The effect of combined supersonic aerodynamic and acoustic pressure loading on the nonlinear dynamic response of isotropic and composite panels is also presented. It is found that for panels at supersonic flow, only acoustic pressure (sonic fatigue) is to be considered for low dynamic pressures ($\lambda << \lambda_{cr}$) and both acoustic and aerodynamic pressures must be considered for significant and high aerodynamic pressures.

Simulation studies for the suppression of nonlinear panel flutter using piezoelectric self-sensing actuators and using different optimal control strategies are presented. The control strategies considered include LQG controller, LQR combined with extended Kalman filter (EKF) for nonlinear systems, and optimal output feedback. The LQG controller performance was found to be much worse than the corresponding LQR controller performance. This is mainly due to the use of linear Kalman filter to estimate the states of nonlinear flutter dynamics. The state estimation is improved by using EKF. The nonlinear dynamic output compensator compromised of LQR control and EKF gives much better performance for nonlinear panel flutter suppression with about 3.5 times increase in the critical dynamic pressure compared to 1.8 times using LQG controller. By using optimal output feedback controller the panel critical dynamic pressure was increased about 2 times which is less than that of EKF+LQR controller. However, the optimal output feedback is much simpler for practical implementation as it does not require the on-line adaptation needed for EKF.

Nonlinear panel flutter suppression with airflow yaw angle is considered using the EKF+LQR controller. Closed loop criteria based on the norm of feedback control gains (NFCG) for actuators and on the norm of Kalman filter estimator gains (NKFEG) for sensors are used to determine the optimal location of self-sensing piezoelectric actuators for different yaw angles. Optimal actuator and sensor location for a range of flow yaw angles is determined by grouping the optimal locations for different angles within the specified range. Using this method with four self-sensing actuators, the critical flutter boundary was increased about 3.5 times over the entire range of yaw angles from 0 to

360° for square isotropic panel. For rectangular graphite/epoxy composite panel with two actuators, the panel critical flutter dynamic pressure is increased to a minimum of 900 over all yaw angles from 0 to 90° compared to 185 for the original uncontrolled panel. Results for a triangular isotropic panel with clamped boundaries showed that the critical flutter dynamic pressure can be increased about 2.5 times for a flow yaw angle range from 90 to 180° using the same methodology with a single piezoelectric actuator.

The main contributions of this research can be summarized as follows:

- Analysis of nonlinear panel flutter of composite panels with yawed supersonic flow using finite element method.
- Analysis of nonlinear composite panels response under combined aerodynamic and high acoustic pressure loading.
- The consideration of state estimation problem for nonlinear panel flutter suppression and the use of nonlinear state estimation based on EKF for improved controller performance.
- Nonlinear flutter suppression of isotropic and composite panels with yawed supersonic flow.

Other minor contributions include, the derivation of coupled structural-electrical nonlinear MIN3 element for composite panels, the modal LUM/NTF solution method, optimal sensor location based on the NKFEG method, and the study of triangular panels.

Future extensions to the current research may include adding thermal load effects, using more rigorous optimization method for optimal piezoelectric sensors and actuator location such as genetic algorithms or gradient methods, and using robust and nonlinear control strategies. In addition, a feasibility study is required to compare the performance of nonlinear panel flutter suppression using piezoelectric actuators and using other types of smart and adaptive structures such as shape memory alloys and active constrained layer damping. Finally, experimental validation is highly desirable to verify the performance of nonlinear panel flutter suppression using the proposed methods.

REFERENCES

1. Dowell, E. H., "Panel flutter: a review of the aeroelastic stability of plates and shells," *AIAA Journal*, Vol. 8, No. 3, 1970, pp. 385-399.
2. Mei, C., Abdel-Motagaly, K., Chen, R., "Review of nonlinear panel flutter at supersonic and hypersonic speeds," *Applied Mechanics Review*, Vol. 52, No 10, 1999, pp. 305-332.
3. Gray, C. E., Jr and Mei, C. "Large amplitude finite element flutter analysis of composite panels in hypersonic flow," *AIAA Journal*, Vol. 31, No. 6, 1993, pp. 1090-1099.
4. Bismarck-Nasr, M. N., "Finite element analysis of aeroelasticity of plates and shells," *Applied Mechanics Review*, Vol. 45, No 12, 1992, pp. 461-482.
5. Zhou, R. C., Xue, D. Y. and Mei, C., "On analysis of nonlinear panel flutter at supersonic speeds," First Industry/Academy Symposium on Research for Future Supersonic and Hypersonic Vehicles, NC A&T State University, Greensboro, NC, 1994, pp. 343-348.
6. Dowell, E. H., *Aeroelasticity of plates and shells*, Noordhoff Int. Pub., Leynden, The Netherlands, 1975.
7. Librescu, L., "Elastostatics and kinetics of anisotropic and heterogeneous shell-type structures," Noordhoff Int. Pub., Leynden, The Netherlands, 1975.
8. Ashley, H. and Zartarian, G., "Piston theory- a new aerodynamic tool for aerolastician," *Journal of Aeronautical Science*, Vol. 23, No. 12, 1956, pp. 1109-1118.
9. Ventres, C. S. and Dowell, E. H., "Comparison of theory and experiment for nonlinear flutter of loaded plates," *AIAA Journal*, Vol. 8, No. 11, 1970, pp. 2022-2030.
10. Dowell, E. H., "Nonlinear oscillations of a fluttering plate II," *AIAA Journal*, Vol. 5, No. 10, 1967, pp. 1856-1862.
11. Gray, C. E. Jr., "Large amplitude finite element flutter analysis of composite panels in hypersonic flow," Ph.D. Thesis, Old Dominion University, Norfolk, VA, 1991.

12. Eisely, J. G., "The flutter of two-dimensional buckled plate with clamped edges in supersonic flow," AFOSR-TN-56-296, 1956.

13. Fung, Y. C., "On two-dimensional panel flutter," *Journal of Aeronautical Science*, Vol. 25, No. 3, 1958, pp. 145-160.

14. Bolotin, V. V., *Nonconservative problems of the theory of elastic stability*, McMillan Co., New York, 1963, 199-312.

15. Dowell, E. H., "Nonlinear oscillations of a fluttering plate I," *AIAA Journal*, Vol. 4, No. 7, 1966, pp. 1267-1275.

16. Ventres, C. S., "Nonlinear flutter of clamped plates," Ph.D. Thesis, Princeton University, Princeton, NJ, 1970.

17. Kobayashi, S., "Flutter of a simply supported rectangular panels in a supersonic flow- two dimensional panel flutter, I simply supported, II clamped panels," *Trans. Japan Soc. of Aeron. and Space Sci.*, Vol. 5, 1962, pp. 79-118.

18. Weiliang, Y. and Dowell, E. H., "Limit-cycle oscillations of a fluttering cantilever plate," *AIAA Journal*, Vol. 29, No. 11, 1991, pp. 1929-1936.

19. Kuo, C. C., Morino, L. and Dungundji, L., "Perturbation and harmonic balance for treating nonlinear panel flutter," *AIAA Journal*, Vol. 10, No. 11, 1972, pp. 1479-1484.

20. Eastep, F. E. and McIntosh, S. C., "The analysis of nonlinear panel flutter and response under random excitation or nonlinear aerodynamic loading," *AIAA Journal*, Vol. 9, No. 3, 1971, pp.411-418.

21. Eslami, H. and Ibrahim, S. R., "Nonlinear flutter of specially orthotropic laminated panels," *Proceedings of the AIAA/ASME/ASCE/AHS/ASC 27th Structure, Structural Dynamics and Materials Conference*, AIAA, San Antonio, TX, 1986, pp. 393-302.

22. Yuen, S. W. and Lau, S. L., "Effects of inplane load on nonlinear panel flutter by incremental harmonic balance method," *AIAA Journal*, Vol. 29, No. 9, 1991, pp. 1472-1479.

23. Morino, L., "A perturbation method for treating nonlinear panel flutter problems," *AIAA Journal*, Vol. 7, No. 3, 1969, pp. 405-410.

24. Morino, L. and Kuo, C. C., Detailed extensions of perturbation methods for nonlinear panel flutter," *ASRL TR-164-2*, MIT, Cambridge, MA, 1971.

25. Smith L. and Morino, L., "Stability analysis of nonlinear differential autonomous systems with applications to flutter," *AIAA Journal*, Vol. 14, No. 3, 1976, pp. 333-341.

26. Olson, M. D., "Finite element approach to panel flutter," *AIAA Journal*, Vol. 5, No. 12, 1967, pp. 226-227.

27. Olson, M. D., "Some flutters solutions using finite element," *AIAA Journal*, Vol. 8, No. 4, 1970, pp. 747-752.

28. Yang, T. Y. and Sung, S. H., "Finite element in three-dimensional supersonic unsteady potential flow," *AIAA Journal*, Vol. 15, No. 12, 1677-1683.

29. Mei, C., " A finite element approach for nonlinear panel flutter," *AIAA Journal*, Vol. 15, No. 8, 1977, pp. 1107-1110.

30. Mei, C. and Rogers, J. L. Jr., "Application of NASTRAN to large deflection supersonic flutter of panels," NASA TM-X-3429, 1976, pp. 67-97.

31. Rao, K. S. and Rao, G. V., "Large amplitude supersonic flutter of panels with ends elastically restrained against rotation," *Int. Journal of Computers and Structures*, Vol. 11, No. 3, 1980, pp. 197-201.

32. Sarma, B. S. and Varadan, T. K., "Nonlinear panel flutter by finite element method," *AIAA Journal*, Vol. 26, No. 5, pp. 566-574.

33. Mei, C. and Weidman, D. J., "Nonlinear panel flutter- a finite element approach," *Computational methods fore Fluid-Structure Interaction Problems*, AMP-Vol. 26, ASME, New York, 1977, pp. 139-165.

34. Mei, C. and Wang, H. C., "Finite element analysis of large amplitude supersonic flutter of panels," *Int. Conf. on Finite Element Methods*, Shanghai, PRC, Gordon and Breach Sci. Pub., Inc., 1982, pp. 944-951.

35. Han, A. D. and Yang, T. Y., "Nonlinear panel flutter using high order triangular finite elements," *AIAA Journal*, Vol. 21, No. 10, 1983, pp. 1453-1461.

36. Dixon, I. R. and Mei, C, "Finite element analysis of large amplitude panel flutter of thin laminates," *AIAA Journal*, Vol. 31, No. 4, 1993, pp. 701-707.

37. Reed, W. H., Hanson, P. W. and Alford, W. J., "Assessment of flutter model testing relating to the National Aerospace Plane," NASP CR 1002, 1987.

38. Xue, D. Y. and Mei, C., "Finite element nonlinear panel flutter with arbitrary temperatures in supersonic flow," *AIAA Journal*, Vol. 31, No. 1, 1993, pp. 154-162.

39. Xue, D. Y., "A finite element frequency domain solution of nonlinear panel flutter with temperature effects and fatigue life analysis," Ph.D. Thesis, Old Dominion University, Norfolk, VA, 1991.

40. Zhou, R. C., Xue, D. Y. and Mei, C., "Finite element time domain modal formulation for nonlinear flutter of composite panels," *AIAA Journal*, Vol. 32, No. 10, 1994, pp. 2044-2052.

41. Kordes, E. E. and Noll, R. B., "Theoretical flutter analysis of flat rectangular panels in uniform coplanar flow with arbitrary direction," NASA TN D-1156, Flight Research Center, Edwards, CA, January 1962.

42. Bohon, H. L., "Flutter of flat rectangular orthotropic panels with biaxial loading and arbitrary flow direction," NASA TN D-1949, Langley Research Center, Hampton, VA, September 1963.

43. Durvasula, S., "Flutter of simply supported, parallelogrammic, flat panels in supersonic flow," *AIAA Journal*, Vol. 5, No. 9, Sept. 1967, pp. 1668-1673.

44. Durvasula, S., "Flutter of clamped panels in supersonic flow," *AIAA Journal*, Vol. 8, 1971, pp. 461-466.

45. Kariappa, V., Somashekar, B. R., and Shah, C. G., "Discrete element approach to flutter of skew panels with in-plane forces under yawed supersonic flow," *AIAA Journal*, Vol. 8, No. 11, Nov. 1970, pp. 2017-20922.

46. Sander, G., Bon, C., Geradin, M., "Finite element analysis of supersonic panel flutter," *International Journal for Numerical Methods in Engineering*, Vol. 7, 1973, pp. 379-394.

47. Shyprykevich, P. and Sawyer, J. W. "Orthotropic panel flutter at arbitrary yaw angles- experiment and correlation with theory," AIAA Paper No. 73-192, Jan. 1973.

48. Sawyer, J. W., "Flutter of elastically supported orthotropic panels including the effects of flow angle," NASA TN D-7491, Langley Research Center, Hampton, VA, May 1974.

49. Friedmann, P. and Hanin, M., "Supersonic nonlinear flutter of orthotropic or isotropic panels with arbitrary flow direction," *Israel Journal of Technology*, Vol. 6 (1-2), 1968, pp. 46-57.

50. Chandiramani, N. K., Plaut, R. H. and Librescu, L., "Nonperiodic flutter of buckled composite panel," *Sadhana Journal*, Vol. 20, No. 2-4, 1995, pp. 671-689.

51. Abdel-Motagaly, K., Chen, R., and Mei, C., "Nonlinear flutter of composite panels under yawed supersonic flow using finite elements," *AIAA Journal*, Vol. 37, No. 9, Sept. 1999, pp. 1025-1032.

52. Tessler, A. and Hughes, T. J. R., "A three-node Mindlin plate element with improved transverse shear," *Computer Methods in Applied Mechanics and Engineering*, Vol. 50, 1985, pp. 71-91.

53. Chen, R., "Finite element nonlinear random response of composite panels of arbitrary shape to acoustic and thermal loads," Ph.D. Dissertation, Old Dominion University, Norfolk, VA, 1995.

54. Gibson, R., *Principles of composite material mechanics*, 1994, McGraw-Hill, Inc.

55. Clarkson, B. L., "Review of sonic fatigue technology," NASA CR-4587, 1994.

56. Wolfe, H. F., Shroyer, C. A., Brown, D. L., and Simmons, L., "An experimental investigation of nonlinear behavior of beams and plates excited to high levels dynamic response," U.S Air Force Research Lab. WL-TR-96-3057, Wright-Patterson AFB, OH, 1995.

57. Rudder, F. F., and Plumblee, H. E., "Sonic fatigue design guide for military aircraft," Air Force Flight Dynamic Lab., AFFDL-TR-74-112, Wright-Patterson AFB, OH, 1975.

58. Holehouse, I., "Sonic fatigue design guide techniques for advanced composite airplane structures," Air Force Wright Aeronautical Labs., AFWAL-TR-80-3019, Wright-Patterson AFB, OH, 1980.

59. Vaicaitis, R., "Time domain approach for nonlinear response and sonic fatigue of NASP thermal protection system," *Proceedings of the AIAA/ASME/ASCE/AHS/ASC 32nd Structures, Structural Dynamics, and Materials Conference*, AIAA, Washington, DC, 1991, pp. 2685-2708.

60. Arnold, R. R., and Vaicaitis, R., "Nonlinear response and fatigue of surface panels by time domain Monte Carlo approach," U.S. Air Force Wright Research and Development Center, WRDC-TR-90-3081, Wright-Patterson AFB, OH, 1992.

61. Vaicaitis, R., and Kavallieratos, P. A., "Nonlinear response of composite panels to random excitation," *Proceedings of the AIAA/ASME/ASCE/AHS/ASC 34th Structures, Structural Dynamics, and Materials Conference*, AIAA, Washington, DC, 1993, pp. 1041-1049.

62. Bolotin, V., V., *Random vibration of elastic systems*, Martinus-Nijhoff, Dordrecht, The Netherlands, 1984, pp. 290-292, 314-316.

63. Chiang, C. K., " A finite element large deflection multiple-mode random response analysis of complex panel with initial stresses subjected to acoustic loading," Ph.D. Thesis, Old Dominion University, Norfolk, VA, 1983.

64. Abdel-Motagaly, K., Duan, B., and Mei, C., "Nonlinear response of composite panels under combined acoustic excitation and aerodynamic pressure," *AIAA Journal*, Vol.38, No.9, 2000, pp. 1534-1542.

65. Rao, S. S., and Sunar, M., " Piezoelectricity and its use in disturbance sensing and control of flexible structures: A survey," *Applied Mechanics Review*, Vol. 47, No 4, 1994, pp. 113-123.

66. Crawley, E. F., "Intelligent structures for aerospace: A technology overview and assessment," *AIAA Journal*, Vol. 32. No. 8, August 1994, pp. 1689-1699.

67. Lee, C. K., "Theory of laminated piezoelectric plates for the design of distributed sensors/actuators. Part I: Governing equations and reciprocal relationships," *Journal of Acoustical Society of America*, Vol. 87, No. 3, March 1999, pp. 1144-1158.

68. Hagood, N. W., Chung, W. H., and Flotow, A. V., "Modelling of piezoelectric actuator dynamics for active control," *Journal of Intelligent Material Systems, and Structures*, Vol. 1, July 1990, pp. 327-354.

69. Tzou, H. S., *Piezoelectric Shells: Distributed sensing and control of continua*, Kluwer Academic Press, Netherlands, 1993.

70. Allik, H., and Hughes, T. Jr., "Finite element methods for piezoelectric vibration," *International Journal for Numerical Methods in Engineering*, Vol. 2, 1970, pp. 151-157.

71. Tzou, H. S., and Tseng, C. I., "Distributed modal identification and vibration control of continua: Piezoelectric finite element formulation and analysis," *Journal of Dynamic Systems, Measurement, and Control*, Vol. 113, Sept. 1991, pp.500-505.

72. Ha, S. K., Keilers, C., and Chang, F., "Finite element analysis of composite structures containing distributed sensors and actuators," *AIAA Journal*, Vol. 30, No. 3, 1992, pp. 772-780.

73. Hwang, W., and Park, H. C., "Finite element modeling of piezoelectric sensors and actuators," *AIAA Journal*, Vol. 31, No. 5, 1993, pp. 930-937.

74. Zhou, R. C., "Finite element analysis for nonlinear flutter suppression of composite panels at elevated temperatures using piezoelectric material," Ph.D. Thesis, Old Dominion University, Norfolk, VA, 1994.

75. Liu, G. R., Peng, X. Q., and Lam, K. Y., "Vibration control simulation of laminated composite plates with integrated piezoelectrics," *Journal of Sound and Vibration*, Vol. 220, No. 5, 1999, pp. 927-847.

76. Suleman, A., and Venkayya, V. B., "A simple finite element formulation for laminated composite plate with piezoelectric layers," *Journal of Intelligent Material Systems and Structures*, Vol. 6, Nov. 1995, pp.776-782.

77. Detwiler, D. T., Shen, M. H., Venkayya, V. B., "Finite element analysis of laminated composite structures containing distributed piezoelectric actuators and sensors," *Finite Elements in Analysis and Design* Vol. 20, 1995, pp. 87-100.

78. Sze, K. Y., and Yao, L. Q., "Modelling smart structures with segmented piezoelectric sensors and actuators," *Journal of Sound and Vibration*, Vol. 235, No. 3, 2000, pp. 495-520.

79. Bevan, J. S., "Piezoceramic actuator placement for acoustic control of panels," Ph.D. Thesis, Old Dominion university, Norfolk, VA, 2000.

80. Dosch, J. J., Inman, D. J., and Garcia, E., "A self-sensing piezoelectric actuator for collocated control," *Journal of Intelligent Material Systems, and Structures*, Vol. 3, Jan. 1992, pp. 166-185.

81. Anderson. E. H., and Hagood, N. W., "Simultaneous piezoelectric sensing/actuation: Analysis and application to controlled structures," *Journal of Sound and Vibration*, Vol. 174, No. 5, 1994, pp. 617-639.

82. Bent, A. A., and Hagood, N. W., "Improved performance in piezoelectric fiber composites using interdigitated electrodes," *Proceedings SPIE, Symposium on Smart Structures and Materials*, Vol. 2441, San Diego, CA, Feb. 1995, pp. 196-212.

83. Wilkie, W. K., Bryant, R. G., High, J. W., Fox, R. L., Hellbaum, R. F., Jalink, Jr. A., Little, B. D. and Mirick, P. H., "Low-Cost Piezocomposite Actuator for Structural Control Applications," *Proceeding SPIE, 7th International Symposium on Smart Structures and Materials*, Newport Beach, CA, Vol. 3991, March 2000, pp. 323-334.

84. Morgan-Matroc, Inc., *Guide to modern piezoelectric ceramics*, Electric Ceramics Division, Bedford, OH, 1993.

85. Maghami, P. G., and Joshi, S. M., "Sensor-actuator placement for flexible structures with actuator dynamics," *Journal of Guidance, Control, and Dynamics*, Vol. 16, No.2, 1993.

86. Lim, K. B., Lake, R. C., and Heeg, J., "Effective piezoceramic actuator placement for an experimental flexible wing," AIAA 96-3758, 35th Aerospace Science Meeting and Exhibit, Jan. 1997, Reno, NV.

87. Devasia, S, Meressi, T., Paden, B., and Bayo, E., "Piezoelectric actuator design for vibration suppression: Placement and sizing," *Journal of Guidance, Control, and Dynamics*, Vol. 16, No.5, 1993.

88. Yang, S. M., and Lee, Y. J., "Vibration suppression with optimal sensor/actuator location and feedback gain," *Smart Mater. Struct.*, Vol. 2, 1993.

89. Wang, B., Burdisso, R. A., and Fuller, C. R., "Optimal placement of piezoelectric actuators for active acoustic control," *Journal of Intelligent Material systems and structures*, Vol. 5, Jan. 1994, pp. 67-77.

90. Nam, C., Kim, Y., and Weisshaar, T. A., "Optimal sizing and placement of piezo-actuators for active flutter suppression," *Smart Mater. Struct.*, Vol. 5, 1996.

91. Kang, Y. K, Park, H. C., Hwang, W., and Han, K. S., "Optimum placement of piezoelectric sensor/actuator for vibration control of laminated beams," *AIAA Journal*, Vol. 34, No. 9, 1996.

92. Chattopadhyay, A., and Seeley, C. E., "A multiobjective design optimization procedure for control of structures using piezoelectric materials," *Journal of Intelligent Material systems and structures*, Vol. 5, May 1994, pp. 403-411.

93. Scott, R. C. and Weisshaar, T. A., "Controlling panel flutter using adaptive materials," *Proceeding of the AIAA/ASME/ASCE/AHS/ASC 32nd Structure, Structural Dynamics and Materials Conference*, Baltimore, MD, 1991, pp. 2218-2229. Also *Journal of Aircraft*, Vol. 31, No. 1, 1994, pp. 213-222.

94. Hajela, P. and Glowasky, R., "Application of piezoelectric elements in supersonic panel flutter suppression," AIAA paper 91-3191, Sept. 1991.

95. Suleman, A. and Goncalves, M. A., "Optimization issues in applications of piezoelectric actuators in panel flutter control," *Proceedings of the SPIE - The international Society for Optical Engineering*, Vol. 3039, 1997, pp. 335-347.

96. Suleman, A., "Adaptive composites modelling and application in panel flutter and noise suppression," *Computers and Structures*, Vol. 76, 2000, pp. 365-378.

97. Surace, G., Ruotolo, R., and DI Terlizzi, D., "Active control laws for panel exposed to supersonic air flow," *Proceedings of the 14th International Modal Analysis Conference*, Dearborn, Michigan, Feb. 1996, pp. 285-291.

98. Frampton, K. D., Clark, R. L.and Dowell, E. H., "Active control of panel flutter with piezoelectric transducers," *Journal of Aircraft*, Vol. 33, No. 4, 1996, pp.768-774.

99. Abou-Amer, S., "Control of panel flutter at high supersonic speed," Ph.D. Thesis, Illinois Institute of Technology, Chicago, IL, 1991.

100. Lai, Z., "Vibration control with piezoelectric actuation applied to nonlinear panel flutter suppression," Ph.D. Thesis, Old Dominion University, Norfolk, VA, 1994.

101. Lai, Z., Xue, D. Y., Huang, J. K. and Mei, C., "Nonlinear panel flutter suppression with piezoelectric actuation," *Journal of Intelligent Material Systems and Structures*, Vol. 6, No. 2, 1995, pp. 274-282.

102. Lai, Z., Huang, J., and Mei, C., "Shape and placement of piezoelectric sensors for panel flutter limit-cycle suppression," *AIAA Journal*, Vol. 34, No. 4, 1996, pp. 855-857.

103. Zhou, R. C., Lai, Z., Xue, D. Y., Haung, J. K. and Mei, C., "Suppression of nonlinear panel flutter with piezoelectric actuators using finite element methods," *AIAA Journal*, Vol. 33, No. 6, 1995, pp. 1098-1105.

104. Zhou, R. C., Mei, C. and Haung, J. K.," Suppression of nonlinear panel flutter at supersonic speeds and elevated temperatures," *AIAA Journal*, Vol. 34, No. 2, 1996, pp. 347-354.

105. Dongi, F., Dinkler, D. and Kroplin, B., "Active panel flutter suppression using self-sensing piezoactuators," *AIAA Journal*, Vol. 34, No. 6, 1996, pp. 1224-1230.

106. Ho, M. T., Chen, R. and Chu, L. C., "Wind-tunnel testing of panel flutter control using piezoelectric actuation and iterative gain tuning," *SPIE Conf. Smart Struct and Matls*, 1997, pp. 564-577.

107. Kim, S. J., and Moon, S. H., "Comparison of active and passive suppression of nonlinear panel flutter using finite element method," *Proceeding of the AIAA/ASME/ASCE/AHS/ASC 41st Structure, Structural Dynamics and Materials Conference*, Atlanta, GA, 2000, pp. 691-699.

108. Lewis, F. L., and Syrmos, V. L., *Optimal control*, 2nd Edition, John Wiley and Sons, Inc., 1995.

109. Brown, R. G., and Hwang, P. Y.C., Introduction to random signals and applied Kalman filtering, 3rd Edition, John Wiley and Sons, Inc., 1997.

110. Azemi, A., and Yaz, E. E., "Comparative study of several nonlinear stochastic estimators," *Proceedings of the 38th IEEE Conference on Decision and Control*, Phoenix, AZ, Dec. 1999, pp. 4549-4554.

111. Mracek, C. P., Cloutier, J. R., and D'Souza, C. A., "A new technique for nonlinear estimation," *Proceedings of the 1996 IEEE international Conference Control Applications*, Dearborn, MI, Sept. 1996, pp. 338-343

112. Ewing, C. M., "An analysis of the state dependent Riccati equation method nonlinear estimation technique," *Proceedings of the AIAA Guidance, Navigation, and Control Conference and Exhibit*, Denver, CO, August 2000, pp. 1093-1103,

113. Santos, A., and Bitmead, R. R., Nonlinear control for an autonomous underwater vehicle (AUV) preserving linear design capabilities," *Proceedings of the 34th IEEE Conference on Decision and Control*, New Orleans, LA, Dec. 1995, pp. 3817-3822.

APPENDIX A

MIN3 ELEMENT STRAIN INTERPOLATION MATRICES

Expressions for the strain interpolation matrices as function of element geometry and element area coordinates are given in this Appendix for the MIN3 triangular element.

$$\begin{Bmatrix}\xi_1\\ \xi_2\\ \xi_3\end{Bmatrix}=\frac{1}{2A}\begin{bmatrix}x_2y_3-x_3y_2 & y_2-y_3 & x_3-x_2\\ x_3y_1-x_1y_3 & y_3-y_1 & x_1-x_3\\ x_1y_2-x_2y_1 & y_1-y_2 & x_2-x_1\end{bmatrix}\begin{Bmatrix}1\\ x\\ y\end{Bmatrix} \tag{A.1}$$

$$\begin{aligned}x_{ij}&=x_i-x_j\\ y_{ij}&=y_i-y_j\end{aligned} \tag{A.2}$$

$$[C_m]=\frac{1}{2A}\begin{bmatrix}y_{23} & y_{13} & y_{12} & 0 & 0 & 0\\ 0 & 0 & 0 & x_{32} & x_{13} & x_{21}\\ x_{32} & x_{13} & x_{21} & y_{23} & y_{13} & y_{12}\end{bmatrix} \tag{A.3}$$

$$[C_{\psi b}]=\frac{1}{2A}\begin{bmatrix}y_{23} & y_{31} & y_{12}\\ x_{32} & x_{13} & x_{21}\end{bmatrix} \tag{A.4}$$

$$[C_b]=\frac{1}{2A}\begin{bmatrix}0 & 0 & 0 & y_{23} & y_{13} & y_{12}\\ x_{32} & x_{13} & x_{21} & 0 & 0 & 0\\ y_{23} & y_{31} & y_{12} & x_{32} & x_{13} & x_{21}\end{bmatrix} \tag{A.5}$$

$$[C_{\psi\psi}]=\frac{1}{2A}\begin{bmatrix}C_{11} & C_{12} & C_{13} & C_{14} & C_{15} & C_{16}\\ C_{21} & C_{22} & C_{23} & C_{24} & C_{25} & C_{26}\end{bmatrix} \tag{A.6}$$

$$[C_{\gamma b}]=\frac{1}{2A}\begin{bmatrix}x_{32} & x_{13} & x_{21}\\ y_{23} & y_{31} & y_{12}\end{bmatrix} \tag{A.7}$$

$$[C_{\gamma\psi}]=\frac{1}{2A}\begin{bmatrix}C_{21}+\xi_1 & C_{22}+\xi_2 & C_{23}+\xi_3 & C_{24} & C_{25} & C_{26}\\ C_{11} & C_{12} & C_{13} & C_{14}+\xi_1 & C_{15}+\xi_2 & C_{16}+\xi_3\end{bmatrix} \tag{A.8}$$

where

$$C_{11}=0.5(y_{12}\xi_2-y_{31}\xi_3)y_{23}$$

$$C_{12}=0.5(y_{23}\xi_3-y_{12}\xi_1)y_{31}$$

$$C_{13} = 0.5(y_{31}\xi_1 - y_{23}\xi_2)y_{12}$$

$$C_{14} = 0.5(x_{13}\xi_3 - x_{21}\xi_2)y_{23} - 0.5x_{21}\xi_1 y_{31} + 0.5x_{13}\xi_1 y_{12}$$

$$C_{15} = 0.5(x_{21}\xi_1 - x_{32}\xi_3)y_{31} - 0.5x_{32}\xi_2 y_{12} + 0.5x_{21}\xi_2 y_{23}$$

$$C_{16} = 0.5(x_{32}\xi_2 - x_{31}\xi_1)y_{12} - 0.5x_{13}\xi_3 y_{23} + 0.5x_{32}\xi_3 y_{31}$$

$$C_{21} = 0.5(y_{12}\xi_2 - y_{31}\xi_3)x_{32} - 0.5x_{21}\xi_1 y_{31} + 0.5x_{13}\xi_1 y_{12}$$

$$C_{22} = 0.5(y_{23}\xi_3 - y_{12}\xi_1)x_{13} - 0.5x_{32}\xi_2 y_{12} + 0.5x_{21}\xi_2 y_{23}$$

$$C_{23} = 0.5(y_{31}\xi_1 - y_{23}\xi_2)x_{21} - 0.5x_{13}\xi_3 y_{23} + 0.5x_{32}\xi_3 y_{31}$$

$$C_{24} = 0.5(x_{13}\xi_3 - x_{21}\xi_2)x_{32}$$

$$C_{25} = 0.5(x_{21}\xi_1 - x_{32}\xi_3)x_{13}$$

$$C_{26} = 0.5(x_{31}\xi_2 - x_{13}\xi_1)x_{21}$$

APPENDIX B

COORDINATE TRANSFORMATION

B.1 Transformation of Lamina Stiffness Matrices

For a composite orthotropic lamina (see Figure B.1), the reduced lamina stiffness matrix, $[Q]$, and shear stiffness matrix, $[Q_S]$, relate the lamina stress and strain in the lamina material coordinate system (123 axes) as follows:

$$\begin{Bmatrix}\sigma_1\\ \sigma_2\\ \tau_{12}\end{Bmatrix}=\begin{bmatrix}Q_{11} & Q_{12} & 0\\ Q_{12} & Q_{22} & 0\\ 0 & 0 & Q_{66}\end{bmatrix}\begin{Bmatrix}\varepsilon_1\\ \varepsilon_2\\ \gamma_{12}\end{Bmatrix},\quad \begin{Bmatrix}\tau_{23}\\ \tau_{13}\end{Bmatrix}=\begin{bmatrix}Q_{44} & 0\\ 0 & Q_{55}\end{bmatrix}\begin{Bmatrix}\gamma_{23}\\ \gamma_{13}\end{Bmatrix} \tag{B.1}$$

These matrices are function of the material engineering constants:

$$Q_{11}=\frac{E_1}{1-\nu_{12}\nu_{21}},\qquad Q_{12}=\frac{\nu_{12}E_2}{1-\nu_{12}\nu_{21}},\qquad Q_{22}=\frac{E_2}{1-\nu_{12}\nu_{21}},$$

$$Q_{66}=G_{12},\qquad Q_{66}=G_{23},\qquad Q_{66}=G_{13} \tag{B.2}$$

The transformed stiffness and shear matrix for a general lamina with lamination angle θ can be expressed in the laminate global coordinate axes (xyz) by using the following stress and strain transformation:

$$\begin{Bmatrix}\sigma_1\\ \sigma_2\\ \tau_{12}\end{Bmatrix}=\begin{bmatrix}C^2 & S^2 & 2CS\\ S^2 & C^2 & -2CS\\ -CS & CS & C^2-S^2\end{bmatrix}\begin{Bmatrix}\sigma_x\\ \sigma_y\\ \tau_{xy}\end{Bmatrix}=[T_\sigma]\begin{Bmatrix}\sigma_x\\ \sigma_y\\ \tau_{xy}\end{Bmatrix} \tag{B.3}$$

$$\begin{Bmatrix}\varepsilon_1\\ \varepsilon_2\\ \gamma_{12}\end{Bmatrix}=\begin{bmatrix}C^2 & S^2 & CS\\ S^2 & C^2 & -CS\\ -2CS & 2CS & C^2-S^2\end{bmatrix}\begin{Bmatrix}\varepsilon_x\\ \varepsilon_y\\ \gamma_{xy}\end{Bmatrix}=[T_\varepsilon]\begin{Bmatrix}\varepsilon_x\\ \varepsilon_y\\ \gamma_{xy}\end{Bmatrix} \tag{B.4}$$

$$\begin{Bmatrix}\tau_{23}\\ \tau_{13}\end{Bmatrix}=\begin{bmatrix}C & -S\\ S & C\end{bmatrix}\begin{Bmatrix}\tau_{yz}\\ \tau_{xz}\end{Bmatrix}=[T_S]\begin{Bmatrix}\tau_{yz}\\ \tau_{xz}\end{Bmatrix} \tag{B.5}$$

$$\begin{Bmatrix}\gamma_{23}\\ \gamma_{13}\end{Bmatrix}=\begin{bmatrix}C & -S\\ S & C\end{bmatrix}\begin{Bmatrix}\gamma_{yz}\\ \gamma_{xz}\end{Bmatrix}=[T_S]\begin{Bmatrix}\gamma_{yz}\\ \gamma_{xz}\end{Bmatrix} \tag{B.6}$$

where $C = \cos\theta$, $S = \sin\theta$. Substituting equations (B.3) through (B.6) in equation (B.1), the lamina transformed reduced stiffness matrices are then:

$$[\overline{Q}]=\begin{bmatrix}\overline{Q}_{11} & \overline{Q}_{12} & \overline{Q}_{16}\\ \overline{Q}_{12} & \overline{Q}_{22} & \overline{Q}_{26}\\ \overline{Q}_{16} & \overline{Q}_{26} & \overline{Q}_{66}\end{bmatrix}=[T_\sigma]^{-1}[Q][T_\varepsilon] \tag{B.7}$$

$$[\overline{Q}_S]=\begin{bmatrix}\overline{Q}_{44} & \overline{Q}_{45}\\ \overline{Q}_{45} & \overline{Q}_{55}\end{bmatrix}=[T_S]^{-1}[Q_S][T_S] \tag{B.8}$$

B.2 Transformation of Piezoelectric Constants

The actuation strain induced by a piezoelectric layer expressed in material coordinates is:

$$\begin{Bmatrix}\varepsilon_1\\ \varepsilon_2\\ \gamma_{12}\end{Bmatrix}=E_i\begin{Bmatrix}d_{i1}\\ d_{i2}\\ 0\end{Bmatrix} \tag{B.9}$$

where i = 3 for tradition monolithic piezoelectric actuators and i = 1 for MFC actuators. Using the strain transformation matrix defined in equation (B.4), the piezoelectric constant can then be express in the laminate reference coordinate as:

$$\begin{Bmatrix}d_x\\ d_y\\ d_{xy}\end{Bmatrix}=[T_\varepsilon]\begin{Bmatrix}d_{i1}\\ d_{i2}\\ 0\end{Bmatrix} \tag{B.10}$$

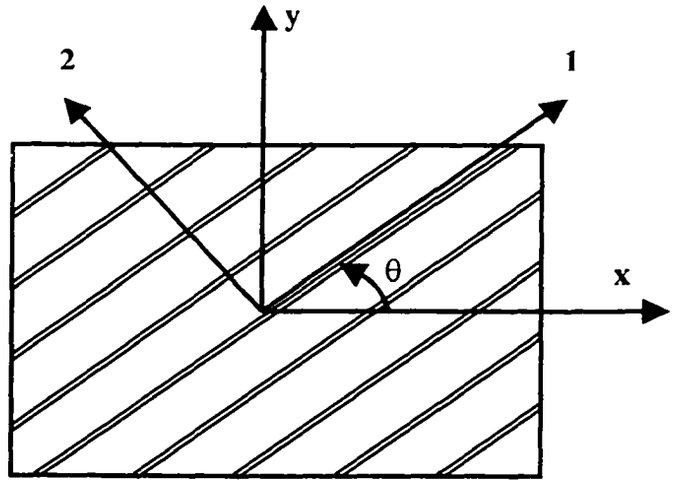

Figure B.1 Composite lamina with general fiber orientation

APPENDIX C

SOLUTION PROCEDURE FOR OPTIMAL OUTPUT FEEDBACK

Given the system state space matrices (A, B, C, D), performance index weighting matrices (Q, R), and initial conditions distribution (X_o), then the optimal output feedback gain can be determined using the following iterative solution procedure:

1. Determine an initial stabilizing gain matrix, K_o, such that $A\text{-}BK_oC$ is stable.
2. k-th iteration:

   - Set $A_c = A\text{-}B(K_y)_kC$

   - Solve for P_k and S_k matrices using $(K_y)_k$ and the following equations:

$$A_c^T P + PA_c + C^T K_y^T RK_y C + Q = 0$$

$$A_c S + SA_c^T + X_0 = 0$$

   - Set $J_k = 0.5\text{tr}(P_kX_o)$

   If $|J_k - J_{k-1}| <$ Tolerance, go to step 3, otherwise:

   Determine the gain update direction:

$$\Delta K_y = R^{-1}B^T PSC^T (CSC^T)^{-1} - (K_y)_k$$

   Update the gain using $(K_y)_{k+1} = (K_y)_k + \alpha\Delta K_y$

   where α is a chosen constant

   Repeat step 2

3. Terminate and set $K_y = (K_y)_{k+1}$

CURRICULUM VITA
for
KHALED ABDEL-MOTAGALY

DEGREES:

- Doctor of Philosophy (Aerospace Engineering), Old Dominion University, Norfolk, VA, Dec. 2001
- Master of Science (Aerospace Engineering), Cairo University, Cairo, Egypt, July 1995
- Bachelor of Science (Aerospace Engineering), Cairo University, Cairo, Egypt, July 1991

PROFESSIONAL CHRONOLOGY:

- Titan Systems Corp.- LinCom division, Houston, TX
  Senior Systems Engineer, July 1999 - Present
- Eagle Aeronautics, Newport News, VA
  Research Scientist, Jan. 1999 - June 1999
- Aerospace Engineering Dept., Old Dominion University, Norfolk, VA
  Research and Teaching Assistant, Jan 1996 - Dec. 1998
- Aerospace Engineering Dept., University of Cincinnati, Cincinnati, OH
  Teaching Assistant, Sept. 1995 - Dec. 1995
- Aerospace Engineering Dept., Cairo University, Cairo, Egypt
  Research and Teaching Assistant, Aug. 1991 - Aug. 1995

HONORS AND AWARDS:

- Member of the national honor society Phi Kappa Phi
- Graduate Scholarship, Old Dominion University, Norfolk, VA, Jan. 1996 - Dec. 1998
- Graduate Scholarship, University of Cincinnati, Cincinnati, OH, Sept. 1995 - Dec. 1995
- Graduate Scholarship, Cairo University, Egypt, Dec. 1992 - Aug. 1995
- Egyptian Engineering Syndicate excellence award for the top aerospace engineering student, 1991

- Honor degree, Cairo University, Egypt, 1991
- Student of the Year, Aerospace Engineering Department, Cairo University, Egypt, 1990-1991

SCHOLARLY ACTIVITIES COMPLETED:

Refereed Journal Articles:

- Abdel-Motagaly, K., Duan, B., and Mei, C., "Nonlinear response of composite panels under combined acoustic excitation and aerodynamic pressure," *AIAA Journal*, Vol.38, No.9, Sept. 2000, pp. 1534-1542.
- Abdel-Motagaly, K., Chen, R., and Mei, C., "Nonlinear flutter of composite panels under yawed supersonic flow using finite elements," *AIAA Journal*, Vol. 37, No. 9, Sept. 1999, pp. 1025-1032.
- Mei, C., Abdel-Motagaly, K., and Chen, R., "Review of nonlinear panel flutter at supersonic and hypersonic speeds," *Applied Mechanics Review*, Vol. 52, No 10, Oct. 1999, pp. 305-332.
- Hassan, S. D., El-Bayoumi, G. M., and Abdel-Motagaly, K., "Two new learning algorithms for rules generation in self-organizing fuzzy logic controllers," *Journal of Engineering and Applied Science*, Faculty of Engineering, Cairo University, Vol. 43, No. 4, Aug. 1996, pp. 765-780.
- Hassan, S. D., El-Bayoumi, G. M., and Abdel-Motagaly, K., "Longitudinal autopilot design for a large scale flexible missile using LQR," *Engineering Research Journal*, University of Helwan, Cairo, Egypt, Vol. 5, No. 6, June 1995, pp. 91-104.

Selected Refereed Proceedings:

- Abdel-Motagaly, K., Rombout, O., Gonzalez, R., Berrier, K., Hasan, D., Strack, D., and Rishikof, B., "Studies on the Attitude Control System Design for the Crew Return Vehicle (X38)," *Advances in the Astronautical Sciences, Guidance and Control*, Volume 104, 2000, pp. 281-297.
- Abdel-Motagaly, K., Duan, B., and Mei, C., "Nonlinear panel response at high acoustic excitations and supersonic speeds," *Proceedings of the 40th AIAA Structure, Structure Dynamics, and Materials Conference*, St. Louis, MO, April 1999, pp. 1518-1529.

- Abdel-Motagaly, K., Chen, R., and Mei, C., "Effect of flow angularity on nonlinear supersonic flutter of composite panels," *Proceedings of the 40th AIAA Structure, Structure Dynamics, and Materials Conference*, St. Louis, MO, April 1999, pp. 1963-1972.
- Aledhaibi, A., Abdel-Motagaly, K., and Huang, J., "Design of self-organizing fuzzy control for robot manipulator," Proceedings of the *4th. Joint Conference on Information Sciences (JCIS)*, Vol. 1, Oct. 1998, Research Triangle Park, NC, pp. 73-75.
- Abdel-Motagaly, K. and Alberts, T., "Robust control design for a flexible manipulator using H_∞/μ synthesis," *Proceeding of the AIAA Guidance, Navigation, and Control Conference*, Boston, Massachusetts, Aug. 1998, pp. 365-372.
- Abdel-Motagaly, K. and C. Mei, "On the control of nonlinear free vibration of a simply supported beam," *Proceedings of the 39th AIAA Structure, Structure Dynamics, and Materials Conference*, Long Beach, CA, April 1998, pp. 3266-3278.
- Lee, R. Y., Abdel-Motagaly, K., and Mei, C., "Fuzzy logic control for nonlinear free vibration of composite plates with piezoactuators," *Proceedings of the 39th AIAA Structure, Structure Dynamics, and Materials Conference*, Long Beach, CA, April 1998, pp. 867-875.
- Hassan, S. D., El-Bayoumi, G. M., and Abdel-Motagaly, K., "Application of fuzzy logic control to the longitudinal autopilot of a large scale flexible missile," *3rd International Conference on Engineering Mathematics and Physics*, Cairo, Egypt, Dec. 1997, pp. 296-308.
- Hassan, S. D., El-Bayoumi, G. M., and Abdel-Motagaly, K., "Attitude control of large scale flexible missile using self-organizing fuzzy logic control," *6th International Conference in Mechanical Design and Production*, Cairo, Egypt, Jan. 1996, pp.741-754.